FACULTY
OF MATHEMATICS
AND PHYSICS
Charles University

DOCTORAL THESIS

Libor Šmejkal

Topological band theory of relativistic spintronics in antiferromagnets

Department of Spintronics and Nanoelectronics, Institute of Physics of the Czech Academy of Sciences,
INSPIRE, Institute of Physics, Johannes Gutenberg Universität Mainz,
Faculty of Mathematics and Physics, Charles University in Prague

Supervisor of the doctoral thesis:	Tomáš Jungwirth
Study programme:	Physics
Study branch:	Physics of Nanostructures

Prague 2019

I declare that I carried out this doctoral thesis independently, and only with the cited sources, literature and other professional sources.

I understand that my work relates to the rights and obligations under the Act No. 121/2000 Sb., the Copyright Act, as amended, in particular the fact that the Charles University has the right to conclude a license agreement on the use of this work as a school work pursuant to Section 60 subsection 1 of the Copyright Act.

In .... date .... signature of the author

Title: Topological band theory of relativistic spintronics in antiferromagnets

Author: Libor Šmejkal

Institute: Department of Spintronics and Nanoelectronics, Institute of Physics of the Czech Academy of Sciences,
INSPIRE, Institute of Physics, Johannes Gutenberg Universität Mainz,
Faculty of Mathematics and Physics, Charles University in Prague

Supervisor: Tomáš Jungwirth, Institute of Physics of the Czech Academy of Sciences, Department of Spintronics and Nanoelectronics, School of Physics and Astronomy, University of Nottingham

Co-supervisor: Jairo Sinova, Institute of Physics, Johannes Gutenberg Universität Mainz, Institute of Physics of the Czech Academy of Sciences, Department of Spintronics and Nanoelectronics

Abstract: Nanoelectronics and spintronics are concerned with writing, transporting, and reading information stored in electronic charge and spin degrees of freedom at the nanoscale. Past few years have shown that two spintronics effects discovered in the 19th century, namely anisotropic magnetoresistance and anomalous Hall effect, can be used also for sensing antiferromagnetism which opened the field of antiferromagnetic spintronics. The more than a century of controversial studies of these effects have shown their relativistic spin-orbit coupling and spin-polarisation symmetry breaking origin. However, a complete understanding of these effects and a fully predictive theory capable of identifying novel suitable antiferromagnetic materials are still lacking.

Here, by extending modern symmetry and topology concepts in condensed matter physics, we have further developed the theory of anisotropic magnetoresistance and spontaneous Hall effect. Our approach is based on magnetic symmetry and topology analysis of antiferromagnetic energy bands, Bloch spectral functions, and Berry curvatures calculated from the state-of-the-art first-principle theory. This guided us to the prediction of two novel, previously unanticipated effects: relativistic metal-insulator transition from antiferromagnetic Dirac fermions, and crystal Hall effect from collinear antiferromagnetism. Signatures of both effects have been already observed, in collaboration with experimentalists, in Mn_2Au and RuO_2 thin films. Our results have contributed to the emergence of the field of topological antiferromagnetic spintronics. The field promises to provide unprecedented insights into many different physics problems, ranging from dissipationless currents to axion dark matter detection.

Keywords: antiferromagnetic Dirac fermions, topological spintronics, anisotropic magnetoresistance, spontaneous Hall effect, *ab initio* calculations

Acknowledgement

I would like to sincerely thank Tomáš that he - during our phone call in April 2013 - invited me to visit his research group, and to Jairo for letting me travel to his group on the shortest-possible-notice, when we met in Spain in September 2015. I would like to acknowledge both of my mentors for our any-time anywhere, any-problem discussions, for all the scientific freedom they have granted me while working on this thesis, and for letting me join their scientific family and meet many great people. It has been an extraordinary time - thank you.

I would like to acknowledge also all friends and colleagues. Special thanks goes to Vaclav for introducing me to Tomáš; to my advisors in Prague - Ilja, and Karel, and to Jakub, and Rafael for all the help with first-principle calculation and supercomputers; David for all the energy placed into our student grant; Karel, and Olena for discussions about model Hamiltonians; Allan, Martin, Jacob, and Yuriy for all the work on our collab papers; Eva, and Eva for helping me with all the PhD administrative and travels; and for all the great support in Mainz offices from Denise, Kei, Andrew, Hjördis and Ricardo.

I would like to appreciate Alena for supporting my route to Prague, Honza and Michael for letting me stay at their flat at the beginning of this work. I dearly thank Laura for all our science travels shaping this work over the years. And finally, I thank very much my parents and my sister Nela for always supporting my pursuit of science.

Contents

List of Abbreviations

AMR anisotropic magnetoresistance. 5, 71, 80

ASA atomic sphere approximation. 53

ASOC asymmetric spin-orbit coupling. 41, 108

CHE crystal Hall effect. 5, 108, 111

CPA coherent potential approximation. 53, 56, 71

DFT density functional theory. 6, 11, 29, 45

DMI Dzialoshinskiy–Moriya interaction. 49, 101, 106

DOS density of states. 72

DP Dirac point. 37, 74, 76

DSM Dirac semimetal. 25

FRD fully relativistic Dirac. 53

FRD-TB-LMTO-CPA fully relativistic Dirac-tight binding-linear muffin tin orbital-coherent potential approximation. 71

FRT finite-relaxation time. 60

LMTO linear muffin tin orbital. 6, 46, 53

LSDA local spin density approximation. 47

MAE magnetocrystalline anisotropy energy. 87

MLG magnetic Laue group. 98, 108

MPG magnetic point group. 18, 22

MSG magnetic space group. 5, 20

NSOT Néel spin-orbit torque. 29, 78

PAW projector-augmented-wave. 53, 63

PBE Perdew–Burke-Ernzerhof. 68

QHE quantum Hall effect. 11

RMIT relativistic metal-insulator transition. 5, 77

SOC spin-orbit coupling. 6, 35, 49, 74

SOT spin-orbit torque. 29, 38

TB tight-binding. 6, 30, 46, 53, 65

TRIM time-reversal invariant momentum. 13

WFM Weak ferromagnetism. 101, 105

Introduction

"Just knowing the correct laws of quantum mechanics does not mean that we understand all the strange phenomena that it allows"

Duncan Haldane

Dutch tulips bulbs, the dot-com bubble, rise of personal computing or bitcoin prices are a few historical examples of black swans. Effects hardly predictable but of magnificent influence characteristic for a typical exponential rise and fall of its value over a certain period as described by Nassim Nicholas Taleb [1]. This thesis is devoted to the investigation of novel topological magnetic phases of matter exhibiting black swans in magnetotransport effects in the emergining field of topological antiferromagnetic spintronics. Here topology refers to robust physical properties preserved under continuous deformations of the parameter space of the system. Antiferromagnetism describes an order magnetically modulated on the atomic scale with zero or negligible net magnetization, as firstly foreseen by Louis Néel [2]. Finally, spintronics studies the spin generation, transport, and detection aiming at a new type of nanoelectronic devices [3]. We will show in this text that antiferromagnets represent a favourable class of materials in topological spintronics research [Šmejkal et al., 2018].

We will focus on two effects - relativistic metal-insulator transition (RMIT) in Dirac quasiparticle antiferromagnets [Šmejkal et al., 2017b, Šmejkal et al., 2018], and spontaneous crystal Hall effect (CHE) from collinear antiferromagnetism [Šmejkal et al., 2019]. Both effects are characterized by an unexpectedly large magnitude and by spikes in dependencies of the effects on the Néel vector orientation. This opens attractive prospects for both fundamental types of research of magnetic topological phases and nanoelectronic applications. The RMIT and associated gigantic intrinsic anisotropic magnetoresistance (AMR) can revolutionize magnetic storage with the possibility of smaller devices, and thus improved integration, and faster readout [Šmejkal and Jungwirth, 2018]. The CHE [Šmejkal et al., 2019] or Dirac fermions in magnets [Šmejkal et al., 2017a] represent possible routes towards low dissipation electron and spin transport with high mobility in the next generation of nanoelectronics materials, or building blocks of quantum transistors [Šmejkal et al., 2018].

Last 15 years of research of topological phases of matter focused primarily on nonmagnetic systems which are less difficult to simulate than their magnetic counterparts. The Hubbard correlations, often arising in magnetic systems, complicate the calculations and are difficult to determine because of typically many competing magnetic ground-states. Furthermore, to realise the magnetic topological phases of matter, it is necessary to study, instead of 230 crystallographic space groups, the 1651 magnetic space group (MSG)s [Šmejkal and Jungwirth, 2018]. From the common intuition gained from studies of Dirac quasiparticle systems as graphene, topological insulators, or 3D Dirac semimetals, our prediction of magnetic 3D Dirac semimetals is surprising since ferromagnetism always spin-splits the bands and thus prevents the required spin degeneracy.

The thesis is divided into four thematic chapters. The first two chapters

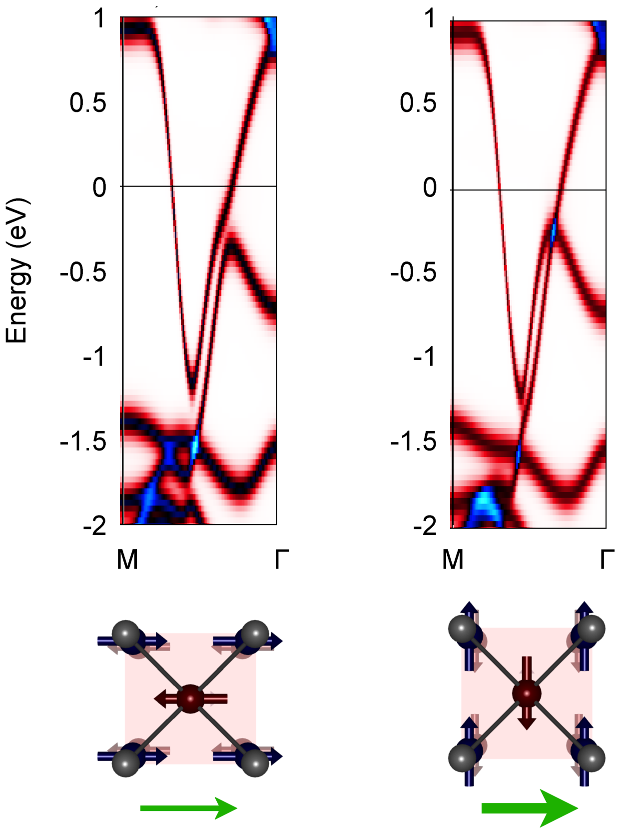

Figure 1: A Bloch spectral function in antiferromagnetic Mn_2Au exhibits a spectral weight redistribution when the Néel vector is rotated (lower panels) from being parallel to perpendicular with respect to the current (green arrows). Panels were adapted from Ref. [Bodnar et al., 2018].

present important symmetry, topology and *ab initio* theory essentials for the understanding of the RMIT and CHE. These two chapters illustrate the dichotomy of relativistic physics manifestation in our effects. First, the magnetic topological quasiparticles in energy bands can take an effective form of Dirac or Weyl quasiparticles [Šmejkal et al., 2017a] known from high energy physics. Second, the existence of AMR and CHE relies on the spin-orbit coupling (SOC), which originates from the *true* Dirac equation describing the many-particle electronic wavefunctions of our materials. Besides the summary of state-of-the-art implementations and approximations used in our theories and calculations, we include also our results on antiferromagnetic Kramers theorem, symmetry protection and classification of antiferromagnetic Dirac fermions, energy band splittings, antiferromagnetic tight-binding models, and Bloch spectral formulation of AMR within the tight-binding (TB) linear muffin tin orbital (LMTO) formalism.

In the first chapter of the thesis, we will formulate a generalised Kramers theorem for antiferromagnets [Šmejkal et al., 2017b] and we will discuss magnetic symmetries, our analysis of topological properties of wavefunctions, and our model systems.

In Chapter 2 we present the relativistic density functional theory (DFT), our numerical methods, and computational framework [Ciccarelli et al., 2016, Bodnar et al., 2018, Wagenknecht et al., 2019b, Wagenknecht et al., 2019a]. We will use it in the latter two chapters to predict material candidates for new magnetic topological semimetals and relativistic spintronics effects. We will also present our Bloch spectral function calculation formalism and we illustrate in Fig. 1 Bloch spectral function for antiferromagnetic Mn_2Au alloys.

The third chapter is devoted to our study of the dependence of the longi-

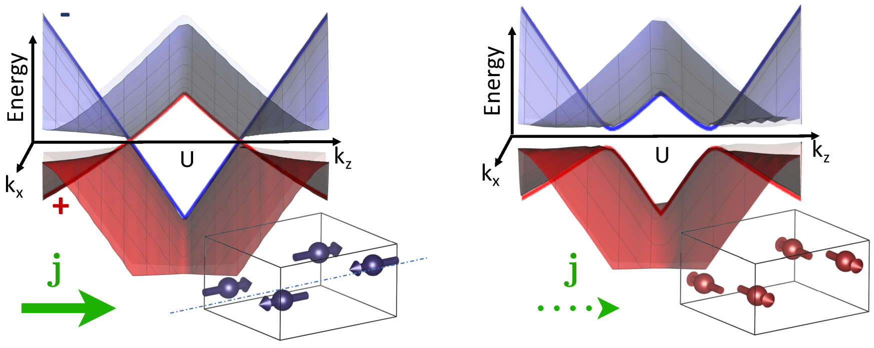

(a)

(b)

Figure 2: Schematics of Dirac quasiparticles and relativistic metal-insulator transition in antiferromagnetic orthorhombic CuMnAs. (a) Topological Dirac semimetal phase for the magnetic moment along the c-crystal axis. (b) Antiferromagnetic semiconductor phase for moments along the a-crystal axis. Panels were adapted from Ref. [Šmejkal et al., 2018].

tudinal conductivity on Néel vector orientation in antiferromagnets from first principles. We start our discussion by identifying antiferromagnetic Dirac quasiparticles in orthorhombic CuMnAs [Šmejkal et al., 2017b]. We show that the symmetry sensitivity to the Néel vector $\mathbf{N}$ orientation allows us to switch on and off Dirac quasiparticle masses, as can be seen from the simplified exemplar band dispersion:

$$E(\boldsymbol{k}) = \pm\hbar v_{\mathrm{F}}\sqrt{k_x^2 + k_y^2 + k_z^2 + \left(\frac{m(\mathbf{N})}{\hbar v_F}\right)^2}, \tag{1}$$

where v_F is the Fermi velocity, $\boldsymbol{k} = \boldsymbol{q} - \boldsymbol{q}_0$ is the crystal momentum measured from the Dirac point at $\boldsymbol{q}_0$, m is the mass (in units of energy). Such an electronic structure exhibits RMIT from the Dirac semimetal state to the semiconductor state with a global bandgap as we show in Fig. 2(a) and (b). The associated huge changes in the conductivity correspond to the ultimate, *topological intrinsic* limit of AMR. In the second part of the third chapter, we present our first principle calculations of the angular dependence of AMR in ferromagnetic NiMnSb establishing the strong crystalline and small non-crystalline AMR contributions [Ciccarelli et al., 2016]. The final part of the chapter is devoted to the first principle study of AMR in a $\mathcal{PT}$ (combination of spatial inversion $\mathcal{P}$ and time reversal $\mathcal{T}$) symmetric antiferromagnet Mn$_2$Au. We show that the dominating contribution to AMR is from a redistribution of the Bloch spectral function linked to the changes of the electronic structure close to the avoided Dirac crossings (see Fig. 1) [Bodnar et al., 2018].

In Chapter 4 we will present our theory of a new type of spontaneous Hall effect [Šmejkal et al., 2019]. We will classify all possible symmetries of the Hall vector $\boldsymbol{\sigma}$:

$$\boldsymbol{\sigma} = \mathbf{j}_H \times \mathbf{E} \tag{2}$$

which determines the Hall transport plane. Here $\mathbf{E}$ is the applied longitudinal electric field, and $\mathbf{j}_H$ is the measured transversal Hall current. The Hall vector is in conventional ferromagnets oriented typically along the magnetization $\mathbf{M}$ as we illustrate in Fig. 3(a).

In recent years the spontaneous Hall effect was also found in zero net moment systems with complex non-collinear, non-coplanar or spin liquid magnetism (Ref. [Šmejkal and Jungwirth, 2018] and references therein). Simple collinear antiferromagnets, on the other hand, are commonly believed to be prevented from Hall effects, referring to the intuitive cancellation of the opposite spin channels due to an effective time-reversal symmetry, as we illustrate in Fig. 3(b) for Mn_2Au with the $\mathcal{PT}$ symmetry. However, collinear antiferromagnets host many appealing properties such as robust intrinsic magnetism, high Néel temperature, and available means of Néel vector reorientation.

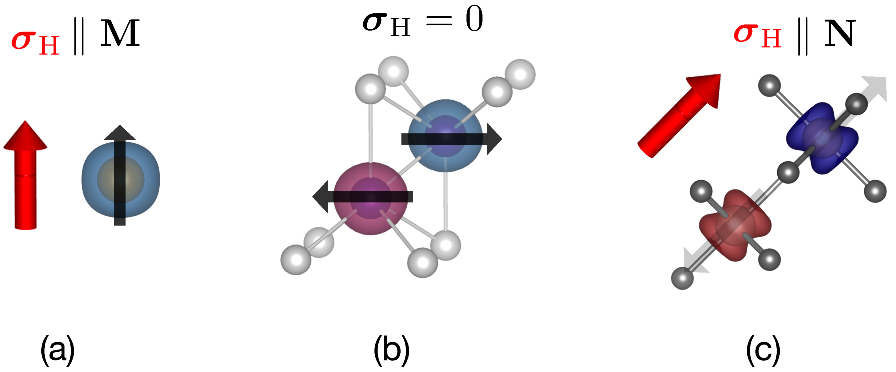

Figure 3: **Crystal Hall effect from collinear antiferromagnetism.** (a) Anomalous Hall effect from net magnetization in a ferromagnet with a spherical magnetization density. (b) In antiferromagnets such as Mn_2Au the anomalous Hall effect is prohibited by symmetry. (c) In antiferromagnets such as RuO_2 the low symmetric magnetization densities can generate crystal Hall effect.

We will show in Chapter 4 that certain collinear antiferromagnets with non-magnetic atoms distributed at low symmetry lattice positions can break required symmetries to generate a large Hall conductivity parallel (or perpendicular) to the Néel vector:

$$\boldsymbol{\sigma}_{\mathrm{CHE}} \parallel \mathbf{N}. \tag{3}$$

We will discuss this crystal Hall effect mechanism and we will identify simple rules for a non-zero Hall conductivity in antiferromagnets and calculate large magnitudes in antiferromagnetic RuO_2 and $CoNb_3S_6$. The Hall conductivities correspond to a large magnitude of intrinsic emergent relativistic magnetic fields which can be expressed in terms of geometric topological properties of Bloch functions, namely the Berry curvatures, as we explain in the first two chapters. To produce an equally strong deflection of electrons in conventional non-magnetic systems, we would need an excessive external magnetic field, e.g. ∼200 T in the case of Mn_3Ge [4].

Generating such a large magnitude of an external magnetic field is unfeasible. The observation that a perfectly compensated collinear antiferromagnet can host strong internal fields is remarkable, since other related relativistic effects, such as canting due to the Dzyaloshinskii-Moriya interaction are usually of a perturbative relativistic origin and have tiny magnitudes. These strong deflecting fields originate from the low symmetry magnetization densities shown in Fig. 3(c). Our investigation not only sheds new light on symmetry breaking mechanisms and theory of spontaneous Hall effects in general but provides evidence of our effect in the RuO_2 antiferromagnet.

Signatures of both AMR in Mn_2Au, and CHE in RuO_2 [5] were confirmed in magnetotransport experiments[Bodnar et al., 2018]. The spectra obtained from the photoemission experiments on tetragonal CuMnAs [Veis et al., 2018] are consistent with the electronic correlation strength of approximately 3 eV which can substantially influence also the Dirac fermions in the orthorhombic CuMnAs. Results presented in this thesis thus provide compelling evidence that antiferromagnetism represents a favourable magnetic order for exploring and exploiting novel and technologically relevant magnetic topological phases of matter and spintronics effects. The antiferromagnetic materials and systems studied in this thesis can find applications ranging from the building blocks of beyond von-Neumann computer architectures, as neuromorphic computers, to more esoteric fundamental research of dark matter detection [Marsh et al., 2019]. Results presented in this thesis contributed to establishing a field of *topological antiferromagnetic spintronics* [Šmejkal et al., 2018].

List of publications

[Bodnar et al., 2018] Bodnar, S. Y., Šmejkal, L., Turek, I., Jungwirth, T., Gomonay, O., Sinova, J., Sapozhnik, A. A., Elmers, H.-J., Kläui, M., and Jourdan, M. (2018). Writing and reading antiferromagnetic Mn2Au by Néel spin-orbit torques and large anisotropic magnetoresistance. *Nature Communications*, 9(1):348.

[Ciccarelli et al., 2016] Ciccarelli, C., Anderson, L., Tshitoyan, V., Ferguson, A. J., Gerhard, F., Gould, C., Molenkamp, L. W., Gayles, J., Železný, J., Šmejkal, L., Yuan, Z., Sinova, J., Freimuth, F., and Jungwirth, T. (2016). Room-temperature spin-orbit torque in NiMnSb. *Nature Physics*, 12(9):855–860.

[Marsh et al., 2019] Marsh, D. J. E., Fong, K. C., Lentz, E. W., Šmejkal, L., and Ali, M. N. (2019). Proposal to Detect Dark Matter using Axionic Topological Antiferromagnets. *Physical Review Letters*, 123(12):121601.

[Šmejkal et al., 2019] Šmejkal, L., González-Hernández, R., Jungwirth, T., and Sinova, J. (2019). Crystal Hall effect in Collinear Antiferromagnets. *arXiv:1901.00445*.

[Šmejkal and Jungwirth, 2018] Šmejkal, L. and Jungwirth, T. (2018). Symmetry and topology in antiferromagnetic spintronics. In Zang, J., Cros, V., and Hoffmann, A., editors, *Topology in magnetism*, pages 267–298. Springer International Publishing.

[Šmejkal et al., 2017a] Šmejkal, L., Jungwirth, T., and Sinova, J. (2017a). Route towards Dirac and Weyl antiferromagnetic spintronics. *Physica Status Solidi - Rapid Research Letters*, 11(4).

[Šmejkal et al., 2018] Šmejkal, L., Mokrousov, Y., Yan, B., and MacDonald, A. H. (2018). Topological antiferromagnetic spintronics. *Nature Physics*, 14(3):242–251.

[Šmejkal et al., 2017b] Šmejkal, L., Železný, J., Sinova, J., and Jungwirth, T. (2017b). Electric Control of Dirac Quasiparticles by Spin-Orbit Torque in an Antiferromagnet. *Physical Review Letters*, 118(10):106402.

[Veis et al., 2018] Veis, M., Minár, J., Steciuk, G., Palatinus, L., Rinaldi, C., Cantoni, M., Kriegner, D., Tikuišis, K. K., Hamrle, J., Zahradník, M., Antoš, R., Železný, J., Šmejkal, L., Marti, X., Wadley, P., Campion, R. P., Frontera, C., Uhlířová, K., Duchoň, T., KuŽel, P., Novák, V., Jungwirth, T., and Výborný, K. (2018). Band structure of CuMnAs probed by optical and photoemission spectroscopy. *Physical Review B*, 97(12):125109.

[Wagenknecht et al., 2019a] Wagenknecht, D., Kudrnovsky, J., Šmejkal, L., Carva, K., and Turek, I. (2019a). Electrical transport with temperature-induced spin disorder in NiMnSb. *Journal of Magnetism and Magnetic Materials*, 474:517–521.

[Wagenknecht et al., 2019b] Wagenknecht, D., Šmejkal, L., Kašpar, Z., Sinova, J., Jungwirth, T., Kudrnovsky, J., Carva, K., and Turek, I. (2019b). Temperature-dependent resistivity and anomalous Hall effect in NiMnSb from first principles. *Physical Review B*, 99(17):174433.

1. Topological antiferromagnetic band theory

"By symmetry we mean the existence of different viewpoints from which the system appears the same. It is only slightly overstating the case to say that physics is the study of symmetry."

Philip Warren Anderson [6]

Before the 1980s the phases of matter were conventionally classified by the symmetry breaking paradigm [7]. The discovery of the quantum Hall effect (QHE) introduced an additional label, the topological index or Chern number of the electronic wavefunctions [7, 8]. QHE refers to the quantization of the Hall conductivity in a quasi-2D electron gas in a strong magnetic field. Topology is concerned with properties of an object preserved under continuous deformations. The conventional spaces in condensed matter physics are the manifolds which are a subset of topological spaces [9]. Topology in electronic structure can be associated with robust quasiparticles in energy bands [10]. For instance, the bandstructure of the trivial insulator can be continuously deformed to the atomic limit, while this is impossible with the bands of topological insulators. Avoided and unavoided band crossings were investigated since the very early days of quantum mechanics [11], and the critical phases of matter existing at the transition between metallic and insulating state were discussed already in 1970s [12]. In part owing to the predictions of the intrinsic spin Hall effect [13, 14] and experimental discovery of graphene [15], many different types of Dirac quasiparticles were predicted and found in non-magnetic systems in the past 15 years: topological insulators [16], Dirac and Weyl semimetals [17, 18, 19, 20], higher-order degeneracies with no high-energy physics counterparts [21], or higher-order topological insulators [22], to name a few. This invasion of topology into physics was recognized by the 2016 Nobel Prize.

The fundamental science exploration of quantized observables and corresponding low dissipation states are driving the search of novel topological phases of matter. However, the intrinsic magnetic systems are less investigated, partly due to the complicated nature of the many-particle and relativistic quantum nature of the (antiferro)magnetic ordering [23, 24]. In this chapter, we focus on the basic classification of Dirac quasiparticles in antiferromagnetic solids within a single particle picture. Such a picture can be useful for understanding energy bands, their topological characterization and associated spin transport effects in itinerant antiferromagnets [25, 26], or in antiferromagnets with localised moments whose bandstructure is possible to describe within DFT + Hubbard correlation U approximation. Firstly, we will introduce an antiferromagnetic generalisation of the Kramers theorem [27, 28]. In the second part of this chapter we will discuss Berry phases [10, 29, 30, 31, 32] and topological characterization of electronic states [33, 34, 35, 36], magnetic symmetries [26] and a Dirac quasiparticle catalogue in antiferromagnets and symmetries of linear response coefficients. In the last part of the chapter, we will formulate and discuss minimal TB models illustrating tunable Dirac quasiparticles in an antiferromagnet, and nodal chains generating spontaneous Hall conductivity in perfect collinear antiferromagnets. We will illustrate the role of discrete symmetries (spatial inversion and time reversal) in the classification of Dirac quasiparticles and Berry phases on exemplar band structures. We will show that antiferromagnetism plays a crucial role both from a fundamental symmetry perspective, as well as from a practical technological viewpoint. The former manifests itself, for instance, in the existence of 3D Dirac antiferromagnets, while 3D Dirac ferromagnetism is prohibited (the energy bands are Zeeman split). The latter is reflected in the abundance of antiferromagnetism in nature when compared to relatively rare ferromagnetism, in the fast internal THz frequencies of the antiferromagnetic order parameter, robust intrinsic magnetism, high Néel temperatures and versatility of a wide palate of reported electronic phases [3, 23, 37, 38]. The results presented in this chapter will be used to understand our fist principle calculations in real materials discussed in Chapters 3 and 4, namely in CuMnAs, Mn_2Au, RuO_2 and $CoNb_3S_6$.

1.1 Antiferromagnetic Kramers theorem

Discrete symmetries such as unit-cell and partial unit-cell translation, time reversal, or spatial inversion have profound consequences on electronic structure, the band splitting, spin polarisations, topological properties of the electronic quasiparticles, and transport effects.

We start discussing time-reversal $\mathcal{T}$ which is an operation which reverses direction of time in our systems. Time-reversal does not change the position operator $\hat{x}$, however, momentum $\hat{p}$ changes sign under $\mathcal{T}$. Since $\mathcal{T}[\hat{x},\hat{p}]\mathcal{T}^{-1} = \mathcal{T}i\hbar\mathcal{T}^{-1} = -[\hat{x},\hat{p}] = -i\hbar$ we need to make the time-reversal operator proportional to complex conjugation, in other words antiunitary. In spinless theories, $\mathcal{T} = \mathcal{K}$, where $\mathcal{K}$ marks complex conjugation operator [32].

We are interested here in spinfull systems. The $\mathcal{T}$ action on the particles spin $\mathbf{S}$ changes its sign, and we define $\mathbf{S} = \frac{\hbar}{2}(\sigma_x, \sigma_y, \sigma_z)$ with the help of Pauli matrices:

$$\sigma_1 = \begin{pmatrix} 0 & 1 \\ 1 & 0 \end{pmatrix}, \quad \sigma_2 = \begin{pmatrix} 0 & -\mathrm{i} \\ \mathrm{i} & 0 \end{pmatrix}, \quad \sigma_3 = \begin{pmatrix} 1 & 0 \\ 0 & -1 \end{pmatrix}. \tag{1.1}$$

The spinfull $\mathcal{T}$ thus acquires an operation rotating the spin, and we use a common convention for choosing the rotation axis along y axis, $mathcalT = e^{-i\pi S_y \hat{\mathcal{K}}}$ [32]. The square of the operator gives, $\mathcal{T}^2 = e^{-i2\pi S_y}$, where we have used Eq. (1.1). Rotating twice integer spin particles gives identity, while rotating twice half-integer spins gives a factor -1. In the half-integer case we can perform matrix exponentiation [32] to obtain:

$$\mathcal{T} = i\sigma_y\mathcal{K}. \tag{1.2}$$

We can verify that our operator squares to -1, as can be demonstrated by Dirac's belt trick [39].

Wigner [40] demonstrated that the time-reversal symmetry enforces Kramers theorem [41]: *In systems with an odd number of half-integer spin particles, the energy levels are at least double degenerate.* The proof can be found elsewhere

[32], and we will focus now on band-degeneracies in Brillouin zones of *magnetic* periodic solids which can be labelled by the quantum number: crystal momentum $\boldsymbol{k}$. The electronic states in periodic crystal are assigned Bloch wavefunctions, modulated plane waves delocalised in real space:

$$\psi_{n\boldsymbol{k}} = e^{i\boldsymbol{k}\cdot\mathbf{r}}u_{n\boldsymbol{k}}(\mathbf{r}), \tag{1.3}$$

where we have introduced the band index n, and the lattice-periodic wavefunction part:

$$u_{n\boldsymbol{k}}(\mathbf{r}) = u_{n\boldsymbol{k}}(\mathbf{r}+\mathbf{R}), \tag{1.4}$$

with $\mathbf{R}$ being lattice vector. Time reversal changes the sign of the crystal momentum, the Hamiltonian at $\boldsymbol{k}$ is transformed to the same Hamiltonian at $-\boldsymbol{k}$ [32] and we obtain for energy:

$$\mathcal{T}E_{n\sigma}(\boldsymbol{k}) = E_{n-\sigma}(-\boldsymbol{k}). \tag{1.5}$$

The Hamiltonian is invariant under $\mathcal{T}$ at specific points in the Brillouin zone, the so called time-reversal invariant momentum (TRIM), which we denote $\mathbf{G}/2$, e.g., $(0,0,0),(\pi,0,0),...,(\pi,\pi,\pi)$ [42]. The corresponding states have thus in time-reversal invariant system the same energy due to the Kramers theorem.

Is there a way how to make states Kramers degenerate for arbitrary crystal momentum? Can we expect Dirac quasiparticle double degenerate dispersion in certain solids? The answer is yes and we need to realise that we can get help from another discrete symmetry: spatial inversion $\mathcal{P}$. $\mathcal{P}$ transforms spin, crystal momentum, and energy bands as:

$$\mathcal{P}E_{n\sigma}(\boldsymbol{k}) = E_{n\sigma}(-\boldsymbol{k}). \tag{1.6}$$

We can combine last equation with Eq. (1.5) to obtain that in systems with both $\mathcal{P}$ and $\mathcal{T}$ symmetries (centrosymmetric non-magnetic systems), energy bands are Kramers degenerate [32].

Does this mean that we cannot obtain double degenerate bands over the entire Brillouin zone in magnetic systems? We will show that also certain antiferromagnetic systems can have double degenerate bands everywhere in the Brillouin zone and we will formulate a generalised Kramers theorem [27].

Theorem 1: Generalized Kramers.

In antiferromagnetic systems with $\mathcal{P}\circ\mathcal{T}$ or $\mathcal{P}$ and $\mathcal{T}\mathbf{t}$ symmetries and in non-magnetic systems with $\mathcal{P}$ and $\mathcal{T}$ symmetries the energy bands are Kramers spin degenerate for arbitrary momentum.

Proof. Let us consider a wavefunction $\psi_{\boldsymbol{k}}$ with energy $E_{\boldsymbol{k}}$. Since $\mathcal{PT}$ is a symmetry of the Hamiltonian, the two operators commute. Consequently

$$H_{\boldsymbol{k}}\phi_{\boldsymbol{k}} = H_{\boldsymbol{k}}\mathcal{PT}\psi_{\boldsymbol{k}} = E_{\boldsymbol{k}}\mathcal{PT}\psi_{\boldsymbol{k}} = E_{\boldsymbol{k}}\phi_{\boldsymbol{k}}. \tag{1.7}$$

This means that the $\mathcal{PT}$ transformed state with a wafunction $\phi_{\boldsymbol{k}} = \mathcal{PT}\psi_{\boldsymbol{k}}$ is also an eigenstate of the Hamiltonian. $\mathcal{PT}$ is antiunitary, $(\mathcal{PT})^2 = -1$ making the $\mathcal{PT}$ partner states,

$$(\phi_{\boldsymbol{k}},\psi_{\boldsymbol{k}}) = (\mathcal{PT}\phi_{\boldsymbol{k}},\mathcal{PT}\psi_{\boldsymbol{k}}) = (\mathcal{PT})^2(\phi_{\boldsymbol{k}},\psi_{\boldsymbol{k}}) = -(\phi_{\boldsymbol{k}},\psi_{\boldsymbol{k}}), \tag{1.8}$$

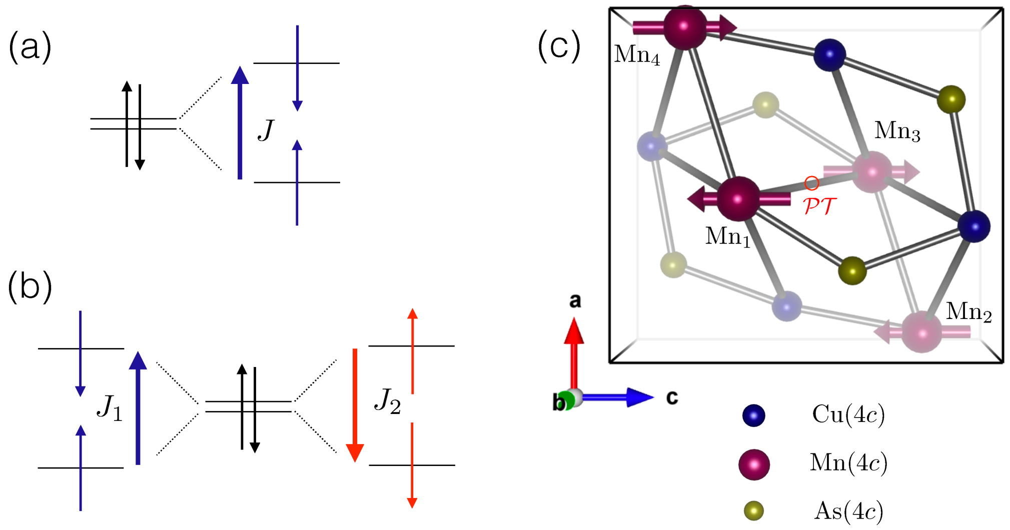

Figure 1.1: Antiferromagnetic Kramers theorem. (a) Ferromagnetic exchange field J splits spin-degenerate bands and prevents Kramers theorem. (b) The effective time-reversal symmetry connecting the antiferromagnetic sublattices can protect the Kramers theorem. (c) Example of an antiferromagnetic crystal with combined time reversal and spatial inversion symmetry $\mathcal{PT}$ - orthorhombic CuMnAs. We number also the Mn atoms and we include the Wyckoff positions labels.

orthogonal, i.e. $(\phi_{\boldsymbol{k}}, \psi_{\boldsymbol{k}}) = 0$, where $(,)$ denotes scalar product. $\phi_{\boldsymbol{k}}$, and $\psi_{\boldsymbol{k}}$ are thus degenerate states and the spectrum of the $\mathcal{PT}$ symmetric Hamiltonian is doubly degenerate for a generic crystal momentum. The theorem is proven analogically for the case of the $\mathcal{P}$ and $\mathcal{T}\mathbf{t}$ symmetry, q.e.d.

Our theorem proves useful in analysing magnetic topological phases of matter since it represents a necessary ingredient for forming a Dirac fermion dispersion in antiferromagnets which we will discuss in the third section of this chapter.

1.2 Berry phases

Before turning our attention to the crystal momentum space we will briefly discuss geometric and adiabatic character of Berry phases [29, 43, 44]. Let us consider quantum systems with a Hamiltonian $H(\boldsymbol{\Lambda}(t))$ where the parameter evolves adiabatically with time t. The eigenstates at a given instant can be obtained from the Schrödinger equation:

$$H(\boldsymbol{\Lambda})|n(\boldsymbol{\Lambda})\rangle = E_n(\boldsymbol{\Lambda})|n(\boldsymbol{\Lambda})\rangle, \tag{1.9}$$

where n labels again the quantum number. To study phases arising during the adiabatic motion we assume solutions in the form:

$$|\psi(t)\rangle = c(t)e^{-i\gamma_n}|n(t)\rangle, \tag{1.10}$$

where the eigenstate $|n(t)\rangle$ is evaluated at $\boldsymbol{\Lambda} = \boldsymbol{\Lambda}(t)$. $\gamma_n(t)$ is the conventional dynamical phase [30]:

$$\gamma_n(t) = \frac{1}{\hbar}\int_0^t E_n(t')dt'. \tag{1.11}$$

We substitute the ansatz (1.10) into the time-dependent Schrödinger equation and we obtain:

$$0 = \dot{c}(t)|n(t)\rangle + c(t)|\dot{n}(t)\rangle. \tag{1.12}$$

By applying $\langle n(t)|$ from the left side of the last equation we get [10]:

$$\dot{c}(t) = ic(t)\, \langle n(t)|i\partial_t n(t)\rangle\, . \tag{1.13}$$

The last equation has a solution, $c(t) = e^{i\phi(t)}$, and we have thus obtained the additional factor called the Berry phase:

$$\phi(t) = \int_0^t A_n\left(t'\right) dt', \tag{1.14}$$

where

$$A_n(t) = \langle n(t)|i\partial_t n(t)\rangle \tag{1.15}$$

is the Berry connection. We can change variables by applying the time-derivative chain rule on $\partial_t|n(\mathbf{\Lambda}(t))\rangle$ to obtain:

$$\phi(t) = \int_{\lambda(0)}^{\lambda(t)} A_n(\lambda)d\lambda, \tag{1.16}$$

where the transformed Berry connection $A_n(\lambda) = \langle n(\lambda)|i\partial_\lambda n(\lambda)\rangle$. As long as the dynamics is adiabatic the Berry phase does not depend on the rate at which the path was travelled through but instead depends only on the path in the parameter space, and sometimes is called *geometrical phase* [10, 32, 45].

In the adiabatic approximation, the Hamiltonian variation with the parameters is small enough such that the Hamiltonian remains in the (non-degenerate) eigenstate during the evolution. This adiabatic condition for a vanishingly small probability of the transition of state n into a different state m can be estimated by the adiabatic perturbation theory (related to the Steinheimer formula[10]) to be [45]:

$$\hbar|\langle m|\dot{H}|n\rangle| \ll |E_m - E_n|^2\, . \tag{1.17}$$

Under this assumption, the system returns into its initial state after cyclic evolution in the parameter space.

Stokes theorem. The cyclic Berry phase can be expressed with the help of the Stokes theorem[46] as:

$$\phi = \oint_{\delta S} \mathbf{A}\cdot d\lambda = \int_S \Omega_{\mu\nu} ds_\mu \wedge ds_\nu, \tag{1.18}$$

where the the second integral is over N dimensional space S with the element $ds_\mu \wedge ds_\nu$ (the wedge product marks in differential geometry higher-dimensional generalisation of the vector product in the context of manifolds and form integrations), while the first integral is over the $N-1$ dimensional boundary, δS. Furthermore, we introduce the Berry curvature:

$$\Omega_{\mu\nu} = \partial_\mu A_\nu - \partial_\nu A_\mu = -2\,\mathrm{Im}\,\langle \partial_\mu n|\partial_\nu n\rangle \tag{1.19}$$

as an antisymmetric real second-rank tensor. In three-dimensional parameter spaces, e.g. crystal momentum, we can take advantage of the pseudovector notation:

$$\mathbf{\Omega} = -\,\mathrm{Im}\,\langle \nabla_\lambda n| \times |\nabla_\lambda n\rangle\, , \tag{1.20}$$

e.g. $\Omega_z \equiv \Omega_{xy} = -2\,\mathrm{Im}\,\langle \partial_x n | \partial_y n \rangle$. This motivates the analogy of the Berry connection $\mathbf{A}(\mathbf{\Lambda})$, and Berry curvature $\mathbf{\Omega}(\mathbf{\Lambda})$ with the electromagnetic field vector potential $\mathbf{A}(\mathbf{R})$ and magnetic field $\mathbf{B}(\mathbf{R}) = \nabla \times \mathbf{A}(\mathbf{R})$ in real space. While the potentials (Berry connection) are gauge-dependent, the fields (Berry curvature) are gauge independent since the $\nabla\times$ operations removed it. We will discuss gauge dependence of the multiband formulation of Berry curvature in the next section [10].

Berry curvatures and Chern numbers in the crystal momentum space

So far we have discussed the generic space of parameters $\mathbf{\Lambda}$. We will illustrate now that we can apply this formalism to periodic Brillouin zone wavevectors, aka crystal momentum torus. The crystal momentum parameter space is unique since it represents internal parameters of the systems, in contrast to external parameters such as magnetic fields [31]. The built-in periodicity is very appealing since a finite Berry phase is accumulated when the state is driven by an external perturbation (e.g. electric field) to vary through the entire Brillouin zone. Since inner products of Bloch wavefunctions (1.3) are ill defined due to the averaging [10], we will use the well-behaving cell-periodic parts of the Bloch functions (1.4) and we will label the states of a solid correspondingly $|u_n(\boldsymbol{k})\rangle$. The **Berry phase** of nth band reads:

$$\phi_n = \oint \mathbf{A}_n(\boldsymbol{k}) \cdot d\boldsymbol{k} \tag{1.21}$$

with crystal momentum **Berry connection**:

$$A_{n\mu}(\boldsymbol{k}) = \langle u_{n\boldsymbol{k}} | i\partial_\mu u_{n\boldsymbol{k}} \rangle \,. \tag{1.22}$$

The **Berry curvature** in the crystal momentum space takes the form:

$$\Omega_{n,\mu\nu}(\boldsymbol{k}) = \partial_\mu A_{n\nu}(\boldsymbol{k}) - \partial_\nu A_{n\mu}(\boldsymbol{k}) = -2\,\mathrm{Im}\,\langle \partial_\mu u_{n\boldsymbol{k}} | \partial_\nu u_{n\boldsymbol{k}} \rangle \,. \tag{1.23}$$

We can transform this formula by inserting quantum unity decomposition of the Hamiltonian, $\langle n' | \nabla n \rangle = \frac{\langle n' | \nabla H | n \rangle}{E_n - E_{n'}}$, to the form

$$\Omega_{n,\mu\nu}(\boldsymbol{k}) = i \sum_{n' \neq n} \frac{\langle n \left| (\partial H / \partial k_\mu) \right| n' \rangle \langle n' \left| (\partial H / \partial k_\nu) \right| n \rangle - (\nu \leftrightarrow \mu)}{(\varepsilon_n - \varepsilon_{n'})^2} . \tag{1.24}$$

This formula is useful in numerical implementations, when we want to circumvent the numerical derivative of the rapidly oscillating Bloch functions. Instead, we evaluate in Eq. (1.24) the derivative of the Hamiltonian.

Chern number. Two-dimensional Brillouin zone has a topology of a torus. The Berry curvature integrated over a two-dimensional torus takes a 2π quantized value [10, 33],

$$\int_{\mathrm{BZ}} \Omega_{n,\mu\nu} d^2 k = 2\pi \mathcal{C}_n , \tag{1.25}$$

where $\mathcal{C}_n$ is a Chern number. This equation represents a specific two-dimensional case of a general mathematical Chern formula proven in any even dimension [10] and it is also sometimes called the TKKN formula [33]. The two-dimensional manifold can be, for instance, a Brillouin zone in the quantum (anomalous) Hall system where the Chern number corresponds to the observable Hall conductivity [47], or spherical surface around three dimensional sphere surrounding Weyl points [32, 48]. Chern number is an example of the topological invariant, a quantity which can be ascribed to bandstructure quasiparticles which does not change upon smooth transformation of the Hamiltonian. Various generalizations of the Chern number were introduced to describe topological quasiparticles in materials, example being the crystalline Chern number and its analogy can be used in Dirac quasiparticle antiferromagnets [27, 28, 49, 50]. We have gauge freedom to transform the Bloch functions as $\widetilde{u_{n\boldsymbol{k}}} = e^{i\alpha(\boldsymbol{k})}u_{n\boldsymbol{k}}$, and the Berry connection depends on the gauge as:

$$\widetilde{\mathbf{A}}_n(\boldsymbol{k}) = \mathbf{A}_n(\boldsymbol{k}) + \nabla_{\boldsymbol{k}}\beta(\boldsymbol{k}). \tag{1.26}$$

In contrast, Chern numbers are invariant under gauge transformations.

Multiband Berry phase and curvature. So far we have explicitly or implicitly considered isolated energy bands, however, the concept of Berry curvature and Chern numbers can be straightforwardly generalised to multiband systems [51, 52, 53, 54]. Multiband cases arise commonly in the metallic system where the bands can be entangled in a complicated way and we will describe a numerical method to calculate the multiband Berry curvature in antiferromagnetic metals from first principles in Chapter 2. Multiband Berry curvatures are called also sometimes nonabelian or noncommutative since the matrices in multiband cases are not diagonal and do not commute in general and thus form nonabelian symmetry groups. The Berry connection generalises to the expression [10, 48]:

$$\mathcal{A}_{mn,\alpha} = i\left\langle u_{m\boldsymbol{k}}\left|\partial_\alpha\right| u_{n\boldsymbol{k}}\right\rangle. \tag{1.27}$$

The corresponding multiband Berry curvature can be written in the covariant form [48, 55]:

$$\mathcal{F}_{mn,\mu\nu} = \Omega_{mn,\mu\nu} - i\left[\mathcal{A}_\mu, \mathcal{A}_\nu\right]_{mn}, \tag{1.28}$$

where:

$$\begin{aligned} \Omega_{mn,\mu\nu}(\boldsymbol{k}) &= \partial_\mu\mathcal{A}_{mn,\nu}(\boldsymbol{k}) - \partial_\nu\mathcal{A}_{mn,\mu}(\boldsymbol{k}) \\ &= i\left\langle\partial_\mu u_{m\boldsymbol{k}}|\partial_\nu u_{n\boldsymbol{k}}\right\rangle - i\left\langle\partial_\nu u_{m\boldsymbol{k}}|\partial_\mu u_{n\boldsymbol{k}}\right\rangle. \end{aligned} \tag{1.29}$$

By a covariant form we mean here that the Berry curvature is in gauge-covariant form as it was in the single band case. This property is not recovered for the naive generalisation of the single band Berry curvature given by Eq. (1.29). This procedure is required since the physical quantities of interest which we calculate from the Berry curvature ought to be gauge-invariant [10].

The observable quantities which can be expressed in terms of Berry phases and also can take quantized values are e.g. polarization, Hall conductivity, and magnetoelectric polarisability [22]. The Hall conductivity can be expressed in the differential geometry form [33, 54, 56]:

$$\sigma_{\mu\nu} = -\frac{e^2}{2\pi h}\int_{BZ}\mathrm{Tr}[d\mathcal{A} + i\mathcal{A}\wedge\mathcal{A}], \tag{1.30}$$

where $\mathcal{A}$ refers to the Berry connection, for the sake of brevity we have dropped the momentum and band indices, and the integral is taken over the entire Brillouin zone (BZ). We will describe the numerical calculation of the Hall conductivity from first principles in Chapter 2.

The diagonal part of the magnetoelectric polarisability tensor [35, 57] is called in axion electrodynamics θ. It can be expressed in terms of the Berry connection:

$$\theta = -\frac{e^2}{4\pi h}\int_{BZ} \mathrm{Tr}\left[\mathcal{A}\wedge d\mathcal{A} + \frac{2i}{3}\mathcal{A}\wedge\mathcal{A}\wedge\mathcal{A}\right], \tag{1.31}$$

where the trace is taken over occupied states. θ can be taken as defining property of topological non-magnetic insulators, where it takes a $\theta = \pi$ value in contrast to trivial non-magnetic insulators with $\theta = 0$. We use this parameter to characterize Dirac quasiparticle antiferromagnets useful for axion dark matter detection [58, 59, 60] and it defines the topological magnetoelectric effect and static magnetic axion insulators [61].

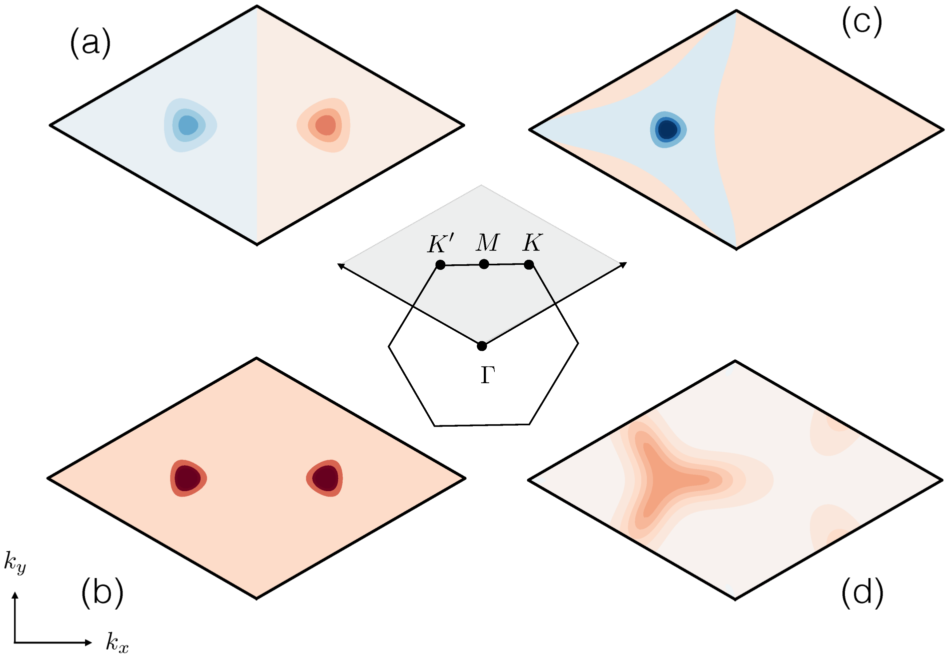

Figure 1.2: Symmetries of Berry curvature in the crystal momentum space. (a) $\mathcal{T}$ preserved and $\mathcal{P}$ broken. The Berry curvature is locally nonzero while its Brillouin zone integral vanishes. (b) $\mathcal{T}$ broken and $\mathcal{P}$ preserved. (c) Both $\mathcal{T}$ and $\mathcal{P}$ broken. (d) As in (c), additionally the system exhibits an integer Chern number and a quantized Hall conductivity. In the middle inset we show the Brillouin zone of the Haldane honeycomb model used for the Berry curvature plots and described in details in the TB model section.

The Berry curvature pseudovector transforms identically as a spin vector and depends on the magnetic point group (MPG) symmetries and we can list useful properties:

1. The Berry curvature is odd under time-reversal:

$$\mathcal{T}\boldsymbol{\Omega}(\boldsymbol{k}) = -\boldsymbol{\Omega}(-\boldsymbol{k}), \tag{1.32}$$

   and thus in the time-reversal symmetric system the integrals over the Berry curvature vanish, as can be seen from Semenoff model of graphene with its Berry curvature shown in Fig. 1.2(a).

2. The spatial inversion symmetry transforms Berry curvature as:

$$\mathcal{P}\boldsymbol{\Omega}(\boldsymbol{k}) = \boldsymbol{\Omega}(-\boldsymbol{k}), \tag{1.33}$$

   and we illustrate this Berry curvature property on the centrosymmetric Haldane model [62] in Fig. 1.2(b).

3. If both $\mathcal{P}$ and $\mathcal{T}$, or more generally only the combined $\mathcal{P}\circ\mathcal{T}$ are present, the Berry curvature vanishes identically. Exemplar systems include the Dirac quasiparticle antiferromagnets (CuMnAs, Mn_2Au).

4. The spatial unitary and antiunitary symmetries operate as [63]:

$$\begin{aligned} \mathcal{M}_y\boldsymbol{\Omega}(\boldsymbol{k}) &= (-\Omega_x, \Omega_y, -\Omega_z)(k_x, -k_y, k_z), \\ \mathcal{C}_{2y}\boldsymbol{\Omega}(\boldsymbol{k}) &= (-\Omega_x, \Omega_y, -\Omega_z)(-k_x, k_y, -k_z), \\ \mathcal{T}\mathcal{M}_x\boldsymbol{\Omega}(\boldsymbol{k}) &= (-\Omega_x, \Omega_y, \Omega_z)(k_x, -k_y, -k_z), \\ \mathcal{T}\mathcal{C}_{2x}\boldsymbol{\Omega}(\boldsymbol{k}) &= (-\Omega_x, \Omega_y, \Omega_z)(-k_x, k_y, k_z). \end{aligned}$$

   Analogical symmetry transformations can be obtained for symmetries derived from the three-fold, four-fold and six-fold rotations [63].

In Fig. 1.2(c-d) we demonstrate a Haldane model with broken both $\mathcal{P}$ and $\mathcal{T}$ and preserved three-fold rotation. While panel (c) illustrates a Chern number equal to zero, panel (d) corresponds to a nonzero Chern number and a quantum anomalous Hall state, as we will explore in greater detail in Section 1.5 on TB models.

Numerical evaluation. Numerically we will evaluate Berry curvatures on finite meshes and thus let us consider state vectors $|u_n\rangle$ discretized along the closed loop. Berry phase can be written as:

$$\phi = -\operatorname{Im}\ln\left[\langle u_0|u_1\rangle\langle u_1|u_2\rangle\ldots\langle u_{N-1}|u_0\rangle\right] \tag{1.34}$$

Here we use the expression for a phase of a complex number [10] and we consider N state vectors $\langle u_{i-1}|u_i\rangle$ with $i = 0, ..., N-1$. We can rotate for each state vector its phase, perform gauge transformations, and since expression (1.34) contains always a pair of bra and ket, the local phase factors out and do not affect the value of the Berry phase. This illustrates that the Berry phase measures how the relative phase $\langle u_{i-1}|u_i\rangle$ varies along the loop. The Berry phase has also an interpretation in differential geometry as an anholonomy angle, loosely corresponding to the choice of the local basis aligned as possible with its neighbours [10, 45].

The expression used in numerical calculations on minimal models [64] can be obtained from the discretized formula:

$$\phi = -\sum_i \operatorname{Im}\ln\det M^{(\boldsymbol{\Lambda}_i,\boldsymbol{\Lambda}_{i+1})} = -\operatorname{Im}\ln\prod_i \det M^{(\boldsymbol{\Lambda}_i,\boldsymbol{\Lambda}_{i+1})}, \tag{1.35}$$

where M is $N_b \times N_b$ matrix:

$$M_{mn}^{(\boldsymbol{\Lambda}_i,\boldsymbol{\Lambda}_{i+1})} = \left\langle u_m^{(\boldsymbol{\Lambda}_i)}|u_n^{(\boldsymbol{\Lambda}_{i+1})}\right\rangle \tag{1.36}$$

where $\boldsymbol{\Lambda}$ are closely spaced discretized points in the parameter space. The Berry phase is calculated around each small plaquette with vertices $\boldsymbol{\Lambda}_i$.

The continuous limit of the discretized formula can be also used to illustrate the interference nature of the Berry phase and its short memory. We can take continuous limit as:

$$\begin{aligned} \ln \langle u_\lambda | u_{\lambda+d\lambda} \rangle &= \ln \left\langle u_\lambda \middle| \left(|u_\lambda\rangle + d\lambda \frac{d\,|u_\lambda\rangle}{d\lambda} + \cdots \right) \right. \\ &= \ln\left(1 + d\lambda \langle u_\lambda | \partial_\lambda u_\lambda \rangle + \cdots \right) \\ &= d\lambda \langle u_\lambda | \partial_\lambda u_\lambda \rangle + \cdots \end{aligned} \tag{1.37}$$

where in the last equality we neglect terms higher than second-order in $d\Lambda$. We obtain

$$\phi = -\operatorname{Im} \oint \langle u_\lambda | \partial_\lambda u_\lambda \rangle \, d\lambda = \oint \langle u_\lambda | \partial_\lambda i u_\lambda \rangle \, d\lambda, \tag{1.38}$$

where we have used the fact that the integrand in the first equality is purely imaginary and corresponds to the Berry connection (potential). By considering only lower order terms in the adiabatic perturbation theory, the time evolved eigenstates have short memory of the path in history [10]. Despite the common intuition prevailing till the 1980s that in quantum mechanics only probabilities and thus squares of wavefunctions matter and not the phases, the latter can be important in interference phenomena. An example of such a coherence effect is the Berry phase arising from spin-split energy bands in the crystal momentum space in magnetic solids which produces an intrinsic contribution to the spontaneous Hall effect [51, 65]. We will investigate an unanticipated symmetry breaking mechanism, the crystal Hall effect, and evaluate its Berry phase contribution in Chapter 4.

1.3 Magnetic symmetry groups and classification of Dirac quasiparticles

Introduction of the antiunitary, time-reversal operator $\mathcal{T}$ leads to the four types of MSGs [26]. The ordinary 230 (Type I, colourless) space groups are labelled by $\mathcal{G}$. In addition, we have three new types of MSG. The type II MSGs (grey) is defined by:

$$\mathcal{G}' = \mathcal{G} + \mathcal{T}\mathcal{G}. \tag{1.39}$$

The type-II MSG is thus obtained by adding the $\mathcal{T}$ operation to the type-I symmetry group and we have thus also 230 of them.

A type III, black-and-white MSGs is constructed as:

$$\mathcal{M}^{\mathrm{III}} = \mathcal{H} + \mathcal{T}\left(\mathcal{G} - \mathcal{H}\right), \tag{1.40}$$

where $\mathcal{H}$ is a halving subgroup of $\mathcal{G}$ and $\mathcal{G} - \mathcal{H}$ contains no pure translations. There is in total of 674 MSGs of type-III. The type-III MSGs have the same size of the Brillouin zone in the non-magnetic and magnetic state and all the important real materials studied in this thesis belong to this class. We illustrate an example of $\mathcal{PT}$ symmetric antiferromagnetic tetragonal crystal CuMnAs in Fig. 1.3(a).

The last, fourth type of MSGs is based on black-and-white Bravais lattices. The black-and-white lattice is formed by introducing a second lattice site generated by the combination of nontrivial translation $\mathbf{t}$ and time reversal $\mathcal{T}$ operations.

Example is $EuCd_2As_2$ antiferromagnet shown in Fig. 1.3(b) with $\mathbf{t} = (0, 0, \frac{1}{2})$. The definition of the type-IV MSG is:

$$\mathcal{M}^{\mathrm{IV}} = \mathcal{G} + \mathcal{T}\left\{\mathcal{E}|\mathbf{t}\right\}\mathcal{G}, \tag{1.41}$$

where $\mathcal{E}$ is an identity operator. The total of 517 MSGs of type-IV can be constructed by taking all the 32 grey point groups and combining them with 36 black-and-white Bravais lattices. Clearly, type IV MPGs do not allow for uncompensated moments since each moment on black sublattice is by definition compensated by the moment on the white sublattice. Consequently, ferromagnetism, ferrimagnetism, but also spontaneous Hall effect are prohibited in the type-IV MPGs.

Out of 230 conventional space groups, there are 157 non-symmorphic ones (spatial operations coupled with partial unit cell translation, e.g. screw rotation). Furthermore, there are 65 Sohncke groups with no improper rotations which are found in chiral crystal structures, out of which 22 groups are itself chiral (11 enantiomorphic pairs) [66].

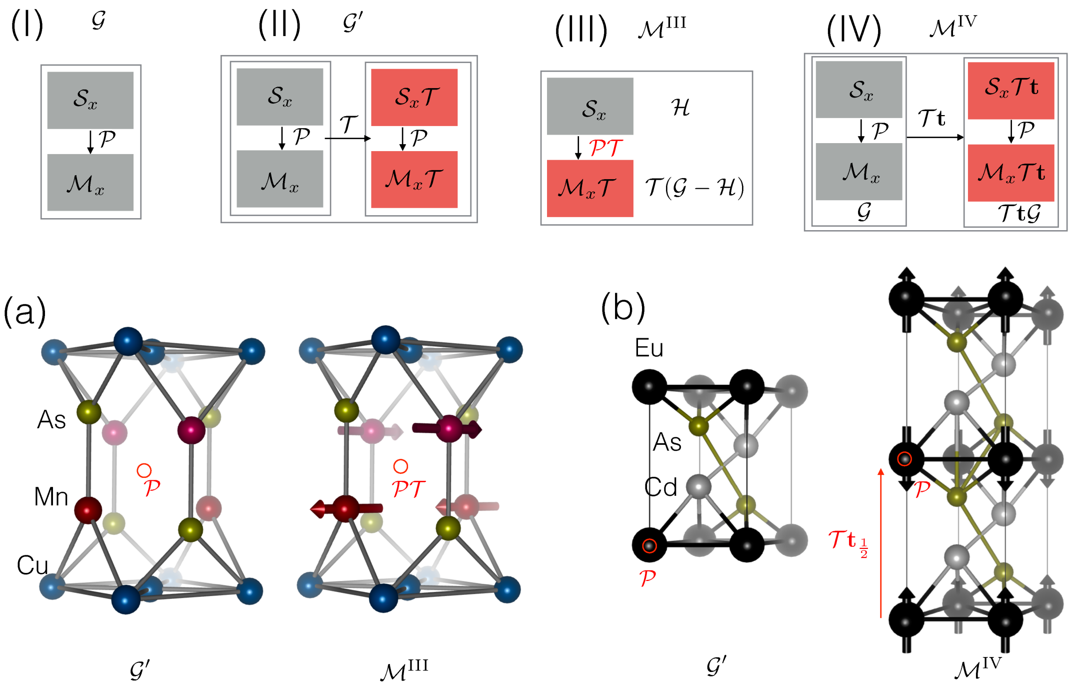

Figure 1.3: Schematics of magnetic symmetry groups of type I, II, III, and IV derived from non-magnetic centrosymetric systems. We mark the important symmetry relations, $\mathcal{S}$ marks screw rotation, $\mathcal{M}$ marks mirror plane. (a) Tetragonal crystal of CuMnAs in the non-magnetic and antiferromagnetic phase. The antiferromagnetic phase hosts a type-III magnetic space group. (b) Crystal of $EuCd_2As_2$ in the non-magnetic and antiferromagnetic state. The magnetic space group is of type-IV, and the unit cell is doubled.

We use here the BNS (Belov-Nerenova-Smirnova) notation, e.g. $Pn'm'a$. Within this notation, the conventional Hermann-Mauguin space groups labelling is extended by two symbols. First, a prime remarks antiunitary operation, e.g., m' refers to mirror plane combined with time reversal. Second, the potential subscripts indicate the magnetic Bravais lattice in the type-IV MSGs. Formally, the band degeneracies can be obtained by analysing little groups in crystal momentum space defined as:

$$\mathcal{G}_{\boldsymbol{k}} \equiv \{g \in \mathcal{G} | g\boldsymbol{k} \equiv \boldsymbol{k}\}. \tag{1.42}$$

Here the crystal momentum vector is defined modulo reciprocal lattice vector and the translation acts trivially in momentum space. We find a n-fold degeneracy if the little group irreducible corepresentation at given $\boldsymbol{k}$ is n-dimensional. Irreducible means that the representation cannot be further decomposed into a direct sum of representations. Corepresentation refers to a group representation with antiunitary elements. The non-magnetic degeneracies can be found by using the Bilbao Crystallographic server and were recently enumerated [21]. Because of the additional crystalline symmetries, solids can host higher-order degeneracies not available in high energy physics, e.g. 3, 6, and 8-fold degeneracies.

The magnetic degeneracies can be found by analysing the tables [67] of remaining 1191 MSGs of type-III and IV as described in Ref.[24]. For the type-III MSG $\mathcal{M}^{\mathrm{III}}$, also the corresponding $\mathcal{G}$, $\mathcal{G}'$, and $\mathcal{H}$ poses the same Brillouin zone, and $\mathcal{G}'$ has more symmetries than $\mathcal{G}$. One can scan tables of type-III MPGs with the numerical index starting with the non-magnetic $\mathcal{G}'$ symmetry groups with degeneracies. Instead of 3-, 6-, and 8-fold degeneracies listed in [24], we focus here on type-III MSGs and 2-fold (Weyl), or 4-fold (Dirac) quasiparticles which seem to be more common in spin-orbit torque (tetragonality) or spontaneous Hall effect (low symmetry) systems.

When we strip partial unit cell translation we obtain MPG which are useful for obtaining the symmetry of the spatially averaged linear response coefficients, or Berry curvature. The type-I (colourless) MPGs are the usual point groups marked $\mathcal{G}$, they do not contain $\mathcal{T}$ at all, and there are 32 of them. Type-II (grey) MPGs are the direct product $\mathcal{M} = \mathcal{G} + \mathcal{T}\mathcal{E}\mathcal{G}$, where $\mathcal{E}$ is the identity operator. They contain explicitly $\mathcal{T}$ and there are 32 of them. Type-III (black and white) MPGs are constructed as $\mathcal{M} = \mathcal{G} + \mathcal{A}\mathcal{G}$, where $\mathcal{A} = \mathcal{T}\mathcal{R}$, is antiunitary symmetry combining time-reversal and crystalline symmetry and does not belong to $\mathcal{G}$. There exist 58 MPGs of type-III. There are in total 22 MPGs with $\mathcal{P}$, and 22 with $\mathcal{P}\mathcal{T}$ [68].

The energy bands can be expanded around the band-touching points and their topological character can be classified based on the ten-fold-way studied also for random matrices [34, 69]. Analysis of the action of internal symmetries: chiral $\mathcal{X}$ (sublattice symmetry $\mathcal{X}^{-1}H(\boldsymbol{k})\mathcal{X} = -H(\boldsymbol{k})$ is not spatial inversion), time-reversal $\mathcal{T}$, and particle-hole $\mathcal{C}$ symmetries leads to the periodic table of topological insulators with 10 different classes. For our topological antiferromagnetic spintronics effects are rather relevant time-reversal $\mathcal{T}$, spatial inversion $\mathcal{P}$, and crystalline unitary and antiunitary symmetries $\mathcal{R}$ and $\mathcal{A} = \mathcal{T}\mathcal{R}$. We focus on catalogue and classification in terms of these symmetries.

Dirac quasiparticle classification

Dirac quasiparticle energy bands require $\mathcal{P}\mathcal{T}$ invariant solid with two double degenerate bands separated from the rest of the band structure. When we choose

$\mathcal{T} = i\sigma_y\mathcal{K}$ (see Section 1.1), we have three possibilities of choosing the $\mathcal{P}$ operator: $\pm\tau_0, \pm\tau_x$ and $\pm\tau_z$, where τ are Pauli matrices referring to the orbital degree of freedom, and σ are Pauli matrices referring to (pseudo)spin degree of freedom. In Tab. 1.1 we derive all $\mathcal{PT}$ allowed representations for the basis matrices, and one can easily check that the listed Γ matrices commute with the $\mathcal{PT}$ symmetry operator.

$\mathcal{P}$	Allowed Γ_j	$d_j(\boldsymbol{k})$, $d_5(\boldsymbol{k})$	Realization
$\pm\tau_0$	$\tau_x, \sigma_x\tau_y, \sigma_y\tau_y, \sigma_z\tau_y, \tau_z$	$d_j(\boldsymbol{k}) = -d_j(-\boldsymbol{k})$,$d_5(\boldsymbol{k}) = d_5(-\boldsymbol{k})$	CuMnAs[28]
$\pm\tau_x$	$\tau_x, \tau_y, \sigma_x\tau_z, \sigma_y\tau_z, \sigma_z\tau_z$	$d_j(\boldsymbol{k}) = d_j(-\boldsymbol{k})$,$d_5(\boldsymbol{k}) = d_5(-\boldsymbol{k})$	Models
$\pm\tau_z$	$\tau_y, \sigma_z\tau_x, \sigma_x\tau_x, \sigma_y\tau_x,\tau_z$	$d_j(\boldsymbol{k}) = -d_j(-\boldsymbol{k})$,$d_5(\boldsymbol{k}) = d_5(-\boldsymbol{k})$	$\mathrm{EuCd_2As_2}$[70]

Table 1.1: We choose $\mathcal{T} = i\sigma_y\mathcal{K}$ allowing the three different representation of spatial inversion $\mathcal{P}$. $d_j(\boldsymbol{k})$ are coefficients in front of Γ matrices in the expansion of Hamiltonian in Eq. (1.43).

The choice of basis has physical meaning in solids. For instance $\mathcal{P} = \tau_z$ swaps orbitals, and the Pauli matrices σ can refer not only to physical spin but also to pseudospin. An example is a graphene, where the $\mathcal{P} = \tau_z$ swaps the two orbitals and pseudospin is a sublattice degree of freedom or valley degree of freedom. The form of $\mathcal{P}$ operator also constraints the odd/even character of expansion coefficients under swapping the direction of the crystal momentum [59]. We see in Tab. 1.1 that the $\mathcal{PT}$ symmetry reduces the number of independent basis Gamma matrices Γ from 16 to 6 (5 excluding unit matrix) [36], and the corresponding Dirac Hamiltonian can be written as:

$$\mathcal{H}(\boldsymbol{k}) = \sum_{j=0}^{5} d_j(\boldsymbol{k})\Gamma_j, \tag{1.43}$$

where $d_j(\boldsymbol{k})$ are functions of crystal momentum. This Hamiltonian can be diagonalized analytically:

$$E_\pm(\boldsymbol{k}) = d_0(\boldsymbol{k}) \pm \sqrt{\sum_{j=1}^{5} d_j^2(\boldsymbol{k})}. \tag{1.44}$$

The 3D Dirac quasiparticles are in general massive since it is generically impossible to tune simultaneously five functions $d_j(\boldsymbol{k})$ to zero by varying just three components of the crystal momentum $\boldsymbol{k}$. Additional crystalline and magnetic symmetries can do the job of protecting crossing for us as we will show later on our models and realistic crystal potentials of CuMnAs in Chapter 3.

Depending on the set of symmetries we can distinguish different types of massive and massless Dirac quasiparticle in non-magnets and antiferromagnets. (We emphasize that as we have seen in the Antiferromagnetic Kramers theorem section 1.1, ferromagnetic 3D Dirac quasiparticles cannot be realised.) We can group the Dirac quasiparticles based on (i) the type of discrete $\mathcal{PT}$ symmetries depending on the MSG, (ii) the dimensionality and mass of the band crossing (nodal points vs nodal lines and topological metal vs insulator), and finally (iii) the stable accidental band-crossing at high symmetry lines, or Kramers band crossings at TRIMs.

We start by discussing the first classification. There are 22 out of 122 MPGs with the $\mathcal{PT}$ symmetry. We distinguish three types of Dirac quasiparticles depending on the type of the MSG operation protecting the Kramers theorem (see section 1.1 of this chapter) and we list the material candidates in Tab. 1.1.

1. ***Non-magnetic* Dirac quasiparticles.** When the system hosts both $\mathcal{P}$ and $\mathcal{T}$ symmetries it belongs to the Type-II MSG. Examples are the non-magnetic Dirac semimetals Na_3Bi,or Cd_3As_2. Massive Dirac quasiparticles of this type are also found in Bi_2Se_3 type topological insulators with two-dimensional massless Dirac surface states.

2. ***Magnetoelectric antiferromagnetic* Dirac quasiparticles.** When both $\mathcal{P}$ and $\mathcal{T}$ symmetries are broken on their own, but their combination $\mathcal{PT}$ is preserved, the system belongs to the Type III MSG, and is also compatible with magnetoelectric response. Examples are massless Dirac semimetal CuMnAs [27], or massive dynamical axion insulator candidates, Fe-doped Bi_2Se_3 [60].

3. ***Non-symmorphic antiferromagnetic* Dirac quasiparticles.** For centrosymmetric systems with antiferromagnetic lattices connected via *non-symmorphic* $\mathcal{T}\mathbf{t}$ symmetry, where $\mathbf{t}$ is partial-magnetic-unit cell translation, we obtain MSG of Type-IV. We show in Fig. 1.3(b) an illustrative antiferromagnet $EuCd_2As_2$. Also antiferromagnetic topological insulator $MnBi_2Te_4$ belong to this class.

To ensure the stable accidental band-crossing, the expression under the square root in Eq. (1.44) must vanish [36, 71]. We can reduce the number of free functions to three by additional crystalline symmetries, which can further reduce the number of Γ matrices in the Hamiltonian (1.43). Depending on additional symmetries we can obtain distinct topological antiferromagnetic phases:

- **Dynamical axion insulator antiferromagnet.** If we have broken inversion and time-reversal symmetries on their own while their combination is still preserved we can obtain dynamical axion insulator antiferromagnet. The Hamiltonian can be obtained from the Hamiltonian of Bi_2Se_3 topological insulator by introducing Fe doping (which can randomly substitute Bi-sites [59] and thus preserving on average the $\mathcal{PT}$ symmetry) which tends for certain concentration to order antiferromagnetically. We have shown that coupling of these Dirac quasiparticles with antiferromagnetic fluctuations [59] can be useful for the detection of axion dark matter [60].

- **(Antiferromagnetic) topological insulator.** If we have in addition $\mathcal{P}$ and $\mathcal{T}\mathbf{t}$ (or possibly other effective $\mathcal{T}$ symmetries [72, 73]) preserved on their own, we can obtain Dirac quasiparticle surface states on a bulk antiferromagnetic insulator [74, 75].

- **Dirac semimetal antiferromagnet.** Finally, the Néel vector provides in principle two tunable parameters in the Gamma matrices expansion in addition to crystal momenta. We can thus expect that for certain orientation of the Néel vector, the antiferromagnetic systems will host crystalline symmetry which will prevent hybridization at the four-fold Dirac crossing. We have found minimal model describing this situation and a realistic material candidate CuMnAs, which we will describe in Chapter 3 of the theses. The Dirac fermions are in this material protected by the non-symmorphic screw rotational symmetry.

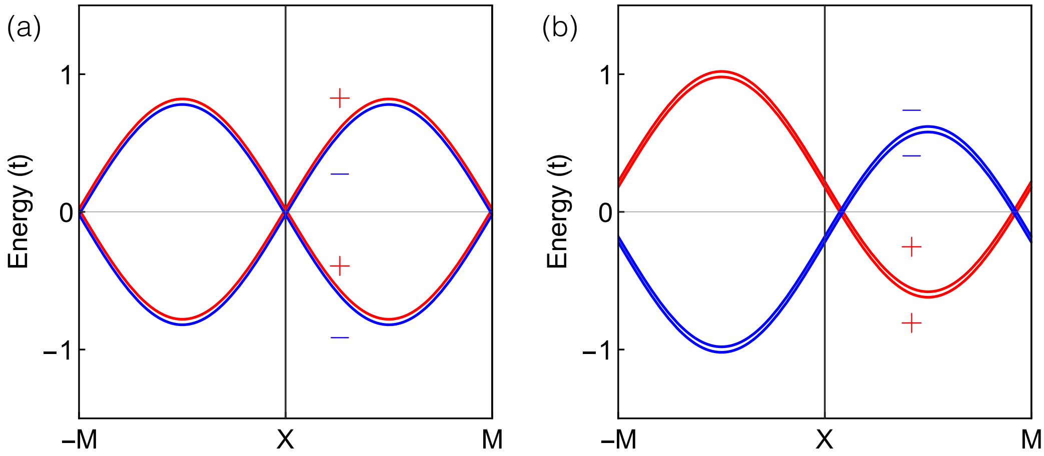

Figure 1.4: (a) TRIM type of non-magnetic Dirac semimetal. (b) Accidental band-touching type of antiferromagnetic Dirac semimetal. (We plot the energy dispersion of the quasi-2D antiferromagnetic model discussed in Eq. (1.83) for $J_n = 0$, and $0.8t$.)

Finally, the generic band touching points [36] (and also Dirac points) can be of the two types: (i) Dirac points at TRIMs, and (ii) accidental band touching induced Dirac points found along the high symmetry lines invariant under higher-order or non-symmorphic rotational symmetries. In the case (i) an argument presented by Young [76] explains the stable crossing. At TRIM, a non-symmorphic symmetry $\mathcal{R}\mathbf{t}$ and $\mathcal{P}$ have simultaneous eigenvalues ± 1 and they commute with $\mathcal{T}$. Since also $\{\mathcal{R}\mathbf{t}, \mathcal{P}\} = 0$, the degeneracy is four-fold. We illustrate Dirac points in Fig. 1.4(a) at TRIM $\frac{\boldsymbol{G}}{2} = X$. In the case (ii), the crystalline symmetry prevents hybridization at some accidental point along the high-symmetry axis (plane) as we will explain on our model in Section 1.6 of this chapter and on CuMnAs in Chapter 3 and we illustrate this case in Fig. 1.4(b). The β-BiO$_2$ is of type (i) [77], and 3D Dirac semimetal (DSM)s Na$_3$Bi [78] and Cd$_3$As$_2$ [79] are of the type (ii) and are protected by the rotational $\mathcal{C}_3$ and $\mathcal{C}_4$ symmetries, respectively. For antiferromagnets, the type (ii) case was discussed for model systems [27, 80], CuMnAs [27, 28], and EuCd$_2$As$_2$ [70], while the type (i) only for model systems [50].

Weyl fermions classification.

Furthermore, we can break $\mathcal{PT}$ symmetry to lift the Kramers degeneracy and to construct Weyl fermion quasiparticles and Weyl semimetals [20]. WSM is described by the generalized two-band Weyl Hamiltonian [81, 82]:

$$H(\boldsymbol{k}) = \sum_{\substack{i=x,y,z \\ j=0,x,y,z}} k_i d_{ij} \sigma_j \tag{1.45}$$

where we measure the crystal momenta from the Weyl points, σ_j ($j = 1, 2, 3$) marks Pauli matrices and σ_0 is unit matrix. Weyl points always come in pairs with opposite topological charges as can be straightforwardly proven in 1D. For each quasiparticle with positive momentum there will be corresponding quasiparticle with negative momentum since the energy dispersion has to match at 1D Brillouin zone boundary to preserve periodicity. The generalisation to higher dimensions was proven by Nielsen and Ninomiya [83]. The Weyl points can be stable in 3D or in 1D, e.g., in the form of edge states in quantum (anomalous) Hall effect [20]. In 3D the effective Hamiltonian uses all three Pauli matrices and thus any small perturbation just shifts but not gaps the Weyl point (consider, for instance, perturbation $m\sigma_z$). The energy dispersion reads:

$$\varepsilon_{\pm}(\boldsymbol{k}) = \sum_{i=x,y,z} k_i d_{i0} \pm \sqrt{\sum_{j=x,y,z} \left(\sum_{i=x,y,z} k_i d_{ij} \right)^2} = T(\boldsymbol{k}) \pm U(\boldsymbol{k}). \tag{1.46}$$

Here $T(\boldsymbol{k})$ corresponds to a *kinetic* term breaking the Lorentz symmetry describing tilting of the cone, and $U(\boldsymbol{k})$ can be seen as a potential energy term [84].

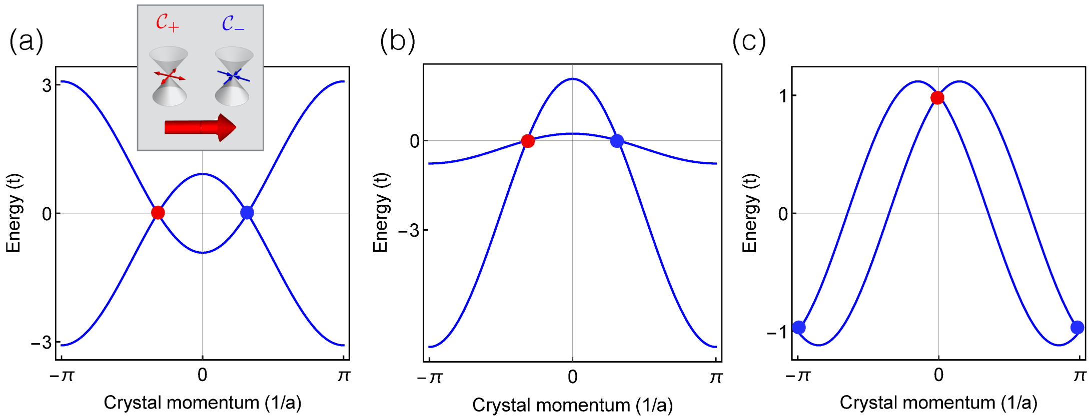

Figure 1.5: Catalogue of Weyl fermions. (a) Magnetic Weyl semimetal ($\mathcal{T}$ broken and $\mathcal{P}$ preserved. (b) The same as (a) but with tilted Weyl cones. (c) Kramers Weyl semimetal.

Depending on the symmetry breaking and terms in the Weyl Hamiltonian we can distinguish several categories. First three categories are mutually exclusive and are defined by the three types of symmetry breaking, namely only $\mathcal{T}$ breaking, only $\mathcal{P}$ breaking, and both $\mathcal{T}$ and $\mathcal{P}$ breaking. When the kinetic energy term $T(\boldsymbol{k})$ is not important we call them type-I. Fourth and fifth category represent alternative dispersion shapes which can be found in all three symmetry types.

1. **Magnetic Weyl fermions.** With only broken $\mathcal{T}$, there exist minimal Weyl semimetals with only two Weyl cones. In the minimal ferromagnetic Weyl semimetal shown in Fig 1.5(a), the Hall conductivity is semi-quantized [81],

$$\sigma_{xy} = -\frac{e^2}{h}\boldsymbol{\Delta}, \tag{1.47}$$

where $\boldsymbol{\Delta} = 2|k_W|$ is the Weyl point separation. The slices of constant k_z between the Weyl points can be seen as 2D quantum anomalous Hall effect

(QAHE) states. We will discuss the Haldane model of the QAHE in Section 1.5.

2. **Noncentrosymmetric Weyl fermions.** In non-magnetic systems with broken $\mathcal{P}$ the Weyl points come (with exception of Kramers-Weyl in next point) in multiples of four (this is due to the Nielsen-Ninomiya theorem [83] combined with $\mathcal{T}$ symmetry). Non-centrosymmetric non-magnetic monopnictides of the TaAs type [85, 86, 87] were shown experimentally as the first systems to host the Weyl fermions.

3. **Generic Weyl fermions.** This type showcases systems simultaneously magnetic and noncentrosymmetric. An example being reported here are LaCeSi type antiferromagnets [88].

4. **Kramers-Weyl fermions.** Weyl points can be found also at TRIMs. They were originally reported in chiral non-magnetic crystal [89, 90], however, our symmetry analysis shows that they can be identified also in magnetic and centrosymmetric systems. In contrast to standard Weyl points in centrosymmetric crystals, they do not have to come in four since they reside at TRIMs. Kramers-Weyl fermions are not energy degenerate what is promising for the observation of quantized photogalvanic effects [89]. Such states are characterised by long Fermi arcs (open surface states) and were suggested to host peculiar negative magnetoresistance [90].

5. **Type-II Weyl fermions.** Furthermore, the first term in the Weyl equation (1.46) can generate tilting of the Weyl cone or modulation by the quadratic dispersion. When the former is important we talk about type-II Weyl semimetal with electron-hole pockets. The type-II Weyl semimetals can host nonlinear (in electric field) Hall effect, e.g. Berry curvature dipole is nonzero when the Weyl cone is tilted [91, 92].

Despite numerous *ab initio* predictions [82, 93], the observation of true magnetic WSMs is very challenging as the existing candidates are often also strongly correlated, disordered, and the symmetry breaking is provided by magnetism which complicated both the experiment and theory. Promising material systems are kagome ferromagnets [82], or antiferromagnets [94] and other candidates can be found in Refs.[23, 82, 93].

1.4 Linear response theory and Dirac-Néel antiferomagnets criteria

We start by writing the electrical current response as a series in applied electric field:

$$\mathbf{j} = \sigma^{(1)}\mathbf{E} + \mathbf{E}\sigma^{(2)}\mathbf{E} + ..., \tag{1.48}$$

where the first term corresponds to the linear response, second term to the quadratic response (e.g. nonlinear Hall effect or magnetoresistance [91, 95]), etc.

Any second rank tensor can be decomposed into part even σ^p (symmetric, polar) and odd σ^a (axial, pseudo) under reversal of magnetic field $\mathbf{H}$ and spin ordering $\mathbf{S}$:

$$\sigma^{p/a}_{\mu\nu}(\mathbf{H},\mathbf{S}) = \frac{\sigma^{p/a}_{\mu\nu}(\mathbf{H},\mathbf{S}) \pm \sigma^{p/a}_{\mu\nu}(-\mathbf{H},-\mathbf{S})}{2}, \tag{1.49}$$

Since the spins can be reversed by the application of time reversal symmetry $\mathcal{T}$ these components are alternatively called $\mathcal{T}$-symmetric or antisymmetric.

Now we can expand the conductivity tensor into series in applied magnetic field:

$$\sigma_{\mu\nu}(\mathbf{H},\mathbf{S}) = \sigma^{(0)}_{\mu\nu}(\mathbf{S}) + \sigma^{(1)}_{\mu\nu k}(\mathbf{S})H_k + \sigma^{(2)}_{\mu\nu kl}(\mathbf{S})H_k H_l + ..., \tag{1.50}$$

where we fix the spin order $\mathbf{S}$. By using the Onsager relation (4.7) [65] and decomposition (1.49) we can derive the transformation properties of the expansion coefficients. For instance,

$$\sigma^{(0),a}_{\mu\nu}(\mathbf{S}) = \frac{\sigma^{(0)}_{\mu\nu}(\mathbf{S}) - \sigma^{(0)}_{\mu\nu}(-\mathbf{S})}{2} = -\frac{\sigma^{(0)}_{\mu\nu}(-\mathbf{S}) - \sigma^{(0)}_{\mu\nu}(\mathbf{S})}{2} = -\sigma^{(0),a}_{\mu\nu}(-\mathbf{S}), \tag{1.51}$$

$$\sigma^{(1),a}_{\mu\nu k}(\mathbf{S})H_k = \frac{\sigma^{(1)}_{\mu\nu k}(\mathbf{S})H_k - \sigma^{(1)}_{\mu\nu k}(-\mathbf{S})\,(-H_k)}{2} = \sigma^{(1),a}_{\mu\nu k}(-\mathbf{S})H_k. \tag{1.52}$$

We summarized the derived transformation properties under $\mathcal{T}$ up to the third order in the following table, where we also list the number of allowed symmetry point groups.

$\mathcal{T}$ even	Longitudinal $\sigma^{(0),p}_{ij}$ (122)	HE $\sigma^{(1),a}_{ijk}$ (122)	QMR $\sigma^{(2),p}_{ijkl}$ (122)
$\mathcal{T}$ odd	Spontaneous HE $\sigma^{(0),a}_{ij}$ (31)	LMR $\sigma^{(1),p}_{ijk}$ (66)	Quad. HE $\sigma^{(2),a}_{ijkl}$ (66)

Table 1.2: Transformation properties of Hall and magnetoresistance tensors.

The effects even in $\mathcal{T}$, longitudinal conductivity $\sigma^{(0),p}_{\mu\nu}$, ordinary Hall effect (HE) $\sigma^{(1),a}_{\mu\nu k}$, and quadratic magnetoresistance (QMR) $\sigma^{(2),p}_{\mu\nu kl}$ are present in all magnetic point groups. The effects odd in $\mathcal{T}$ are called in literature magnetic and are present only in a subset of MPGs. The spontaneous Hall effect is present in 31 ferromagnetic point groups, the linear magnetoresistance (LMR) $\sigma^{(1),p}_{ijk}$ and quadratic Hall effect $\sigma^{(2),a}_{ijkl}$ are present in 66 magneto-piezoelectric point groups. Now we focus on a specific linear response but we formulate it for two generic operators, not only for the response of a charge current to an electric field.

Change in the expectation value of an observable A_ν due a time dependent perturbation B_μ can be written within the Kubo linear response theory [96, 97] as two operator correlation function:

$$\chi_{\mu\nu}(\mathbf{H}) = \int_0^\infty dt \int_0^\beta d\lambda\, \mathrm{Tr}\, \rho(\mathbf{H}) A_\nu B_\mu(t + i\hbar\lambda; \mathbf{H}), \tag{1.53}$$

where $\rho(\mathbf{H})$ is the density operator for the canonical ensemble [97], the operators are in Heisenberg picture and $\mathbf{H}$ is the magnetic field intensity.

Considering independent electron approximation and zero frequency and zero temperature leads to an expression [98, 99]:

$$\chi^{(2)}_{\mu\nu} = -\frac{i}{V} \sum_{k,n,m} \frac{f_{nk} - f_{mk}}{\varepsilon_{nk} - \varepsilon_{mk}} \frac{\left\langle \psi_{nk} \middle| \hat{A}_\nu \middle| \psi_{mk} \right\rangle \left\langle \psi_{mk} \middle| \hat{B}_\mu \middle| \psi_{nk} \right\rangle}{\varepsilon_{nk} - \varepsilon_{mk} + i\Gamma}, \tag{1.54}$$

where $f_{mk} = f(\epsilon_{mk})$ is the Fermi distribution function, ε_{mk} and ψ_{mk} are the eigenvalues and eigenstates of the Hamiltonian and Γ is the quasiparticle spectral broadening (scattering rate). We are interested in this theses in effects depending on the applied electric field to (semi)metallic antiferromagnets. We can thus choose $B_j = -ev_j$, where v_j is velocity component due to the applied field, and formally separate the transport coefficient into two parts [98, 100, 101]:

$$\chi_{\mu\nu} = \chi^{I}_{\mu\nu} + \chi^{II}_{\mu\nu}. \tag{1.55}$$

The first part,

$$\chi^{(I)}_{\mu\nu} = -\frac{eh}{\pi} \sum_{\boldsymbol{k},n,m} \frac{\Gamma^2 \mathrm{Re} \langle n\boldsymbol{k}|A_\nu|m\boldsymbol{k}\rangle \langle m\boldsymbol{k}|(\mathbf{v}\cdot\mathbf{E})_\mu|n\boldsymbol{k}\rangle}{[(E_F-\epsilon_{n\boldsymbol{k}})^2+\Gamma^2][(E_F-\epsilon_{m\boldsymbol{k}})^2+\Gamma^2]} \tag{1.56}$$

is energy degenerate [98] and dissipative current driven part, and under time-reversal changes sign when the two operators have different transformation properties under time-reversal. This part is sometime called Boltzmann-like, and can be within Green's functions formalism of longitudinal charge conductivity expressed by the Kubo-Greenwood formula.

The second part is usually considered in the $\Gamma \to 0$ limit and can be written as:

$$\chi^{(II)}_{\mu\nu} = -2\hbar e \sum_{\boldsymbol{k},n\neq m} \frac{\mathrm{Im} \langle n\boldsymbol{k}|A_\nu|m\boldsymbol{k}\rangle \langle m\boldsymbol{k}|(\mathbf{v}\cdot\mathbf{E})_\mu|n\boldsymbol{k}\rangle}{(\epsilon_{n\boldsymbol{k}}-\epsilon_{m\boldsymbol{k}})^2}, \tag{1.57}$$

as is energy non-degenerate [98], nondissipative electric field driven part, which changes sign under time-reversal if both operators transform under time-reversal in the same manner. In contrast, the spatial inversion changes sign of both $\chi^{(I)}$, and $\chi^{(II)}$ if the inversion partner eigenvalues of operators A, and B are different.

Since our systems are promising candidates for a novel type of spin conductivities and staggered Néel spin-orbit torque (NSOT) we summarize the transformation properties in Tab. 1.3.

A	$\chi^{(I)}$	$\chi^{(II)}$
$-e\mathbf{v}$	even (conductivity)	odd (anomalous Hall conductivity)
$\frac{1}{2}\{\mathbf{s},\mathbf{v}\}$ [101]	odd (spin current)	even (spin Hall conductivity)
$\mathbf{M}\times\nabla_{\mathbf{M}}H(\boldsymbol{k})$[100]	odd (field-like torque)	even (antidamping-like torque)

Table 1.3: Transformation properties under time-reversal operation of spintronics response tensors to electric field.

Remarkably, the nonequilibrium steady-state properties can be according to the linear response theory expressed in terms of solely equilibrium ground state wavefunctions and operators. This method is thus conveniently implemented within diverse first-principle DFT formalisms. Examples of spintronics quantities of interests hosted in our materials are charge conductivities, anisotropic magnetoresistance, spontaneous Hall effect, spin Hall effect, magnetic spin Hall effect, spin-orbit torque (SOT), and NSOT.

We will use the Kubo-Greenwood formulation to evaluate the longitudinal conductivity and anisotropic magnetoresistance of our antiferromagnetic Dirac semimetal model and the disordered antiferromagnets in Chapter 3. The nondissipative part corresponds to the charge Hall conductivity and can be expressed in terms of the Berry curvature (cf. (1.24)) and we will use it to calculate the Berry curvature in nodal chain antiferromagnetic model and in Chapter 4 for the calculations of the Hall conductivity.

We are now in a position to formulate symmetry criteria allowing for the simultaneous presence of Dirac quasiparticles and NSOT [27, 102, 103, 104]. We can illustrate the serendipitous overlap of symmetry criteria by comparing the graphene Dirac quasiparticle systems to the tetragonal CuMnAs crystal shown in Fig. 1.3(a) where the NSOT has been experimentally verified [103].

1. The two-Mn-site primitive cell of CuMnAs favours band crossings and a semimetallic density of states character. This is analogical to the two-C-site graphene crystal further discussed in Section 1.5.

2. In the paramagnetic phase, the Kramers degeneracy is guaranteed due to the $\mathcal{T}$ and $\mathcal{P}$ symmetries of the CuMnAs crystal shown in Fig. 1.3(a). In the AF phase, the AF Kramers theorem applies since the combined $\mathcal{PT}$ symmetry is preserved, although the $\mathcal{T}$ symmetry and the $\mathcal{P}$ symmetry are each broken [25, 27, 28, 105].

3. Finally, the combined $\mathcal{PT}$ symmetry also provides for the NSOT control of the antiferromagnetic Néel vector [102, 106]. Furthermore, because the A and B Mn-sites are non-centrosymmetric, a non-equilibrium spin polarization $\delta \mathbf{s}_{A,B}$ is generated under the applied electric current. The nonequilibrium spin-polarisations are opposite on the opposite sublattices since the inversion symmetry is broken in the opposite sense, aka the two Mn-sites are connected by the inversion in the non-magnetic state. This spin-polarisation can be calculated from the formula 1.56. In turn, the current-induced non-equilibrium spin polarization and the equilibrium antiferromagnetic moments are both staggered and commensurate. The exchange interaction couples them and the resulting current-induced SOT was shown to efficiently reorient the Néel vector [102, 103, 104].

To further control the Dirac quasiparticle masses we require, in addition, symmetry dependence on the Néel vector orientation.

- We need at least one orientation of the Néel vector $\mathbf{N}$ which prevents hybridization of bands and protects the four-fold degeneracy of Dirac crossings of two Kramers pair bands. In our case of CuMnAs model, we identified off-centred mirror symmetry present for $\mathbf{N} \parallel [100]$. In contrast, the Dirac quasiparticles in graphene are not symmetry protected and the Dirac points gap in the presence of SOC, producing a quantum spin Hall effect [107].

1.5 Tight-binding method and spin-orbit coupling

TB models simplify the problem of electronic structure description of the in-principle infinite Hilbert space to an only very limited number of atomic-like basis functions corresponding usually to orbitals centred at atoms in the crystal and usually describing important valence and conduction bands of the system. The

TB models played an important role in understanding topological insulators and semimetals since many properties such as Berry phases and Hall conductivities can be calculated explicitly and transparently for the minimal models. After introducing the general TB scheme and an example of graphene Haldane TB model, we will formulate our two topological antiferromagnetic models.

The TB Hamiltonian eigenstates can be expanded as [10]

$$\psi_n(\mathbf{r}) = \sum_j C_{nj}\varphi_j(\mathbf{r}-\mathbf{r}_j), \tag{1.58}$$

where φ_j are atomic-like orbitals, and C_{nj} are expansion coefficients of the n-th eigenstate on the orbital labelled by j. We use the shorthand composite index notation where $j = \{\alpha\nu\}$ comprises orbital index ν and α labels the basis atoms. By substituting Eq. (1.58) into the Schrödinger equation we obtain a matrix equation for the coefficients:

$$\left(H - E_n S\right) C_n = 0. \tag{1.59}$$

Here the matrices

$$H_{ij} \quad = \langle \varphi_i | H | \varphi_j \rangle \,, \tag{1.60}$$

$$S_{ij} \quad = \langle \varphi_i | \varphi_j \rangle \,, \tag{1.61}$$

are the Hamiltonian and overlap matrices of dimensions $M \times M$, where M is the total number of orbitals in the system. Diagonal elements of H are called site energies and the off-diagonal terms are hoppings. The hopping terms are usually truncated at few nearest neighbours, and the overlap matrix is assumed to be unit matrix and referred to as orthogonal tight-binding. We have thus transformed the differential Schrödinger equation in a large Hilbert space to a sparse matrix equation which can be conveniently solved numerically.

To obtain crystal momentum Hamiltonians, we construct Bloch-like basis states via Fourier transformation. We have gauge freedom in constructing the states as manifested in multi-sublattice systems. We present here two common conventions related by a unitary gauge transformation. The first, periodic gauge convention [10, 64] expands Bloch-like crystal momentum basis functions as:

$$\left|\chi_j^{\boldsymbol{k}}\right\rangle = \sum_{\mathbf{R}} e^{i\boldsymbol{k}\cdot(\mathbf{R}+\mathbf{t}_j)} \left|\phi_{\mathbf{R}j}\right\rangle, \tag{1.62}$$

and we use the normalization to a single unit cell and the basis is labelled by $\mathbf{t}_j$. The Bloch eigenstates can be expanded in terms of these basis functions:

$$\left|\psi_{n\boldsymbol{k}}\right\rangle = \sum_j C_j^{n\boldsymbol{k}} \left|\chi_j^{\boldsymbol{k}}\right\rangle. \tag{1.63}$$

The Hamiltonian transformed into the Bloch basis can be obtained from the following equation:

$$H_{ij}^{\boldsymbol{k}} = \left\langle \chi_i^{\boldsymbol{k}} | H | \chi_j^{\boldsymbol{k}} \right\rangle = \sum_{\mathbf{R}} e^{i\boldsymbol{k}\cdot(\mathbf{R}+\mathbf{t}_j-\mathbf{t}_i)} H_{ij}(\mathbf{R}). \tag{1.64}$$

In the second, Bloch gauge [10, 64] convention the definitions do not contain the *basis* phase factor $e^{i\boldsymbol{k}\cdot\mathbf{t}_j}$ and we have:

$$\begin{aligned}
\left|\widetilde{\chi}_j^{\boldsymbol{k}}\right\rangle &= \sum_{\mathbf{R}} e^{i\boldsymbol{k}\cdot\mathbf{R}} \left|\phi_{\mathbf{R}j}\right\rangle, \\
\left|\psi_{n\boldsymbol{k}}\right\rangle &= \sum_{j} \widetilde{C}_j^{n\boldsymbol{k}} \left|\widetilde{\chi}_j^{\boldsymbol{k}}\right\rangle, \\
\widetilde{H}_{ij}^{\boldsymbol{k}} &= \left\langle \widetilde{\chi}_i^{\boldsymbol{k}} | H | \widetilde{\chi}_j^{\boldsymbol{k}} \right\rangle = \sum_{\mathbf{R}} e^{i\boldsymbol{k}\cdot\mathbf{R}} H_{ij}(\mathbf{R}).
\end{aligned} \tag{1.65}$$

In the periodic gauge, the Hamiltonian is manifestly cell periodic [42],

$$H(\boldsymbol{k}+\boldsymbol{G}) = H(\boldsymbol{k}), \tag{1.66}$$

in analogy to cell periodic $u_{n\boldsymbol{k}}(\mathbf{r})$ functions in Eq. (1.4). This convention is less common in literature, however, PythTB [64] package implements this one. We will use in our numerical calculations the periodic gauge since we have seen in the second section that the cell periodic functions are convenient for the definition and calculation of the Berry phase. In the Bloch gauge the Hamiltonian is not periodic and the coefficients are analogical to Bloch functions. The conventions are related by:

$$\widetilde{H}_{ij}^{\boldsymbol{k}} = e^{i\boldsymbol{k}\cdot(\mathbf{t}_i-\mathbf{t}_j)} H_{ij}^{\boldsymbol{k}}, \tag{1.67}$$

$$\widetilde{C}_j^{n\boldsymbol{k}} = e^{i\boldsymbol{k}\cdot\mathbf{t}_j} C_{j,n\boldsymbol{k}}. \tag{1.68}$$

After we choose the convenient gauge, we solve the eigenvalue equation:

$$H_{\boldsymbol{k}} C_{n\boldsymbol{k}} = E_{n\boldsymbol{k}} C_{n\boldsymbol{k}}, \tag{1.69}$$

where $H_{\boldsymbol{k}}$ is an $M \times M$ matrix of elements $H_{ij}^{\boldsymbol{k}}$, and $C_{n\boldsymbol{k}}$ is a column vector of the elements $C_j^{n\boldsymbol{k}}$. The eigenvalues can be obtained from the corresponding secular equation: $\det\left(H_{\boldsymbol{k}} - E_{n\boldsymbol{k}}\right) = 0$.

Haldane graphene model We will illustrate the TB method, gauge transformation and basic topological characterization of energy bands on minimal two-band models of graphene [15] and its Haldane quantum anomalous Hall extension [62]. We start with the simplest TB honeycomb lattice nearest neighbour Hamiltonian describing graphene. We choose the graphene unit cell translation vectors $\mathbf{a}_1 = (1,0), \mathbf{a}_2 = \left(\frac{1}{2}, \frac{\sqrt{3}}{2}\right)$ giving rise to the reciprocal lattice unit cell translational vectors $\mathbf{b}_1 = (1,0), \mathbf{b}_2 = \left(\frac{1}{2}, \frac{\sqrt{3}}{2}\right)$ as we show in Fig. 1.6(a), and inset of Fig. 1.2. The unit cell contains two atoms labelled A, and B. The Hamiltonian is thus a 2×2 matrix which can be expanded in terms of Pauli matrices and the sublattice degree of freedom is thus commonly called pseudospin. The nearest neighbour hopping Hamiltonian in the pseudospin second quantization basis (c_A, c_B) reads:

$$H(\mathbf{r}) = -\sum_{\langle ij\rangle} t_{ij} \left(c_i^{\dagger} c_j + h.c.\right), \tag{1.70}$$

where $h.c.$ stands for the hermitian conjugate term. Each C atom has three neighbours at relative vectors $\boldsymbol{\delta}_i$. The Hamiltonian in crystal momentum space takes the form in the Convention II:

$$H = \sum_{k} \left(c_{Ak}^{\dagger} c_{Bk}^{\dagger}\right) \begin{pmatrix} 0 & \sum_{i=1}^{3} t_i e^{i\boldsymbol{k}\cdot\delta_i} \\ \sum_{i=1}^{3} t_i e^{-i\boldsymbol{k}\cdot\delta_i} & 0 \end{pmatrix} \begin{pmatrix} c_{Ak} \\ c_{Bk} \end{pmatrix}. \tag{1.71}$$

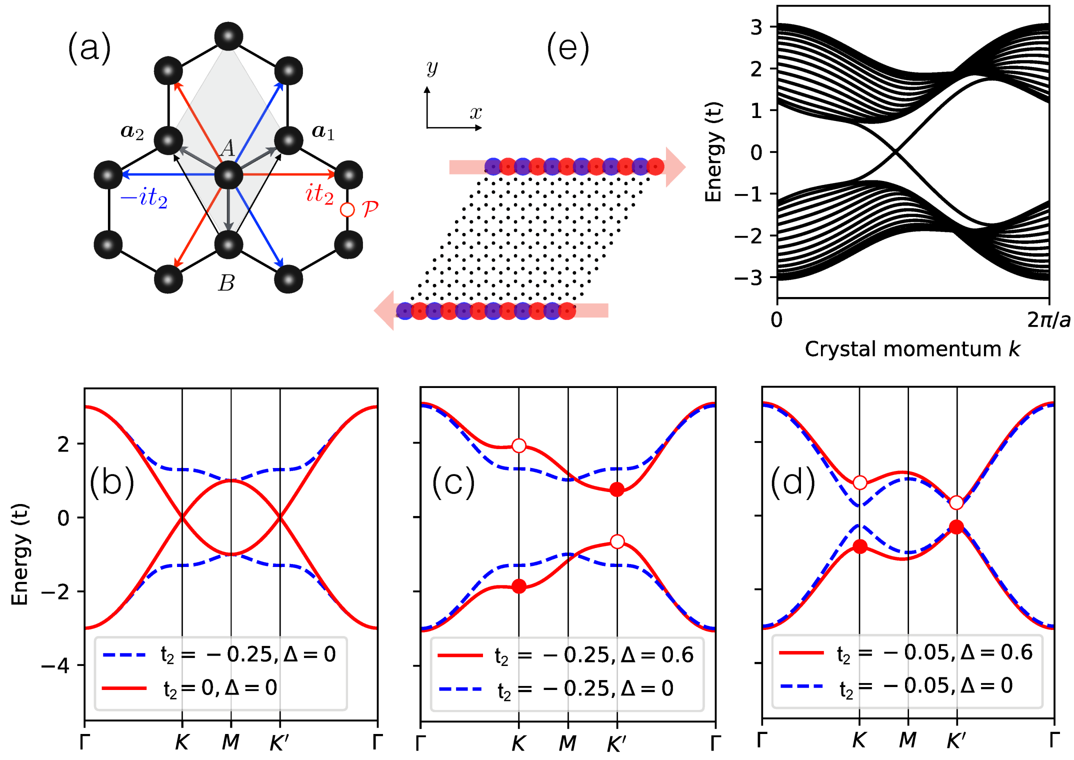

Figure 1.6: Haldane graphene magnetic model. (a) Graphene honeycomb crystal with marked inversion centre $\mathcal{P}$. (b) Centrosymmetric ($\Delta = 0$) graphene and Haldane graphene energy bands. (c) Haldane model energy bands in the topological phase with marked band-inversion (full and empty circles). (d) Haldane model energy bands in topologically trivial phase. (e) Two counterpropagating edge state localisation in the ribbon of the graphene crystal (left) and the surface energy spectrum showing the two counterpropagating edge modes in the bandgap (right). The surface spectrum corresponds to the topological phase.

This form illustrates that in the chosen basis the Hamiltonian is not in Bloch periodic form, $H(\boldsymbol{k} + \mathbf{G}) \neq H(\boldsymbol{k})$. We can transform the Hamiltonian to the periodic Bloch form by

$$c_B \rightarrow c_B e^{i\boldsymbol{k}\boldsymbol{\delta}_3}, \tag{1.72}$$

where $\boldsymbol{\delta}_3$ connects $A - B$ atoms in Fig. 1.6. The energy bands can be obtained analytically:

$$\epsilon_{\pm}(\boldsymbol{k}) = \pm t\sqrt{3 + 2\cos\left(\sqrt{3}k_x a\right) + 4\cos\left(\sqrt{3}k_x a/2\right)\cos\left(3k_y a/2\right)}, \tag{1.73}$$

and are shown in Fig. 1.6(b) by the full red line.

This simple graphene Hamiltonian does have $\mathcal{P} = \sigma_x$ (swaps A, and B sites), $\mathcal{T} = \mathcal{K}$ (representation when spin-orbit interaction is switched-off), and also particle-hole symmetry $\sigma_z H^{\star}(-\boldsymbol{k})\sigma_z = -H(\boldsymbol{k})$. The Dirac points at K and K' are protected *locally* by the $\mathcal{P}$, and $\mathcal{T}$ symmetries [32]. Local protection means that small perturbation shifts Dirac points in momentum space but does not gap the Dirac points, but the Dirac points are not protected to annihilate with each other. The Berry phase π of the massless Dirac point can be straightforwardly estimated by the two-level system Berry phase formula and can be associated with vorticity [32]. The graphene crystal possesses also threefold rotational symmetry C_{3z} which protects the Dirac points globally meaning pins their position at K, and K'.

We will now illustrate the $\mathcal{P}$ and $\mathcal{T}$ symmetry breaking on energy bands of Haldane model [62] which we previously discussed in terms of its Berry curvature maps around Fig. 1.2. Haldane found, that the Landau levels are not necessarily needed to obtain quantized Hall conductivity. Alternatively, a mechanism of spontaneously broken time-reversal symmetry in the system is sufficient. He illustrated the idea on a model TB Hamiltonian of spinless electrons on the graphene lattice with two additional terms [17, 62]:

$$H = H_0 + \Delta \sum_i c_i^\dagger c_i + t_2 \sum_{\langle\langle ij \rangle\rangle} e^{i\nu_{ij}\phi} c_i^\dagger c_j. \tag{1.74}$$

The first term is the nearest neighbour hopping in graphene from Eq. (1.70). The second one is a mass term (see blue dashed line in Fig. 1.6(b)) originating from inversion symmetry breaking due to the chemical non-equivalence of the two basis atoms as e.g. in boron nitride crystal and removes the six-fold symmetries [62]. The final term, is a complex Haldane phase term which breaks time-reversal symmetry. $\nu_{ij} = \text{sign}\left(\mathbf{d}_1 \times \mathbf{d}_2\right)_z = \pm 1$, where $\mathbf{d}_i$ are the bonds along the next-nearest-neighbour vectors (red and blue arrows in Fig. 1.6(a) for $\phi = \frac{\pi}{2}$). We see that the phases are chosen as to be compensated when summed over the whole unit cell.

The Fourier transformed crystal momentum Hamiltonian can be written in a compact form as:

$$H_{\boldsymbol{k}} = \epsilon(\boldsymbol{k}) + \boldsymbol{d}(\boldsymbol{k}) \cdot \boldsymbol{\sigma}, \tag{1.75}$$

We list the parametrization:

$$\begin{align}
\epsilon(\boldsymbol{k}) &= 2t_2 \cos\phi \left[\cos(\boldsymbol{k}\cdot\boldsymbol{a}_1) + \cos(\boldsymbol{k}\cdot\boldsymbol{a}_2) + \cos\left(\boldsymbol{k}\cdot(\boldsymbol{a}_1 - \boldsymbol{a}_2)\right)\right], \tag{1.76}\\
d_1(\boldsymbol{k}) &= t_1 \left(\cos(\boldsymbol{k}\cdot\boldsymbol{k}_1) + \cos(\boldsymbol{k}\cdot\boldsymbol{a}_1) + 1\right), \tag{1.77}\\
d_2(\boldsymbol{k}) &= t_1 \left(\sin(\boldsymbol{k}\cdot\boldsymbol{a}_1) + \sin(\boldsymbol{k}\cdot\boldsymbol{a}_2)\right), \tag{1.78}\\
d_3(\boldsymbol{k}) &= \Delta + 2t_2 \sin\phi \left[\sin(\boldsymbol{k}\cdot\boldsymbol{a}_1) - \sin(\boldsymbol{k}\cdot\boldsymbol{a}_2) - \sin\left(\boldsymbol{k}\cdot(\boldsymbol{a}_1 - \boldsymbol{a}_2)\right)\right] \tag{1.79}
\end{align}$$

In order to make first three terms in the Hamiltonian invariant under $\mathcal{T}$, we have $\epsilon(\boldsymbol{k}) = \epsilon(-\boldsymbol{k})$, $d_1(\boldsymbol{k}) = d_1(-\boldsymbol{k})$, $d_2(\boldsymbol{k}) = -d_2(-\boldsymbol{k})$, and $d_3(\boldsymbol{k}) = d_3(-\boldsymbol{k})$. Similarly, to preserve $\mathcal{P} = \sigma_x$ around the $A - B$ bond centre, we have $\epsilon(\boldsymbol{k}) = \epsilon(-\boldsymbol{k})$, $d_1(\boldsymbol{k}) = d_1(\text{-}\mathbf{k})$, $d_2(\boldsymbol{k}) = -d_2(\text{-}\mathbf{k})$, and $d_3(\boldsymbol{k}) = -d_3(-\boldsymbol{k})$. The $\mathcal{P}$ symmetry is broken by the Semenoff mass, e.g. $\Delta \neq 0$. Finally, $\mathcal{T}$ symmetry is broken by $\epsilon(\boldsymbol{k}) \neq 0$, when $\phi \neq 0, \pi$.

In Fig. 1.6(c), and (d) we plot the energy bands for a topological and trivial phase. We see that the origin of the band inversion is the interplay of the Seemenof mass and Haldane terms, and when they are both present the K, and K' valleys are not equivalent. The Berry curvature integration is quantized in the topological phase and gives a Chern number. The topological phase also hosts two counterpropagating edge state on opposite edges of a ribbon used in numerical calculation and shown in Fig. 1.6(e). The inversion symmetry breaking mass term Δ shifts the crossing of the counterpropagating edge modes off the point $\frac{\pi}{a}$. Although not discussed in a general context, this conclusion indicates the role of broken both time-reversal and spatial inversion symmetry for the quantized Hall conductivity and we will use this implication in constructing spontaneous Hall antiferromagnet model in Section 1.7 and we will observe that the crystal chirality due to the non-centrosymmetricity plays a central role in symmetry breaking mechanism responsible for the spontaneous Hall effect in collinear antiferromagnets.

Spin-orbit coupled lattices

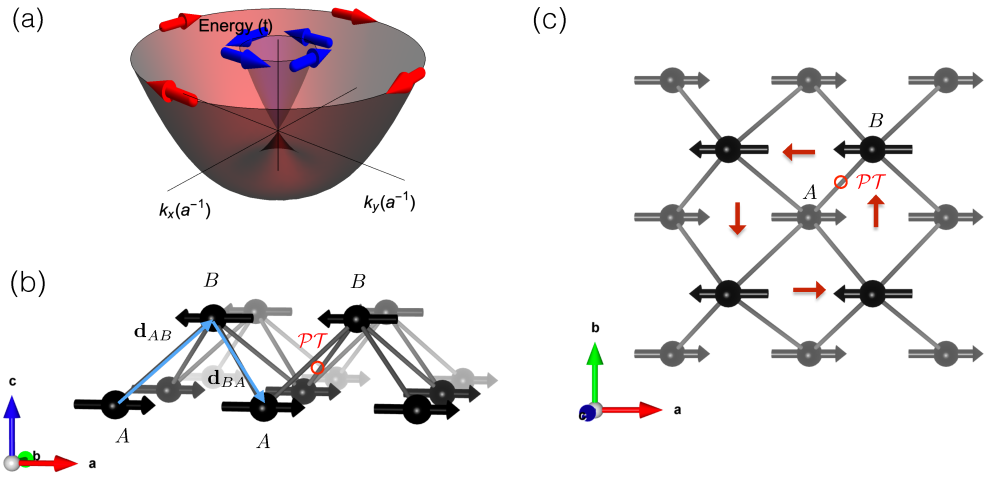

Figure 1.7: Spin-orbit coupling and symmetries of an antiferromagnetic quasi-two-dimensional crinkled crystal. (a) Notorious Rashba spin-orbit dispersion and spin-orbit coupling. (b) Side view with marked $\mathcal{PT}$ symmetry. (c) Top view with spin-orbit fields corresponding to the next-nearest neighbour hoppings on the A sublattices marked with red arrows.

To facilitate transparent understanding of our topological antiferromagnetic effects we will construct two crystals with additional TB SOC and antiferromagnetic terms. Antiferromagnetic ordering can originate from various microscopic mechanism: Anderson superexchange, Hubbard correlations, itinerant electrons, frustrated magnetic interactions, spin-liquid etc. The mean-field expression can be derived from the Hubbard term $H_U = U\sum_i n_{i\uparrow}n_{i\downarrow}$ and we can consider a collinear staggered on-site term [108]:

$$H_U \approx -U\sum_i \sum_{f=x,y,z} c^\dagger_{iA}\left[m_f\sigma_f\right]c_{iA} + U\sum_{f=x,y,z} c^\dagger_{iB}\left[m_f\sigma_f\right]c_{iB}. \tag{1.80}$$

SOC is a consequence of relativistic effects from the Dirac equation as we will discuss in Chapter 2. In the energy bands, SOC in combination with local (global) inversion asymmetry manifests by spin-splitting and local (global) spin-polarisations. We have listed all the possible spin polarisation symmetries in Refs.[23, 109] arising from the global or local non-centrosymmetricity which can be constructed from the Rashba, Dresselhaus, or Weyl symmetry. Rashba corresponds to the surface inversion asymmetry and we show typical energy bands splitting around TRIM and spin-polarisation in Fig. 1.7(a). We note that analogical spin-momentum locking arises at the surfaces of topological insulators [110]. The local inversion asymmetries are producing localised spin-polarisations around atoms [102, 111, 112] which were shown useful for manipulation of $\mathcal{PT}$ antiferromagnets [102, 103]. Dresselhaus corresponds to the bulk inversion asymmetry and manifests, for instance, in NiMnSb [109]. Finally, Weyl spin polarisation arises in Kramers-Weyl-like crossings discussed in Section 1.3.

Effective SOC due to the specific symmetries of crystals with a heavy elements can be derived from a real space Hamiltonian [42, 113]:

$$H_{\mathrm{SOC}}(r) = \sum_{\langle i,j,k \rangle} i\lambda(r_i - r_j)\left(\mathbf{d}_{ik} \times \mathbf{d}_{kj}\right) \cdot \boldsymbol{\sigma} c_i^\dagger c_j \tag{1.81}$$

In Fig. 1.7(b) we illustrate the construction of spin-orbit fields for the electron second nearest neighbour hopping ($A_i - A_j$ or $B_i - B_j$). During the hopping the electron traverses the nearest neighbour atom from the second sublattice. We have constructed the crystal as two non-centrosymmetric Rashba systems combined into one with opposite sublatices exhibiting opposite inversion symmetry breaking. In Fig. 1.7(c) we illustrate the spin-orbit fields from this term for the sake of brevity only for one unit cell and sublattice A. In the finite slab geometries required for the calculation of the edge states or conductance, a discretised version of the second quantized Hamiltonian can be used:

$$H_{\mathrm{SOC}} = \frac{\lambda}{2a} \sum c_i^\dagger c_{i+\delta_x} - c_i^\dagger c_{i-\delta_x} - i\left(c_i^\dagger c_{i+\delta_y} + c_i^\dagger c_{i-\delta_y}\right) + h.c., \tag{1.82}$$

where δ_x, δ_y mark shifts by one unit cell in x, y directions. Eq. (1.82) corresponds to the Rashba spin-orbit coupling on the A sublattice, for the B sublattice we obtain term with the same structure but opposite sign. We will formulate in the next two sections lattice SOC Hamiltonians modelling Dirac quasiparticle antiferromagnet and spontaneous Hall antiferromagnet.

1.6 Dirac quasiparticle antiferromagnet model

Here we present our Dirac quasiparticle antiferromagnetic model based on our paper [27]. We show the crystal structure in Fig. 1.8(a) and the Brillouin zone in Fig. 1.8(b).

Now we construct a minimal model of the tetragonal CuMnAs antiferromagnetic sublattice. We consider $s-d$ type itinerant TB model with only the Mn atoms and with one orbital per atom of s symmetry. We start with only a single layer of the crinkled quasi-2D square crystal shown in Figs. 1.7(b,c) by neglecting the coupling between the stacked quasi-2D planes. This is justified since the distance between the planes is larger than first and second nearest neighbour distances within the quasi-2D plane. The crinkling generates model SOC term among the second nearest neighbour bonds (inter-sublattice hoppings). In the real space we construct the Hamiltonian (1.81) for our crystal. We consider inter-sublattice $A-B$ hopping t (nearest-neighbour term), intra-sublattice $A-A$ hopping (second nearest neighbour term), the second-neighbour SOC of magnitude λ [107], and J_n labels the antiferromagnetic exchange coupling strength. We

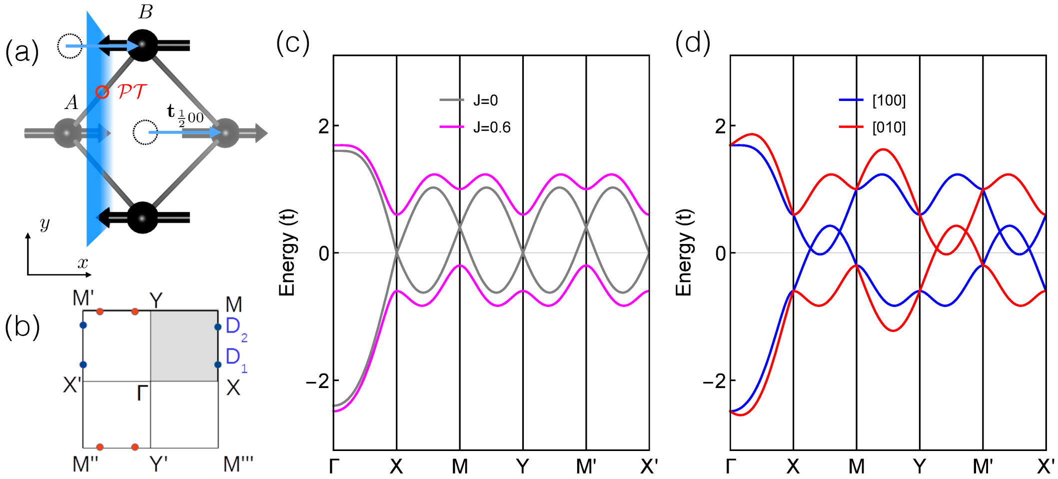

Figure 1.8: Antiferromagnetic Dirac semimetal model. (a) Unit cell with marked off-centred mirror symmetry. (b) Brillouin zone with marked position of Dirac points D_1, and D_2. (c) Energy bands of the non-magnetic and antiferromagnetic states with Néel vector along [001] direction. (d) Energy bands for the Néel vector along [100] and [010] directions.

use the gauge convention I (Eq. (1.62)) and we transform the real space second quantized Hamiltonian (1.81) into the crystal momentum space,

$$
\begin{aligned}
H = &-2t\tau_x \cos\frac{k_x}{2}\cos\frac{k_y}{2} - t'(\cos k_x + \cos k_y) + \\
&\lambda\tau_z\left(\sigma_y \sin k_x - \sigma_x \sin k_y\right) + \tau_z J_n \boldsymbol{\sigma}\cdot\mathbf{N}\,,
\end{aligned}
\tag{1.83}
$$

where the wavevector $k_{x(y)}$ is in units of the inverse lattice constant. $\boldsymbol{\tau}$ and $\boldsymbol{\sigma}$ are Pauli matrices describing the orbital site A/B and spin degrees of freedom, respectively. As we have seen earlier in Eq. (1.44) the 4×4 Dirac Hamiltonian (1.83) can be diagonalized analytically,

$$
\begin{aligned}
E_{\boldsymbol{k}\pm} = &-t'(\cos k_x + \cos k_y) \pm [4t^2\cos^2\frac{k_x}{2}\cos^2\frac{k_y}{2} + \\
&(J_nN_x - \lambda\sin k_y)^2 + (J_nN_y + \lambda\sin k_x)^2 + J_n^2N_z^2]^{1/2}\,.
\end{aligned}
\tag{1.84}
$$

We plot in Fig. 1.8(c) the energy bands measured from the Fermi energy for parameters set as $\lambda = 0.8t$, $J_n = 0.6t$, and $t' = 0.08t$ and magnetic moment along the c-crystal axis. For comparison we also plot the bands in the non-magnetic state ($J_n = 0$) [76].

Our model hosts two Dirac point (DP)s for the Néel vector $\mathbf{N}\|[100]$, as shown in Fig. 1.8(d). We indicate the two DPs in the first Brillouin zone along the $M - X$ axis at wave-vectors:

$$
\boldsymbol{Q}_1 = (\pi, \arcsin\frac{J_n}{\lambda}) \text{ and } \boldsymbol{Q}_2 = (\pi, \pi - \arcsin\frac{J_n}{\lambda}),
\tag{1.85}
$$

as we show in Figs. 1.8(b,d).

We will now show explicitly that the DPs are protected by an off-centred mirror line symmetry, $\widetilde{\mathcal{M}}_x = \left\{M_x|\tfrac{1}{2}00\right\}$. $\widetilde{\mathcal{M}}_x$ is a combination of the mirror symmetry M_x along the (100)-plane and the half-unit cell translation along the [100] axis. We mark the symmetry in Fig. 1.8(a) and the eigenvalues are $m_\pm = \pm i$. The hybridization of the Kramers partner bands can be prohibited and the four-fold degeneracy of the DP is protected by the $\widetilde{\mathcal{M}}_x$ symmetry (as we show in Fig. 1.4(b)) when [27]:

1. The crossing is located at the Brillouin zone sub-manifold invariant under $\widetilde{\mathcal{M}}_x$, e.g. $k_x = 0, \pm\pi$ planes.

2. The two Kramers pair bands with the wave-functions $\psi_{\boldsymbol{k}}$ and $\mathcal{PT}\psi_{\boldsymbol{k}}$ can be labelled by the same eigenvalue of $\widetilde{\mathcal{M}}_x$. We use the commutation relation of $\widetilde{\mathcal{M}}_x$ and $\mathcal{PT}$ to obtain that this condition is met only at $k_x = \pm\pi$.

3. The two pairs of Kramers partners forming the crossing are assigned the opposite eigenvalue of $\widetilde{\mathcal{M}}_x$. We verify this by $k \cdot p$ perturbation theory expanded around the DPs. Around the $\boldsymbol{Q}_1$ point in the $k_x = \pi$ plane the dispersion reads:
$$E_{\mathbf{Q}_1 + k_y, \pm} = \pm \hbar v_{F,y} k_y, \tag{1.86}$$
and the two Kramers pairs follow:
$$\widetilde{\mathcal{M}}_x \psi_{\boldsymbol{k}\pm} = \widetilde{\mathcal{M}}_x \mathcal{PT} \psi_{\boldsymbol{k}\pm} = \mp i \psi_{\boldsymbol{k}\pm}. \tag{1.87}$$

We illustrated the symmetry eigenvalue assignment to the bands in Fig. 1.4(b).

Our CuMnAs model exhibits the lowest-order ($\mathbf{N}$-independent) component of non-equilibrium spin polarisations $\delta\mathbf{s}_{A,B}$ which are staggered and can generate an efficient field-like SOT, dubbed the NSOT [102, 103]. We can define a tensor corresponding to the even under time-reversal spin-orbit field $\delta\mathbf{s} = \chi^{\text{even}}\mathbf{E}$ (see Eq. (1.56)), where $\mathbf{E}$ is applied electric field. Explicitly, the $\mathcal{T}$-even field is (i) staggered $\chi_A^{\text{even}} = -\chi_B^{\text{even}}$, and (ii) of Rashba symmetry $\chi_{A,12}^{\text{even}} = \chi_{A,21}^{\text{even}}$ [102, 106] (12 are spatial indexes). The field allows for the control of the orientation of $\mathbf{N}$ in the (001)-plane in the direction perpendicular to the applied in-plane current. In Figs. 1.8(b),(d) we see that for $\mathbf{N} \parallel [010]$, the DPs move to the $M' - Y$ line and they are protected now by the $\widetilde{\mathcal{M}}_y = \left\{M_y | 0\frac{1}{2}0\right\}$ symmetry.

Remarkably, since at intermediate in-plane angles there is no symmetry remaining which would protect DPs, the entire spectrum is gapped. We show bands for the transition from $\mathbf{N} \parallel [100]$ to [110] in Fig. 1.9(a,b). This represents RMIT driven by the Néel vector reorientation. The DP band-gap $\Delta(Q_1) \sim \sqrt{1 - \cos(\phi)}$, is a continuous function of the in-plane Néel vector angle ϕ measured from the [100] axis. The transport counterpart of the RMIT is the *topological* AMR which we define as,
$$\text{AMR} \equiv [\sigma(\phi) - \sigma_{\text{min}}]/\sigma_{\text{max}}. \tag{1.88}$$
Here $\sigma(\phi)$ is the ϕ-dependent conductivity with current along the [100] axis and $\sigma_{\text{min(max)}}$ labels the conductivity minimum (maximum). We calculate the AMR of our model via standard Boltzmann equation (1.56) applied for the longitudinal conductivity [82]. The resulting angular dependence is the plot in Fig. 1.9(c). High AMR values correspond to $\phi = 0(\pi/2)$ with the massless DPs at $M - X$ $(M' - Y)$. The difference in magnitudes of the AMR at $\phi = 0(\pi/2)$ corresponds to the anisotropic dispersion of the DPs. The spikes in AMR are a distinct feature

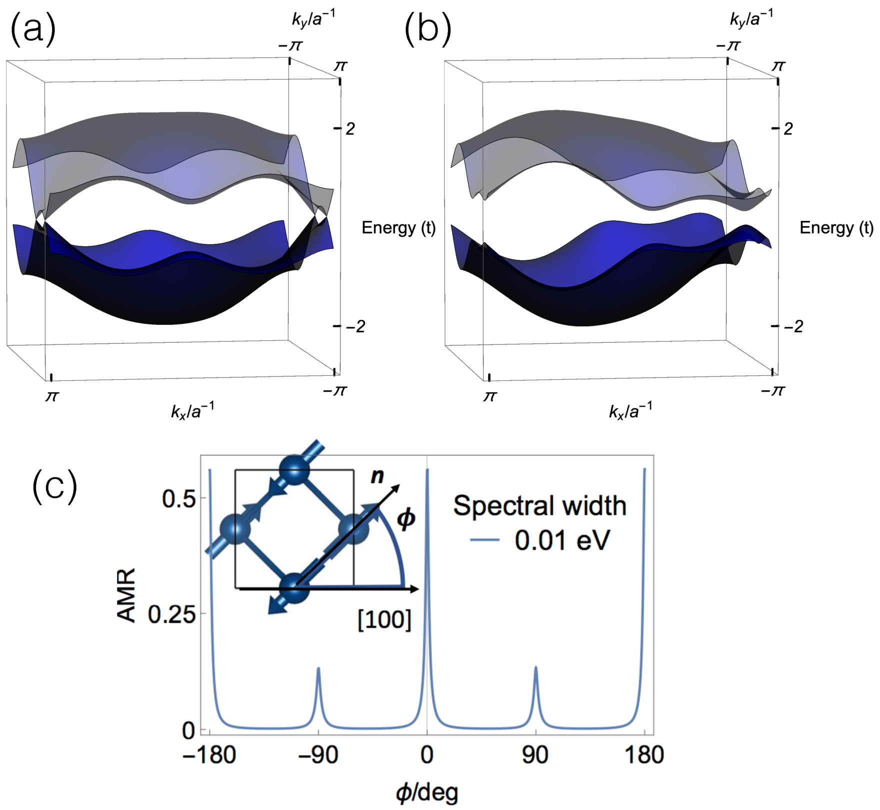

Figure 1.9: **Relativistic metal-insulator transition and topological intrinsic anisotropic magnetoresistance.** (a) Topological Dirac metal to (b) insulator transition in our minimal model driven by the Néel vector reorientation from (a) [100] to (b) [110]. (c) Schematics of the corresponding angular dependence of the topological anisotropic magnetoresistance.

of our topological AMR since the conventional AMR in a magnetic metal exhibits harmonic angular dependence [114].

We can generalize our model to 3D by reinstating the couplings between the quasi-2D planes. Our Hamiltonian (1.83) is renormalized as:

$$\begin{aligned} 2t\tau_x &\overset{3D}{\rightarrow} (2t + t_z\cos k_z)\tau_x + t_z \sin k_z \tau_y, && (1.89)\\ t'(\cos k_x + \cos k_y) &\overset{3D}{\rightarrow} t'(\cos k_x + \cos k_y) + t'_z \cos k_z, && (1.90)\\ \text{and}\lambda &\overset{3D}{\rightarrow} \lambda - \lambda_z \cos k_z. && (1.91) \end{aligned}$$

Now $\widetilde{\mathcal{M}}_x$ protects, instead of DPs in 2D, nodal lines in 3D. We obtain equations describing these lines:

$$\boldsymbol{Q}_1 \overset{3D}{\rightarrow} (\pi, \arcsin\frac{J_n}{\lambda - \lambda_z \cos k_z}). \tag{1.92}$$

This formula gives an open nodal line for $\lambda_z < \lambda/2$, as shown in Fig. 1.10(a,b) for $\lambda_z = 0.2t$. Note that in our Dirac antiferromagnet model, the nodal lines are dispersive in contrast to the paramagnetic $J_n = 0$ model [49]. We have shown in our paper [27] also energy bands of the realistic material candidate, tetragonal CuMnAs, where we found nodal lines deep in the Fermi see (about 3 eV below the

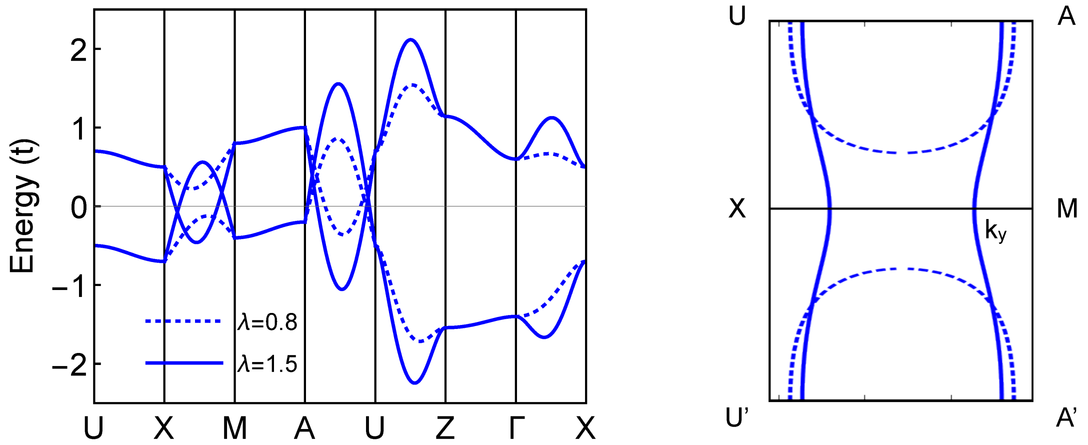

(a) (b)

Figure 1.10: **Antiferromagnetic Dirac nodal line semimetal model.** (a) Energy bands of the full 3D crystal. (b) The open and closed nodal lines in the Brillouin zone.

Fermi level). In Chapter 3 we discuss a realistic material candidate - orthorhombic CuMnAs utilizing the first-principle calculations.

In the following section, we discuss a minimal model of collinear antiferromagnetism generating nonzero Hall conductivity.

1.7 Spontaneous Hall and nodal chain antiferromagnets

We start to construct our minimal model for spontaneous Hall effect from a body centred tetragonal lattice with two atoms with opposite magnetic moments and single s-like orbital per lattice site. This model has a black and white magnetic point group $4/mmm1'$ generated by the $\mathcal{T}_{\text{eff}} = \mathcal{T}\mathbf{t}_{AB}$ symmetry combining time reversal with a half-lattice unit cell translation $\mathbf{t}_{AB} = \left(\frac{1}{2}\frac{1}{2}\frac{1}{2}\right)$ connecting the two sublattices A,B. This symmetry prevents a non-zero Berry curvature and spontaneous Hall effect. Now (by extending the Haldanes idea [62]) we construct spin-orbit fields $B_{SO,k} = \lambda_{ij}\mathbf{d}_k$ on the links connecting the i, j (A, B) sublattices in a way to break the effective $\mathcal{T}_{\text{eff}}$ but preserve the inversion symmetry $\mathcal{P}$ as we show in Fig. 1.11(a). The real space SOC (1.81) can be written as:

$$H_{\text{SOC}} = \sum_{ij,k} \lambda_{ij}\mathbf{d}_k \cdot \boldsymbol{\sigma} c_i^\dagger c_j, \tag{1.93}$$

where the summation is taken over the nearest neighbours i, j and over all the spin-orbit fields k on the bonds connecting them. The corresponding Hamiltonian in the gauge I in the crystal momentum space,

$$\begin{aligned} H(\boldsymbol{k}) = & -4t\tau_x \cos\frac{k_x}{2}\cos\frac{k_y}{2}\cos\frac{k_z}{2} + \tau_z J_n \boldsymbol{\sigma}\cdot\mathbf{N} + \\ & 4i\lambda \sin\frac{k_z}{2}\left(\sigma_{xy}^{(-)}\sin\frac{k_x+k_y}{2} + \sigma_{xy}^{(+)}\sin\frac{k_x-k_y}{2}\right), \end{aligned} \tag{1.94}$$

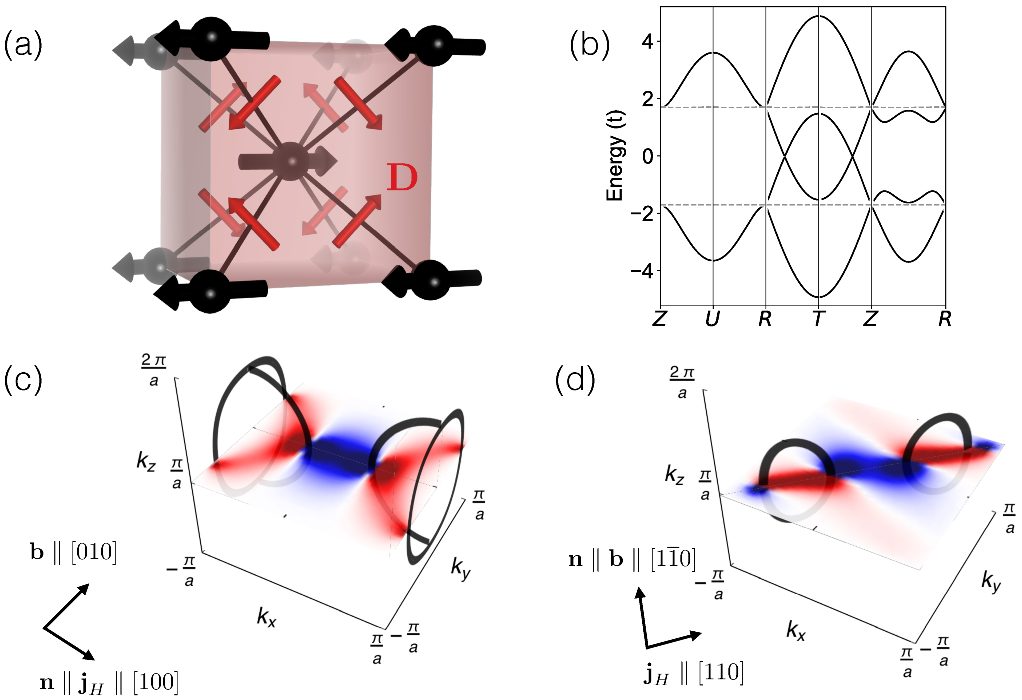

Figure 1.11: **Minimal model calculations of a spontaneous Hall effect in a nodal chain antiferromagnet.** (a) A minimal model of a collinear antiferromagnetic order (black arrows) and spin-orbit fields (red arrows) corresponding in rutile structure to the local chirality of the electron hopping on a bond connecting the nearest neighbour sites of magnetic sublattices. (b) Energy bands calculated for the Néel vector along the [100]-axis with (full line), and without (dashed line) spin-orbit coupling. (c) Berry curvature component Ω_y at the $k_z = \pi$ plane (color plot) and nodal lines in the electronic bands (black lines) for the Néel vector along the [100]-axis. (d) Same as (c) for the Néel vector along the $[1\bar{1}0]$-axis. The model parameters are: $\lambda = 0.4t$ $J_n = 1.7t$.

consists of the first nearest neighbour hopping t, the SOC of strength λ, and $\sigma_{xy}^{(\pm)} = \sigma_x \pm \sigma_y$. The wavevector $k_{x/y/z}$ is in units of the inverse lattice constant, and $\boldsymbol{\tau}$ and $\boldsymbol{\sigma}$ are Pauli matrices describing again the crystal sublattice A, B and spin degrees of freedom, respectively. Our model can be solved analytically:

$$E_{\pm\pm}(\boldsymbol{k}) = \pm\sqrt{T_{\boldsymbol{k}}^2 + J_n^2 + \Lambda_{\boldsymbol{k}}^2 \pm \sqrt{4(J_z^2 + T_{\boldsymbol{k}}^2)\Lambda_{\boldsymbol{k}}^2 + 4(J_y\Lambda_{1,\boldsymbol{k}} - J_x\Lambda_{2,\boldsymbol{k}})}}, \tag{1.95}$$

where

$$\begin{aligned} J_n^2 &= J_x^2 + J_y^2 + J_z^2, && (1.96)\\ T_{\boldsymbol{k}} &= 4t\cos k_x/2\cos k_y/2\cos k_z/2, && (1.97)\\ \Lambda_{1,\boldsymbol{k}} &= 8\lambda\sin k_z/2\cos k_x/2\sin k_y/2, && (1.98)\\ \Lambda_{2,\boldsymbol{k}} &= 8\lambda\sin k_z/2\sin k_x/2\cos k_y/2, && (1.99)\\ \Lambda_{\boldsymbol{k}} &= \Lambda_{1,\boldsymbol{k}} + i\Lambda_{2,\boldsymbol{k}}. && (1.100) \end{aligned}$$

and we plot in Fig. 1.11(b) the resulting bands for $J_n = 0.6t$, and $\lambda = 0.8t$ (full lines), and $\lambda = 0.0t$ (dashed lines). While the exchange and asymmetric spin-orbit coupling (ASOC) (second and third term in Eq. (1.94)) separately do not break $\mathcal{T}$ symmetry; their combination does break the MPG $\mathcal{T}$-symmetry. In turn, we do not have Kramers theorem and the bands are for generic momentum not degenerate [82, 105]. As we see in Fig. 1.11(b-d) the model is at a half-filling an antiferromagnetic generalisation of the topological nodal-chain semimetal [115] protected also by the multiple mirror symmetries present in our model.

For the Néel vector along the [001] axis, the $\mathcal{T}\mathbf{t}_{AB}$ symmetry is not anymore present, however, we have still multiple mirror and rotation point group symmetries preventing Hall conductivity. The spontaneous Hall effect is allowed only when $\mathbf{N}$ has a projection to the (001) plane. We show this on the intrinsic Hall conductivity which we obtained by integrating the Berry curvature (1.30) in the crystal momentum space. For $\mathbf{N} \parallel [100]$, we obtain non-vanishing integral component $\Omega_y(\boldsymbol{k})$ and we illustrate this in Fig. 1.11(c) showing that $\int dk_x \Omega_y(\boldsymbol{k})$ is even in k_y. The corresponding spin-orbit entangled bands around the nodal-lines generate a Berry curvature effective field in crystal momentum space akin to an ordinary magnetic field generated by real space loop currents. The reconfiguration of the nodal-lines between $\mathbf{N} \parallel [100]$ and $[1\bar{1}0]$ results in a dramatic change in Berry curvature maps, as shown in Figs. 1.11 (c,d) and thus we expect a large anisotropy of the spontaneous Hall effect.

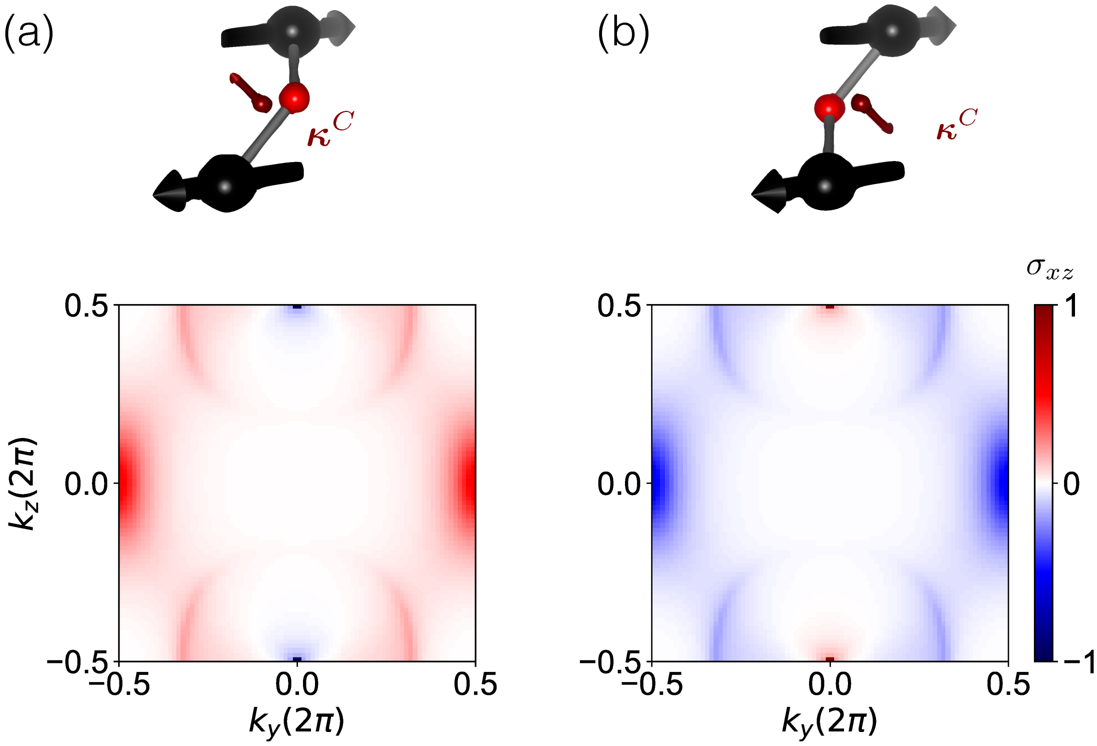

Figure 1.12: **Crystal chirality control of Berry curvature.** (a-b) Two possible orientations of spin-orbit fields generated by the non-magnetic (red) atom interlaced along the bond connecting the two antiferromagnetic sublattices (top). The corresponding Berry curvature maps (bottom).

We can also give the vector $\mathbf{D}_{ij}^{k}$ a specific material interpretation by referring to electron hopping along with the nonmagnetic atom along with the bond between two magnetic sites such as in the rutile RuO_2 crystal which we will discuss in detail in Chapter 4. Here, $\mathbf{D}_{ij}^k = \mathbf{d}_i \times \mathbf{d}_j$, where $\mathbf{d}_i$ and $\mathbf{d}_j$ are unit vectors connecting two nearest-neighbour Ru atoms with the common interlaced oxygen atom as we show in Fig. 1.12(a). Flipping the sign of this "Dzyaloshinskii-Moriya" vector $\mathbf{D}_{ij}^k$ in (1.94), and thus the spin-orbit term, corresponds to the transformation between the two "enantiomorphs" in the crystal shown in Fig. 1.12(a,b). The transformation flips also the sign of the spontaneous Hall conductivity and thus transparently illustrates the possibility to control the Hall conductivity by the local crystal chirality.

We have also calculated the electronic structure of our model with canted moments. We have observed only slight renormalization of the bands with a large Berry curvature contribution around the Fermi level and consequently also the Berry curvature changes only slightly. This demonstrates that the dominating contribution in such a canted antiferromagnet is from the antiferromagnetism and the conventional ferromagnetic anomalous Hall effect is small. We discuss the spontaneous Hall effect in collinear antiferromagnets in great detail in Chapter 4 [116].

1.8 Summary: catalogue of Dirac quasiparticle antiferromagnets

In this chapter, we have introduced the basic results of our topological antiferromagnetic band theory. We have formulated and proven the antiferromagnetic generalisation of the Kramers theorem. The antiferromagnetic Kramers theorem allows for 3D Dirac quasiparticles in antiferromagnets with effective time-reversal symmetries combining time-reversal $\mathcal{T}$ and spatial inversion $\mathcal{P}$. The 3D Dirac quasiparticles are not compatible with ferromagnetic ordering. We have classified the antiferromagnetic Dirac and Weyl quasiparticles based on the $\mathcal{T}$ and $\mathcal{P}$ symmetries and their representation revealing two types of antiferromagnetic Dirac semimetals: magnetoelectric (type-III MSG) and non-symmorphic (Type-IV MSG). We list the simplified catalogue in following table.

magnetism	nonmagnetic	antiferromagnetic	
symmetries	Type II $\mathcal{P}$,$\mathcal{T}$	Type III $\mathcal{P} \circ \mathcal{T}$	Type IV $\mathcal{P}$,$\mathcal{T}\mathbf{t}$
Topological metal	Cd_3As_2[79]	CuMnAs [27, 28]	$EuCd_2As_2$[70]
Topological insulator	Bi_2Se_3 [110]	Fe-Bi_2Se_3 [59]	$MnBi_2Te_4$ [117]

We have also formulated symmetry criteria allowing to simultaneously host Dirac quasiparticles and NSOT. We will discuss the former in greater detail in Chapter 3 on the realistic material candidate CuMnAs. We have shown how to use the existing symmetry tables to reveal high symmetry points and lines in Brillouin zone which can host band degeneracies.

We have discussed also the symmetries of single-band Berry curvature and its nonabelian extension required for the calculation of Berry curvature in metallic systems. In contrast to single-band Berry curvature, the multiband generalisation is in general not gauge invariant. However, it can be transformed into the gauge covariant form. We will use this form in Chapter 4 to evaluate the spontaneous Hall conductivity in antiferromagnets. We have also discussed the separation of linear response coefficient into Boltzmann and Berry curvature like formulas. We have seen that the former picture can be applied to understand anisotropic magnetoresistance and field-like NSOT in minimal antiferromagnetic models.

Finally, we have discussed the multi-sublattice formulation of the TB models. We have shown that the Hamiltonian in the crystal momentum space depends on the gauge choice of the Fourier transformation factors and for the transport calculations, it is convenient to work in the periodic gauge convention I. We have presented the derivation of spin-orbit coupled minimal antiferromagnetic model Hamiltonians. We formulated two such Hamiltonians for two novel effects we predicted in our works. First, the Dirac quasiparticle antiferromagnet hosting relativistic metal-insulator transition driven by the reorientation of the Néel vector and associated with a large, previously unidentified topological contribution to the anisotropic magnetoresistance [27]. Second, a nodal-chain antiferromagnet hosting a new type of spontaneous Hall effect in perfectly compensated collinear antiferromagnet [116]. We will discuss details of the former in Chapter 3, and of the latter in Chapter 4.

2. First principle theory of relativistic antiferromagnets

"Perfection is achieved, not when there is nothing more to add, but when there's nothing left to take away."

Antoine de-Saint Exupery

For topological phases of matter and spintronics transport effects are essential to understand the consequences of SOC arising from relativistic quantum field theory. The relativistic quantum description of materials relies in principle on the calculation of the many-particle wavefunction Ψ_l of N interacting electrons with spins. According to quantum theory [30, 118], the measure

$$\Psi_\ell \left(\mathbf{r}_1\sigma_1, \ldots, \mathbf{r}_N\sigma_N\right) \Psi_\ell^* \left(\mathbf{r}_1\sigma_1, \ldots, \mathbf{r}_N\sigma_N\right) d\mathbf{r}_1 \ldots d\mathbf{r}_N \tag{2.1}$$

represents a probability of finding first particle at position $\mathbf{r}_1$ with spin σ_1, in the infinitesimal region $d\mathbf{r}_1$ around the spatial point $\mathbf{r}_1$, and similarly for all the other particles. Corresponding density matrix describing the mixed quantum mechanical state is written as [30]:

$$\begin{array}{l} \rho\left(\mathbf{r}'_1\sigma'_1, \ldots, \mathbf{r}'_N\sigma'_N | \mathbf{r}_1\sigma_1, \ldots, \mathbf{r}_N\sigma_N\right) \\ = \sum_{\ell=1}^{n} c_\ell \Psi_\ell \left(\mathbf{r}'_1\sigma'_1, \ldots, \mathbf{r}'_N\sigma'_N\right) \Psi_\ell^* \left(\mathbf{r}_1\sigma_1, \ldots, \mathbf{r}_N\sigma_N\right) \end{array}, \tag{2.2}$$

where n labels state degeneracy. Neglecting spin and looking at single time instant, the complex wavefunction depends on $3N$ variables. Thus, we obtain a humongous number of possibilities of choosing complex scalar field per point in real space $\infty^{2\infty^{3N}}$ (mapping from ∞^{3N} to ∞^2 [119]). Even just storing a wavefunction table for nitrogen atom with 7 electrons and extremely coarse real-space grid with only 10 points along a linear dimension we would get 10^{21} points corresponding to 1.5×10^4 tons of 64 GB SD cards [120]. Such a description of a quantum system is not only unfeasible for simulating realistic materials but is also unwanted. While various aspects of the richness of the wavefunctions can be proven useful for quantum computing in future, for us, there can be a lot of information contained in the many-particle wavefunction which is redundant. After all, we are rather interested in the observable manifestation of the relativistic quantum effects which can generate useful spin transport and low dissipation movement of electrons.

Tremendous simplification of this problem, celebrated by the Nobel Prize in 1998, can be achieved by utilizing DFT. The central advantage of DFT is the mapping of the problem of determining the impractically rich many particle wavefunction to the calculation of a spin density matrix [121] $n_{\alpha\beta}(\mathbf{r})$ which is function of only *three* spatial coordinates. Furthermore, α, β correspond to spin, and the density matrix can be expressed in terms of *effective single particle Kohn-Sham wavefunctions* $\psi_{i\alpha}$:

$$n_{\alpha\beta}(\mathbf{r}) = \sum_{\substack{i=1 \\ \varepsilon_{i\alpha}, \varepsilon_{i\alpha} \leq \varepsilon_F}}^{N} \psi_{i\beta}(\mathbf{r}) \psi_{i\beta}^*(\mathbf{r}). \tag{2.3}$$

From this ground state electronic density we can determine observables of interest, for instance, topological quasiparticles in electronic energy bands, disordered Bloch spectral functions in alloys, anisotropic magnetoresistance, or spontaneous Hall conductivity.

In this chapter, we will introduce the main ideas of the relativistic DFT in antiferromagnetic materials, and its numerical implementation within pseudopotential and TB-LMTO methods. Finally, we will describe numerical schemes employed on supercomputers for calculating intrinsic Hall conductivity within the Berry curvature approach, and anisotropic magnetoresistance in disordered alloys within the Kubo-Greenwood framework.

2.1 Relativistic Kohn-Sham-Dirac theory

By employing the Born-Oppenheimer adiabatic approximation we can decouple the equation of motion for electrons and nuclei [120]. Since we want to formulate relativistic and magnetic single-particle Kohn-Sham Hamiltonian, we start with studying single-particle Dirac equation. The Hamiltonian density of relativistic quantum field theory of electrons in an external field can be written as [118, 122]:

$$\mathcal{H}(\mathbf{r}) =: \psi^{\dagger}(\mathbf{r}) \left[\frac{\hbar c}{\mathrm{i}} \boldsymbol{\alpha} \cdot \nabla + \beta m c^2 - e\phi(\mathbf{r}) + e\boldsymbol{\alpha} \cdot \mathbf{A}(\mathbf{r}) \right] \psi(\mathbf{r}) : + \mathcal{H}_{\mathrm{ext}}(\mathbf{r}). \tag{2.4}$$

Here the internal fields described by wavefunctions $\psi(\mathbf{r})$ are quantized and interact in the radiation part $\mathcal{H}_{\mathrm{ext}}(\mathbf{r})$ with the classical external fields [123] and the external classical fields due to the nuclei are neglected, : ... : denotes normal ordering [122]. The rest mass, reduced Planck constant, and speed of light are denoted as m, $\hbar$, and c, and the Clifford-algebra structure [119] of the Dirac equation is captured by the Dirac matrices in the standard representation [118], where:

$$\boldsymbol{\alpha} = \begin{pmatrix} 0 & \boldsymbol{\sigma} \\ \boldsymbol{\sigma} & 0 \end{pmatrix}, \beta = \begin{pmatrix} \mathbf{1} & 0 \\ 0 & -\mathbf{1} \end{pmatrix}, \tag{2.5}$$

and we span the 2D subspaces via the Pauli matrices (1.1) and the unit matrix.

The DFT is based on two Kohn-Sham-Hohenberg theorems. Hohenberg and Kohn [124] expressed the ground state energy in terms of a functional of the electron density. Kohn and Sham [125] then considered the Schrödinger equation of N noninteracting Kohn Sham electrons and the corresponding density to uniquely describe the physics of N interacting electrons. We state the usual form of the two theorems without proofs which can be found in many textbooks, e.g. [118].

Theorem 2: Hohenberg, and Kohn.

The total ground state energy can be expressed as a unique functional of the electron density.

Theorem 3: Kohn, and Sham.

The ground state energy is obtained by minimizing the energy functional with respect to the electronic density while the number of electrons N is fixed. The ground state of these N interacting electrons is described by the N single-particle Kohn Sham equations.

The total energy density in external scalar electric potential ϕ and magnetic vector potential $\mathbf{A}$ can be written as,

$$E[\varrho, \boldsymbol{j}] = \mathcal{F}[\varrho, \boldsymbol{j}] + \int \mathrm{d}^3 r \varrho(\mathbf{r})\phi(\mathbf{r}) - \frac{1}{c}\int \mathrm{d}^3 r \boldsymbol{j}(\mathbf{r}) \cdot \mathbf{A}(\mathbf{r}) \tag{2.6}$$

and can be determined by varying the energy as a functional of the electronic density, and current density:

$$\begin{aligned} \varrho(\mathbf{r}) &= -e\langle : \psi^\dagger(\mathbf{r})\psi(\mathbf{r}) : \rangle, \\ \boldsymbol{j}(\mathbf{r}) &= -e\langle : \psi^\dagger(\mathbf{r})\boldsymbol{\alpha}\psi(\mathbf{r}) : \rangle. \end{aligned} \tag{2.7}$$

During the minimization process the total number of electrons can be formally included as Lagrange multiplier. We explicitly mark in the equations normal ordering since otherwise the positron solutions would give unwanted negative energies.

Finally, $\mathcal{F}[\varrho, \boldsymbol{j}]$ marks the Kohn-Sham universal functional

$$\mathcal{F}[\varrho, \boldsymbol{j}] = \mathcal{K}[\varrho, \boldsymbol{j}] + U_{\text{Hartree}}\,[\varrho, \boldsymbol{j}] + E_{\text{xc}}[\varrho, \boldsymbol{j}], \tag{2.8}$$

where the $\mathcal{K}[\varrho, \boldsymbol{j}]$ is the kinetic energy of the noninteracting Kohn-Sham electrons with the same densities as interacting original electrons, $U_{\text{Hartree}}\,[\varrho, \boldsymbol{j}]$ is the electron-electron interaction energy within Hartree approximation, and $E_{\text{xc}}[\varrho, \boldsymbol{j}]$ is the exchange and correlations potential which is in general unknown and needs to be approximated, e.g. within the local spin density approximation (LSDA).

Non-collinear magnetic and electric fields

In the realistic Hall effect and magnetoresistance measurements the crystal is exposed to the external electric and magnetic fields. While the scalar fields can be treated in straightforward way, in both nonrelativistic and relativistic approximations, the magnetic field and related orbital moments represent additional formal complications. The single-particle Kohn-Sham-Dirac equation reads [118]:

$$\left(c\boldsymbol{\alpha} \cdot \left(\hat{\mathbf{p}} - e\mathbf{A}^{\text{eff}}(\mathbf{r})\right) + \beta mc^2 + v^{\text{eff}}(\mathbf{r})\right)\psi_i(\mathbf{r}) = \varepsilon_i\psi_i(\mathbf{r}). \tag{2.9}$$

Formally, the equation has a form of a single-particle Dirac equation. However, ψ_i, ε, and v^{eff}, $\mathbf{A}^{\text{eff}}$ are now effective Kohn-Sham wavefunctions, eigenenergies and effective potentials, respectively. The effective potentials v^{eff}, $\mathbf{A}^{\text{eff}}$ are expressed as a sum of internal and external potentials. In principle, the corresponding exchange and correlation potential can be solved by relativistic Monte-Carlo methods [118]. Eqs. (2.9), and (2.7) are solved self-consistently. By introducing a useful notation [118] we can write down the energy functional including the external fields as:

$$\begin{aligned} E\left[J_\mu(\mathbf{r})\right] &= K\left[J_\mu(\mathbf{r})\right] + G\left[J_\mu(\mathbf{r})\right] \\ &+ \int \left(n(\mathbf{r})v(\mathbf{r}) - \mathbf{m}(\mathbf{r}) \cdot \mathbf{B}(\mathbf{r}) + \mathbf{J}(\mathbf{r}) \cdot \mathbf{A}^{\text{ext}}(\mathbf{r}) - \frac{1}{c}\frac{\partial \mathbf{g}(\mathbf{r})}{\partial t} \cdot \mathbf{A}^{\text{ext}}(\mathbf{r})\right) d\mathbf{r}. \end{aligned} \tag{2.10}$$

The last two terms correspond to the diamagnetic effects and are difficult to treat numerically. Since these effects are often weak, the existing DFT codes usually neglect these two terms. The resulting expression is taking the form:

$$\left(\boldsymbol{\alpha}\cdot\hat{\mathbf{p}}+\beta mc^2+v^{\mathrm{eff}}(\mathbf{r})-\mathbf{m}(\mathbf{r})\cdot\mathbf{B}^{\mathrm{eff}}(\mathbf{r})\right)\psi_i(\mathbf{r})=\varepsilon_i\psi_i, \tag{2.11}$$

with the corresponding electronic and magnetization densities:

$$\begin{aligned} n(\mathbf{r}) &= \sum_{i=1}^{N}\psi_i^{\dagger}(\mathbf{r})\psi_i(\mathbf{r}), && (2.12)\\ \mathbf{m}(\mathbf{r}) &= \mu_{\mathrm{B}}\sum_{i=1}^{N}\psi_i^{\dagger}(\mathbf{r})\beta\boldsymbol{\sigma}\psi_i(\mathbf{r}). && (2.13)\end{aligned}$$

The magnetic density functional can be written also in a compact way as [126]

$$\boldsymbol{\rho}=\frac{1}{2}\left(n\mathbf{1}+\boldsymbol{\sigma}\cdot\mathbf{m}\right)=\frac{1}{2}\begin{pmatrix} n+m_z & m_x-im_y\\ m_x+im_y & n-m_z\end{pmatrix}. \tag{2.14}$$

Analogously, the electric and magnetic potentials can be decomposed as:

$$\begin{aligned} &v^{\mathrm{eff}}\left(\mathbf{r}\right)=v(\mathbf{r})+\tfrac{e^2}{4\pi\epsilon_0}\int\tfrac{n(\mathbf{r}')}{|\mathbf{r}-\mathbf{r}'|}d\mathbf{r}'+\tfrac{\delta E_{\mathbf{xc}}[n(\mathbf{r}),\mathbf{m}(\mathbf{r})]}{\delta n(\mathbf{r})},\\ &\mathbf{B}^{\mathrm{eff}}\left(\mathbf{r}\right)=\mathbf{B}^{\mathrm{ext}}\left(\mathbf{r}\right)+\tfrac{\delta E_{\mathbf{xc}}[n(\mathbf{r}),\mathbf{m}(\mathbf{r})]}{\delta\mathbf{m}(\mathbf{r})}.\end{aligned} \tag{2.15}$$

Importantly, the energy functional is now expressed in terms of quantities known from magnetism and nonrelativistic DFT, which allows us to use the numerical methods developed for solving the nonrelativistic Kohn-Sham equations. Since we couple the fields only to the spin of the electrons, this approximation is called spin-only relativistic DFT. In Fig. 2.1 we show an example of charge and magnetization densities of a non-collinear antiferromagnet IrMn$_3$, extensively explored in the spintronics context, calculated in the VASP code. We note that the approximation tends to fail for systems which are at the present moment not useful for practical spintronics applications, e.g., f-electron materials or stars with huge internal magnetic field [127].

The net magnetic moment can be calculated as a sum of the orbital and spin part:

$$\mathbf{m}(\mathbf{r})\approx-\mu_{\mathrm{B}}\langle:\psi^{\dagger}(\mathbf{r})\left[\frac{1}{\mathrm{i}}\mathbf{r}\times\boldsymbol{\nabla}+\boldsymbol{\Sigma}\right]\psi(\mathbf{r}):\rangle. \tag{2.16}$$

The numerical prefactor has value 5.2×10^{-3} in Rydberg atomic units and thus magnetic effects are small and represent challenges for the numerical evaluations.

We note that we use here the ordering of the spin components up-down-down-up corresponding to the spin angular momentum operator $\frac{1}{2}\gamma^5\boldsymbol{\gamma}$, where $\boldsymbol{\gamma}$ are Dirac matrices. Alternative references use the basis up-down-up-down, spin angular momentum operator $\frac{1}{2}\gamma^5\boldsymbol{\alpha}$ and in turn, there is an additional $\boldsymbol{\beta}$ matrix in front of the magnetic interaction terms.

In calculations of non-collinear magnetic moments, the magnetic part of the exchange correlation potential can be assumed to point locally along the spin density:

$$\mathbf{B}_{\mathrm{xc}}(\mathbf{r})=\hat{S}(\mathbf{r})B_{\mathrm{LSDA}}(\varrho(\mathbf{r}),\mathbf{S}(\mathbf{r})). \tag{2.17}$$

Practically, we will constrain in our calculations the field to point along the single spin-quantization axis within each atomic sphere. This approximation

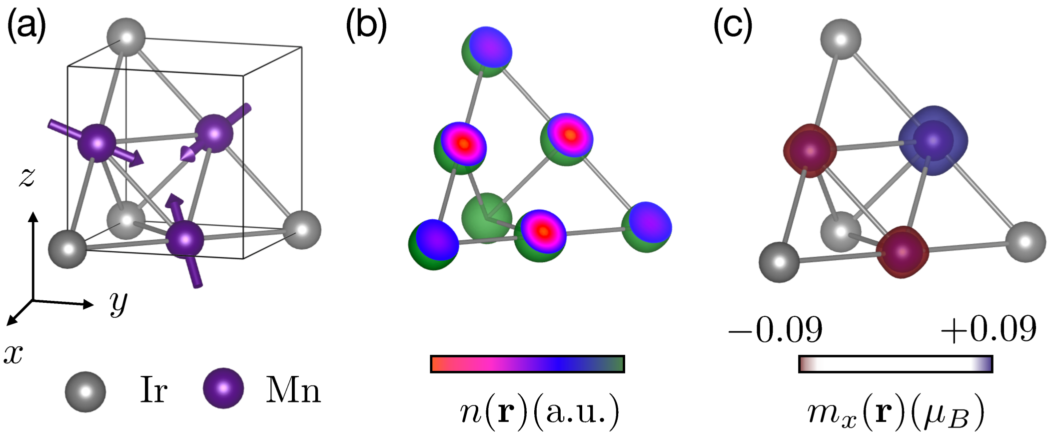

Figure 2.1: **Non-collinear antiferromagnetic magnetization density calculated from density functional theory.** (a) Unit cell of non-collinear antiferromagnet Mn_3Ir. (b) Electronic charge density $n(\mathbf{r})$ generated from the PROCAR file of VASP code. (b) Corresponding magnetization density $m_x(\mathbf{r})$ isosurface.

turns out to work well in magnetic transitional metals and we will adopt here the approximation. The orbital moment is in these systems quenched, represents only small correction to the net moment, and will not change qualitative conclusions obtained from the spin-only LSDA.

Relativistic effects

Relativistic corrections, in the expansion of the fine structure constant of the kinetic term in Eq. (2.8), are represented by the SOC. The additional Darwin term can be also important, e.g., in the description of band inversion in topological insulators [128]. The SOC can be seen as a dynamical kinetic effect. The SOC correction contributes to the magnetic anisotropies, antisymmetric Dzialoshinskiy–Moriya interaction (DMI), and is a necessary ingredient of theories of the spontaneous anomalous Hall effect in most magnetic materials (identified so far). In contrast, the relativistic perturbations to the Hartree term (e.g. the Breit interaction) contribute to the shape anisotropy and dipole-dipole interactions [118, 122]. The corrections are in principle present also in the exchange-correlations terms, however, they tend to be smaller than the errors originating from the approximation to the functional *per se* [122].

To study the form of the SOC we can rewrite the four-component bi-spinor $\psi^T = (\phi, \chi)$ Dirac equation as two coupled spinor equations:

$$\begin{aligned} c(\boldsymbol{\sigma}\cdot\boldsymbol{p})\chi &= (\varepsilon - V - mc^2)\,\phi, \\ c(\boldsymbol{\sigma}\cdot\boldsymbol{p})\phi &= (\varepsilon - V + mc^2)\,\chi, \end{aligned} \tag{2.18}$$

where V marks now the (effective) potential, and $\boldsymbol{p}$ momentum.

To gain additional insight and also derive further approximations (e.g. atomic sphere approximation) it is convenient to assume a spherically symmetric potential [121, 123, 129]. We can classify the equations of motions and solutions of the Dirac equation by crystal momentum (Bloch theorem employing the crystal periodicity) and by the additional quantum numbers. The total angular momentum can be written as a sum of the orbital $\mathbf{L}$ and spin $\mathbf{\Sigma}$ part:

$$\mathbf{J} = \mathbf{L} + \hbar\frac{1}{2}\mathbf{\Sigma}, \tag{2.19}$$

where $\mathbf{\Sigma} = \boldsymbol{\sigma} \otimes \mathbf{1}$. In contrast to nonrelativistic (and zero SOC) theory, $\mathbf{L}$ and $\mathbf{\Sigma}$ are not conserved on their own. However, the total angular momentum $\mathbf{J}^2$, J_z, and $\boldsymbol{K}$

$$\boldsymbol{K} = \begin{pmatrix} \boldsymbol{\sigma}\cdot\mathbf{L} + \hbar & 0 \\ 0 & -\boldsymbol{\sigma}\cdot\mathbf{L} - \hbar \end{pmatrix} \tag{2.20}$$

commute with the Dirac Hamiltonian in the spherical potential approximation, have common set of eigenvalues[121]:

$$-\kappa\hbar, j(j+1)\hbar^2 \text{ and } j_z\hbar, \tag{2.21}$$

and are related as $\kappa = \pm\left(j + \frac{1}{2}\right)$, which is a nonzero integer. For $\kappa > (<) 0$ the spin is parallel (antiparallel) to the total angular momentum in the nonrelativistic limit. The relativistic notation can be conveniently written as

$$\psi = \begin{pmatrix} \phi \\ \chi \end{pmatrix} = \begin{pmatrix} g(r) & \mathcal{Y}^{j_z}_{je} \\ if(r) & \mathcal{Y}^{j_z}_{j'_\ell} \end{pmatrix}, \tag{2.22}$$

where f, and g are standard radial functions known from the radial solutions to the Schrödinger equation [129]. Furthermore, the Pauli spinors can be combined with spherical harmonics Y_l^m (m, l are standard nonrelativistic magnetic and angular momentum quantum numbers):

$$\mathcal{Y}^{j_z}_{j_\ell} = \pm\sqrt{\frac{\ell + j_z + \frac{1}{2}}{2\ell+1}}\, Y_\ell^{j_z - 1/2}\begin{pmatrix} 1 \\ 0 \end{pmatrix} + \sqrt{\frac{\ell \mp j_z + \frac{1}{2}}{2\ell+1}}\, Y_\ell^{j_z + 1/2}\begin{pmatrix} 0 \\ 1 \end{pmatrix}, \tag{2.23}$$

where we used shorthand notation $j = \ell \pm 1/2$, and the following identities hold:

$$\begin{aligned} &\kappa = j + \tfrac{1}{2} \quad \text{then } \ell = j + \tfrac{1}{2}, \ell' = j - \tfrac{1}{2}, \\ &\kappa = -\left(j + \tfrac{1}{2}\right) \quad \text{then } \ell = j - \tfrac{1}{2}, \ell' = j + \tfrac{1}{2}. \end{aligned} \tag{2.24}$$

In turn the set of Eq. (2.18) can be written in the radial form as:

$$\begin{aligned} \hbar c\left(\frac{\mathrm{d}f}{\mathrm{d}r} - \frac{(1+\kappa)}{r}f\right) &= -\left(\varepsilon - V - mc^2\right)g, \\ \hbar c\left(\frac{\mathrm{d}g}{\mathrm{d}r} + \frac{(1+\kappa)}{r}g\right) &= \left(\varepsilon - V - mc^2\right)f, \end{aligned} \tag{2.25}$$

where we have used the identity [121]:

$$\boldsymbol{\sigma}\cdot\mathbf{p} \equiv \frac{(\boldsymbol{\sigma}\cdot\mathbf{r})}{r^2}(\boldsymbol{\sigma}\cdot\mathbf{r}(\boldsymbol{\sigma}\cdot\mathbf{p})) = \frac{(\boldsymbol{\sigma}\cdot\mathbf{r})}{r}\left(-\mathrm{i}\hbar\frac{\mathrm{d}}{\mathrm{d}r} + \mathrm{i}\boldsymbol{\sigma}\cdot\mathbf{L}\right). \tag{2.26}$$

We are in the position to derive the *scalar relativistic approximation* [130, 131]. In this approximation the SOC interaction is separated and is included variationally or in perturbation theory. We can rewrite the second Eq. (2.25) as:

$$f = \frac{\hbar}{2Mc}\left(\frac{\mathrm{d}g}{\mathrm{d}r} + \frac{(1+\kappa)}{r}g\right), \tag{2.27}$$

where $M = m + \frac{\varepsilon - mc^2 - V}{2c^2}$ generates a *mass-velocity* correction, e.g., the mass of the electron increases with its velocity approaching speed of light. We substitute the last equation into the first Eq. (2.25) and we proceed with the differentiation:

$$\begin{gathered}
-\frac{\hbar^2}{2M}\frac{1}{r^2}\frac{\mathrm{d}}{\mathrm{d}r}\left(r^2\frac{\mathrm{d}g}{\mathrm{d}r}\right) + \left[V + \frac{\hbar^2}{2M}\frac{\kappa(\kappa+1)}{r^2}\right]g, \\
-\frac{\hbar^2}{4M^2c^2}\frac{\mathrm{d}V}{\mathrm{d}r}\frac{\mathrm{d}g}{\mathrm{d}r} - \frac{\hbar^2}{4M^2c^2}\frac{\mathrm{d}V}{\mathrm{d}r}\frac{(1+\kappa)}{r}g = \varepsilon' g.
\end{gathered} \tag{2.28}$$

This equation takes the form of the Schrödinger equation with two additional terms. The last but one term in Eq. (2.28) is the Darwin term, and finally the last term is the SOC term. The Darwin term does not have classical analogue and corresponds to the *Zitterbewegung*, the fluctuations around mean position of the electron due to the interference between positive and negative energy states. The scalar relativistic approximation is obtained by dropping the SOC term, and can be formally solved as Schrödinger equation. The SOC can be added in the last step of the calculation. The four-component wavefunction is rewritten as [131]:

$$\tilde{\psi} = \begin{pmatrix} \tilde{g} Y_L \chi_s \\ \mathrm{i}\left(\frac{\sigma\cdot \mathrm{x}}{r}\right)\left(-\tilde{f} + \frac{1}{2Mcr}\tilde{g}\sigma\cdot \mathrm{L}\right) Y_L \chi_s \end{pmatrix} \equiv \begin{pmatrix} \tilde{\phi} \\ \tilde{\chi} \end{pmatrix} \tag{2.29}$$

where $\chi_+ = \begin{pmatrix} 1 \\ 0 \end{pmatrix}, \chi_- = \begin{pmatrix} 0 \\ 1 \end{pmatrix}$. Finally, the Dirac Hamiltonian is applied to the wave function $\tilde{\phi}$ and we obtain [121]:

$$H_{\mathrm{D}}\tilde{\psi} = \varepsilon'\tilde{\psi} + \frac{\hbar}{(2Mc)^2}\frac{1}{r}\frac{\mathrm{d}V}{\mathrm{d}r}\begin{pmatrix} (\boldsymbol{\sigma}\cdot\mathbf{L})\mathbf{1} \\ 0 \end{pmatrix}\tilde{\psi}, \tag{2.30}$$

where the last term is the spin-orbit interaction. This term measures how much the relativistic solution differs from the radial scalar relativistic wavefunction $\tilde{\phi}$ (large component). Technically, the SOC term is computed in the given basis and is added in the variational process [132]. In nonmagnetic systems, spins are degenerate and this term lifts this spin degeneracy. However, *certain types of collinear antiferromagnetism may remove this degeneracy already without SOC* as we will see in Chapter 4 in $\mathrm{RuO_2}$ antiferromagnet and the crystal Hall effect. The validity of this approximation was discussed by MacDonald [131], and details within linear methods in band theory were formulated by Andersen [133].

Approximations to potential and wafunctions

Local spin density approximation (LSDA). The exchange correlation potential is generically unknown, and the (relativistic) Monte-Carlo determination can represent an overwhelming task. The exchange correlation potential functional is commonly approximated within the LSDA as a function of the local electronic density $n(\mathbf{r})$ [120]:

$$v_{\mathrm{xc}}^{\mathrm{LSDA},\pm}\left[n_+,n_-\right](\mathbf{r})=\frac{\delta E_{\mathrm{xc}}^{\mathrm{LSDA}}\left[n_+,n_-\right](\mathbf{r})}{\delta n_\pm(\mathbf{r})}, \tag{2.31}$$

where

$$E_{\mathrm{xc}}^{\mathrm{LSDA}}\left[n_+,n_-\right](\mathbf{r})=\int n(\mathbf{r})\mathcal{E}_{\mathrm{xc}}\left[n_+,n_-\right](\mathbf{r})\mathrm{d}^3\mathbf{r}. \tag{2.32}$$

The meaning of the approximation is to divide the inhomogeneous electronic gas into infinitesimal regions approximated to have homogeneous electron gas with the density $n(\mathbf{r})$. In our TB-LMTO calculations of $\mathrm{IrMn_3}$ and $\mathrm{Mn_2Au}$ alloys, we use the Vosko-Wilk-Nusair parametrization [134].

Generalised gradient approximation (GGA). LSDA is known to overestimate the correlations and underestimate the exchange energy. More accurate potentials were developed and their proper usage depends on the problem at hand, they were organized into *Jacobs ladder* according to their accuracy [135]. For our antiferromagnetic systems, GGA is convenient which expresses the energy in terms of not only the density but also its gradients $\nabla n(\mathbf{r})$. Spin-polarised GGA can be written as [136, 137]:

$$E_{\mathrm{xc}}^{\mathrm{GGA}}[n]=\int n(\mathbf{r})\mathcal{E}_{\mathrm{xc}}\left[n_+(\mathbf{r}),n_-(\mathbf{r}),\nabla n_+(\mathbf{r}),\nabla n_-(\mathbf{r})\right]\mathrm{d}^3\mathbf{r}. \tag{2.33}$$

We will use the Perdew Burke Erzenhorf (PBE)[137, 138, 139] implementation of the GGA approximation in the VASP calculations.

Electronic correlations on the DFT+U level. DFT is known to describe well-delocalised s and p electrons, however, DFT can fail to describe more localised d or f orbitals. Furthermore, many antiferromagnetic systems are also strongly correlated, and certain systems require to stabilise in DFT calculation the antiferromagnetic order by the inclusion of the Hubbard repulsion U among the electrons. This problem can be alleviated by adding the Hubbard potential to the localised orbitals. The total energy within DFT+U is given as [120, 140]:

$$E[n(\mathbf{r}),\{n_i\}]=E^{LDA}[n(\mathbf{r})]+\frac{U}{2}\sum_{i\neq j}n_in_j-E_{\mathrm{dc}}(U,J), \tag{2.34}$$

where the second term is the Hubbard interaction, $n_{i,j}$ are electron occupancies of the subspace with correlated orbitals (e.g. of d-type), and the last term is the double-counting correction depending on the Hubbard U and exchange parameter J. The last term needs to be subtracted since the on-site interaction energy was already accounted for in the effective LSDA potential.

Three most used forms of the approximation include fully localised, around-mean field and spherically symmetric (Dudarev) approach [141]. We will use for the $\mathrm{RuO_2}$ the last approximation, which takes the form:

$$E_{\mathrm{LSDA+U}}=E_{\mathrm{LSDA}}+\frac{(U-J)}{2}\sum_\sigma\left[\left(\sum_i n_{ii}^\sigma\right)-\left(\sum_{i,j}n_{ij}^\sigma n_{ji}^\sigma\right)\right]. \tag{2.35}$$

We note that the correction now depends only on the difference $U-J$ and considers spherically averaged U, and J.

While the LSDA works well for itinerant systems with screened correlations, the DFT+U can describe well systems with strong correlations. In the systems where the electronic correlation strength is comparable to the bandwidth, the dynamical mean-field theory (DMFT) and nonlocal extensions were developed [142]. However, the DMFT in systems with strong SOC suffers from sign problem in the Monte-Carlo solvers of the corresponding impurity problem. This is at present an unsolved problem which is NP-hard. This type of problems presumably requires to invent new mathematical tools as fundamental as the quantum theory itself. Finally, we remark, the DMFT has interesting common roots with the CPA method described later in this chapter.

The electronic structure methods can be, besides the type of approximations to the exchange-correlation potential and relativistic corrections to the momentum, grouped according to the used approximations in the Schrödinger equation [143]:

- **Effective potential form.** All electrons (full or spherical potential) - pseudopotential - structureless jellium.
- **Wavefunction approximations.** Real space grids - nonlinear methods (augmented plane waves, Kohn-Korringa-Rostocker scattering and Green functions) - linear (LMTO) - linear combination of atomic orbitals.

We will discuss later in this chapter the two wavefunction approximations which we will use in our simulations of topological antiferromagnets: pseudopotential projector-augmented-wave (PAW) and TB-LMTO methods. In our papers, we use also full potential methods such as FLAPW (implemented in FLEUR, and ELK codes), but we will not discuss these methods here.

2.2 Dirac linear muffin-tin orbitals and Green's functions method

A computationally suitable *ab initio* method for calculations of relativistic spintronics effects in antiferromagnets with heavy elements is the fully relativistic Dirac (FRD)-TB-LMTO-atomic sphere approximation (ASA) in combination with coherent potential approximation (CPA) for the alloying disorder. The FRD method is sometimes also called spin-polarized Dirac (SPD) [118, 131, 144], and besides using the spin-only DFT Dirac-Kohn-Sham Hamiltonian, it relies on several approximations. For details on the general theory and implementation, we refer to the original works by Andersen [133], Ebert[145], Solovyev, and Schick [146, 147, 148], and books by Skriver [149] and Turek [150]. Here we outline the physics of the approximations relevant to our *antiferromagnetic topological relativistic quantum* description of the AMR and spontaneous Hall effect within the linear response theory.

Linear muffin tin method and atomic sphere approximation. The muffin tin method partitions the solid into non-overlapping spheres and interstitial regions (see Fig. 2.2(a)) and substitutes the interstitial potential by a flat function. Further simplification is achieved by the ASA, where the space is filled only by the slightly overlapping spheres with a Wigner-Seitz radius r_S such that the total volume of the spheres corresponds to the crystal unit cell volume. In the spin-only variant, the ASA considers [148]:

1. The effective potential $V_{\text{eff}}[\rho, \mathbf{m}]$ by a spherically symmetric potential $V_{\mathbf{R}}(r)$ within each Wigner-Seitz sphere, and
2. the effective spin-dependent potential $\mathbf{B}_{\text{eff}}$ as a magnetic field $\mathbf{B}_{\mathbf{R}}(r) = B_{\mathbf{R}}\mathbf{n}_{\mathbf{R}}$, where $B(r)$ is a spherically symmetric amplitude, and $\mathbf{n}_{\mathbf{R}}$ is a unit vector. Without loss of generality we can choose $\mathbf{n}_{\mathbf{R}} = \mathbf{e}_z$, where $\mathbf{e}_z$ is the unit vector along the z axis, and simplify the Kohn-Sham-Dirac Hamiltonian (Eq.(2.9)):

$$H_{KSD} = c\boldsymbol{\alpha} \cdot \mathbf{p} + (\beta - I_4)mc^2 + V^{\text{eff}}(r) + \mu_B \Sigma_z \beta B(r). \tag{2.36}$$

The variational principle for the Schrödinger equation leads to the eigenvalue equation [150, 151]:

$$\det\left(EO_{ij} - H_{ij}\right) = 0, \tag{2.37}$$

where H_{ij} is the Hamiltonian matrix, and O_{ij} is the overlap matrix in the given basis (recall the TB section in Chapter 1).

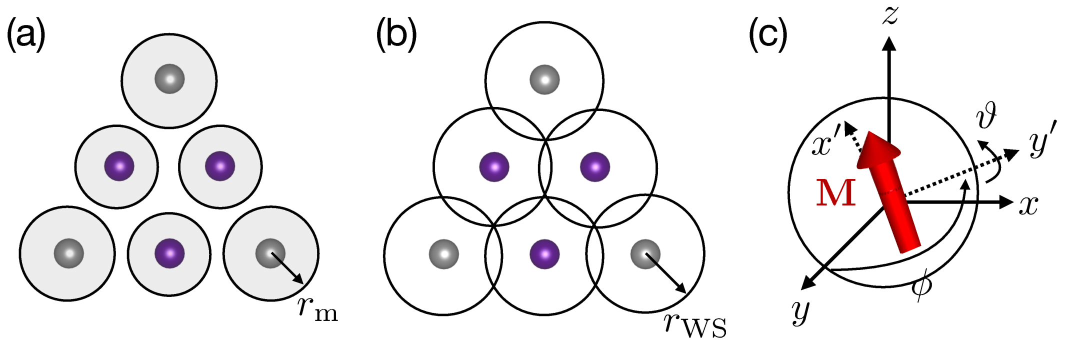

Figure 2.2: **Crystal partitioning and Euler angles.** (a) Linear muffin tin orbital method and muffin tin radius r_m. (b) Atomic sphere approximations and Wigner-Seitz radius r_{WS} (c) Euler angles parametrization for magnetic moments.

The trial wavefunctions can be expanded in terms of muffin tin orbital basis functions $\chi_i(r)$ as

$$\psi_{\boldsymbol{k}}(\boldsymbol{r}) = \sum_L c_L \varphi_\ell(r) Y_L(r, E) \equiv \sum_L c_L \chi_\ell(r), \tag{2.38}$$

where $\varphi_\ell(r)$ are solutions of the spherically symmetric Schrödinger equation, L is a composite quantum number index, and $Y_L(r, E)$ are spherical harmonics. Unfortunately, the basis is energy dependent and in turn also the secular equation for determining eigenvalues is energy dependent, which slows down the numerical calculation. Andersen suggested to expand the single muffin tin-like potential $\chi_L(\mathbf{e}, \boldsymbol{r})$ around a reference energyE_v [133, 151]:

$$\chi_L(r, E) = \chi_L\left(r, E_v\right) + \dot{\chi}_L\left(E_v, r\right)\left(E - E_v\right). \tag{2.39}$$

Here $\dot{\chi}_L$ is the energy derivative of orbital χ_L evaluated at the reference energy $E = E_v$. The corresponding secular equation takes a form:

$$\det |H_{LL}(\boldsymbol{k}) - \varepsilon_{\boldsymbol{k}} O_{LL}(\boldsymbol{k})| = 0, \tag{2.40}$$

where all the energy eigenvalues $\varepsilon_{\boldsymbol{k}}$ can be obtained in single diagonalization which tremendously speeds up the numerical evaluation. The overlap matrices and Hamiltonian can be expressed [150] in terms of muffin tin orbitals, single sphere solutions in terms of spherical harmonics, and TB structure constants of the systems [150], and similarly the Hamiltonian matrix. Consequently, the secular equation (2.37) can be transformed to form:

$$\det \left(E\delta_{\mathbf{R}L,\mathbf{R}'L'} - H^{\text{orth}}_{\mathbf{R}L,\mathbf{R}'L'} \right) = 0, \tag{2.41}$$

in a new orthogonal basis and defines the potential parameters which we list in the following paragraph.

Relativistic quantum numbers. The Hamiltonian can be conveniently expressed in terms of TB-LMTO quantities as [148, 150, 152]:

$$H = C + (\sqrt{\Delta})^{+} S^0 \left(1 - \gamma S^0\right)^{-1} \sqrt{\Delta}. \tag{2.42}$$

Here C, $\sqrt{\Delta}$ and γ are variables parametrising the potential and are site diagonal, S^0 are matrices of the canonical structure constants. For the sake of brevity, we drop the site index and relativistic quantum numbers $\Lambda = (\mu\kappa)$ (Eq. (2.24)) following the notation of Turek [150]. Unlike the nonrelativistic and nonmagnetic standard LMTO method, the $C, \sqrt{\Delta}$ and γ matrices are not diagonal in these quantum numbers. Otherwise, the form of the Hamiltonian is formally preserved.

We note an additional approximation used for the magnetic version of the Hamiltonian [148] which is not commonly discussed. The matrix elements

$$\{\kappa\mu|\sigma_z|\kappa'\mu'\} = \delta_{ll'}\delta_{\mu\mu'} \sum_{s=\pm\frac{1}{2}} \operatorname{sgn}(s) C(lj\frac{1}{2}; \mu - s, s) C(lj'\frac{1}{2}; \mu - s, s) \tag{2.43}$$

can be expressed in terms of Clebsch-Gordan coefficients C. The coupling between solutions with a different l is proportional to the magnetic SOC in the form:

$$H_{\text{MSOC}} \sim \frac{1}{c^2 r} \frac{dB(r)}{dr} \mathbf{L} \cdot \mathbf{S}. \tag{2.44}$$

Usually $B(r)$ (the spherically symmetric amplitude of the effective magnetic field in Eq. (2.17)) might be treated as slowly varying with respect to r, and the magnitude is small of the order of $1/c^2$ and thus the term is neglected. However it was noted that this term might contribute importantly to magnetocrystalline anisotropies and in systems with rapidly varying effective magnetic field. In certain complicated antiferromagnetic textures the justification of this approximation remains an open problem.

Green's functions and relativistic structure constants. The linear response Kubo formulas for the transport coefficients can be conveniently expressed with the help of Green's functions. The Green's function (resolvent $(z - H)^{-1}$ of the Hamiltonian (2.42) [153]) within TB-LMTO can be written as:

$$G(z) = \lambda^\alpha(z) + \mu^\alpha(z) g^\alpha(z) \tilde{\mu}^\alpha(z). \tag{2.45}$$

Here the site-diagonal matrices,

$$
\begin{aligned}
\lambda^{\alpha}(z) &= \mu^{\alpha}(z)(\gamma-\alpha)\left[(\sqrt{\Delta})^{+}\right]^{-1}, \\
\mu^{\alpha}(z) &= (\sqrt{\Delta})^{-1}\left[1+(\alpha-\gamma)P^{\alpha}(z)\right], \\
\tilde{\mu}^{\alpha}(z) &= \left[1+P^{\alpha}(z)(\alpha-\gamma)\right]\left[(\sqrt{\Delta})^{+}\right]^{-1}
\end{aligned}
\tag{2.46}
$$

are expressed in terms of TB-LMTO (superscript α) screened potential functions:

$$
P^{\alpha}(z) = \left[\sqrt{\Delta}(z-C)^{-1}(\sqrt{\Delta})^{+}+\gamma-\alpha\right]^{-1}. \tag{2.47}
$$

The auxiliary Green's function,

$$
g^{\alpha}(z) = \left[P^{\alpha}(z)-S^{\alpha}\right]^{-1}, \tag{2.48}
$$

can be written in terms of screened structure constants:

$$
S^{\alpha} = S^{0}\left(1-\alpha S^{0}\right)^{-1}, \tag{2.49}
$$

where α is site-diagonal matrix of screened constants. The auxiliary Green's function is convenient for the numerical treatment and the relation (2.45) was proven in Appendix of paper by Turek [152].

Coherent potential approximation. CPA [150, 153, 154, 155, 156, 157] is a method for calculating Green's functions of disordered systems. In the context of electronic structure theory, CPA was proven successful for understanding the substitutional disorder in alloys, and in recent years also finite temperature effects from first principles, e.g. magnons, and phonons. We discuss its specific implementation in our paper [158]. We will consider random substitutional disorder which can be described by a random alloy configuration. The configuration is determined by the occupation numbers, and physical quantities are determined by the configurational averaging. For a simple physical quantity we can write:

$$
\langle\langle\hat{X}\rangle\rangle = \sum_{\mathcal{C}} p(\mathcal{C})\langle\hat{X}\rangle(\mathcal{C}), \tag{2.50}
$$

where $p(\mathcal{C})$ is the probability of occurrence of the configuration $\mathcal{C}$. A single particle Hamiltonian, $H = H_0 + U$, can be separated into the part with full translational invariance H_0 and the random configuration depend part U with a corresponding random configurationally averaged Green's function:

$$
\hat{\bar{G}}(z) \equiv \langle\hat{G}(z)\rangle = \sum_{c} p(\mathcal{C})\hat{G}(z,\mathcal{C}). \tag{2.51}
$$

The disordered Green's function can be expressed in terms of the self-energy $\Sigma(z)$ [157]:

$$
\hat{\bar{G}}(z) = \left[z\hat{1}-\hat{H}_0-\hat{\Sigma}(z)\right]^{-1}. \tag{2.52}
$$

Different approximations for calculating averaged Green's functions are based on the approximations to the self-energy. Examples include virtual crystal approximation (used, for instance, in combination with VASP [132]), or self-consistent Born approximation. Here we describe the CPA which can be derived from the Dyson equation.

The Hamiltonian can be decomposed by introducing a self-energy:

$$\hat{H} = \left[\hat{H}_0 + \hat{\Sigma}(z)\right] + [\hat{U} - \hat{\Sigma}(z)] \tag{2.53}$$

and we can rewrite the Green's function:

$$\hat{G}(z) = \hat{\bar{G}}(z) + \hat{\bar{G}}(z)[\hat{U} - \hat{\Sigma}(z)]\hat{G}(z) = \{\hat{1} - \hat{\bar{G}}(z)[\hat{U} - \hat{\Sigma}(z)]\}^{-1}\hat{\bar{G}}(z). \tag{2.54}$$

We can express the Green's function with the help of a matrix $T(z)$, which is in the scattering theory known as the T-matrix:

$$\hat{G}(z) = \hat{\bar{G}}(z) + \hat{\bar{G}}(z)\hat{T}(z)\hat{\bar{G}}(z), \tag{2.55}$$

with

$$\hat{T}(z) = [\hat{U} - \hat{\Sigma}(z)]\hat{1} - \hat{\bar{G}}(z)[\hat{U} - \hat{\Sigma}(z)]^{-1}. \tag{2.56}$$

By the configurational averaging we obtain an exact condition

$$\langle T(z) \rangle = 0. \tag{2.57}$$

Furthermore, we decompose the quantities into the contributions from lattice sites, $\hat{U} - \hat{\Sigma}(z) = \sum_{\mathbf{R}} \hat{v}_{\mathbf{R}}(z), \quad \hat{v}_{\mathbf{R}}(z) = \hat{U}_{\mathbf{R}} - \hat{\Sigma}_{\mathbf{R}}(z)$, and similarly for self-energy. Soven[154] assumed uncorrelated perturbation potentials $v_{\mathbf{R}}$ and $v_{\mathbf{R}'}$ to arrive at a condition for the site self-energy[159]:

$$\langle \left[\hat{U}_{\mathrm{R}} - \hat{\Sigma}_{\mathrm{R}}(z)\right] \left\{\hat{1} - \hat{\bar{G}}(z) \left[\hat{U}_{\mathrm{R}} - \hat{\Sigma}_{\mathrm{R}}(z)\right]\right\}^{-1} \rangle = 0. \tag{2.58}$$

We briefly visualise the physical meaning of Soven approximation. Nodal self-energy contribution defines effective non-random atoms placed on the lattice sites (e.g. Au atoms placed on Mn site in $\mathrm{Mn_2Au}$ alloys). Real atoms on each site which randomly substitute the effective atom then generate zero scattering on average.

The Soven equation gives an iteration recipe for the determination of the CPA self-energy, and simple examples can be found in Ref. [159]. The CPA can advantageously (e.g. in comparison to virtual crystal approximation) describe band splitting due to the strong disorder. This scenario is reminiscent of the DMFT description of the metal-insulator transition. For the correlated perturbation extension of CPA, e.g., cluster CPA was developed.

The CPA can be conveniently implemented within the TB-LMTO framework [150]. The screened potential functions in the auxiliary Green's functions (2.48) generalise to the coherent potential functions $\mathcal{P}^{\alpha}(z)$, and the averaged auxiliary Green's function takes the form [150, 152]:

$$\langle g^{\alpha}(z) \rangle = \bar{g}^{\alpha}(z) = \left[\mathcal{P}^{\alpha}(z) - S^{\alpha}\right]^{-1}, \tag{2.59}$$

where $\mathcal{P}^{\alpha}(z)$ are site diagonal matrices. The corresponding physical configurationally averaged Green's function can be written as:

$$\bar{G}_{\mathrm{R,R'}}(z) = \left[\left(z - H^{\mathrm{eff}}(z)\right)^{-1}\right]_{\mathrm{R,R'}} \tag{2.60}$$

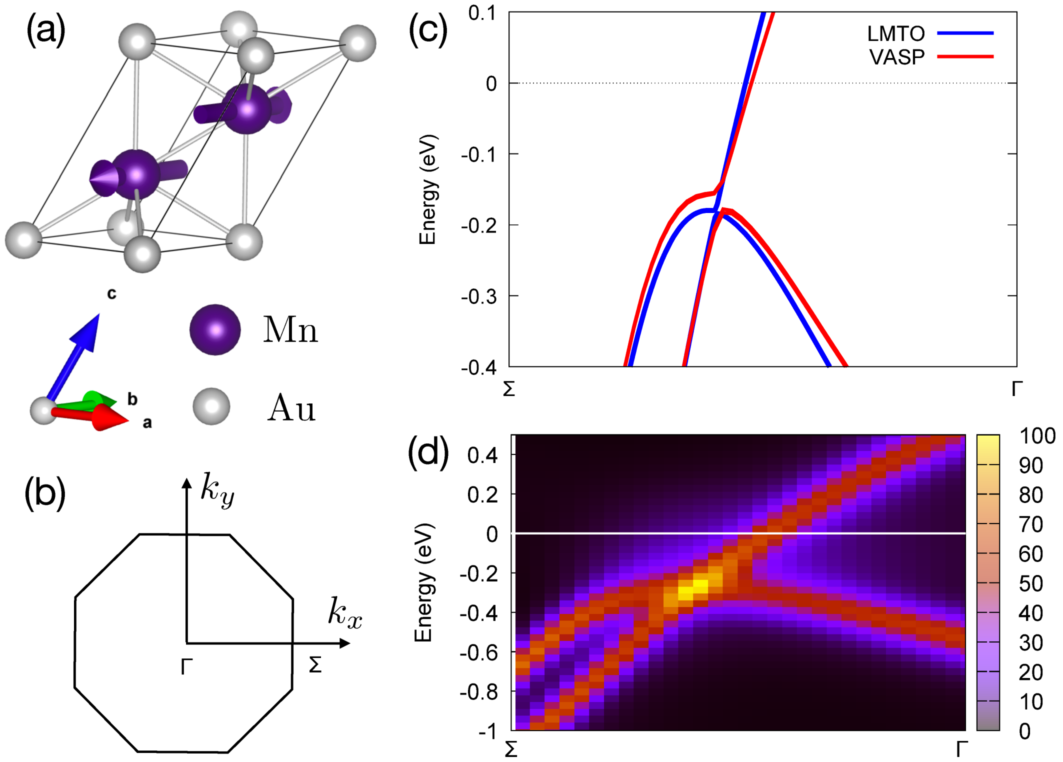

Figure 2.3: Bloch spectral function calculations in $\mathrm{Mn_2Au}$ alloys. (a) Primitive unit cell of the antiferromagnetic crystal. (b) Body centred cubic Brillouin zone cut notation. (c) Comparison of energy bands obtained in VASP and TB-LMTO. (d) Bloch spectral function calculation around avoided band crossing.

where the effective Hamiltonian,

$$H^{\mathrm{eff}}_{\mathrm{R,R'}} = \tilde{C}_{\mathrm{R}}(z)\delta_{\mathrm{R,R'}}, \tilde{\Delta}^{1/2}_{\mathrm{R}}(z)\left[S(1-\tilde{\gamma}(z)S)^{-1}\right]_{\mathrm{R,R'}}\tilde{\Delta}^{1/2}_{\mathrm{R'}}(z), \tag{2.61}$$

has formally the same structure as in the conventional orthogonal LMTO formalism. However, the random potential parameters are substituted by the non-random and energy dependent complex coherent potential parameters $\tilde{C}_{\mathrm{R}}(z), \delta_{\mathrm{R}}$, and $\tilde{\gamma}(z)$. The coherent potential parameters are again site-diagonal, but are not diagonal in quantum number indices L, L'.

Bloch spectral function and life-time of quasiparticles. Energy shifts and electron lifetime can be estimated either from the self-energy function or from the Bloch spectral function. The latter can be calculated from the configurationally averaged physical Green's function:

$$\mathcal{A}_{\mathrm{B}L}(\boldsymbol{k}, E) = -\frac{1}{\pi}\,\mathrm{Im}\,\bar{G}_{\mathrm{B}L,\mathbf{B}L}(\boldsymbol{k}, E+i0), \tag{2.62}$$

where $\mathbf{B}$ labels the multicomponent atomic basis of the alloy, and L is again a shorthand composite label of quantum numbers. The analysis can simplify to the self-energy of a given band, when $|\Sigma_{LL'}(z)| << |\Sigma_{LL}(z)|$ for $L \neq L'$. The Bloch spectral function in disordered systems substitutes the energy bands of perfect systems. The Bloch spectral function $\mathcal{A}(\boldsymbol{k}, E) \approx \sum_i \mathcal{A}_i(\boldsymbol{k}, E)$ can be suggestively rewritten with the help of

$$\mathcal{A}_i(\boldsymbol{k}, E) \approx -\frac{1}{\pi} \frac{\operatorname{Im} \Sigma_i\left(\boldsymbol{k}, E_i+i 0\right)}{\left[E-E_i-\operatorname{Re} \Sigma_i\left(\boldsymbol{k}, E_i\right)\right]^2+\left[\operatorname{Im} \Sigma_i\left(\boldsymbol{k}, E_i+i 0\right)\right]^2}, \tag{2.63}$$

where i corresponds to the particular band of the non-random reference Hamiltonian. This approximation works well when the bands interact by disorder or hybridization only weakly with each other. An example of spectral functions evaluated close to the Fermi level in Au-rich $\mathrm{Mn_2Au}$ is shown in Fig. 2.3(d). We show also a comparison of energy bands calculated in VASP and TB-LMTO of stoichiometric antiferromagnetic $\mathrm{Mn_2Au}$ in Fig. 2.3(c).

The CPA potentials are numerically obtained from an iterative self-consistent procedure:

$$W_R^{\alpha,(n+1)}(z)=\mathcal{P}_R^{\alpha,(n)}(z)-\left[\bar{g}_{R,R}^{\alpha,(n)}(z)\right]^{-1}, \tag{2.64}$$

where $W_R^{\alpha,(n)}(z)$ is a coherent interactor described in detail in Chapter 10 of [150].

2.3 Kubo-Greenwood formula

We can express the Kubo formula (1.53) within the Green's function formalism as Bastin formula [160, 161]:

$$\tilde{\sigma}_{\mu\nu}=\frac{ie^2\hbar}{V}\int_{-\infty}^{+\infty} d\varepsilon f(\varepsilon) \operatorname{Tr}\left(v_\mu \frac{dG^+(\varepsilon)}{d\varepsilon} v_\nu \delta(\varepsilon-H)-v_\mu \delta(\varepsilon-H) v_\nu \frac{dG^-(\varepsilon)}{d\varepsilon}\right)_c, \tag{2.65}$$

where V is volume factor. We have added configurational averaging and we have used the identity [161]:

$$\lim_{s\to 0^+} \frac{1}{\left(\varepsilon_n-\varepsilon\right)\left(\varepsilon_n-\varepsilon+is\right)}=\lim_{s\to 0^+} \frac{d}{d\varepsilon}\left(\frac{1}{\varepsilon_n-\varepsilon+is}\right). \tag{2.66}$$

While the original derivation given by Bastin employed an explicit Schrödinger form of the Hamiltonian and velocities, Crépieux and Bruno have shown the validity of this approach also within Dirac and Pauli approaches [161]. Employing integration by parts on part of the last equation, Streda [56] was able to separate the formula into $\tilde{\sigma}_{\mu\nu}=\tilde{\sigma}_{\mu\nu}^{\mathrm{I}}+\tilde{\sigma}_{\mu\nu}^{\mathrm{II}}$ with the two contributions at zero temperature and frequency given by:

$$\begin{aligned}\tilde{\sigma}_{\mu\nu}^{\mathrm{I}}&=\frac{e^2\hbar}{4\pi V} \operatorname{Tr}\left\langle v_\mu\left(G^+-G^-\right) v_\nu G^- - v_\mu G^+ v_\nu\left(G^+-G^-\right)\right\rangle_c, \\ \tilde{\sigma}_{\mu\nu}^{\mathrm{II}}&=-\frac{e^2}{4i\pi V} \operatorname{Tr}\left\langle\left(G^+-G^-\right)\left(r_\mu v_\nu-r_\nu v_\mu\right)\right\rangle_c\end{aligned} \tag{2.67}$$

The Kubo-Streda formula can be implemented within the TB-LMTO formalism [162] with the help of auxiliary averaged CPA Green's functions and vertex corrections [163]. For the diagonal longitudinal conductivity, $\tilde{\sigma}_{ij}^{II}$ is zero and we obtain Kubo-Greenwood formula, which can be expressed in terms of TB-LMTO-ASA CPA quantities as [104, 152, 158, 164, 165]

$$\sigma_{\mu\nu}=-\frac{e^2}{\pi\hbar V_0 N} \operatorname{Tr}\left\{\Im\bar{g}^\alpha\left(E_F\right)\left[X^\mu, S^\alpha\right] \Im\bar{g}^\alpha\left(E_F\right)\left[X^\nu, S^\alpha\right]\right\}+\text{v.c.}, \tag{2.68}$$

where for the sake of numerical convenience the conductivity is expressed in terms of auxiliary quantities, and the vertex corrections (*v.c.*) are calculated as described by Carva [163]. The numerical implementation uses an intra-atomic current approximation [164]. The true continuous coordinate is substituted by a step function (position matrix diagonal in position vector and quantum numbers) within each atomic sphere. The conductivity thus describes only the net electron motion between neighbouring atomic sites. In our calculations of Mn_2Au alloys, the vertex corrections turn out to be negligible and isotropic (less than 1% of the total conductivities). Details of the application of CPA TB-LMTO for calculating quantities at nonzero temperature were discussed by Wagenknecht [158]. Details of Kubo-Streda calculations of spontaneous Hall conductivity are presented by Turek [162]. In our test spontaneous Hall calculations in non-collinear antiferromagnets within FRD-TB-LMTO-CPA, we neglect the term called Fermi sea in [162].

The finite-relaxation time (FRT) model corresponds to the spin and orbital independent scattering which is technically accounted for by adding a finite imaginary constant (Im z) to the Fermi energy in corresponding Green's functions in the Kubo-Bastin equation. The FRT model gives zero vertex corrections and does not allow to separate the phonon and spin-disorder contributions to the conductivity tensor.

Computational scheme

We calculated conductivity tensor within FRD-TB-LMTO-ASA in combination with RTA or CPA in NiMnSb, and Mn_2Au, and non-collinear antiferromagnets presented in Chapter 3 and 4. Technically the calculation is carried out in the following steps:

1. The electronic structure and the potential function are calculated within the FRD-TB-LMTO-ASA method. The input file *inpge* contains information about lattice vector, atomic positions, and parameter controlling the spread of the TB basis ($CUTRAT$). *inpch* is composed of chemical occupation of atomic sites and their number of valence electrons considered in the calculation. We list the input parameters of the systems in Tab. 2.1. *inpmd* comprises orientations of local magnetisations in three Euler angles (ϕ, θ, ψ) in π units illustrated in Fig 2.2(c). For instance, in the case of the non-collinear antiferromagnets IrM_3, we introduce the Euler angles $\phi/\pi, \theta/\pi, \psi/\pi$ for the Mn atoms in the weak ferromagnetic phase and antiferromagnetic phase described in Chapter 4 and listed in Tab. 2.2.

   The starting potential functions are stored in *inpmd.* The file is constructed from atomic potential functions stored in *atoms.all.* The functions need to be concatenated (*cat* command) together in the correct order and recalculated for the entered Wigner-Seitz radius (see Tab. 2.1). In the final step, the potential functions are transformed into the relativistic basis with relativistic quantum numbers. Finally, *input* controls the DFT loop. In this file we set the basis type *spd* or *spdf* (orbital quantum number NL), number of spin components (NS), NSYM and INVE (symmetry flags, we have implemented only several symmetries, INVE control inversion symmetry), the

	CuMnAs(o)	NiMnSb	Mn_2Au	$IrMn_3$	$Rh_{0.5}Pt_{0.5}Mn_3$
a(Å)	6,577	5,925	3,330	3,785	3,820
b(Å)	3,854				
c(Å)	7,310		8,537		
Volume(Å^3)	185,290	207,980	94,662	54,225	55,743
Number of atoms	12	12+4	6	4	4
r_{WS}(Å)	1,545	1,459	1,556	1,479	1,493
Valence electrons	11-7-5	10-7-0-5	11-7	9-7	9-10-7

Table 2.1: Parameters of calculated materials. NiMnSb unit cell comprises of also empty-sphere to fill the empty lattice site in the half-Heusler structure.

number of crystal momentum points along one dimension (NK), the number of energy points for the Green's function contour integrals (NE), the number of DFT iterations, the type of the exchange-correlation potential, and mixing parameters for the CPA and DFT loop. The fortran compiled program *rbes* is run via:

```
./rbes &>tmp&,
```

where we redirect the output into a temporary file *tmp*. Output files are *outit* (information of the iteration DFT procedure and final physical parameters: magnetic moments, total energy, Fermi energy, iteration change in energy), *outld* (final potential parameters), *outcp*, *outsz* (coherent potential functions and spin components).

2. The Kubo formula calculations proceed by evaluating (possibly averaged) auxiliary Green's functions and velocities, and vertex corrections. *inpge*, *inpch*, and *inpmd* can be copied from the DFT step. *outld* from the DFT step is copied as *inppp* while adding at the second line the energy (possibly Fermi energy) at which the conductivity tensor is evaluated. The control parameters are stored in the *inprr* file containing information about the number of crystal momentum points for the Kubo formula integration (NKF), NSYM, INVE. The calculated conductivity tensor is saved in the *outrr* file. We parallelised conductivity crystal momentum integration in OpenMP allowing us to calculate larger systems with finer meshes. The calculation is executed as:

```
./rrere  &>tmp &.
```

The mesh of 160 × 160 × 160 k-points in the Brillouin zone was commonly used for transport calculations if not specified otherwise. Smaller numbers of k-points than common for, e.g., pure metals, are required because of the large self-energy term originating from chemical or temperature disorder. In Fig. 2.4 we plot an example of the convergence of our parallelised calculations of the longitudinal conductivity and anisotropic magnetoresistance in Mn_2Au alloys within FRT.

	Weak ferromagnetic		Antiferromagnetic	
Euler angles	ϕ/π	ϑ/π	ϕ/π	ϑ/π
$\boldsymbol{S}_{\mathrm{Mn}_1}$	-0.75000	0.19591	-0.25	-0.50
$\boldsymbol{S}_{\mathrm{Mn}_2}$	-0.14758	0.63386	-0.50	0.25
$\boldsymbol{S}_{\mathrm{Mn}_3}$	-0.35241	-0.63386	0.00	0.75

Table 2.2: Euler angle parametrization of sublattice moments in non-collinear antiferromagnetic phases.

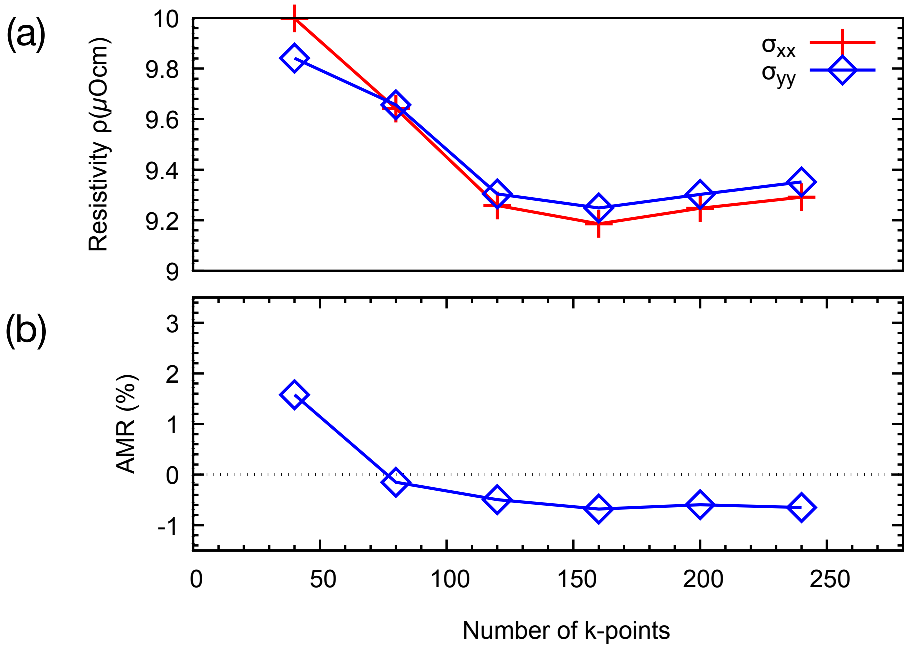

Figure 2.4: Convergence of resistivity and anisotropic magnetoresistance (AMR) calculations in $\mathrm{Mn_2Au}$ antiferromagnet. (a) Longitudinal resistivity (b) AMR vs number of sampling points along single dimension in the Brillouin zone.

2.4 Plane wave pseudopotential method

The solution of the Schrödinger equation for free electrons are plane waves. For a weak potential it is possible to expand the wavefunction in the plane wave series [151]:

$$\psi_{\boldsymbol{k}}(\mathbf{r}) = \sum_{\boldsymbol{G}} C_{\boldsymbol{k}-\boldsymbol{G}} |\boldsymbol{k} - \boldsymbol{G}\rangle. \tag{2.69}$$

This expansion can be substituted into the Schrödinger equation to obtain:

$$\left(\varepsilon^0_{\boldsymbol{k}-\boldsymbol{G}} - \varepsilon_{\boldsymbol{k}}\right) C_{\boldsymbol{k}-\boldsymbol{G}} + \sum_{\boldsymbol{G}'} v\left(\boldsymbol{G}' - \boldsymbol{G}\right) C_{\boldsymbol{k}-\boldsymbol{G}'} = 0. \tag{2.70}$$

This equation has a nontrivial solution if:

$$\det\left| \left(e^0_{\boldsymbol{k}-\boldsymbol{G}} - e_{\dot{k}}\right) \delta_{\boldsymbol{G},\boldsymbol{G}'} + v\left(\boldsymbol{G}' - \boldsymbol{G}\right) \right| = 0. \tag{2.71}$$

The equation contains formally infinite number of plane waves an in practical calculation the size has to be truncated. Since the potential $v(\boldsymbol{G})$ rapidly changes close to the nuclei, its Fourier transform requires large $\boldsymbol{G}$ in the expansion, and thus in general Fourier components will not decay fast with increasing $\boldsymbol{G}$. This problem can be migitiated by using pseudopotentials.

A pseudowavefunction matches the real wavefunction for $r > r_{\text{cut-off}}$ and the rapid oscillations for $r < r_{\text{cut-off}}$ are substituted by nodeless functions. Similarly, the potential diverges close to the nuclei and we can substitute this part by some smoother form, where the complete pseudopotential has the same scattering properties as the real one. For instance, Hamman et al. [166] substituted within certain core radius the all-electron wavefunction by a soft nodeless pseudowavefunction while requiring conservation of the norm within this radius. Outside the radius, the wavefunctions are identical. For localised orbitals such as $3d$, this leads to the requirement of a large basis set of plane waves. Vanderbilt suggested using atomically localised augmentation charges to relax the condition of the norm. A drawback of the method in terms of a complicated practical construction of the pseudopotential can be mitigated by the PAW method developed by Blöchl [167]. He transforms systematically the all-electron wavefunction to the pseudopotential wavefunction to avoid the complex augmentation charges or many plane waves needed in the basis. The formal link between the ultrasoft pseudopotential method by Vanderbilt and the PAW method by Blöchl was discussed by Kresse and Joubert [168] and its method numerically implemented in VASP code.

PAW method. Within the PAW formalism the psudopotential wavefunction is derived from the all electron wavefunction by means of a linear transformation:

$$\left|\Psi_n\right\rangle = \left|\widetilde{\Psi}_n\right\rangle + \sum_i \left(\left|\phi_i\right\rangle - \left|\widetilde{\phi}_i\right\rangle\right)\left\langle \widetilde{p}_i \middle| \widetilde{\Psi}_n\right\rangle. \tag{2.72}$$

All electron wavefunctions and partial waves are denoted as $\widetilde{\Psi}_n$ and $\widetilde{p}_i$, respectively. The pseudopotential counterparts are marked by the tilde symbol. The index $i = (\mathbf{R}, l, m, \epsilon_{kl})$ is composed of angular quantum numbers and reference energy.

All-electron ψ_i are calculated for the reference atom, pseudopotential $\tilde{\phi}_i$ are identical to all-electron ones outside the cut-off radius and are required to match continuously at the radius. The radius is often chosen about one half of the distance between nearest neighbour atoms. Finally, the projector functions are constructed as dual quantities to the pseudopotential partial waves:

$$\left\langle \widetilde{p}_i \middle| \widetilde{\phi}_j\right\rangle = \delta_{ij}. \tag{2.73}$$

Details of the methods and the link between PAW and the ultrasoft pseudopotential can be found in Ref. [168].

Variational inclusion of spin-orbit coupling. The VASP code implements SOC effects in the variational scheme as a correction to the nonrelativistic Schrödinger equation, rather than fully relativistic treatment implemented within TB-LMTO and discussed in the previous section.

SOC originates mainly from the regions close to the nuclei and the effects are assumed to be negligible outside of the PAW radii. Under this assumption, the SOC term can be written as an all electron, one center contribution:

$$\widetilde{H}_{\text{SOC}} = \sum_{ij} \left|p_i\right\rangle \left\langle \phi_i \right| H_{\text{SO}} \left| \phi_j \right\rangle \left\langle p_j\right|. \tag{2.74}$$

The spin-orbit elements are in the zero order approximation given as:

$$H_{\mathrm{SOC}}^{\alpha\beta} = \frac{\hbar^2}{(2m_e c)^2}\frac{K(r)}{r}\frac{dV(r)}{dr}\boldsymbol{\sigma}^{\alpha\beta}\cdot\mathbf{L}, \tag{2.75}$$

where $\boldsymbol{\sigma}$ are Pauli matrices and the angular momentum operators $\mathbf{L} = \mathbf{r}\times\mathbf{p}$, $V(r)$ is the spherical part of the effective potential within the PAW sphere, and $K(r) = K(r) = \left(1 - \frac{V(r)}{2m_e c^2}\right)^{-2}$. The spin-orbit term action on the pseudowavefunction can be expressed as:

$$\left|\tilde{\psi}_n^{\alpha}\right\rangle = \sum_{\alpha\beta}\tilde{H}_{\mathrm{SOC}}^{\alpha\beta}\left|\tilde{\psi}_n^{\beta}\right\rangle. \tag{2.76}$$

Here the spinor up and down components are labelled α and β, respectively. We employ the two-component non-collinear magnetism formalism [132]. The spin orbit operator can be derived from Eq. (2.75) by the transformation to spherical harmonics, $\phi_i(\mathbf{r}) = R_i(|\mathbf{r}|)Y_{l_i m_i}(\hat{\mathbf{r}})$:

$$\tilde{H}_{\mathrm{SO}}^{\alpha\beta} = \frac{\hbar^2}{(2m_e c)^2}\sum_{ij}|\tilde{p}_i\rangle R_{ij}\vec{\sigma}_{\alpha\beta}\cdot\vec{L}_{ij}\langle\tilde{p}_j|, \tag{2.77}$$

where

$$R_{ij} = 4\pi\int_0^{r_c} R_i(r)\frac{K(r)}{r}\frac{dV(r)}{dr}R_j(r)dr, \tag{2.78}$$

$\vec{L}_{ij} = \left\langle Y_{l,m_i}|\vec{L}|Y_{l_j m_j}\right\rangle$, and $Y_{l,m}$ label the real spherical harmonics. The spherical harmonic basis can be used for calculating projected quantities, e.g., local spin polarisations [111].

2.5 Wannier functions and intrinsic Hall conductivity

We have seen in Chapter 1 how to express the intrinsic Hall conductivity in terms of the Berry curvature by comparing the linear response expression in Eq. (1.57) to the Berry curvature formula [55]:

$$\Omega_{\alpha\beta}(\boldsymbol{k}) = -2\,\mathrm{Im}\sum_v\sum_c \frac{\left\langle u_{v\boldsymbol{k}}\left|\frac{\partial\hat{H}(\boldsymbol{k})}{\partial k_\alpha}\right|u_{c\boldsymbol{k}}\right\rangle\left\langle u_{c\boldsymbol{k}}\left|\frac{\partial\hat{H}(\boldsymbol{k})}{\partial k_\beta}\right|u_{v\boldsymbol{k}}\right\rangle}{[E_c(\boldsymbol{k}) - E_v(\boldsymbol{k})]^2}. \tag{2.79}$$

The Berry curvature rapidly oscillates in the crystal momentum space and the large contributions, *hotspots*, can originate from spin-orbit avoided crossings or bands split by other mechanisms. The precise evaluation of the Berry curvature and the associated intrinsic Hall conductivity thus requires millions of crystal momentum sampling points. Furthermore, the summation in Eq. (2.79) runs over many Bloch states.

This problem is suitable for Wannier interpolation scheme developed by Souza, Marzari, Wang, Vanderbilt and others [54, 169, 170, 171] which is schematically described around Fig. 25 of the review article [171]. Within this approach, the Wannier functions are determined by using conventional Bloch states calculated *ab initio* in a certain energy range on a coarse grid. In the second step, the

Wannier function interpolation on a finner mesh is constructed and the Berry curvature and linear response quantities as Hall conductivity are calculated on the finer mesh. In Fig. 2.5 (a) we show Wannier interpolated bands on top of the VASP DFT calculation of antiferromagnetic $\mathrm{RuO_2}$ antiferromagnet (Hubbard $U = 1.6\ eV$). Fig. 2.5 illustrates the Berry curvature of antiferromagnetic $\mathrm{RuO_2}$ calculated along with the high symmetry line (bottom panel (a)) and map (b) using the Wannier90 code.

Wannier functions can be defined as duals to the Bloch functions:

$$|\psi^{\mathrm{W}}_{n\boldsymbol{k}}\rangle = \sum_{\mathbf{R}} e^{i\boldsymbol{k}\cdot\mathbf{R}}|\mathbf{R}n\rangle \quad (n = 1, \ldots, J). \tag{2.80}$$

This is an analogous formula to the TB method with the Wannier projected functions effectively representing the atomic orbitals. However, the Wannier atomic orbitals are obtained from first-principles rather than by the Slater-Koster method. The gauge freedom in choosing the phase factors of Bloch functions allows us to optimize the Wannier functions into its maximally localised form by reducing the tails of the Wannier functions in the real space. The gauge freedom in choosing the Bloch states can be expressed by an unitary operator

$$|\mathbf{R}n\rangle = \frac{V}{(2\pi)^3}\int_{\mathrm{BZ}} d\boldsymbol{k} e^{-i\boldsymbol{k}\cdot\mathbf{R}} \sum_{m=1}^{J} U^{(\boldsymbol{k})}_{mn} |\psi_{m\boldsymbol{k}}\rangle\,. \tag{2.81}$$

Within the method, the localisation potential is constructed as:

$$W = \sum_n \left[\left\langle \mathbf{0}n \left| r^2 \right| \mathbf{0}n \right\rangle - \langle \mathbf{0}n|\mathbf{r}|\mathbf{0}n\rangle^2\right] = \sum_n \left[\left\langle r^2 \right\rangle_n - \bar{\mathbf{r}}^2_n\right] \tag{2.82}$$

and measures the spread of the Wannier functions around their centres. The localisation potential is transformed into the crystal momentum space and minimized with respect to the $U^{(\boldsymbol{k})}_{mn}$ matrices. The Hamiltonian matrix in the Wannier gauge reads:

$$H^{\mathrm{W}}_{\boldsymbol{k},nm} = \left\langle \psi^{\mathrm{W}}_{\boldsymbol{k}n}|H|\psi^{\mathrm{W}}_{\boldsymbol{k}m}\right\rangle = \sum_{\mathbf{R}} e^{i\boldsymbol{k}\cdot\mathbf{R}}\langle \mathbf{0}n|H|\mathbf{R}m\rangle. \tag{2.83}$$

The eigenenergies can be obtained by a transformation:

$$H^{\mathrm{H}}_{\boldsymbol{k},nm} = \left[U^{\dagger}_{\boldsymbol{k}} H^{\mathrm{W}}_{\boldsymbol{k}} U_{\boldsymbol{k}}\right]_{nm} = \delta_{nm}\bar{\epsilon}_{n\boldsymbol{k}}. \tag{2.84}$$

This transformation formally defines Hamiltonian gauge quantities, including wavefunctions, in which the Hamiltonian takes a diagonal form (recall the non-abelian Berry curvature analysis in Chapter 1). The corresponding transformation for Bloch functions reads:

$$\left|\psi^{\mathrm{H}}_{\boldsymbol{k}}\right\rangle = \left|\psi^{\mathrm{W}}_{\boldsymbol{k}}\right\rangle U_{\boldsymbol{k}}. \tag{2.85}$$

For the DFT wavevectors we recover the eigenvalues and eigenvectors of the DFT calculations. At arbitrary wavectors we obtain a smooth interpolation between DFT wavevectors, if we consider a set of disentangled bands. In the case of entangled bands, the interpolation is set to work well only within a fixed (so called frozen) energy window. The evaluated Hamiltonian matrices in the Wannier gauge can be inexpensively evaluated by fast Fourier transformation and diagonalization of matrices (2.84) of rank J.

To obtain the Berry curvature in the Hamiltonian gauge we differentiate both sides of the gauge transformation (2.81) and we substitute the expressions into an alternative formula for Berry curvature:

$$\mathcal{F}_{\alpha\beta} = \partial_\alpha A_\beta - \partial_\beta A_\alpha = i \langle \partial_\alpha u | \partial_\beta u \rangle - i \langle \partial_\beta u | \partial_\alpha u \rangle . \tag{2.86}$$

After a technical manipulation we obtain:

$$\mathcal{F}^{\mathrm{H}}_{\alpha\beta} = \overline{\mathcal{F}}_{\alpha\beta} - \left[D_\alpha, \bar{A}_\beta \right] + \left[D_\beta, \bar{A}_\alpha \right] - i \left[D_\alpha, D_\beta \right], \tag{2.87}$$

where $\overline{\mathcal{F}}_{\alpha\beta}$, $\bar{A}_\beta$, and $D_\alpha = U^\dagger \partial_\alpha U$ are quantities in the Wannier gauge, e.g. $\bar{A}_{\boldsymbol{k}} = U^\dagger_{\boldsymbol{k}} A^{\mathbf{w}}_{\boldsymbol{k}} U_{\boldsymbol{k}}$. By summing the diagonal terms

$$\mathcal{F}^{\mathrm{tot}}_{\alpha\beta} = \sum_{n=1}^{J} f_n \mathcal{F}^{\mathrm{H}}_{\alpha\beta,nn} \tag{2.88}$$

we obtain the total Berry curvature:

$$\begin{aligned} \mathcal{F}^{\mathrm{tot}}_{\alpha\beta} = & \sum_{n}^{J} f_n \overline{\mathcal{F}}_{\alpha\beta,nn} + \sum_{mn}^{J} (f_m - f_n) \Big(D_{\alpha,nm} \bar{A}_{\beta,mn} \\ & - D_{\beta,nm} \bar{A}_{\alpha,mn} + i D_{\alpha,nm} D_{\beta,mn} \Big) . \end{aligned} \tag{2.89}$$

The summation is now running over a small set of J Wannier bands. Energy eigenvalues, occupation factors, U and D matrices are automatically obtained by the Wannierization scheme. The Berry connection and Berry curvature information is encoded in matrix elements:

$$A^{\mathrm{W}}_\alpha = \sum_{\mathbf{R}} e^{i\boldsymbol{k}\cdot\mathbf{R}} \langle \mathbf{0} | r_\alpha | \mathbf{R} \rangle \tag{2.90}$$

and the Berry curvature is obtained by analytical curl of this equation.

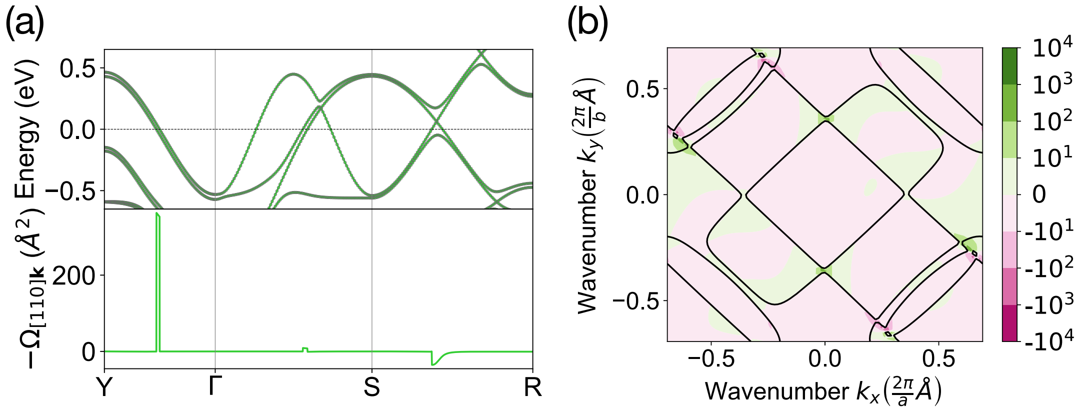

Figure 2.5: Berry curvature calculations in the RuO$_2$ antiferromagnet. (a) (top panel) Energy bands calculated in VASP (red circles) and by Wannier interpolation (green line). (bottom panel) Berry curvature calculated by Wannier interpolation. (b) Berry curvature map in $k_z = 0$ crystal momentum plane for Hubbard $U = 1.6$ eV.

By Brillouin zone integration we get an expression for the Hall conductivity:

$$\sigma^{\rm AH}_{\alpha\beta} = -\frac{e^2}{\hbar}\int_{\rm BZ}\frac{d\boldsymbol{k}}{(2\pi)^3}\mathcal{F}^{\rm tot}_{\boldsymbol{k},\alpha\beta}. \qquad (2.91)$$

We will study the Berry curvature and Hall conductivity pseudovectors in antiferromagnets in great detail in Chapter 4 of this text.

Computational scheme

The VASP code can be run in three magnetic (flag NONCOLMAG = .TRUE.) and SOC (flag LSOC=.TRUE.) approximations: (i) no SOC, and collinear magnetism; (ii) no SOC, and non-collinear magnetism; and (iii) SOC and non-collinear magnetism. We describe the practical calculation of the Berry curvature and Hall conductivity by employing the VASP code in combination with Wannier90 code to generate an effective TB Wannier Hamiltonian.

Practically, we evaluate the Hall conductivity, in four steps.

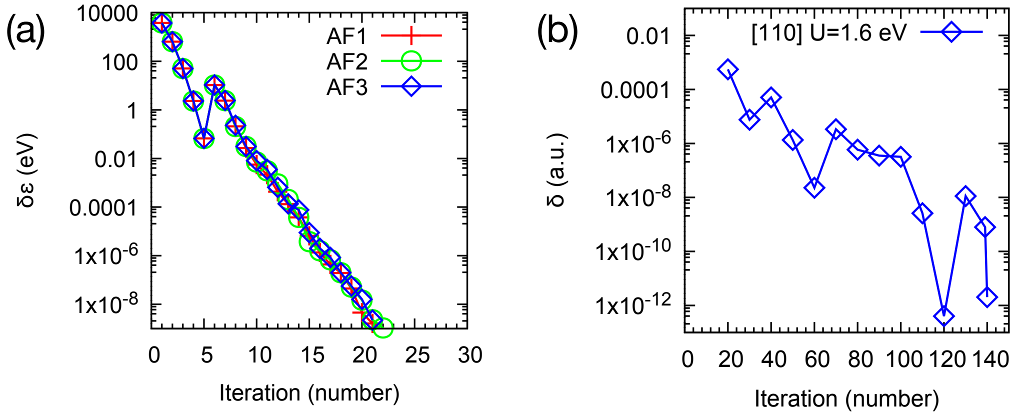

Figure 2.6: **Convergence of VASP and Wannier90 calculations in orthorhombic CuMnAs and RuO$_2$ antiferromagnets.** (a) Changes in energy vs number of iterations in VASP. (b) Changes in control parameter of Wannierization vs number of iterations.

1. First principle self-consistent calculation. We set-up and run a self-consistent VASP calculation. We *cat* input pseudopotential files to create POTCAR. In POSCAR we set the crystal lattice geometry and atomic positions. In KPOINTS file we set the number of crystal momentum points used in the self-consistent calculation. INCAR file contains control parameters of the calculation, e.g., energy cut-off, type of potential, starting magnetization orientations and magnitudes, SOC flag, LDA+U settings, number of processors, etc. We also switch off symmetries (ISYM=-1), since we study low symmetry magnets with SOC and we do not want to reduce the Brillouin zone. We set-up supercomputer parameters and the calculation parameters (include modules, time and memory requirements, etc.) and run the VASP code in parallel:

```
srun /home/user/vaspfolder/bin/vasp_ncl
```

We use an accurate, magnetic and relativistic mode of our calculations. For relatively small unit cells (e.g. 6 atoms of RuO_2), the self-consistent cycles take around 5-48 hours of real-time when using 4 nodes with 16-32 processors each, giving in total 64-128 processors. One should keep in mind that in VASP it is convenient to set the number of processors to be congruent with the number of crystal momentum points.

We can also calculate the structure by setting a non-self-consistent calculation (ICHARG=11) and defining the wavevector path in the momentum space in KPOINTS. We show exemplary energy bands for antiferromagnetic RuO_2 with moments along the [110] crystal direction calculated in VASP. In our calculations, we use the PAW pseudopotential in combination with the GGA Perdew–Burke-Ernzerhof (PBE) parametrization [137, 138]. For RuO_2 and orthorhombic CuMnAs we use an energy cut-off of 500 eV, in the case of $CoNb_3S_6$, and Mn_2Au we use 300 eV. We show the convergence for the CuMnAs calculation in Fig. 2.6(a).

2. Non-self-consistent first principle calculation of matrix overlaps and projections. In the second step we set up the basic *wannier90.win* file by including the number of bands (for our RuO_2 crystal we set 96) and Wannier functions (56), and we choose the projection states (Ru: s, d, and O: s, p). We run VASP in the nonparallel and non-self-consistent mode (ICAHRG=11) with two Wannier90 flags: NBANDS = (rule of thumb is 1.4 times the number of electrons), and flag LWANNIER90 = .TRUE.

```
/home/user/vaspfolder/bin/vasp_ncl
```

VASP calculates overlaps and projections required for the next step.

3. Disentanglement of bands and Wannierization. We add to the *wannier90.win* file disentanglement a Wannierization setting. We also *grep* the Fermi energy from the VASP calculation and set it in the *wannier90.win* file. We run the Wannier procedure

```
wannier90.x wannier90
```

We show in Fig. 2.6(b) the convergence of control parameters during the calculation the Wannier functions.

4. Post-processing: Berry curvature and Hall conductivity. In the last step, we set the parameters for the Fermi surface, energy bands, Berry curvature, and Hall conductivity in *wannier90.win*. We run the wannier90 library in post-processing parallel mode

```
srun postw90.x wannier90
```

As a prerequisite, we need VASP compiled in non-collinear mode and linked with Wannier90. At the moment of writing, we use an older version of Wannier90 compatible with VASP in the second step, and for wannierization and post-processing (step 3 and 4) we use the latest version of Wannier90. Post-processing can be alternatively calculated in WannierTools or home-made routines for integration.

2.6 Summary: first-principle methods

In this chapter, we have reviewed the relativistic first-principle theory of electronic structure. We have described TB-LMTO and PAW methods. The former is useful for understanding effects originating from disorder scattering and extrinsic contributions to the anisotropic magnetoresistance in high symmetry materials (where ASA is applicable and the atoms have similar Wigner-Seitz radii). The latter is useful in combination with maximally localised Wannier functions for calculations of the intrinsic spontaneous Hall conductivity in antiferromagnets with lower symmetry. We have developed:

- parallelisation of the codes for the transport calculation of the Kubo-Greenwood formula within the Green's function CPA + TB-LMTO method,

- scripts to calculate and visualise crystal momentum and energy-resolved Bloch spectral functions (see Fig. 1), three-dimensional energy bands (see Fig. 2), spin-projected quantities, magnetization density isosurfaces, etc.,

- set-up of VASP, TB-LMTO and our codes on supercomputing centres - METACENTRUM, IT4INNOVATION, MOGON (ranked as number 65 (19 within Europe) in 2017 and 131 in 2019 computational performance worldwide list), and TYPHOON.

- contribution to the calculation of the spin-resolved, finite-relaxation time, and finite-temperature codes and methodology described in our papers which are part of David Wagenknecht's thesis [158, 172].

We have compared first principle methods implemented in VASP and TB-LMTO and we have tested our convergence and band structure results against our calculations in full-potential FLAPW codes FLEUR and ELK. We describe these calculations in Refs. [27, 104]. Our spin-resolved conductivity calculations within TB-LMTO for antiferromagnetic FeRh exhibit large sublattice conductivities. This technical observation inspired our work in Chapter 4. We have tested the computational framework on numerous magnetic system: ferromagnetic NiCo, and NiMnSb, antiferromagnetic FeRh, CuMnAs, non-collinear antiferromagnet Mn_3Sn, antiferromagnetic MnPt, and non-collinear antiferromagnetic alloys $IrMn_3$, and Mn_2Au, and obtained results consistent with existing literature.

We studied the convergence and time-scaling of our calculations, and we explored the applicability of these methods for the description of the relativistic spin transport and topological quasiparticles. The limitation of the CPA relates to our usage of the ASA, which likely can artificially relax band touching (unphysically prevent hybridization). However, the method works well for the calculation of scattering effects, as we will illustrate on our large anisotropic magnetoresistance prediction in Mn_2Au alloys, which is consistent with experimental data [104].

On the other hand, the effective Wannier TB + VASP + Berry curvature method is useful for studying the symmetry protection of topological quasiparticles, and magnetic symmetry properties of low symmetry crystals, and intrinsic band structure effects as we will describe in the next two chapters.

3. Anisotropic magnetoresistance in Dirac antiferromagnets

"Antifragility is beyond resilience or robustness. The resilient resists shocks and stays the same; the antifragile gets better."

Nassim Nicholas Taleb

In this chapter, we study a Dirac fermion antiferromagnet candidate CuMnAs and AMR in ferromagnetic NiMnSb and antiferromagnetic Mn_2Au by magnetic symmetry analysis and first-principle calculations. In the first part, we discuss the tetragonal and orthorhombic CuMnAs electronic structure and the magnetic ground-state of the orthorhombic CuMnAs. We demonstrate the presence of Dirac fermions [23, 27, 28, 38, 82, 173] in CuMnAs antiferromagnetic energy bands and their protection by the non-symmorphic screw axis symmetry. We also show that this material can host the relativistic metal-insulator transition which we have introduced in Chapter 1 on the TB model.

In the second part, we present conventional phenomenology of crystalline and non-crystalline AMR in ferromagnets [174, 175, 176, 177, 178]. We also calculate the AMR in NiMnSb ferromagnet from our first-principle fully relativistic Dirac-tight binding-linear muffin tin orbital-coherent potential approximation (FRD-TB-LMTO-CPA) method [109, 152, 158, 172]. NiMnSb was used to demonstrate SOT due to its noncentrosymmetric unit cell [109]. We observe opposite sign of the AMR to the sign commonly observed in elemental ferromagnets Fe, Co, Ni, and their alloys [152].

In the last part, we study the electronic structure, residual resistivity, and AMR in Mn_2Au alloys by employing our FRD-TB-LMTO-CPA theory. Our calculation of Au-rich Mn_2Au predicts residual resistivities and a large AMR $\sim$ 6%, consistent with current-induced Néel vector reorientation experiments [104]. We show that this correspondence can be explained with the help of our Bloch spectral function calculations described technically in Chapter 2. Finally, we summarize different contributions to the AMR. Results presented in this chapter fill the gap between minimal model theories with free fitting parameters, and the so far black box *ab initio* calculations in specific materials using no free parameters. Our theory is based on (i) magnetic symmetry analysis depending on the Néel vector orientation, and (ii) Bloch spectral function calculated within CPA and visualised over the large part of the high symmetry lines in the Brillouin zone.

3.1 Electronic structure of tetragonal CuMnAs

We start by briefly discussing symmetries of the tetragonal CuMnAs [179, 180] with its crystal structure shown in Fig. 1.3(a). Tetragonal CuMnAs is driving antiferromagnetic spintronics research since the manipulation of the Néel vector was for the first time observed in this material [103]. The nonmagnetic crystal of CuMnAs exhibits the $P4/nmm$ MSG. Our calculations on the minimal Dirac

Néel vector	Magnetic space group	Important symmetry
[100]	$Pm'nm(8)$	$\mathcal{PT}$,$\tilde{\mathcal{M}}_x$
[110]	$P2_1'/c(4)$	$\mathcal{PT}$
[001]	$Pn'm'a'$ (8)	$\mathcal{PT}$

Table 3.1: Dependence of the magnetic space group on the Néel vector orientation in tetragonal CuMnAs. The numbers in brackets mark number of symmetry operations.

quasiparticle antiferromagnet points towards the possibility of the Dirac nodal lines in the antiferromagnetic tetragonal CuMnAs [27]. The density of states (DOS) exhibits semimetallic character with a dip near the Fermi level and is sensitive to the electronic correlations [82]. The comparison of DOS with photoemission spectroscopy data point towards Hubbard $U \sim 3$ eV.

In the energy bands calculated with SOC for the $\mathbf{N}||[100]$, we indeed obtained nodal lines with an open geometry. The MSG reduces to eight symmetry elements: Identity, off-centred mirror planes $\tilde{\mathcal{M}}_x$ and $\tilde{\mathcal{M}}_z = \left\{M_z|\frac{1}{2}\frac{1}{2}0\right\}$, nonsymmorphic screw-axis $\mathcal{S}_{2y}$=$\left\{C_{2y}|0\frac{1}{2}0\right\}$, and four $\mathcal{PT}$ conjugated symmetries. When we rotate the Néel vector to $\mathbf{N}||[110]$ and $\mathbf{N}||[101]$, $\tilde{\mathcal{M}}_z$ and $\mathcal{S}_{2y}$ remain symmetries of the system, respectively. In both cases we have obtained gapped nodal-lines. These symmetries are thus excluded from protecting the nodal-lines. The nodal-lines are protected as in the model by the $\tilde{\mathcal{M}}_x$ symmetry. This protection is distinct from the earlier identified screw-axis protection in nonmagnetic ZrSiS [181]. The dependence of the MSG on the Néel vector orientation is listed in Tab. 3.1.

The field-like NSOT has the same symmetry as in the minimal model from Chapter 1 and allows for the current-induced manipulation of the Néel vector [103, 106]. This illustrates the possibility to control the Dirac crossings in realistic material. Tetragonal CuMnAs is, however, not a convenient candidate for observing the relativistic metal-insulator transition since the Dirac crossings are buried in the Fermi sea [27]. Remarkably, this drawback can be mitigated, according to our calculations, by lowering the symmetry from tetragonal to orthorhombic and we will discuss in the next section the electronic structure of orthorhombic CuMnAs in greater detail.

3.2 Electronic structure of orthorhombic antiferromagnetic CuMnAs

The volume of the unit cell of the orthorhombic phase is doubled with respect to the tetragonal CuMnAs crystal. The space group *Pnma* (number 62) is centrosymmetric and we list the experimental unit cell parameters and Wyckoff positions in Tab. 3.2. There are four Mn atoms and we have calculated electronic structure of the three antiferromagnetic orderings which preserve the size of the nonmagnetic unit cell (and thus will be of Type-III MSG) [173]: AF1 $\uparrow\uparrow\downarrow\downarrow$, AF2 $\uparrow\downarrow\uparrow\downarrow$, and AF3 $\uparrow\downarrow\downarrow\uparrow$. We list the MSGs and the calculated total ground state energies in VASP in Tab. 3.3. The AF2 phase is centrosymmetric with a ferro-

Atom	Wyckoff position	Experimental coordinates
Cu	4c ($.m.$)	0.62230 0.25000 0.06000
Mn	4c ($.m.$)	0.54020 0.25000 0.67800
As	4c ($.m.$)	0.24590 0.25000 0.12340

Table 3.2: Wyckoff positions of the orthorhombic CuMnAs. The experimental lattice parameters are 6.5773, 3.8540, and 7.3096Å. Remaining atomic positions are determined for the Wyckoff position $4c$ as $(x, \frac{1}{4}, z)$, $(-x+\frac{1}{2}, \frac{3}{4}, z+\frac{1}{2})$, $(-x, \frac{3}{4}, -z)$, and $(x+\frac{1}{2}, \frac{1}{4}, -z+\frac{1}{2})$. $.m.$ denotes site symmetry group containing only identity and glide-mirror plane $\left\{\mathcal{M}_y|(0\frac{1}{2}0)\right\}$. The experimental parameters are taken from [182] (Tab.II).

magnetic symmetry group and thus can in principle host the spontaneous Hall effect. We will discuss the possibility of spontaneous Hall effects in collinear antiferromagnets in Chapter 4. The phases AF1 and AF3 exhibit antiferromagnetic symmetry groups with $\mathcal{PT}$ symmetry and the AF1 phase tends to be the energy ground-state [28, 173].

We show the corresponding energy bands in Fig. 3.1. The phases AF1 and AF2 fulfil the prerequisites for the antiferromagnetic Kramers theorem and the energy bands (see Fig. 3.1(a) and (c)) are Kramers degenerate. Both phases exhibit also band-crossings close to the Fermi level. The location of these crossings in the lowest energy phase AF1 is pinned at the Fermi level. In further discussion, we will present calculations in the AF1 phase only. We show its unit cell in Figs. 1.1(c) and 3.3(a) with a marked $\mathcal{PT}$ symmetry centre.

A more detailed inspection of the non-spin-orbit coupled energy bands points towards the existence of the nodal line in the $\Gamma - X - U$ crystal momentum plane (we use the conventional orthorhombic Brillouin zone notation). This nodal-line is related to the presence of the off-centred mirror plane $\tilde{\mathcal{M}}_y = \left\{\mathcal{M}_y|0, \frac{1}{2}, 0\right\}$ [27, 28, 49, 183] (in the spin space group aka magnetic symmetry group without SOC [184]). We remark that in our papers [27, 82] we used FLEUR [185] and ELK [186] codes for the band structure calculations, while in this thesis we present mostly the VASP calculations which give consistent results with our paper and other works [28, 173].

Phase	Space (point) group	Energy	Important symmetry/effect
AF1 ↑↑↓↓	$Pn'm'a'(m'm'm')$	0	$\mathcal{PT}$ Dirac fermions
AF2 ↑↓↑↓	$Pnm'a'(m'm'm)$	+2.5 eV	$\mathcal{P}$ Spontaneous Hall effect
AF3 ↑↓↓↑	$Pnm'a(mmm')$	+0.2 eV	$\mathcal{PT}$ Dirac fermions

Table 3.3: Magnetic symmetry groups, calculated ground-state energy, and characteristic symmetry/effect for different collinear antiferromagnetic states with the propagation vector $\mathbf{q} = 0$ and easy axis along the c-axis in orthorhombic CuMnAs. The order of the magnetic moments symbolised by arrows corresponds to the positions of Mn atoms in fractional units: (0.5402 , 0.25, 0.678), (-0.0402, 0.75, 1.178), (-0.5402, 0.75, -0.678), and (1.0402, 0.25, -0.178).

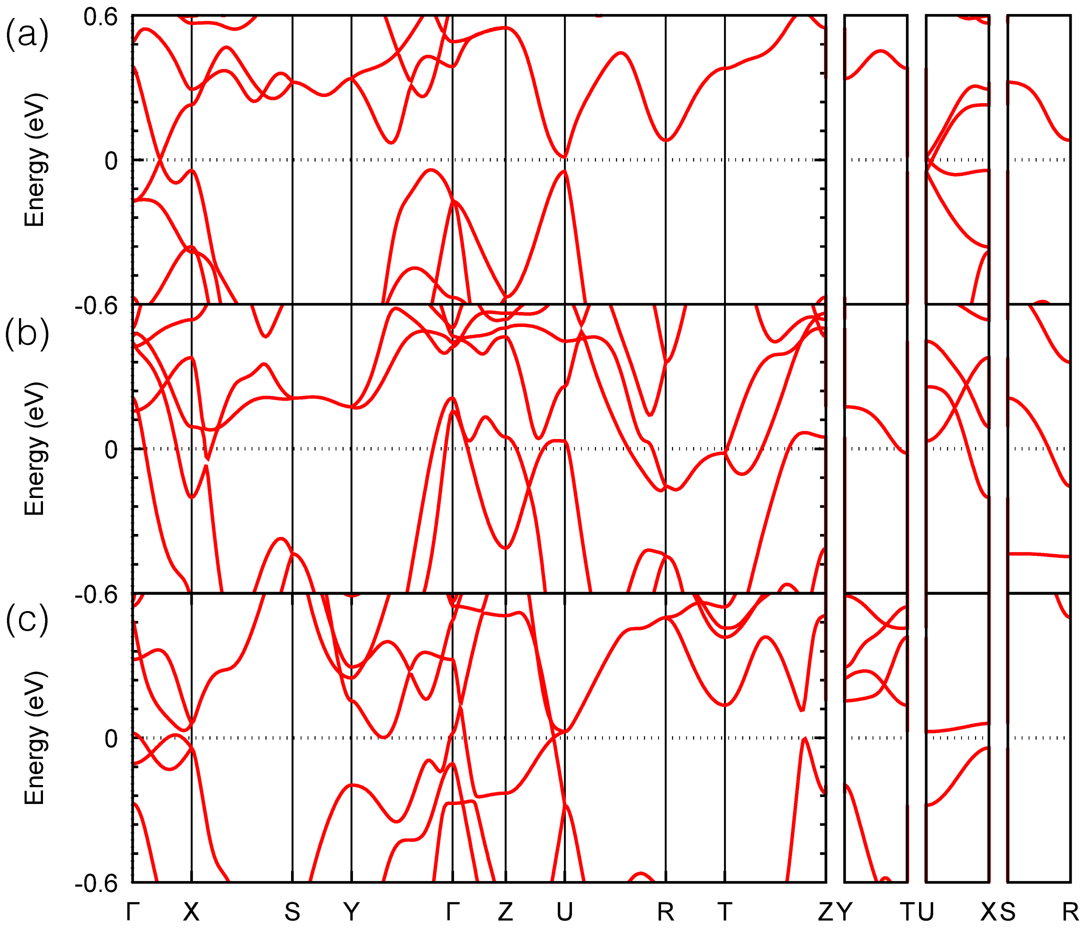

Figure 3.1: Bandstructure of CuMnAs in an antiferromagnetic state (a) AF1, (b) AF2, and (c) AF3. The energy zero is shifted to the Fermi energy.

3.3 Dirac fermions in CuMnAs

The nodal line present in the calculations without SOC is visible along the $\Gamma - X$, $U - X$, and $Z - X$ high symmetry lines. In the calculations with SOC and for $\mathbf{N} \parallel$ [001], the DPs between $\Gamma - X$ and between $Z - X$ become massive. The nodal-line gaps entirely, except at the DP between $U - X$, as we show in Fig. 3.2(a). In Fig. 3.2(b) we plot the corresponding DOS which exhibits a square dependence on energy in the close vicinity of the Fermi level. We list in Tab. 3.4 the dimensional dependence of the conventional parabolic band and Dirac fermions DOS vs. energy.

Dispersion $E(k)$	Parabolic ak^2	Linear ak
$D_{1d}(E)$	$\frac{1}{\sqrt{a(E-E_0)}}$	$\frac{1}{a}$
$D_{2d}(E)$	$\frac{\pi}{a}$	$\frac{2\pi}{c_k^2}(E-E_0)$
$D_{3d}(E)$	$2\pi\sqrt{\frac{E-E_0}{a^3}}$	$\frac{4\pi}{a^3}(E-E_0)^2$

Table 3.4: Energy dependence of the density of state in 1, 2, and 3 dimensions and for parabolic and linear dispersion.

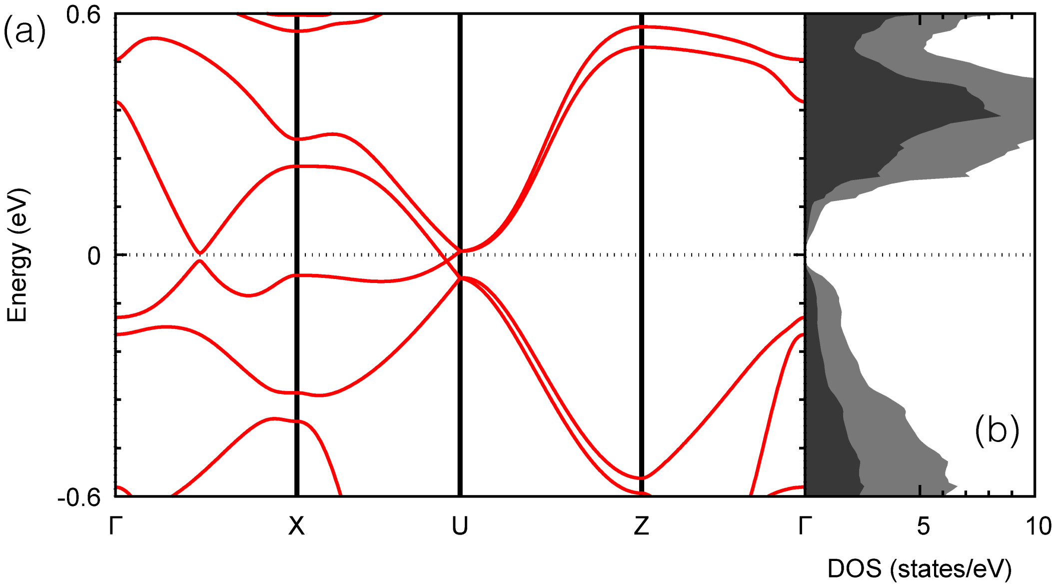

Figure 3.2: (a) Energy bands of orthorhombic CuMnAs antiferromagnet with spin-orbit coupling calculated with Néel vector along the [001] crystal direction. (b) The DOS indicates point-like touching at the Fermi level.

According to this table, our quadratic dispersion is an indication of the presence of Dirac fermions in the energy bands. We will now demonstrate that owing to an additional non-symmorphic screw rotation symmetry $\mathcal{S}_z = \left\{\mathcal{C}_{2z}|\frac{1}{2}0\frac{1}{2}\right\}$ ($\mathcal{C}_{2z}$ is a two-fold rotation), we observe an antiferromagnetic topological DSM state.

We have seen in Chapter 1 that $\mathcal{PT}$ action on the position, spin, and crystal momentum is as follows:

$$(x, y, z) \xrightarrow{\mathcal{PT}} (-x, -y, -z)\,, \tag{3.1}$$

$$(s_x, s_y, s_z) \xrightarrow{\mathcal{PT}} (-s_x, -s_y, -s_z)\,, \tag{3.2}$$

$$(k_x, k_y, k_z) \xrightarrow{\mathcal{PT}} (k_x, k_y, k_z)\,. \tag{3.3}$$

We list here also the transformation properties of the screw axis (shown in Fig. 3.3(a)):

$$(x, y, z) \xrightarrow{\mathcal{S}_{2z}} \left(-x + \frac{1}{2}, -y, z + \frac{1}{2}\right), \tag{3.4}$$

$$(s_x, s_y, s_z) \xrightarrow{\mathcal{S}_{2z}} (-s_x, -s_y, s_z)\,, \tag{3.5}$$

$$(k_x, k_y, k_z) \xrightarrow{\mathcal{S}_{2z}} (-k_x, -k_y, k_z)\,. \tag{3.6}$$

There are four high-symmetry lines invariant under $\mathcal{S}_{2z}$:

$$(k_x = 0 \text{ or } \pi, k_y = 0 \text{ or } \pi, k_z)\,. \tag{3.7}$$

The square of the symmetry gives minus from the 2π rotation of the spin and translation by one unit cell along the c-axis:

$$\mathcal{S}_{2z}^2 = -e^{-ik_z}. \tag{3.8}$$

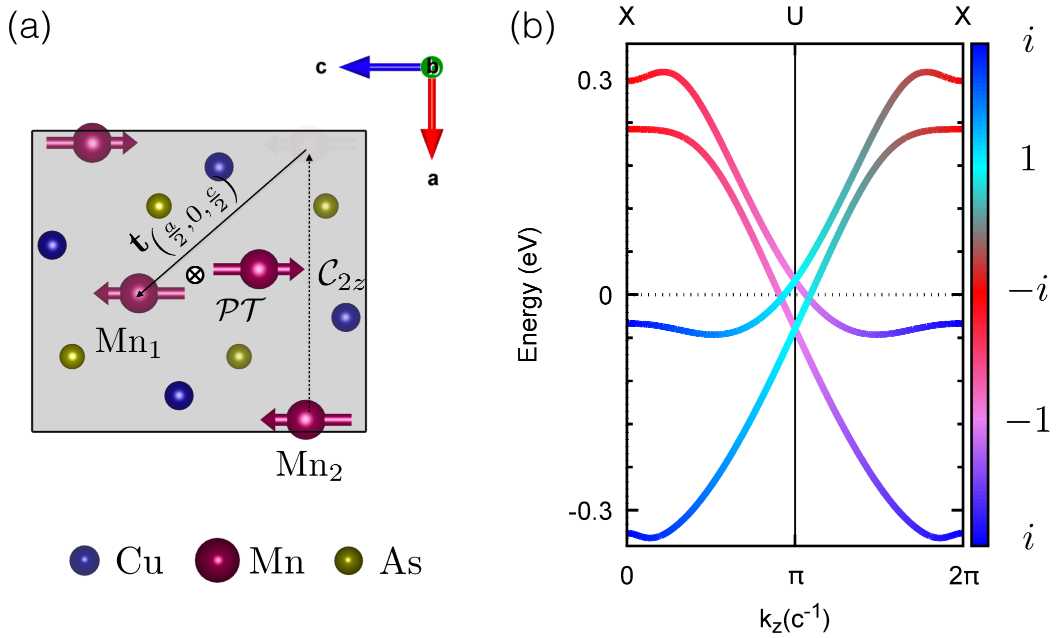

Figure 3.3: (a) Crystallographic and magnetic structure of orthorhombic CuMnAs in the AF1 phase with a marked screw rotation symmetry and $\mathcal{PT}$ symmetry. (b) Dirac fermion dispersion and screw rotational symmetry eigenvalue along the $X-U-X$ line in the Brillouin zone.

The corresponding eigenvalues of the screw rotational symmetry are:

$$s_{2z}^{\pm} = \pm i e^{-i\frac{k_z}{2}}, \tag{3.9}$$

and they can be used to label the Bloch states on these symmetry invariant subspaces. We see that the off-centred factor along a-axis squares to unity. Furthermore, we observe that the dependence of the eigenvalues on the crystal momentum, which is characteristic of the non-symmorphic symmetries and makes them distinct from the off-centred symmetries [49, 69, 187]. The off-centred factor, however, enters the mutual relationship of Kramers partner states and chooses which of the symmetry invariant Brillouin zone manifolds host the assignment of the symmetry eigenvalues to the energy bands preventing hybridization. For the Kramers partner state we obtain a relationship:

$$\mathcal{S}_{2z} \circ (\mathcal{PT})|\psi(k)\rangle = e^{-ik_x} s_{2z}^{-} \mathcal{PT}|\psi(k)\rangle. \tag{3.10}$$

From this equation we can conclude that for $k_x = \pi$ the band-crossing is stable. We show the screw rotational symmetry eigenvalues (3.9) along the $X-U-X$ symmetry line in Fig. 3.3(b). The double-degenerate bands have the same symmetry eigenvalue and the two Kramers doublet forming the crossing have always opposite symmetry eigenvalues. Analogical stabilization of energy bands was found also in nonmagnetic systems [187, 188].

Finally, we show also the energy dispersion along with the three orthogonal directions around the Dirac points in Fig. 3.4(a-c). Consistent with our symmetry analysis and DOS we see a linearly dispersing band away from the DP. The Dirac states comprise mainly Mn 3d states as can be seen from the atomic composition

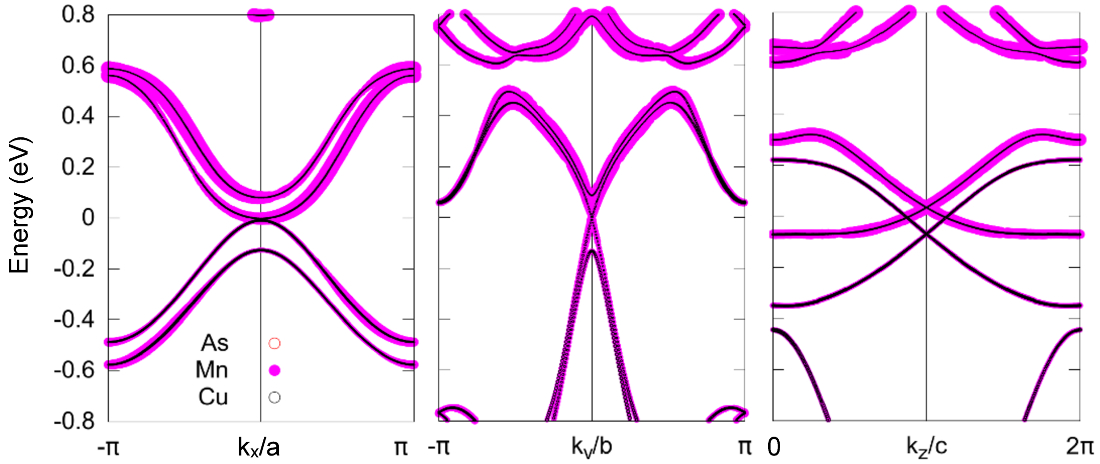

Figure 3.4: Energy dispersion cuts around the Dirac points along (a) k_x, (b) k_y, and (c) k_z crystal momentum directions. In all panels we plot also the atomic composition.

in the figures. This plot was calculated in ELK [27, 186]. We also point out a quite substantial anisotropy of the Dirac dispersion with the Fermi velocities: $v_{F,y} = 3,8 \times 10^5 ms^{-1}, v_{F,z} = 1,8 \times 10^5 ms^{-1}$.

3.4 Relativistic metal-insulator transition

We also identify the orthorhombic CuMnAs antiferromagnet as a candidate for our RMIT. The DPs are the only states around the Fermi level, and they are gapped for any other direction of the Néel vector other than [001]. This can be seen by inspecting Tab. 3.5 where we list the symmetry dependence on the Néel vector rotation. The DP protecting symmetry is present only for the Néel vector along the [001] crystal axis. The $\mathcal{PT}$ symmetry is present for any orientation of the Néel vector.

Néel vector	Magnetic space (point) group	Symmetry elements (number)
[001]	$Pn'm'a'(m'm'm')$	$\mathcal{PT}$, $\mathcal{C}_{2x}\mathbf{t}_{\frac{abc}{2}}$, $\mathcal{C}_{2y}\mathbf{t}_{\frac{b}{2}}$, $\mathcal{C}_{2z}\mathbf{t}_{\frac{ac}{2}}$ (8)
[100]	$Pnm'a(mmm')$	$\mathcal{PT}$, $\mathcal{C}_{2y}\mathbf{t}_{\frac{ac}{2}}$, $\mathcal{M}_{x}\mathbf{t}_{\frac{abc}{2}}$, $\mathcal{M}_{z}\mathbf{t}_{\frac{ac}{2}}$ (8)
[010]	$Pn'ma(m'mm)$	$\mathcal{PT}$, $\mathcal{C}_{2x}\mathbf{t}_{\frac{abc}{2}}$,$\mathcal{M}_{y}\mathbf{t}_{\frac{b}{2}}$,$\mathcal{M}_{z}\mathbf{t}_{\frac{ac}{2}}$ (8)
[111]	$P\bar{1}(\bar{1})$	$\mathcal{PT}$ (1)

Table 3.5: Dependence of the magnetic space group on the easy axis orientation for the antiferromangetic order ”AF1”. $\mathbf{t}_{\frac{abc}{2}}$ marks partial unit cell translation vector $\left(\frac{a}{2}, \frac{b}{2}, \frac{c}{2}\right)$.

In Fig. 3.5 we illustrate the RMIT in CuMnAs. We plot the DSM state for the Néel vector along the [001] crystal axis (top panel and red line), and the semiconducting states for the Néel vector along the [100] (central blue line panel) and [111] directions (bottom blue line panel). For the Néel vector along the [100] direction, the DP mass along the $\Gamma - X$ line is nonzero but small corresponding

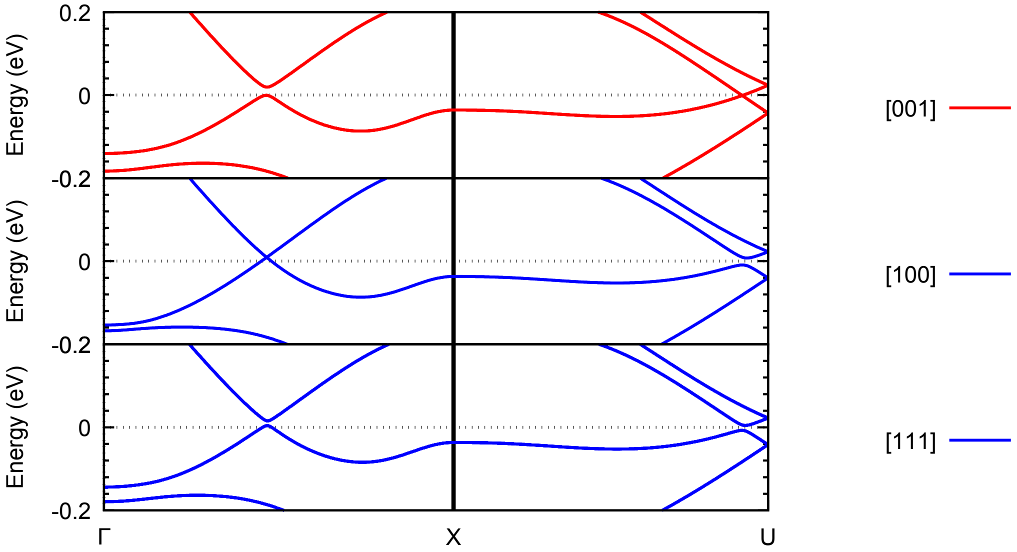

Figure 3.5: Energy bands in orthorhombic CuMnAs calculated with spin-orbit coupling and antiferromagnetic moments along [001] (top), [100] (centre), and [111] (bottom) crystal directions.

to a gap of approximately 1 meV.

We remark that the band structure depends on the Hubbard U. While the DPs are stable up to $U \sim 3\ eV$ in our calculations, the position of the DPs shifts up in energy with increasing U. This can, together with possibly strong disorder sensitivity [189] and small energy band gaps, complicate the observation of Dirac fermions and the RMIT. In the final section on orthorhombic CuMnAs, we will discuss the possibilities to control the Néel vector orientation.

3.5 Reorientation of the Néel vector

In principle, we can control the Néel vector orientation by the NSOT or electric gating. The latter is possible due to the semiconducting DOS for certain orientations of the Néel vector [23, 190]. We will now demonstrate that the former is possible since the orthorhombic CuMnAs fulfils the criteria for Dirac-Néel antiferromagnets formulated in Chapter 1: orthorhombic CuMnAs has $\mathcal{PT}$ symmetry and noncentrosymmetric Mn Wyckoff positions. The magnetic anisotropy energy is small for an arbitrary rotation at the resolution limit of our DFT method, preferring slightly in-plane (001) Néel vector. Remarkably, also orthorhombic CuMnAs provides efficient inverse spin galvanic effect as the Mn-sublattices are (i) $\mathcal{PT}$ partners in pairs 1-3/2-4, (ii) screw axis $\mathcal{S}_{2z}$ partners 1-2/3-4, as depicted in the Fig. 3.3(a), leading to the conclusion that an even tensor $\chi^{\mathrm{I}}_{\mu\nu}$ (see Eq. (1.56)) is staggered in the (001)-plane. Its form is the same as in tetragonal CuMnAs [106], except $\chi^{\mathrm{I}}_{A,12} \neq \chi^{\mathrm{I}}_{A,21}$ in general, allowing for the manipulation of the Néel order within/towards the (001) plane. Remarkably, for the spin-axis $\mathbf{N}$ prepared along [110] and electric field along the [001] direction, there is an efficient second order in magnetization even field $\chi^{\mathrm{I},(2)}_{A,\mu\nu,kl}$ in the [001] direction allowed by symmetry which in principle enables a reversible reorientation towards the [001] axis. This torque can be possibly enhanced by the presence of real disorder and hetero-structure geometry [191].

We arrived at this conclusion by analysing the symmetry with the help of the symmetry code developed by Železný et al.[106]. The analysis is based on the application of *Neumann principle* for the linear response coefficient of the non-equilibrium spin-polarization $\delta\mathbf{s}_A$ at the magnetic sublattice a induced by an applied electric field: $\delta\mathbf{s}_a = \chi_a\mathbf{E}$ (recall the linear response table presented in Chapter 1). We employ the expansion of the tensor χ_a in terms of the magnetic moment directions within an exchange approximation (no tilting):

$$\chi^{\text{even}}_{a,\mu\nu}(\hat{\mathbf{N}}) = \chi^{(0)}_{a,\mu\nu} + \chi^{(2)}_{a,\mu\nu\alpha\beta}\hat{N}_\alpha\hat{N}_\beta + \dots, \tag{3.11}$$

where $\hat{\mathbf{N}}$ is the spin-axis direction. The zero order (field-like) term in orthorhombic CuMnAs is given by

$$\chi^{(0)}_A = \begin{pmatrix} 0 & x_{12} & 0 \\ x_{21} & 0 & x_{23} \\ 0 & x_{32} & 0 \end{pmatrix}, \qquad \chi^{(0)}_B = \begin{pmatrix} 0 & x_{12} & 0 \\ x_{21} & 0 & -x_{23} \\ 0 & -x_{32} & 0 \end{pmatrix}. \tag{3.12}$$

These are the lowest order efficient fields with only two nonzero components $x_{12} \neq x_{21}$ of the analogical form to tetragonal CuMnAs, except now x_{21} is in general different from x_{12}. Since the chemistry around the Fermi level (SOC strength) in orthorhombic CuMnAs is similar to the tetragonal CuMnAs case we can expect similar magnitudes for critical switching currents as in the aforementioned tetragonal CuMnAs, e.g., of the order of $j_c \approx 10^6 - 10^7\ A/cm^2$ [103].

In the case of the higher order terms, the situation is more complicated. For example, for the spin-axis $\hat{\mathbf{N}} = (1, 1, 0)$:

$$\chi^{(2)}_A = \begin{pmatrix} x_{11} & x_{12} & x_{23} \\ x_{21} & x_{22} & x_{23} \\ x_{31} & x_{32} & x_{33} \end{pmatrix}, \qquad \chi^{(2)}_B = \begin{pmatrix} x_{11} & x_{12} & -x_{23} \\ x_{21} & x_{22} & -x_{23} \\ -x_{31} & -x_{32} & x_{33} \end{pmatrix}. \tag{3.13}$$

Therefore, for the spin-axis along [1,1,0] and electric field along the [001] direction, there is an efficient field in the [001] direction allowed by symmetry. However, this field will depend on the spin-axis direction and when the spin-axis tilts from the [1,1,0] direction field no longer has to be oriented in the [001] direction.

3.6 Anisotropic magnetoresistance in ferromagnetic half-metal NiMnSb

The sensitivity of electronic transport to the current direction is called anisotropic resistance and can be found in systems with broken cubic symmetry. The transport anisotropy arises, for instance, in tetragonal nonmagnetic crystals like CuMnAs (above the Néel temperature) where the crystal looks differently along the a and c-crystal axes and the electrons thus scatter differently. Ferromagnets are particularly attractive here since ferromagnetism not only breaks the cubic symmetry but the current magnitude can depend on the ferromagnetic moment rotation.

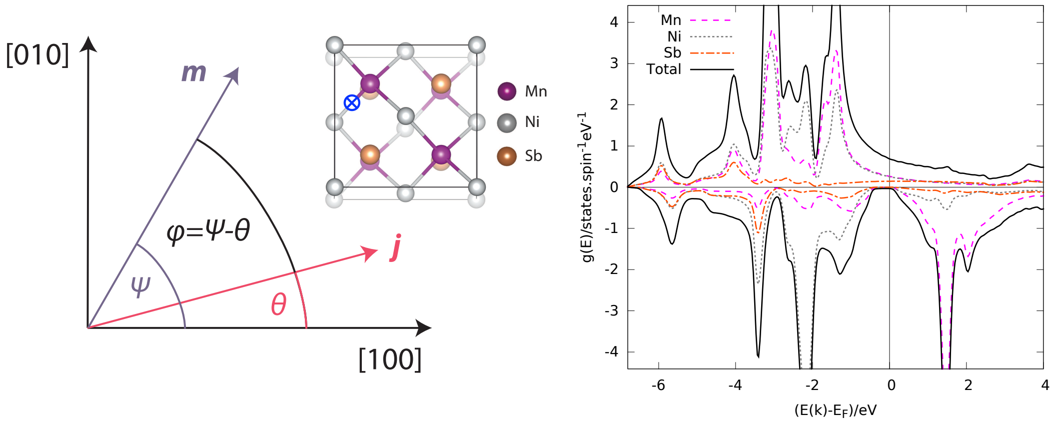

(a) (b)

Figure 3.6: NiMnSb crystal and DOS. (a) Mutual orientation of the magnetization, current (Hall bar), and the crystalline axes of the NiMnSb crystal shown in the inset. (b) The half-metallic DOS of ferromagnetic NiMnSb calculated by FRD-TB-LMTO including the atom-resolved contributions.

The commonly leading contribution is the resistance dependence on the current direction with respect to the magnetization axis. This effect is called (spontaneous) AMR [23, 27, 104, 193, 194] and was discovered more than 150 years ago [195]. We define here AMR as:

$$\Lambda_{100} \equiv \frac{\rho_{L,100}(\phi = 0) - \rho_{L,100}(\phi = 90^\circ)}{\bar{\rho}}, \tag{3.14}$$

where the subscript refers to the given crystal direction, ϕ is the angle between the applied current and the magnetization direction, ρ_L refers to the longitudinal resistivity, and bar marks its mean value within the transport plane, all over the whole crystal. AMR can be employed for electrically detecting different directions of magnetization. It was used, for instance, in the first generation of magnetoresistive field sensors in the read-heads of hard-disks [196]. The pioneering works of the past decade have shown that AMR can be used for the electrical readout in experimental AF memory devices [103, 114, 197, 198, 199].

However, there are two challenges in AMR research and development. First, the AMR magnitudes are usually constrained to fractions or units of per cent of the signal. Second, we are lacking general theory with predictive power for searching materials with large AMR ratios. The existing *ab initio* calculations are consistent with the observed magnitude of the effect in conventional systems, such as elemental ferromagnets and their alloys [152, 200, 201]. However, partly since the *ab initio* methods were applied to complicated many-band ferromagnetic metals as a black-box theory [177], they were so far unable to identify appealing physical pictures of the microscopic mechanism of AMR. On the other hand, the existing phenomenological models [174, 176, 175, 202] require several fitting parameters and a clear-cut correspondence to the *ab initio* parameters was so far not established [177].

As we have seen in Chapter 1, the existence and the form of AMR are dictated by the symmetries of the considered system and the transport measurement geometry. The commonly accepted picture of AMR relies on the simultaneous presence of spin-polarisation and relativistic SOC [152]. The magnitude and sign are governed by microscopic mechanisms of two distinct origins [177]. First, a mechanism of anisotropic group velocities. Second, a scattering mechanism due to the disorder potential which due to the SOC breaks the isotropy of the wave function scattering. This asymmetry can have contributions from (a) the unpolarised bands and spin-polarized impurities, and (b) spin-polarized bands and nonmagnetic impurities. These contributions can be revealed by inspecting the Boltzmann equation (no vertex corrections) derived from Eq. 1.56. We will discuss here the phenomenology of AMR and our *ab initio* calculations of AMR in complex ferromagnet NiMnSb (crystal shown in Fig. 3.6(a)), before turning our attention to a detailed analysis of AMR in antiferromagnetic Mn_2Au alloys. We show the half-metallic DOS of NiMnSb in Fig. 3.6(b). We see that one of the spin channels is completely suppressed around the Fermi level.

Phenomenology of anisotropic magnetoresistance

The phenomenological formula for the angle dependent longitudinal and transversal resistivity in the crystallographic basis, shown in Fig. 3.6(a) (previously derived for GaMnAs with zincblend lattice [203]), can be used for half-Heusler NiMnSb:

$$\begin{aligned} \frac{\Delta\rho_L}{\overline{\rho}} &\equiv \frac{\rho_L - \overline{\rho}}{\overline{\rho}} = C_I \cos 2(\psi-\theta) + C_{IC}\cos 2(\psi+\theta) + C_C \cos 4\psi + C_U \sin 2\psi \,, \\ \frac{\rho_T}{\overline{\rho}} &= C_I \sin 2(\psi-\theta) - C_{IC} \sin 2(\psi+\theta)\,. \end{aligned} \tag{3.15}$$

Here $\rho_{L/T}$ are the longitudinal/transverse resistivities, $\overline{\rho}$ is the average longitudinal resistivity, ψ is the angle between the magnetization $\mathbf{m}$ and the [100] crystallographic direction (see Fig. 3.6(a)), and θ is the angle between the current $\mathbf{j}$ and the [100] crystallographic direction, as we schematically show in Fig. 3.6(a). The first term in both equations represents the non-crystalline AMR which depends only on the angle between current and magnetization directions. This contribution is commonly found in polycrystalline ferromagnetic alloys [152]. The second term in both equations describes a mixed crystalline-non-crystalline AMR contribution. The last two terms in the longitudinal resistivity equation describe the crystalline AMR (CAMR). This component depends only on the mutual orientation of the magnetization and crystalline axes. Specifically, the third term corresponds to the cubic CAMR, while the last term describes the uniaxial CAMR which in NiMnSb is due to the growth strain.

We can now use these equations to rewrite the AMR for currents applied along different crystal directions (corresponding to the different Hall bar orientations in the experiment):

$$\begin{aligned} \frac{\Delta\rho_{L,100/010}(\phi)}{\overline{\rho}} &= C_C \cos 4\phi + (C_I + C_{IC})\cos 2\phi \pm C_U \sin 2\phi, \\ \frac{\Delta\rho_{L,110/1\bar{1}0}(\phi)}{\overline{\rho}} &= -C_C \cos 4\phi + (C_I - C_{IC})\cos 2\phi \pm C_U \cos 2\phi, \end{aligned} \tag{3.16}$$

where $\phi = \psi - \theta$ is the angle between the magnetization and current. We obtained experimental values for the parameters C_I, C_C, C_{IC} and C_U from fitting the experimental data by using formulas (3.16):

- C_U can be obtained from the difference between signals obtained in the [110] and [1$\bar{1}$0] crystal directions (Hall bar orientations),
- C_I can be estimated from the sum of the AMR data measured along the [100] and [110] directions, and
- C_{IC} and C_C are determined from the sum of the [110] and [1$\bar{1}$0] bar measurements.

Measurements of the AMR were performed by the group of Chiara Ciccarelli by rotating the NiMnSb magnetization in the plane by an applied saturating magnetic field [109]. Hall bars were patterned along [100], [010], [110] and [1$\bar{1}$0] crystal directions. We show the measured data in Fig. 3.7(b) for 4 μm wide Hall bars patterned from a 37 nm thick NiMnSb film. There are small differences in the measured AMR signals between Hall bars fabricated from different parts of the wafers. We attribute the differences to the variations from the nominal widths of the two Hall bar devices, and consequently to different strains, caused by uneven milling of the devices.

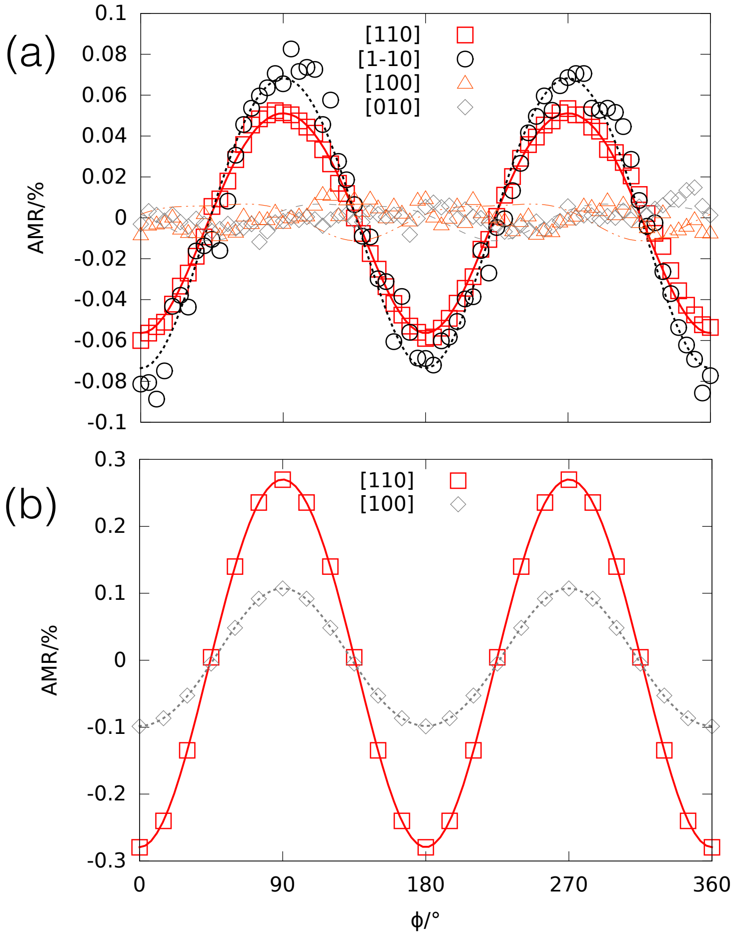

Figure 3.7: Measured and calculated anisotropic magnetoresistance (AMR) in NiMnSb. (a) Angular dependence of the AMR measured in NiMnSb Hall bar (data set 1 [109]). (b) Angular dependence of the AMR for a Ni-rich system calculated from first-principle by the FRD-TB-LMTO+CPA method (symbols). The lines correspond to the phenomenological fit.

We summarize the results in Tab. 3.6, and in Fig. 3.7(a). The AMR in our NiMnSb devices is dominated by the non-crystalline term C_I and the mixed crystalline-non-crystalline term C_{IC}. The crystalline terms C_U and C_C are an order of magnitude smaller. This leads to the $\cos 2\phi$ AMR dependence in the [110] and [1$\bar{1}$0] bars and a negative AMR sign ($\rho_L(\mathbf{m} \parallel \mathbf{j}) < \rho_L(\mathbf{m} \perp \mathbf{j})$) which is consistent with previous estimates of AMR in NiMnSb [204]. A similar angular dependence was previously obtained in (Ga,Mn)As and (Ga,Mn)(As,Sb) [205]. Importantly, the sign is the same as in (Ga,Mn)As [177] and opposite to the AMR sign in most conventional transition metal ferromagnets (where $\rho_L(\mathbf{m} \parallel \mathbf{j}) > \rho_L(\mathbf{m} \perp \mathbf{j})$ [152]). The AMR along the [100] and [010] direction is at least an order of magnitude smaller due to the mutual cancellation of the C_I and C_{IC} terms. This explains why bars oriented along the [100] and [010] direction could not be used in our spin-orbit torque ferromagnetic resonance experiments [109].

Λ_{100}/%	Λ_{110}/%	C_I	C_{IC}	C_C	C_U
-0.01	-0.15	-0.032 (3%)	0.031 (3%)	0.003 (38%)	0.009 (9%)
-0.01	-0.12	-0.032 (1%)	0.026 (3%)	0.001 (77%)	-0.003 (187%)

Table 3.6: Experimental values of the AMR magnitude given by Eq. (3.14) and the constants obtained from fitting to Eq. (3.16). Numbers in parentheses correspond to the relative error bars. The two rows correspond to different data sets 1 and 2 - different Hall bar devices patterned on the same wafer.

Microscopic calculations

We have employed the FRD-TB-LMTO+CPA [152, 164] method in combination with Kubo formula [152, 162] as we have described in Chapter 2. We have calculated the conductivity tensor at zero temperature in disordered NiMnSb. We have used s, p, and d basis. The effect of f basis orbitals can be pronounced in the phonon and magnon effects which we do not consider here [158, 172]. We have achieved the LSDA self-consistency with the Vosko-Wilk-Nusair exchange-correlation potential [134]. We use the atomic basis (Ni, Mn, Sb) at the (0, 0.25, 0.75) position of the conventional unit cell body diagonal and an empty sphere at the 0.5 positions. The ordering in the basis is important and is related to the orientation of the inversion symmetry breaking.

We set the lattice constant to the experimental value 5.927 Å[206]. We have used fine crystal momentum mesh up to 10^8 k-points in the whole Brillouin zone for the Kubo-Greenwood calculation. The use of the relatively large number of k-points for the calculation of the symmetric part of the conductivity tensor allows us to converge the full angular dependence of the AMR and to determine the microscopic parameters in the phenomenological Eq. (3.16).

According to the experiment [207], the disorder strength in NiMnSb samples may be linked to the c-axis parameter. An increase in the Mn concentration corresponds to an increasing c-axis lattice parameter. The swapping disorder is most likely realized in the epitaxially grown NiMnSb, e.g., some of the Ni-sites are substituted by Mn or vice versa. The concentrations are estimated to be from 20 % Ni-rich to 20 % Mn-rich [207]. The experimental c-axis lattice constant in our experiments is 5.951 Å and corresponds to the slight surplus of Ni. We thus consider in our calculations swapping disorder ranging from 10 % Ni surplus to 10 % Mn surplus. Firstly, we calculated the residual resistivity (see also Ref.[158])

and saturated magnetization of 3.49 μ_B for 10 % Ni-rich NiMnSb, 4.05 μ_B for stoichiometric NiMnSb, and 3.74 μ_B for 10 % Mn-rich NiMnSb. The decrease in the total magnetization in our calculations for the disordered NiMnSb is consistent with experiment [207], and the sublattice magnetic moments in stoichiometric NiMnSb are consistent with the previously reported values [208, 209].

In the calculation of residual resistivities we set the imaginary part of the complex energy to $\Gamma = 10^{-5}$ Ry giving ~ 10 $\mu\Omega$cm (~ 85 $\mu\Omega$cm) for 10 % Ni (Mn) - rich calculations. In the case of Ni-rich disorder, the calculations reproduce the range of residual resistivities observed for NiMnSb grown by different techniques [210, 211, 212]. The 10 % Mn-rich case is close to the upper boundary for the disorder in our films since the calculated residual resistivity exceeds the measured room temperature value ~ 50 $\mu\Omega$cm [109].

$\Lambda_{100}/\%$	$\Lambda_{110}/\%$	C_I	C_{IC}	C_C
-0.21	-0.55	-0.189 (0.2 %)	0.086 (0.2 %)	0.004 (4 %)

Table 3.7: First principles calculations of the AMR in 10 % Ni rich NiMnSb. The numbers in parentheses are the relative error bars.

In our AMR calculations, we did not consider strain effects since the strain related crystalline terms tend to be small in the measured samples. We used FRT model to include the effect of temperature (phonons contribution [213]) by broadening the imaginary part of the complex energy up to Imz ~ 2.10^{-3} Ry. This gives resistivity ~ 27 $\mu\Omega$cm in 10 % Ni-rich system and corresponds to the previously reported experimental values at room temperature [210, 211, 212], and to the value calculated within Landauer-Büttiker formalism [109]. Due to the experimental known c-axis constant corresponding to the surplus of Ni, we calculated the detailed angular dependence of the AMR for 10 % Ni-rich system only. We calculated the complete conductivity tensor for several magnetization angles and current directions along the [100] and [110] axes. From these dependencies we obtained the coefficients C_I, C_{IC} and C_C using Eq. (3.16). The angular dependence together with the phenomenological fit is shown in Fig. 3.7(b), and summarized in the Tab. 3.7.

We see that our calculations are successfully explaining:

- the experimental negative sign of AMR,
- cosine squared phenomenological angular dependence,
- the same magnitude as the experimental value, and
- larger magnitude of AMR for [110] than [100] Hall bars due to the partial cancellation of the C_I and C_{IC} terms.

All of these results are obtained for the experimentally relevant Ni-rich disorder. More results and analysis of transport in NiMnSb, including large (skew-scattering) anomalous Hall conductivity are presented in our other works [158, 172]. Our study successfully explains the AMR in NiMnSb and established our FRD-TBLMTO-CPA method for calculating AMR in multi-sublattice complex magnets.

3.7 Electronic structure of Mn_2Au

We will now study the relativistic transport in Mn_2Au alloys. We start by discussing the electronic structure and symmetries of stoichiometric Mn_2Au. The nonmagnetic crystal of Mn_2Au possesses the MSG $I4/mmm$ (number 139) consisting of 32 symmetry operations. Half of the operations are generated from the other half by applying half-unit cell translation along the body diagonal of the conventional unit cell (6 atoms per unit cell shown in Fig. 3.8(a)). The symmetry operations contain also inversion centred at the Au atom (Wyckoff position 2a) and thus the bands are in the nonmagnetic state Kramers degenerate. The Mn atoms sit at the noncentrosymmetric Wyckoff position (4e) and thus the bands are locally spin polarised even in the nonmagnetic state. In other words, the equilibrium spin-projection on the Mn atoms is spin polarised, as we illustrate schematically on the wavefunctions in Fig. 3.8(a). The time-reversal symmetry constraints the degeneracy of states $\psi_{-\mathbf{k}m\uparrow}(-\mathbf{r})$, and $\psi_{\mathbf{k}m\downarrow}(\mathbf{r})$. The spatial inversion partner states, e.g. spin-up states $\psi_{-\mathbf{k}m\uparrow}(-\mathbf{r})$ and $\psi_{\mathbf{k}m\uparrow}(\mathbf{r})$ (marked in red), are however localised on different Mn atoms connected via $\mathcal{P}$ (and analogically the blue spin-down states).

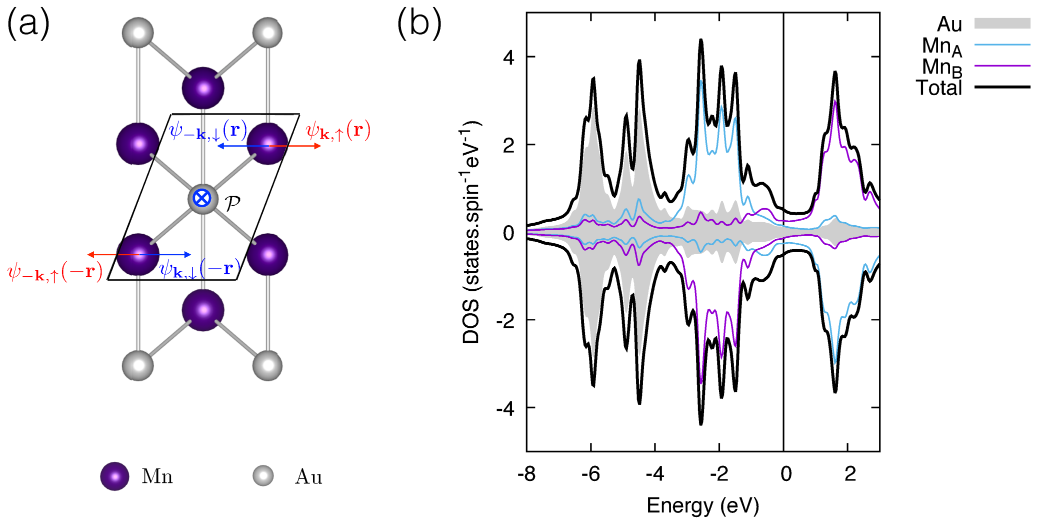

Figure 3.8: Mn_2Au crystal and DOS (DOS). (a) Primitive (the black parallelogram) and the conventional unit cell of Mn_2Au. $\mathcal{P}$ marks the centre of inversion in the nonmagnetic state and the red and blue arrow denote wavefunction projections at the noncentrosymmetric Mn-sites. (b) DOS in the stoichiometric antiferromagnetic state. The spin up and down channels are perfectly compensated.

Analogical symmetry arguments apply for the nonequilibrium spin polarisation in the antiferromagnetic state where a staggered NSOT can be generated due to the redistribution of the spins [102]. The reorientation of the Néel vector consistent with this mechanism was observed in the current induced experiments in Mn_2Au [104, 214].

The magnetic symmetry group of Mn_2Au in the simple collinear antiferromagnetic state reported in the experiments [215] depends on the orientation of the Néel vector as we summarize in the Tab. 3.8. We remark that the space groups are of type-III and that the primitive (minimal) unit cell contains only

Néel vector	Space (point) group	Symmetry elements (number)
[100]	$Im'mm(mmm')$	$\mathcal{PT}$, $\mathcal{C}_{2x}\mathbf{t}_{\frac{abc}{2}}$, $\mathcal{C}_{2y}\mathbf{t}_{\frac{b}{2}}$, $\mathcal{C}_{2z}\mathbf{t}_{\frac{ac}{2}}$ (16,8)
[110]	$Fm'mm(mmm')$	$\mathcal{PT}$, $\mathcal{C}_{2y}\mathbf{t}_{\frac{ac}{2}}$, $\mathcal{M}_x\mathbf{t}_{\frac{abc}{2}}$, $\mathcal{M}_z\mathbf{t}_{\frac{ac}{2}}$ (32,8)
[001]	$C2/m'(2/m')$	$X = \{E, \mathcal{C}_{2x\overline{y}}\} + X\mathcal{PT} + \mathbf{t}_{\frac{ab}{2}}$ (8,4)

Table 3.8: Dependence of the magnetic space group on the easy axis orientation for the antiferromagnetic Mn_2Au. $\mathbf{t}_{\frac{abc}{2}}$ marks partial unit cell translation vector $\left(\frac{a}{2}, \frac{b}{2}, \frac{c}{2}\right)$. In the brackets are listed numbers of space, and point group symmetry operation.

3 atoms (lower number of atoms is favourable for the numerically expensive *ab initio* calculations). Consequently, the nonmagnetic and magnetic Brillouin zone coincides with the nonmagnetic one [66].

We show in Fig. 3.8(b) the antiferromagnetic DOS for the moments along the [100] direction, calculated within FRD-TB-LMTO. We observe the perfectly compensated Mn antiferromagnetic sublattices with a strong either spin up or spin down component at the Fermi level. In Fig. 3.9(a) we show the energy band dependence on the Néel vector orientation. The details of band deformations are plotted in Fig. 3.9(b-c). As we have seen in Chapter 2 by comparing TB-LMTO and PAW method when the method uses an approximation with a higher symmetry than the real crystal we can expect additional crossing relaxation (enforcing unavoided crossing). We likely observe this scenario for $\mathbf{N}\|$ [010] in Fig. 3.9(b), since we did not identify any available symmetry which would relax and protect this crossing.

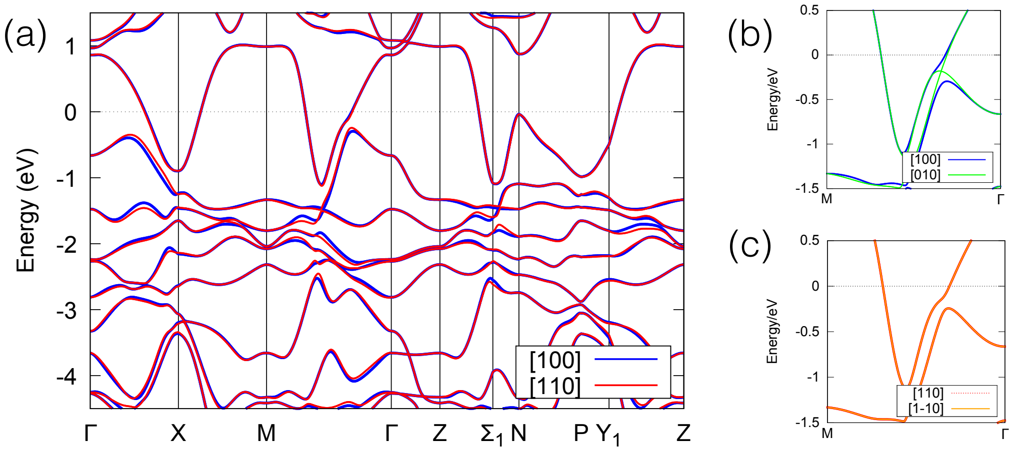

Figure 3.9: **Band structure of a stoichiometric $\mathbf{Mn_2Au}$ antiferromagnet.** (a) Energy bands for the Néel vector oriented along [100] and [110] crystal directions. (b-c) Details of the band dispersion along a $\mathrm{M} - \Gamma$ line for the different orientations of the Néel vector.

	$\mathbf{M}_{sub(orb)}$	T_N(K)	MAE(meV)	AMR (%)
FeRh	3.09(0.07)	400	1.09 [110], 1.63 [111]	1.9 (5% Rh rich)
Mn_2Au	3.69(0.01)	1450	2.82 [001], 0.008 [100]	6.3 (0.5% Au rich)

Table 3.9: Summary of material specific parameters determined experimentally and by our *ab initio* calculations.

3.8 Anisotropic magnetoresistance in Mn_2Au

We have calculated residual resistivity and AMR of several topical antiferromagnets like FeRh, MnTe, MnPt, CuMnAs, $IrMn_3$, and Mn_2Au. All these antiferromagnets exhibit AMR in a range from a fraction of a per cent to a few per cent. An exception is alloys of $IrMn_3$ where we found AMR of up to 27 %. We include a comparison of a few calculated parameters for FeRh and Mn_2Au in Tab. 3.9

According to our calculations, the in-plane magnetocrystalline anisotropy energy (MAE) in Mn_2Au is at the resolution limit of our method which is consistent with the current induced experiments [104]. The out-of-plane MAE is consistent with a previous work [216].

Residual resistivity and anisotropic magnetoresistance calculations

We consider two types of disorder effects: off-stoichiometry - a surplus of Au placed on the Mn sublattice, and inter-site swapping between Mn and Au atoms. This choice is motivated by experiment [104]. The off-stoichiometry was analysed by energy dispersive x-ray spectroscopy in 500 nm thick Mn_2Au films. The resulting concentrations are 66.2 ± 0.3 % Mn and 33.8 ± 0.3 % of Au, indicating around 0.5 % of Au excess. Identification of the possible small inter-site disorder was experimentally not accessible [104].

We have used our FRD-TBLMTO-CPA method described in Chapter 2 to calculate the residual resistivity and AMRs Λ_{100}, and Λ_{110}. We use the *spd*-type basis, LSDA and the Vosko-Wilk-Nusair exchange-correlation potential [134]. In the Kubo-Greenwood calculations, we used very fine crystal momentum mesh up to 10^{10} grid points. We have constructed an effective CPA medium corresponding to a random averaging of the occupancies of the disordered sites for the two types of disorder.

The residual resistivity is determined by the inversion of the full conductivity tensor obtained from our conductivity calculations $\rho = \sigma^{-1}$. We show in Fig. 3.10 the residual resistivity calculations for the Au surplus and Mn-Au swapping disorder in the disorder strength range of $0.5 - 5$ %. We observe that the Mn-Au swapping disorder produces a much larger residual resistivity than the Au-surplus disorder. The resistivity magnitudes are consistent with the experimental values ($\simeq 8$ $\mu\Omega$cm [217]). This corroborates the chosen types of disorder and our computational method.

Fig. 3.10(b) shows the corresponding AMR calculations. We estimate AMR for a different crystal orientations as:

$$\Lambda_{[abc]} = -2\frac{\sigma_{\mathbf{N}\|\boldsymbol{j}_{[abc]}} - \sigma_{\mathbf{N}\perp\boldsymbol{j}_{[abc]}}}{\sigma_{\mathbf{N}\|\boldsymbol{j}_{[abc]}} - \sigma_{\mathbf{N}\perp\boldsymbol{j}_{[abc]}}} = 2\frac{\rho_\| - \rho_\perp}{\rho_\| + \rho_\perp}, \tag{3.17}$$

where $[abc]$ marks the current vector orientation. We have calculated the AMR for the two types of disorder within the CPA approximation and also within the RTA (setting constant spectral broadening to the Green's functions in the stoichiometric calculation). We set the broadening of the imaginary part of the complex energy $\mathrm{Im}z \sim 13\,\mathrm{meV}$ corresponding to the residual resistivity $\simeq 10\ \mu\Omega\mathrm{cm}$. These values correspond to the experimental low-temperature values.

We can draw the following conclusions from the calculations:

- The comparison of RTA and the CPA calculated resistivities with the corresponding experimental values indicates the strength of disorder in experimental samples to be at least 0.5 % Au-rich disorder.

- The relaxation time approximation gives too small magnitudes of AMR, $\Lambda_{100} \sim 1\%$ and $\Lambda_{110} \sim 0.1\%$, and this model likely does not explain the magnitudes observed in the experiment.

- We obtain large AMR values for small degrees of disorder, e.g. 6.3 % for 0.5 % excess of Au. This value is consistent with experimental value 6.25 % [104] and thus the scattering effects within CPA are likely the origin of the large AMR.

- Our calculations exhibit strong crystalline contribution to the AMR. $\Lambda_{100} > \Lambda_{110}$ for both types of disorder. This trend is observed also experimentally [104].

- We obtain positive AMR, $\sigma(\mathbf{E} \perp \mathbf{N}) > \sigma(\mathbf{E} \parallel \mathbf{N})$ for $\mathbf{N} \parallel [100]$, the same sign as in elemental ferromagnetic alloys [152] and opposite to AMR in NiMnSb and GaMnAs. For $\mathbf{N} \parallel [110]$ the AMR changes its sign in dependence on disorder strength and type in our calculations.

- Lower disorder values around 0.1% give 10–20 times smaller residual resistivities than observed in the experiment. $\Lambda_{[100]}(x = 0.1\ \%) \sim (3.7 \pm 1.5)\%$. At such a small concentration, the calculations require increased k-point grids and number of iterations and thus we obtain larger relative errors.

Density of states and Bloch spectral function

To elucidate the much larger resistivity for Mn-Au swapping disorder we have calculated the atomically resolved DOS for both types of disorder. In Fig. 3.11(a) we show that in the case of Mn-Au swapping disorder, a corresponding virtual bound state arises around the Fermi-level. This virtual-bound-state is not observed in the Au-rich calculations shown in Fig. 3.11(b). The presence of virtual bound states in Mn-Au swapping disorder explain the larger residual resistivities.

Finally, to understand the AMR mechanism we calculate also Bloch spectral functions within CPA as described in Chapter 2. Analysis of the AMR with CPA

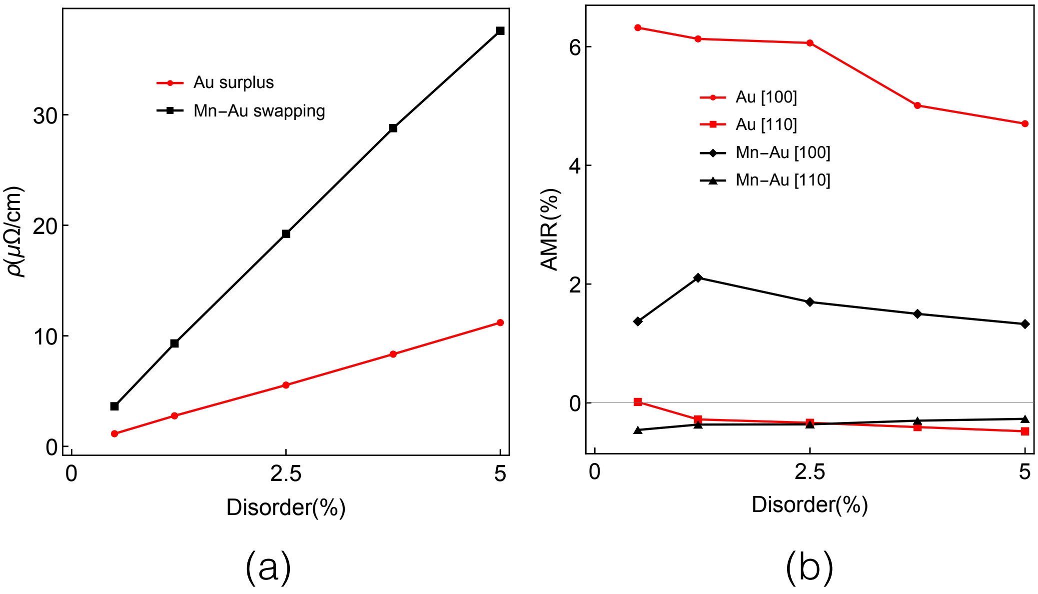

Figure 3.10: **Calculated resistivity and anisotropic magnetoresistance (AMR) in Mn_2Au alloys.** (a) Calculated residual resistivities due to Au excess and due to Mn - Au site swapping. (b) Calculated AMR due to Au excess and due to Mn - Au site swapping and dependence on the Néel vector orientation.

Bloch spectral functions is justified in our calculations since the vertex corrections turned out to be negligible in our calculations, and the disorder strength seems to only smear out the energy bands and does not produce additional bands for the Au-rich disorder, as we see by comparing Figs. 3.9(a) and 3.12. We see that the Bloch spectral functions are anisotropic and crystal momentum dependent.

Fig. 3.12(b-c) show the redistribution of spectral weight at the Fermi level along the $M - \Gamma$ line. Within this simplified picture, the sharper spectral weight along the electron's velocity direction can, in turn, increase the relaxation time and the conductivity. The sharper Bloch spectral weight for $\mathbf{E} \perp \mathbf{N}$ than $\mathbf{E} \parallel \mathbf{N}$ is consistent with $\sigma(\mathbf{E} \perp \mathbf{N}) > \sigma(\mathbf{E} \parallel \mathbf{N})$ and a positive sign of AMR. This effect can be explained by sensitivity of the Bloch spectral weight at the Fermi level to the redistribution of Bloch spectral function in the Fermi sea where the disordered band hybridization at a band-crossing is avoided ($\mathbf{E} \parallel \mathbf{N}$) or unavoided ($\mathbf{E} \perp \mathbf{N}$). The large AMR is thus a consequence of the convolution of (i) an intrinsic effect of energy bands sensitivity to the Néel vector reorientation in the Fermi sea, and (ii) its propagation due to the nonmagnetic Au-rich disorder to the Fermi-level states.

We have seen the ultimate limit of this effect in orthorhombic CuMnAs, where this is related to the sensitivity of Dirac quasiparticle masses to symmetry changes due to the Néel vector rotation. We can thus consider the observed AMR in Mn_2Au as a precursor to an "intrinsic" (topological) AMR.

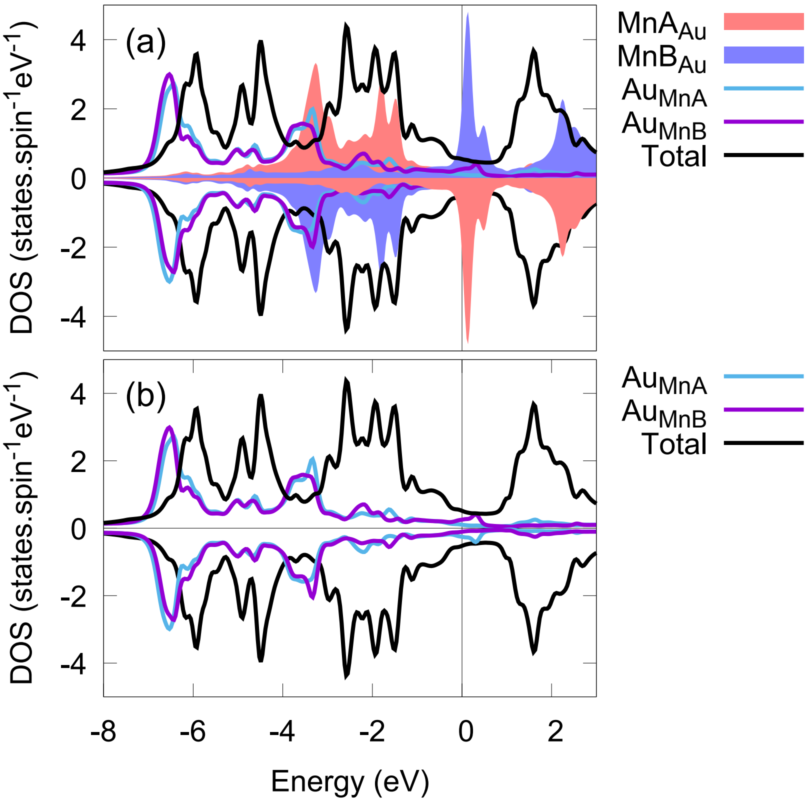

Figure 3.11: **Atom and spin resolved density of states (DOS) of Mn_2Au alloys.** (a) DOS for 0.5% Mn - Au swapping. The red and blue states around Fermi level are the virtual bound state in the Mn on Au (total) DOS. (b) DOS for 0.5% excess of Au on Mn-sites.

3.9 Summary: *intrinsic* anisotropic magnetoresistance

Dirac quasiparticle antiferromagnet CuMnAs. In this chapter, we have identified a realistic material candidate for a topological phase of matter in the form of an antiferromagnetic three-dimensional DSM. We have analysed its non-symmorphic symmetry protection and we have shown that the system hosts also relativistic metal-insulator transition. Recent experimental studies of the orthorhombic CuMnAs crystals show the importance of the stoichiometry in the CuMnAs phases [173, 189] and are not conclusive about the observation of the massless Dirac fermions. Instead, small band-gaps and low mobility massive fermions have been observed, possibly due to the undesirable easy axis direction [218, 219]. Alternative materials to study are $EuCd_2As_2$[70, 220] and FeSn kagome antiferromagnet [221]. Two-dimensional Dirac fermions were reported by DMFT study in antiferromagnetic $BaFe_2As_2$ [222].

Antiferromagnetic anisotropic magnetoresistance. The understanding of spontaneous AMR is conventionally understood entirely in terms of anisotropic scattering rates or velocities which produces a small

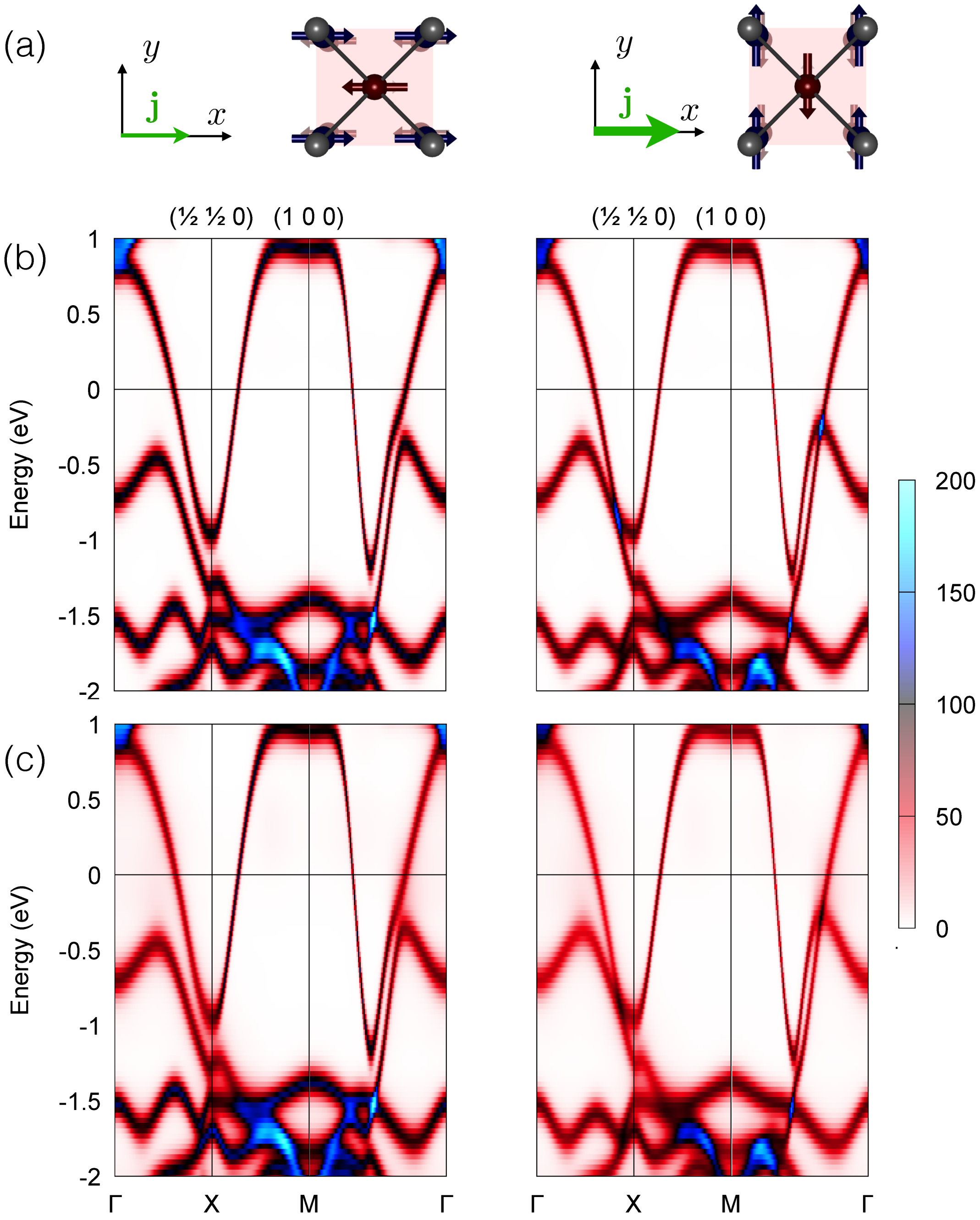

Figure 3.12: **Bloch spectral function in Au-rich Mn_2Au alloys.** Left/right column of panels corresponds to the Néel vector $\mathbf{N}$ along [100]/[010] crystal axis. (a) The conductivity relation $\sigma_{xx}(\mathbf{N} \parallel [010]) > \sigma_{xx}(\mathbf{N} \parallel [100])$ is marked by the green arrows. Bloch spectral function along high symmetry lines for (b) 0.5%, and (c) 5% of Mn surplus on Mn-sites.

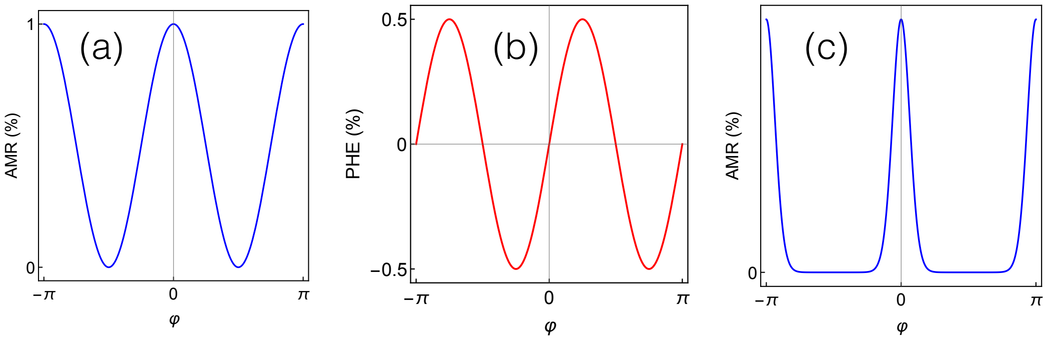

Figure 3.13: Schematics of angular dependencies of (a) non-crystalline anisotropic magnetoresistance, (b) corresponding planar Hall effect, and (c) intrinsic anisotropic magnetoresistance from relativistic metal-insulator transition due to the antiferromagnetic Dirac fermions.

(maximum of a few per cent) signals. This was part of the reason why the effect - once causing a revolution as a new read-out mechanism in hard-drives - was in the 1990s substituted by orders of magnitude larger giant magnetoresistance.

Here we have shown that the AMR has also a previously overlooked ”intrinsic” mechanism originating from the sensitivity of the band structure symmetry on the Néel vector orientation. The effect is enhanced close to the band-touching. This allows us to predict two contributions to AMR:

- The ultimate (gigantic) limit of ”intrinsic” AMR corresponding to the relativistic metal-insulator transition. The effect originates from $\mathcal{PT}$ symmetric antiferromagnetic Dirac fermions at the Fermi level. We identify a realistic material candidate: the orthorhombic CuMnAs antiferromagnet.

- Scattering rate renormalization propagated from the anisotropy of the band-touchings in the Fermi sea. The sensitivity of band touchings to the Néel vector orientation is captured by magnetic symmetries as long as the nonmagnetic (magnetic) random substitutional (or e.g. symmetric phonon) disorder preserves the magnetic symmetry group. We have seen this contribution in Mn_2Au Bloch spectral calculations.

AMR can be detected in patterned Hall bar devices in the longitudinal or transversal resistivity. When the **non-crystalline AMR** (magnetization with respect to current direction) is the leading contribution, a cosine square dependence in the longitudinal channel is expected and we show a schematic angular dependence in Fig. 3.13(a). AMR can be measured also in the corresponding transversal resistivity $\rho_{xy} = \Delta\rho_L \sin\phi\cos\phi$ which is odd in the mutual angle of magnetization and current direction as we see in Fig. 3.13(b). This AMR is sometimes called planar Hall effect, however, it does not transform under magnetic field as the odd Hall

AMR sign	Magnetic material
$\rho_L(\mathbf{m} \parallel \mathbf{j}) > \rho_L(\mathbf{m} \perp \mathbf{j})$	NiCo (Fe [152]), CuMnAs(150 K[103]),Mn_2Au[104]
$\rho_L(\mathbf{m} \parallel \mathbf{j}) < \rho_L(\mathbf{m} \perp \mathbf{j})$	NiMnSb (GaMnAs[205]), CuMnAs(300 K[103])

Table 3.10: Anisotropic magnetoresistance signs in ferromagnets and antiferromagnets.

effect, but is even in field (magnetic moment). Our prediction of large AMR in Mn_2Au was likely verified in the current induced experiments on Au-rich Mn_2Au alloys. The theoretical and experimental values are in striking correspondence, indicating indeed the topology/symmetry origin of this large AMR even in alloyed disordered crystals.

We also list the sign of AMR in several topical antiferromagnets in Tab. 3.10. Finally, the intrinsic AMR from the relativistic metal-insulator transition is manifested in the form of spikes (see Fig. 3.13(c)) corresponding to the conductive Dirac channels, as was found for the Dirac quasiparticle antiferromagnet [27], and later also for Weyl magnetic junctions [223]. This **intrinsic AMR** can be seen as the ultimate limit of the crystalline AMR which does depend on the crystalline orientation and symmetry. Signatures of crystalline AMR were observed in MnTe antiferromagnet [198]. More detailed studies, for instance, the dependence of the AMR on the crystallinity and disorder in magnetic fields, will in the future provide stronger links between the experiment and theory. In any case, our relativistic metal-insulator transition is particularly favourable for new topological relativistic quantum read-out technologies, including the topological antiferromagnetic transistor. Since antiferromagnets with large AMRs are serendipitously also good materials for current-induced switching by the Néel spin-orbit torques or electrical gating, this mechanism can be used to switch between the topological Dirac metal and insulator phases via Néel vector rotations.

4. Spontaneous Hall effect from collinear antiferromagnetism

"Creativity is just connecting things. When you ask creative people how they did something, they feel a little guilty because they didn't really do it, they just saw something."

Steve Jobs

The net motion of an electron in solid commonly follows the direction of the applied electric field. The electrons can acquire transversal component of their movement in an applied magnetic field, this ordinary Hall effect was discovered in 1879 [224]. In 1881 [225], Hall also measured order of magnitude stronger effect in ferromagnets. The appearance of this transversal voltage in certain magnets in the vanishing applied magnetic field is known as the spontaneous Hall effect [226, 227], also called anomalous [65] or extraordinary [228]. The Hall voltage can be measured across Hall bar microdevices, schematically illustrated in Fig. 4.1(a). An external magnetic field flux $\boldsymbol{B} = \mu_0 \mathbf{H}$ is applied to orient the magnetic domains and the spontaneous Hall resistivity can be determined from the Hall hysteresis shown schematically in Fig. 4.1(b) after subtracting the ordinary Hall effect linear in $\mathbf{H}$ from the phenomenological expression:

$$\rho_H = R_H \mathbf{H} + R_S \mathbf{M}. \tag{4.1}$$

While phenomenologically the spontaneous Hall term is often taken as proportional to magnetization in ferromagnets or canted antiferromagnets, the spontaneous Hall effect, in general, does not have to scale linearly with magnetization $\mathbf{M}$. Different microscopic mechanisms were discovered in (i) systems without dipolar fields (antiferromagnetic spin-liquid candidates) [229], (ii) complex magnetization (skyrmionic) textures [230], or (iii) non-collinear antiferromagnets [231, 232].

In certain non-collinear antiferromagnets an additional Hall resistivity arises:

$$\rho_H = R_H \mathbf{H} + R_S \mathbf{M} + \rho_{AF}. \tag{4.2}$$

The typical Hall hysteresis loop is shown in Fig. 4.1(b). A $\mathrm{Mn_3Sn}$ antiferromagnetic crystal unit cell is shown in the inset of Fig. 4.1(b) and exhibits ferromagnetic MPG. This can be seen by recognizing that when we tilt the moments towards the [100] direction to obtain a net ferromagnetic moment, the symmetries of the crystal (e.g. mirror symmetry $\mathcal{M}_x$) do not change.

The works on the non-collinear antiferromagnets have shown that the large Hall conductivity is produced by the asymmetry between left-and right-handed electrons deflected due to the non-collinear antiferromagnetic energy bands [105, 231, 232]. In contrast, the spontaneous Hall effect in collinear antiferromagnets has been commonly implicitly [233] or explicitly [234, 235] anticipated to vanish. Certainly, in collinear antiferromagnets with Kramers spin-degenerate bands, this compensation is enforced by an effective antiferromagnetic time-reversal symmetry (e.g. $\mathcal{PT}$), and the spontaneous Hall effect is forced to vanish. We show

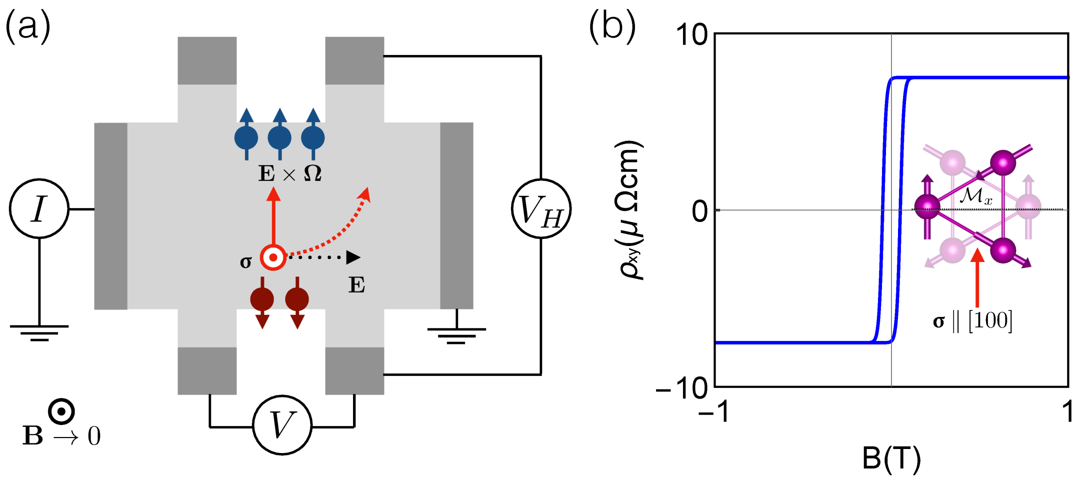

Figure 4.1: (a) A Hall bar set-up geometry, and (b) a schematic Hall hysteresis loop in a non-collinear antiferromagnet. The Hall vector is marked in panels as $\boldsymbol{\sigma}$.

in this chapter that we can find a previously overlooked spontaneous Hall effect mechanism arising from low symmetric local magnetization isosurfaces around globally perfectly compensated antiferromagnetic atoms. This asymmetry arises due to the intercalated nonmagnetic atoms in combination with collinear antiferromagnetism [116].

4.1 Symmetry classification of Hall vectors from antiferromagnetism

Similarly as in the case of AMR or NSOT, the existence of the spontaneous Hall effect is determined by symmetry transformations. According to Tab. 4.1, the spontaneous Hall tensor is an antisymmetric rank-two tensor which is equivalent to an axial (pseudovector) **Hall vector**

$$\boldsymbol{\sigma} \sim \mathbf{E} \times \mathbf{j}_H \tag{4.3}$$

with components $\sigma_x = \epsilon_{\mu\nu x}\sigma_{\mu\nu}$, where $\epsilon_{\mu\nu x}$ is Levi-Civita antisymmetric tensor.

We see that the Hall conductivity is dissipationless since Joule heating is proportional to $\mathbf{j}\cdot\mathbf{E}$ and is given only by the symmetrical part of the conductivity tensor. For the $(\mathbf{E}\times\mathbf{j}_H)\cdot\mathbf{E}$ as measuring the volume spanned by the three vectors is zero. We will start by enumerating symmetries which exclude the Hall vector and we illustrate examples in Fig. 4.2.

1. *Effective antiferromagnetic $\mathcal{T}$-symmetry*, $\mathcal{T}_{\mathrm{AF}}$, in the type-II MPG prohibits an odd under $\mathcal{T}$ Hall pseudovector $\boldsymbol{\sigma}$. Examples from this family are the well-explored collinear metal antiferromagnets FeRh or GdPtBi (see Fig. 4.2(a)) [114, 236], invariant under the $\mathcal{T}\mathbf{t}_{\frac{1}{2}}$ space group operation where $\mathbf{t}_{\frac{1}{2}}$ is the half-unit cell translation. (Berry curvature does not have to be zero when the inversion symmetry is broken, but the Brillouin zone Berry curvature integral vanishes, as we have described in Chapter 1.)

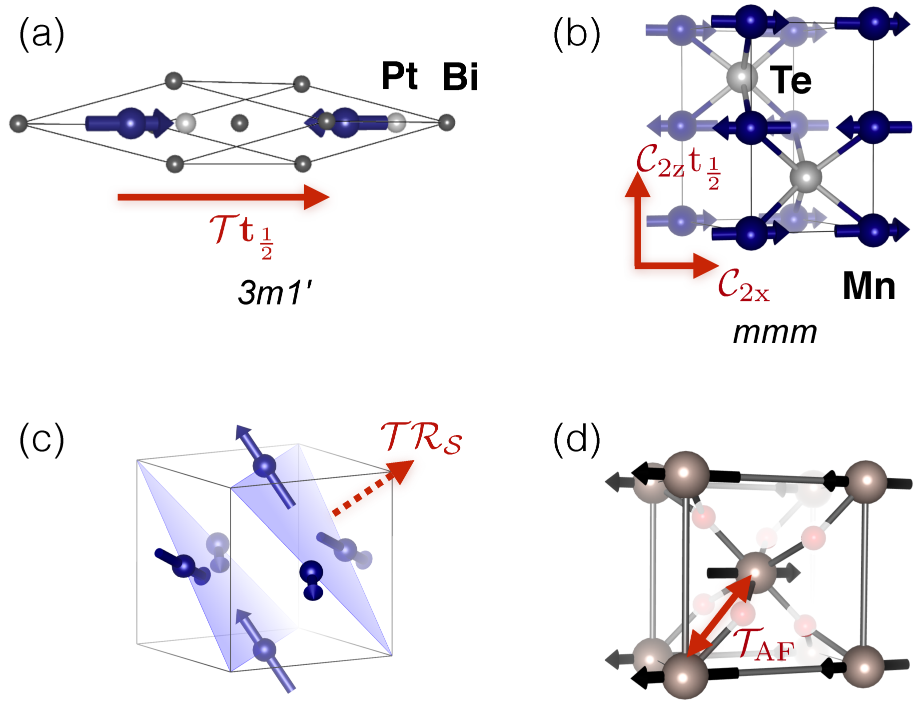

Figure 4.2: **Type of symmetries preventing spontaneous Hall conductivity in antiferromagnets.** (a) $\mathcal{T}\mathbf{t}_{\frac{1}{2}}$-symmetric GdPtBi. (b) Multiple rotational (mirror) symmetries in MnTe with moments along [100] axis. (c) The effective spin rotational symmetry $\mathcal{T}\mathcal{R}_{\mathcal{S}}$ in certain coplanar magnets without SOC prohibits spontaneous Hall effect in the non-collinear antiferromagnets of Mn_3Ir type with switched-off SOC. (d) Hidden effective antiferromagnetic time-reversal symmetry when the electronic structure allows to neglect the effects of the nonmagnetic atoms in rutile crystal, e.g. NiF_2 [184].

2. *Effective antiferromagnetic* symmetry, $\mathcal{T}_{\mathrm{AF}}$, which preserves Kramers theorem. There are type-III and type-II MPGs which do not only exclude $\boldsymbol{\sigma}$ but also enforce vanishing Berry curvature identically. These are systems fulfilling the antiferromagnetic Kramers theorem: examples are CuMnAs and Mn_2Au discussed in detail in the previous chapter belong to the $\mathcal{P}\mathcal{T}$-symmetric MPGs prohibiting $\boldsymbol{\sigma}$.

3. Hall vector $\boldsymbol{\sigma}$ can be excluded by multiple spatial symmetries (unitary or antiunitary) in the Type-I or Type-III MPGs. Here an example is mutually orthogonal multiple rotational or mirror symmetries as occurring, e.g., in RuO_2 with the Néel vector along the [001] crystal axis or MnTe with the Néel vector along [100] shown in Fig. 4.2(b).

4. *Spin space group symmetries.* In (certain) coplanar antiferromagnets without SOC (which can be described by the spin space groups [184]), we can have the effective time-reversal symmetry $\mathcal{T}\mathcal{R}_{S}$ combining time reversal with spin rotation [63] as we show in Fig. 4.2(c). As a consequence, collinear ferromagnets and antiferromagnets and non-collinear co-planar antiferromagnets require the relativistic SOC to generate a nonzero Hall vector.

An example is non-collinear antiferromagnet $\mathrm{IrMn_3}$ with neglected SOC, or organic antiferromagnets with a vanishing SOC.

5. Another possibility is an antiferromagnet with *effectively* higher symmetries than its magnetic symmetry group. If the low energy states are well separated in energy from the rest of the electronic structure the low energy Hamiltonian can have higher symmetry than the original crystal. An example could be $\mathrm{NiF_2}$ with negligible effect of F atoms [184] shown in Fig. 4.2(d).

The last two possibilities can be thought of as an effective or ”hidden” symmetries when there are additional constraints on the Hamiltonian of the system.

In summary, 19 out of 32 Type-I, all 32 Type-II, and 40 out of 58 Type-III MPGs exclude the existence of the Hall pseudovector $\boldsymbol{\sigma}$. Any system which materializes in one of the remaining 31 MPGs [26, 237] allows for $\boldsymbol{\sigma}$ and, therefore, is a candidate material for a spontaneous Hall effect. Now we will classify all the possible antiferromagnetic order and crystal symmetries allowing for the spontaneous Hall effect. The shape of the conductivity tensor and its antisymmetric part can be for a given crystal determined by the Neumann principle [66, 238, 239]. According to the principle *”the symmetry of any physical property of a crystal must include the symmetry elements of the point group of the crystal.”* [238, 239]

At zero temperature we can derive from the linear response Kubo formula (1.53) the following transformation properties [97, 240]:

$$\sigma_{\mu\nu}(\mathbf{H}) = \sum_{kl} \sigma_{kl}(\mathbf{H}) D_{k\mu}(P_R) D(P_R)_{l\nu}, \tag{4.4}$$

$$\sigma_{\mu\nu}(-\mathbf{H}) = \sum_{kl} \sigma_{lk}(\mathbf{H}) D_{k\mu}(P_R) D(P_R)_{l\nu}. \tag{4.5}$$

First equation holds for the unitary, and second for the antiunitary operations, respectively. $D_{\mu\nu}$ are three-dimensional matrices representing the rotational and translation part. We used the fact that $D_{\mu\nu}$ are real and $\mathbf{H}$ is a pseudovector. Furthermore, we can write for improper rotations $R = \mathcal{P}P_R$: $D(R) = \det(D(R))D(P_R)$, where P_R denotes the proper rotation. And since in the conductivity response function the determinant factor appears twice its second power always gives unity. We can thus study only magnetic Laue group (MLG), which substantially decreases the number of symmetry groups to consider from 122 to 32. For the derivation of the shape of the conductivity tensor it is enough also to use the generating elements of the group only. That follows from the closure property of the symmetry group.

We list the 31 MPGs [66, 237, 243] allowing for a spontaneous Hall effect in Tab. 4.1. We sort the MPGs into the two main columns depending on whether they are globally noncentrosymmetric or not. Note that the corresponding 10 magnetic Laue groups (centrosymmetric) contain complete information about the possible shapes of the conductivity tensor. We list also the direction of the allowed Hall vector $\boldsymbol{\sigma}$ orientations, and exemplary materials. The collinear and non-collinear antiferromagnets or ferrimagnets (the latter two types are marked in italic in Tab. 4.1) are taken from the MagnDATA database [244, 245] or from the listed references.

Centrosymmetric		Noncentrosymmetric		Material	Tensor
MPG	$\boldsymbol{\sigma}$	MPG	$\boldsymbol{\sigma}$		
$\bar{1}$	arb.	$\mathbf{1}$	arb.	Fe_2O_3 *Mn_2FeSbO_6* Cr_2S_3	$\begin{pmatrix} \sigma_{xx} & \sigma_{xy} & \sigma_{xz} \\ \sigma_{yx} & \sigma_{yy} & \sigma_{yz} \\ \sigma_{xz} & \sigma_{zy} & \sigma_{zz} \end{pmatrix}$
$2/m$	$\parallel \mathbf{a}_{\mathcal{C}_2}$ $\perp \mathcal{M}$	$\mathbf{2}$ m	$\parallel \mathbf{a}_{\mathcal{C}_2}$ $\perp \mathcal{M}$	$BiCrO_3$ MnTe[198] $LiFeP_2O_7$	$\begin{pmatrix} \sigma_{xx} & 0 & \sigma_{xz} \\ 0 & \sigma_{yy} & 0 \\ \sigma_{xz} & 0 & \sigma_{zz} \end{pmatrix}$
$\bar{3}$ $4/m$ $6/m$	$\parallel \mathbf{a}_{\mathcal{C}_2}$	$\mathbf{3}\ \mathbf{4}\ \mathbf{6}\ \bar{4}\ \bar{6}$	$\parallel \mathbf{a}_{\mathcal{C}_2}$	*Mn_3NiN* *Mn_3CuN*	$\begin{pmatrix} \sigma_{xx} & \sigma_{xy} & 0 \\ -\sigma_{xy} & \sigma_{xx} & 0 \\ 0 & 0 & \sigma_{zz} \end{pmatrix}$
$2'/m'$	$\perp \mathbf{a}_{\mathcal{T}\mathcal{C}_2}$ $\in \mathcal{T}\mathcal{M}$	$\mathbf{2'}$ m'	$\perp \mathbf{a}_{\mathcal{T}\mathcal{C}_2}$ $\in \mathcal{T}\mathcal{M}$	$CaMnO_3$[241] $MnTiO_3$ Mn_5Si_3[234]	$\begin{pmatrix} \sigma_{xx} & \sigma_{xy} & \sigma_{xz} \\ -\sigma_{xy} & \sigma_{yy} & \sigma_{yz} \\ -\sigma_{xz} & -\sigma_{yz} & \sigma_{zz} \end{pmatrix}$
$m'm'm$	$\parallel \mathbf{a}_{\mathcal{C}_2}$ $\perp \mathcal{M}_z$	$\mathbf{2'2'2}\ m'm'2$ $m'm2'$	$\parallel \mathbf{a}_{\mathcal{C}_2}$ $\perp \mathcal{M}_y$	RuO_2[242] $CoNb_3S_6$[235] $LaMnO_3$	$\begin{pmatrix} \sigma_{xx} & \sigma_{xy} & 0 \\ -\sigma_{xy} & \sigma_{yy} & 0 \\ 0 & 0 & \sigma_{zz} \end{pmatrix}$
$\bar{3}m'$ $4/m'm'm$ $6/m'm'm$	$\parallel \mathbf{a}_{\mathcal{C}_n}$	$\mathbf{42'2'}\ 4m'm'\ \bar{4}2'm'$ $\mathbf{32'}\ 3m'\ \mathbf{62'2'}$ $6m'm'\ \bar{6}m'2'$	$\parallel \mathbf{a}_{\mathcal{C}_n}$	*Mn_3Pt*	$\begin{pmatrix} \sigma_{xx} & \sigma_{xy} & 0 \\ -\sigma_{xy} & \sigma_{xx} & 0 \\ 0 & 0 & \sigma_{zz} \end{pmatrix}$

Table 4.1: **Catalogue of Hall-vector admissible magnetic point groups and collinear/non-collinear antiferromagnets examples.** First three rows list Type-I, and last three rows Type-III magnetic point groups, respectively. Notation of rotational axes and mirror planes is the same as in the main text. $\in \mathcal{M}$ marks Hall-vector lying in the mirror plane $\mathcal{M}$, $\in \mathcal{T}\mathcal{M}$ marks Hall vector in the antiunitary mirror plane (mirror plane coupled with time-reversal symmetry $\mathcal{T}$), **a** marks the axis of the rotational symmetry (twofold or n=3,4,6), and ”arb.” marks an arbitrary orientation of the Hall vector. Magnetic Laue groups are printed in bold font.

Furthermore, the collinear antiferromagnetism with allowed small canting cannot be found in crystals with 3-, 4-, and 6- fold symmetry operations. This leaves us with 12 weak ferromagnetic MPGs and corresponding 4 MLGs [246, 247]. These are the only symmetry groups where the simple collinear antiferromagnets allowing for the spontaneous Hall effect can crystallize in. All of the 31 ferromagnetic point groups are compatible also with ferromagnetism, ferrimagnetism, and non-collinear or non-coplanar antiferromagnetism. In the MagnDATA database, the most common MPG allowing for a Hall vector is the $m'm'm$. This symmetry class is also compatible with collinear antiferromagnetism. This demonstrates the possibility to search for a large spontaneous Hall effect within the abundant class of robust collinear antiferromagnets.

From Tab. 4.1 we can also conclude that in the low symmetry groups the Hall vector and net magnetization (or just the direction of the allowed but zero *ghost* magnetization) does not have to be parallel, as pointed out in the early work on spontaneous Hall effect [248]. Namely in the MPG groups 1 and $\bar{1}$, the orientation of the Hall vector is arbitrary, while in the MPG groups $2'/m'$, $2'$, and m' the Hall vector is constrained to be perpendicular to a given antiunitary rotation axis or lie within given antiunitary mirror plane. We note that this non-collinearity among the Hall vector and magnetization is realised also in conventional elemental ferromagnets when the magnetization is rotated off the high symmetry crystal axis

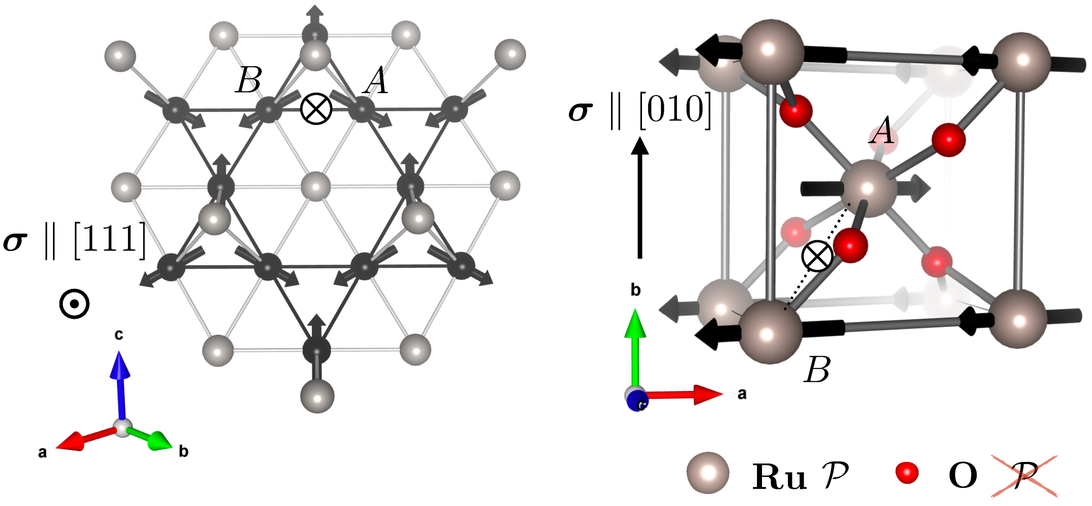

(a) (b)

Figure 4.3: **Dzyaloshinskii-Moriya weak ferromagnetic antiferromagnets.** (a) Kagome lattice found in the (111) planes of the cubic non-collinear antiferromagnets of Mn_3Ir type with marked noncetrosymmetric AB midpoint and net magnetization $\mathbf{M} \parallel [111]$. (b) Rutile crystal of RuO_2 type with collinear antiferromagnetism and the noncetrosymmetric AB midpoint due to the O atom.

as was confirmed in *ab initio* calculation [249]. In the remaining 26 MPGs, the Hall vector is constrained to point along a certain direction in the crystal. Here a special case is high symmetry ferromagnets where the Hall vector is parallel to magnetization:

$$\mathbf{j}_H \sim \mathbf{E} \times \mathbf{M}. \tag{4.6}$$

Kleiner [97] discussed the possibility to derive the Onsager relations in certain magnetic groups. Usually, the Onsager relations generalised for magnetic systems are stated in the form, [250, 251, 252]:

$$\sigma_{ij}(\mathbf{H}, \mathbf{S}) = \sigma_{ji}(-\mathbf{H}, -\mathbf{S}). \tag{4.7}$$

where the conductivity tensor depends on an external magnetic field $\mathbf{H}$, and the internal spin arrangement $\mathbf{S}$. However, our prediction of the crystal Hall effect due to the complex crystal structure emphasizes that in general, the symmetries of complete magnetisation density needs to be considered. There have been attempts to characterize certain complicated magnetic densities by the cluster multipole order which can be used instead of magnetization or spin ordering [63, 98]. The local magnetization can be obtained by projecting the magnetization density on atoms in DFT calculations. However, during this process, the shape of the magnetization density can be lost [63]. While in certain cases it turns out useful to neglect the complications from nonmagnetic atoms and discuss the magnetic subsystem only (as e.g. by using spin space groups spin waves in rutile structures [184]), this description is in general incomplete, as will be manifested in the crystal Hall conductivity calculations.

Dzyaloshinskii-Moriya antiferromagnets

In Tab. 4.1 we list also materials and we see that the non-collinear antiferromagnets of the Mn_3Pt type belong to one of the 19 MPGs which are not compatible with collinear antiferromagnetism. Weak ferromagnetism (WFM) usually refers to the canted collinear antiferromagnetic state. However, the non-collinear antiferromagnets allowing for the net magnetization can be also canted.

Symmetry breaking allowing for a net magnetic moment in antiferromagnetic systems can be generated by the DMI which can be nonzero when there is no inversion centre between two magnetic sublattices [253]. Microscopically, DMI can originate from two mechanisms. First, Moriya [254] added the spin-orbit interaction to the Anderson superexchange perturbation theory explaining phenomenological canting terms linear in relativistic corrections commonly applied to insulating antiferromagnets such as Fe_2O_3 or NiF_2. Second, Smit [255] and Fert [256] considered a RKKY type of interaction arising in metallic systems with magnetic moments interlaced by nonmagnetic atoms at noncetrosymmetric positions. Dzyaloshinskii[257] suggested that the canted effect can be captured by the magnetic Hamiltonian:

$$H = -\frac{1}{2}\sum_{a,b=1}^{n} J_{ab}\vec{S}_a\vec{S}_b - \frac{1}{2}\sum_{a,b=1}^{n} \vec{S}_a\boldsymbol{D}_{ab}\vec{S}_b - \sum_{a=1}^{n} \vec{S}_a\boldsymbol{K}_a\vec{S}_a. \tag{4.8}$$

The first term represents the isotropic Heisenberg exchange, the second term is the two-site exchange anisotropy, and the last term is the single ion anisotropy.

For the $PtMn_3$ crystal we have $D' = D_{12} = D_{23} = D_{31}$, and $D = D_{11} = D_{22} = D_{33}$ [258]. DMI arises since the kagome lattice lacks inversion centre between two magnetic atoms[259] (as we illustrate in Fig. 4.3(a)). Phenomenologically, DMI takes a complicated form in this crystal [260]. A rigid rotation of the triangular order in the (111) plane can be parametrised by a single angle ϕ [258, 261]. The magnetocrystalline energy takes for this rotation a simple form [258]:

$$E(\phi) = \left(2K + \frac{3}{2}(D + D')\right)\sin^2\phi, \tag{4.9}$$

where K is the on-site anisotropy, and D (D') is the symmetric (antisymmetric) part of the two-site anisotropy tensor defined above. The rotation of the triangular order by 90 degrees corresponds in the $IrMn_3$ to a high anisotropic energy barrier of 10.42 meV [258] and we calculate comparable value 8.96 meV (by our FRD-TB-LMTO method for $n_k = 28^3$ sampling points). These large magnetic anisotropies (and corresponding excessive spin-flop fields) are presumably the reason why the spontaneous Hall effect was not observed in $IrMn_3$ so far [262], but rather in $PtMn_3$ [263].

In the collinear rutile antiferromagnets (see Fig. 4.3(b)) with the Néel vector $\mathbf{N}$ along [100] and an allowed (perturbatively) weak ferromagnetic moment $\mathbf{M}$, the lower orders in energy expansion take a form [264, 265, 246]:

$$E(\mathbf{N},\mathbf{M}) = \frac{A}{2}\mathbf{M}^2 + \frac{a}{2}N_z^2 + \frac{b}{2}M_z^2 + d\left(N_xM_y + N_yM_x\right), \tag{4.10}$$

where the first term is an isotropic exchange. The remaining terms are of relativistic origin and the last term is the DMI. The relativistic origin means that

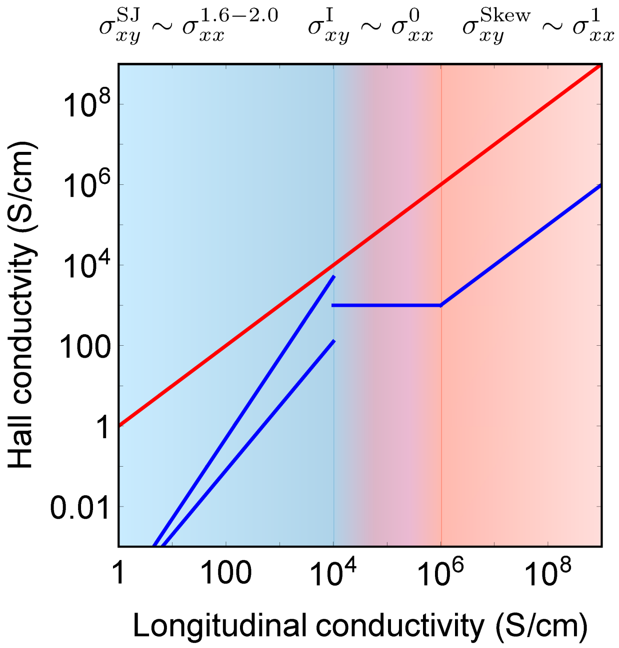

Figure 4.4: **Extrinsic and intrinsic contribution scaling.** Three different regimes (blue lines) of spontaneous Hall effect and the corresponding phenomenological scaling vs longitudinal conductivity. The red line corresponds to the Hall angle of unity.

the net moment due to the canting is of the $\frac{v}{c^2}$ order [264]. Our *ab initio* total energy calculations in VASP in RuO_2 give $E_{[001]} - E_{[100]} = 5.35$ meV and $\mathbf{M} = 0.05\mu_B \sim \frac{|d|}{A} \sim \frac{v}{c^2}$ per unit cell (two magnetic Ru atoms).

4.2 Microscopic spontaneous Hall effect mechanisms genealogy

In the previous section, we discussed the symmetry condition allowing for the spontaneous Hall conductivity in antiferromagnets. Here we discuss the possible microscopic mechanisms determining the magnitude and, in low symmetry cases, also the orientation of the Hall vector. The controversial history of the spontaneous Hall effect is reviewed, for instance, by Nagaosa et al. [65]. Here we will list the main milestones leading to the recognition of the spontaneous Hall effect as a Fermi liquid topological property captured by the Berry phase [51, 52, 54] in the intrinsic regime, corresponding to the intermediate longitudinal conductivities shown in Fig. 4.4 .

In the conventional picture of the (spontaneous) anomalous Hall effect (AHE) in ferromagnets, the Hall voltage arises due to the asymmetry of left-right scattered electrons [65]. Microscopically, this asymmetry is commonly attributed to the combined effect of ferromagnetic spin-polarization and SOC [152]. While the former breaks $\mathcal{T}$ symmetry, the latter adds breaking of the effective time-reversal symmetry ($\mathcal{T}\mathcal{R}_S$ [54]), namely a symmetry operation which combines time-reversal with spin rotation [63].

The identified contributions include an extrinsic scattering related term and an intrinsic band structure effect which is expressed in terms of the Berry curvature of the occupied spectrum. The extrinsic contribution includes skew and side-jump scattering on the spin-orbit coupled impurities. Side-jump is associated to dominate the low longitudinal conductivity regime (weak hopping and in this regime we plot two blue lines bordering the possible scaling in Fig. 4.4) while skew-scattering dominates the high longitudinal conductivity regime. The latter diverges in the clean limit as can be seen for instance in our *ab initio* calculations in NiMnSb crystals [158]. In this limit, the skew-scattering Hall conductivity is proportional to the SOC energy and lifetime, and inversely proportional to the bandwidth [266]. Many works following the ideas of Smit [227] and Berger [267] focused on extrinsic contributions. Also, Kubo-formula approaches, including the CPA method presented in Chapter 2, were developed [200, 162]. This allowed for calculating the Hall conductivity from first principles in disordered metallic systems, recently also extended to finite temperature calculations with frozen phonons and magnons [158].

Intrinsic contribution mechanisms. The intrinsic contribution is present in the absence of any scattering, originates from the pure band structure and was originally controversially discussed by Karplus and Luttinger [228, 226]. Later in the 1980s when the research focused on the freshly discovered quantization of the Hall conductivity in strong magnetic fields, the relation of the quantized Hall conductivity to the Chern number was pointed out by Thouless and Streda [33, 56].

The concept of Berry curvature has been later applied to Bloch electrons in ferromagnetic metals. Before Jungwirth et al.[51] and Onoda et al.[268] works recognized the role of topological properties of wavefunctions in the theory of metallic spontaneous Hall effect, Sundaram and Niu [269] derived the anomalous contribution to the velocity of Bloch electrons. In this picture, the transport equation comprising the cross product of applied voltage and magnetization includes a Berry curvature vector:

$$\dot{\mathbf{r}} = \frac{1}{\hbar}\frac{\partial \mathcal{E}_{n\boldsymbol{k}}}{\partial \mathbf{k}} - \dot{\boldsymbol{k}} \times \boldsymbol{\Omega}_n(\boldsymbol{k}). \tag{4.11}$$

Hall vector is thus microscopically determined by the Berry phase effects of Bloch electrons. This term can dominate in the intermediate conductivity regime relevant also for our antiferromagnetic systems. The band splitting due to SOC produce a transfer of Chern number among bands. These anticrossing then represent major contributions (*hotspots*) to the Berry curvature in the crystal momentum space. The 2D limit gives a contribution to the Hall conductivity from the anticrossing:

$$\frac{e^2}{h} = 3.87.10^{-5}\Omega^{-1}, \tag{4.12}$$

and in 3D the contribution is:

$$\frac{e^2}{ha} = 10^3\Omega^{-1}cm^{-1}, \tag{4.13}$$

when we choose lattice constant $a \approx 4\mathring{A}$[266].

We have seen in Chapter 1 that in the presence of broken $\mathcal{P}$, $\mathcal{T}$, or both symmetries adiabatic Berry phases arise in addition to conventional Fermi liquid theory. This conclusion was demonstrated in the case of Hall conductivity by Haldane in 2004 [52]. The Fermi sea formulation of Hall conductivity expression seems to be countering the Fermi liquid theory and pointing towards analogy to Landau diamagnetism theory. Haldane has recast the Hall conductivity formula

Year	Discovery description
1879	Hall effect in nonmagnetic systems [224]
1881	Spontaneous Hall effect without magnetic field [225]
1953	Intrinsic spin-orbit generated anomalous velocity [228]
1955	Side jump and skew scattering extrinsic mechanisms [226, 227, 267]
1980	Quantum Hall effect in strong magnetic fields [270]
1988	Haldane quantum anomalous model without magnetic field [62]
2002	Berry curvature in real materials and 2D models [51, 268]
1996	”Topological” Hall effect from spin chirality [271, 272]
2010	Spontaneous Hall effect without magnetic dipolar order [229]
2013	Quantum Hall effect in magnetised topological insulators at mK [273]
2014	Anomalous Hall effect in non-collinear antiferromagnets [105, 231, 232]
2018	Spontaneous Hall effect from collinear antiferromagnetism [116]

Table 4.2: Time line of Hall effect related discoveries.

to show that it is possible to reinterpret the formula as originating from topological quasiparticles at Fermi surface. A practical numerical scheme based on the covariant Berry curvature and Wannier functions was derived for the metallic cases with many entangled bands [10] as we have explained in Chapter 1 and 2.

Symmetry breaking mechanisms. Additional insight into the origin of the intrinsic spontaneous Hall effect was obtained by identifying different combinations of SOC and spin-polarization effects in energy bands. The observation of the spontaneous Hall conductivity of few S/cm in spin-liquid candidates with antiferromagnetic correlations [229] has demonstrated that no dipolar order is required for the nonzero spontaneous Hall conductivity. Predictions of the spontaneous Hall effect in non-coplanar antiferromagnets indicates the possibility of a spin-chirality origin of the Hall signal and no necessity for the relativistic SOC. The spontaneous Hall effect originating from the nontrivial magnetization textures is sometimes called a topological Hall effect and was identified also in skyrmionic textures.

The anomalous Hall effect in a magnetic field was observed also in nonmagnetic semimetal $ZrTe_5$ and its origin was attributed to the Weyl points generated from the Dirac cones by the external magnetic field [274]. Our discovery of the crystal Hall effect originating from collinear antiferromagnetism thus identifies arguably the minimal-complexity and robust antiferromagnetic order in the hierarchy of symmetry breaking mechanisms of the spontaneous Hall effect.

4.3 Spontaneous anomalous Hall effect in non-collinear antiferromagnets

Ab initio calculations predicted large spontaneous Hall conductivities in room-temperature non-collinear antiferromagnets $IrMn_3$ [105] and Mn_3Sn [275]. The predictions were shortly verified experimentally in Mn_3Sn [231], Mn_3Ge [232], and $PtMn_3$ [263]. The non-collinear antiferromagnet $PtMn_3$ has a Cu_3Au $L1_2$ crystal structure with a cubic high symmetry nonmagnetic space group $Pm\overline{3}m$ (number 221). Mn atoms form a kagome lattice in the (111) planes as we illustrate in

Fig. 4.3(a). Below the Néel temperature, this class of antiferromagnets can host several non-collinear antiferromagnetic phases [260]. When the antiferromagnetic order points towards the centre of triangles shown in Fig. (4.3)(a), the crystal has MSG $R\bar{3}m'$ and MPG $\bar{3}1m'$, respectively and we have listed the orientations of local quantization axes in Chapter 2.

The symmetry group allows for a ferromagnetic moment and the ferromagnetic nature of the group is preserved even in the perfectly compensated antiferromagnetic state. We can determine from our Tab. 4.1 the form of the conductivity tensor in the crystal frame of reference with the main axes along the crystal axis [100], [010], and [001]:

$$\sigma_{abc} = \begin{bmatrix} \sigma_{11} & \sigma_{12} & \sigma_{13} \\ \sigma_{13} & \sigma_{11} & \sigma_{12} \\ \sigma_{12} & \sigma_{13} & \sigma_{11} \end{bmatrix}. \tag{4.14}$$

According to our classification, the Hall vector is oriented along the [111] direction as we mark in Fig. 4.3(a). We can transform the tensor into the basis with main axes along [$\bar{1}$10],[$\bar{1}\bar{1}$2], and [111] crystal directions where the conductivity tensor takes a more familiar form:

$$\sigma_{xyz} = \begin{bmatrix} \sigma_{\parallel} & \sigma_H & 0 \\ -\sigma_H & \sigma_{\parallel} & 0 \\ 0 & 0 & \sigma_{\perp} \end{bmatrix}. \tag{4.15}$$

Here the components in the two bases are related as:

$$\sigma_H = \frac{\sqrt{3}}{2}\left(\sigma_{12} - \sigma_{13}\right), \tag{4.16}$$

$$\sigma_{\parallel} = \sigma_1 - \frac{1}{2}\left(\sigma_2 + \sigma_3\right), \tag{4.17}$$

$$\sigma_{\perp} = \sigma_{11} + \sigma_{12} + \sigma_{13}. \tag{4.18}$$

This also illustrates that there is an AMR with respect to the non-collinear antiferromagnetic order. The symmetric conductivity has in the second basis two different diagonal components $\sigma_{\parallel}$ and $\sigma_{\perp}$, where $\parallel$ ($\perp$) denotes currents flowing in (out-of) the plane of the triangular non-collinear antiferromagnetic order.

System	lattice (Å)	Hall conductivity (Scm^{-1})
$PtMn_3$	3.833	81 [263]
$IrMn_3$	3.772	172 ($n_{kz} = 512$), 218 [105]
$Ir_{1.12}Mn_{2.88}$	3.772	227 ($n_{kz} = 800$ Typhoon)
$Rh_{0.95}Pt_{0.05}Mn_3$	3.820	-133 ($n_{kz} = 128$ Tarkil)
$PtMn_3$ "AF"	3.833	0.0

Table 4.3: List of considered non-collinear antiferromagnets, used lattice constants of the cubic unit cell, and obtained Hall conductivity values with marked method/supercomputer and compared to existing literature. All but the last systems are in the magnetic "WFM" phase, the last one is in the "AF" phase.

The antiferromagnetic ordering in $PtMn_3$ is sometimes called WFM since it is also compatible with the existence of a tiny net magnetic moment obtained by tilting the moments towards the [111] direction due to the DMI, as explained in Section 4.1. The direction of the net moment is commensurate with the Hall vector orientation. The first-principle calculations in $IrMn_3$ and $PtMn_3$ demonstrate that the Hall conductivity can be sizeable 218 [105] and 81 [263] S/cm, respectively. This magnitude is comparable to the anomalous Hall effect elemental ferromagnets.

We summarize our and reported calculations in Tab. 4.3. We used TB-LMTO method to evaluate the Fermi surface (2.67) term in the non-collinear antiferromagnet $IrMn_3$ within the finite RTA with $\mathrm{Im}z$ up to 10^{-5} Ry, and we calculated also two types of random alloying disorder treated by the CPA. We tested Ir distributed over Mn sites ($Ir_{1.12}Mn_{2.88}$) and $Rh_{0.5}Pt_{0.5}Mn_3$ (Rh and Pt do have similar Wigner-Seitz radius and the possibility of this alloying was reported in literature [276]).

We will proceed by discussing the symmetry-breaking mechanism in the non-collinear antiferromagnets. The leading symmetry breaking in $PtMn_3$ and similar materials are generated by the non-collinear antiferromagnetic order. The Pt Wyckoff positions are centrosymmetric and the MSG does not change if we remove the Pt atoms from the $PtMn_3$ crystal. This justifies neglecting the nonmagnetic atoms in the magnetic multipole symmetry analysis of AHE order parameters [63]. Also since all the Wyckoff positions are centrosymmetric, the nonzero Berry curvature and thus Hall conductivity can be generated solely by the nontrivial non-collinear magnetic texture breaking time-reversal symmetry. We emphasize the similarities with the standard anomalous Hall effect in elemental ferromagnets. The SOC lifts, due to the DMI, the degeneracy between two magnetic states connected by the reversal of all local magnetizations and translates the symmetry breaking into the orbital sector [54, 63, 258].

The non-collinear antiferromagnetic order can be assigned chirality [258]:

$$\boldsymbol{\kappa} = \frac{2}{3\sqrt{3}} \left(\mathbf{S}_1 \times \mathbf{S}_2 + \mathbf{S}_2 \times \mathbf{S}_3 + \mathbf{S}_3 \times \mathbf{S}_1 \right) . \tag{4.19}$$

Rotating the triangular antiferromagnetic order within the (111) plane by 90 degrees changes the MSG (MPG) to an antiferromagnetic one $R\bar{3}m$ ($\bar{3}1m$) and there is no Hall conductivity as we list in Tab. 4.3. This illustrates the possibility to control the Hall signal not only by tuning among various antiferromagnetic order [263] but also by rotation of the non-collinear antiferromagnetic order.

4.4 Crystal anisotropic collinear antiferromagnetism in RuO_2

The spontaneous Hall effect in collinear antiferromagnets is in literature often anticipated to vanish. Rightfully so in the case when the system materializes in an antiferromagnetic MLG. The cancellation of the scattering or Berry curvature contributions from the opposite sublattices is enforced by the symmetry connecting the sublattice with opposite moments (e.g. $\mathcal{PT}$ or $\mathcal{T}\mathbf{t}_{\frac{1}{2}}$, where $\mathbf{t}_{\frac{1}{2}}$ is a half-unit-cell translation). We can thus ask ourselves whether we can find a perfectly compensated collinear antiferromagnet with allowed and sizeable spontaneous Hall signal. By interlacing the collinear moments with nonmagnetic atoms,

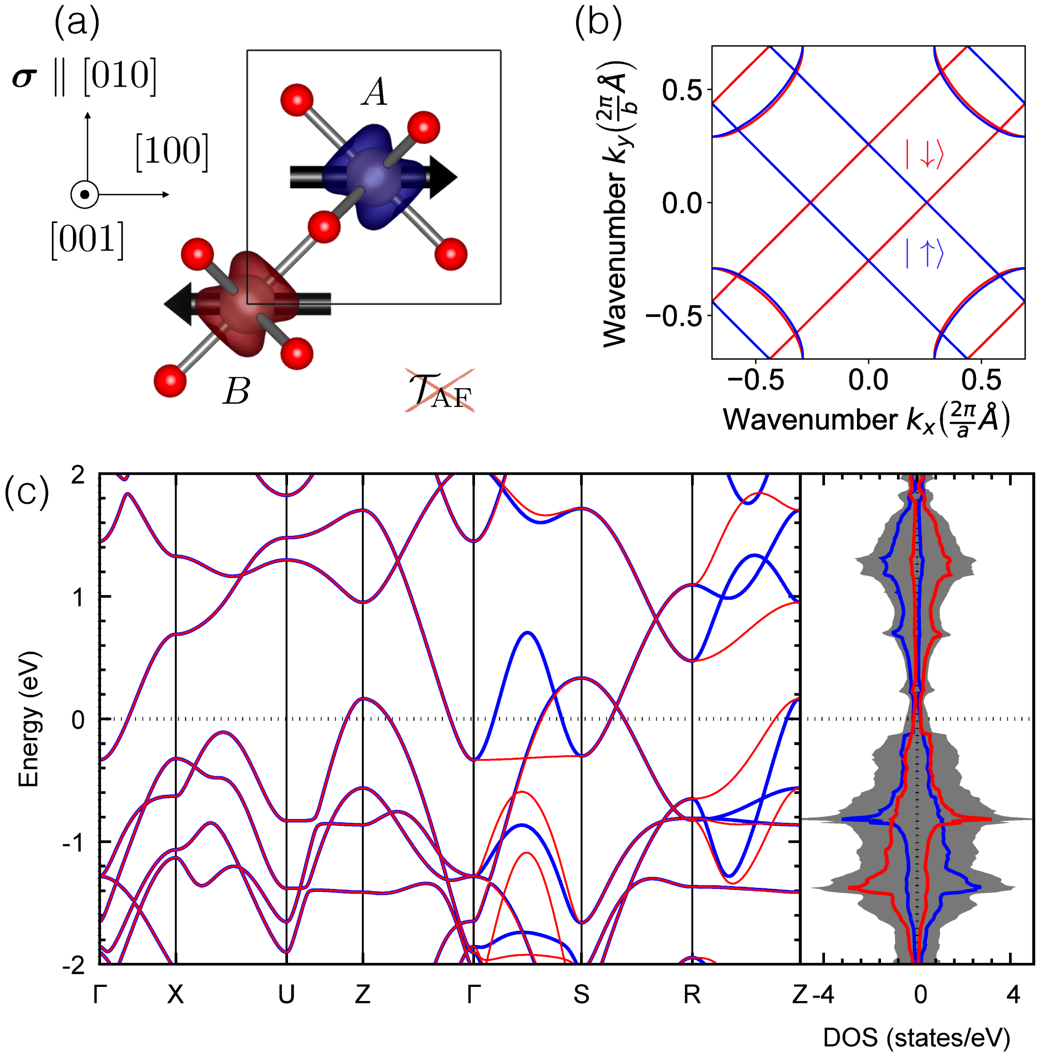

Figure 4.5: **Crystal symmetry breaking and electronic structure of $\mathbf{RuO_2}$ without SOC.** (a) Magnetization density isosurface are breaking antiferomagnetic sublattices $\mathcal{T}_{\mathrm{AF}}$ symmetry. (b) Fermi surface in the $k_z = 0$ plane. (c) Spin-resolved band structure.

we can break the $\mathcal{T}_{\mathrm{AF}}$ symmetry, as we show in Fig. 4.3(b), and Fig. 4.5(a) on the rutile antiferromagnet RuO$_2$. Collinear antiferromagnetism with the quantization axis along the [100] direction corresponds to the MSG $Pn'n'm$ (Type-III), magnetic point group (MPG) $m'm'm$, and MLG $2'2'2$. The symmetry generators are $\mathcal{P}$, glide mirror plane $\mathcal{M}_y\mathbf{t}$ ($\mathbf{t} = (\frac{a}{2}, \frac{a}{2}, \frac{c}{2})$), and an antiunitary rotation $\mathcal{T}\mathcal{C}_{2z}$. These symmetries also do not change when we cant the perfectly antiparallel magnetic moments towards the [010] direction. This illustrates the ferromagnetic nature of the symmetry groups even in a fully compensated antiferromagnetic state with the Hall vector: $\boldsymbol{\sigma} = (0, \sigma_{xz}, 0)$. This spontaneous symmetry breaking due to the crystal structure reflects the local crystal chirality,

$$\boldsymbol{\chi}_{AB}^{(C)} = \mathbf{d}_A \times \mathbf{d}_B. \tag{4.20}$$

The local crystal chirality appears due to the nonmagnetic atoms at the noncentrosymmetric positions, where $\mathbf{d}_A$ and $\mathbf{d}_B$ are vectors connecting two nearest-neighbour Ru atoms with the common interlaced O atom, as we have seen on the minimal tight-binding model in Fig. 1.12.

In the nonmagnetic state, the bands are Kramers degenerate due to the $\mathcal{P}$ and $\mathcal{T}$ symmetries protecting the nonmagnetic Kramers theorem. The distribution of O atoms in the collinear antiferromagnetic state deforms the magnetization densities around the Ru sublattices as we show in Fig. 4.5(a). Here we plot the magnetization densities calculated without SOC. The magnetization density on sublattice A is perfectly compensated by the magnetization density on sublattice B as we can see from Fig. 4.5(a), and the DOS in Fig. 4.5(c) calculated without SOC.

Note that among the rutile antiferromagnets [66, 243], a metallic phase is rare. The recently discovered [242, 277] itinerant antiferromagnetism in industrially relevant RuO$_2$ is just an exceptional example of a metallic rutile antiferromagnet. Our DFT calculations [116] confirm that for a medium strength Hubbard parameter ($U \sim 1-3$ eV), antiferromagnetism and metallic DOS coexist, consistent with previous reports [242, 277]. We set in all plots U$\sim$ 2 eV if not specified otherwise. For smaller values, $U < 1$ eV, we obtained vanishing antiferromagnetic moments, while for large values, $U > 3$ eV, the system becomes an insulator.

The perfect antiferromagnetic compensation arises due to the symmetry connecting the sublattices by a 90-degree rotation combined with a half-unit cell translation along the body-diagonal of the crystal. The magnetization density explicitly illustrates breaking of the $\mathcal{T}_{\mathrm{AF}}$ symmetry. In Fig. 4.5(b) and (c) we observe strong splitting of the spin-up $|\uparrow\rangle$ (blue lines) and spin-down channels $|\downarrow\rangle$ (red lines) in the energy bands and Fermi surface cut. The strong splitting of the energy bands is a fingerprint of the time-reversal symmetry breaking. The main contribution to the symmetry breaking is due to the locally anisotropic antiferromagnetic isosurfaces which are modulated by the non-magnetic atoms in the crystal structure justifying the name CHE.

When we switch on the relativistic corrections, the local noncetrosymmetricity also generates ASOC $\sim \boldsymbol{k} \times \nabla V \cdot \mathbf{s}$, which additionally lowers the symmetry. The resulting band structure is locally spin-polarised and also spin mixed and generates the required asymmetry between left and right moving electrons. With the large atomic SOC is turned on, only minute corrections to the DOS occur [116]. They result in a small net magnetic moment, $\mathbf{M} = \mathbf{M}_A + \mathbf{M}_B$, of a magnitude $\sim 0.05\ \mu_{\mathrm{B}}$ (due to DMI) [278]. Here $\mathbf{m}_{A/B}$ are magnetizations of the antiferromagnetic A and B sublattices. In comparison, the Néel vector $\mathbf{N} = (\mathbf{M}_A - \mathbf{M}_B)/2$ has a magnitude $\sim 1.17\ \mu_{\mathrm{B}}$.

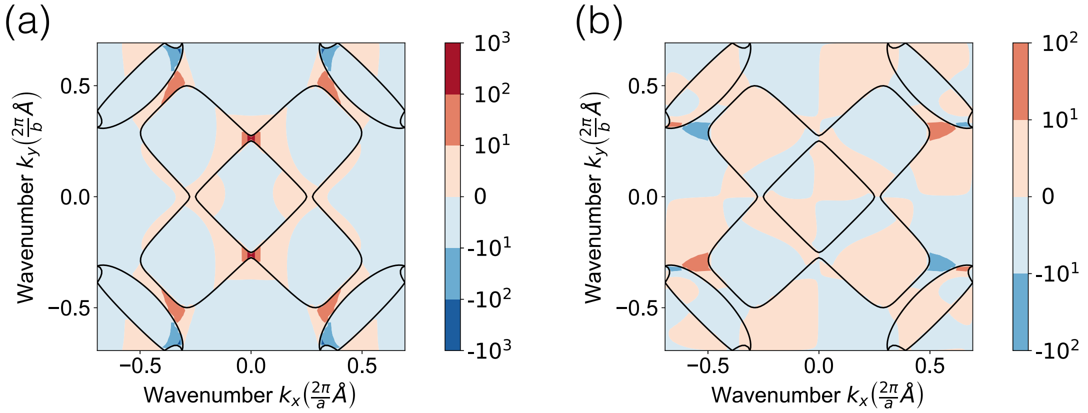

Figure 4.6: **Fermi surface cut and Berry curvature components in the crystal momentum $k_z = 0$ plane.** (a) $\Omega_y(k_x, k_y, 0)$ (b) $\Omega_z(k_x, k_y, 0)$. The $\Omega_x(k_x, k_y, 0)$ component vanishes. The figures were calculated by the Wannier90 method.

We show the crystal momentum Berry curvature map Ω_y in Fig. 4.6(a) and Ω_z in Fig. 4.6(b). The integrated component $\int dk_x \Omega_y(\boldsymbol{k})$ is even in k_y as we expect from the symmetry analysis and is nonvanishing. In contrast, $\mathcal{M}_y$, $\mathcal{P}$, and $\mathcal{TC}_{2z}$ imply that $\int dk_x \Omega_x(\boldsymbol{k}) = 0$, and $\mathcal{M}_y$, and $\mathcal{TC}_{2z}\mathcal{M}_y$ yield $\int dk_z \Omega_z(\boldsymbol{k}) = 0$ consistent with our calculations.

Furthermore, in Fig. 4.7 we study the additional splitting of energy bands due to the SOC. In panels (c,d) we observe the largest contributions to the Berry curvature due to the splitting along the $Y - \Gamma$ line. These Berry curvature "hotspots" [279] are localised around spin-orbit split bands to the opposite energy side of the Fermi surface similarly as in Fe [54, 279], or non-collinear antiferromagnets [105]. The large magnitude can be traced back to the presence of symmetries protecting the degeneracy of the bands in the calculation without SOC (e.g. to the spin-space group [184]). The SOC than breaks the spin-space symmetry and the resulting *local in crystal momentum band-gap* generates a peak in the Berry curvature.

With this, we arrive at the important signature of this crystalline symmetry breaking by the nonmagnetic atoms. As we show in Fig. 4.7(a-b) we can distribute the O atoms in two ways corresponding to the opposite local crystal chiralities (4.20). Wyckoff position of Ru is $2a$, and of O is $4f$ ($x = -0.30375$) in the phase with chirality +, and 4g (x = +0.30375) in the phase with chirality -.

Swapping the local crystal chiralities also rotates the deformed magnetization densities as we show in Fig. 4.7(a-b). Note that we *did not* change the orientation of the Néel vector. The local crystal chirality change also flips the sign of the Berry curvature as we see from Fig. 4.7(d). This confirms the crystalline mechanism origin of the Hall signal.

We note that the symmetry breaking in realistic rutile antiferromagnets is more complicated than in the minimal nodal-chain model from the first chapter. In the minimal model, the symmetry breaking is caused by the ASOC only, in the

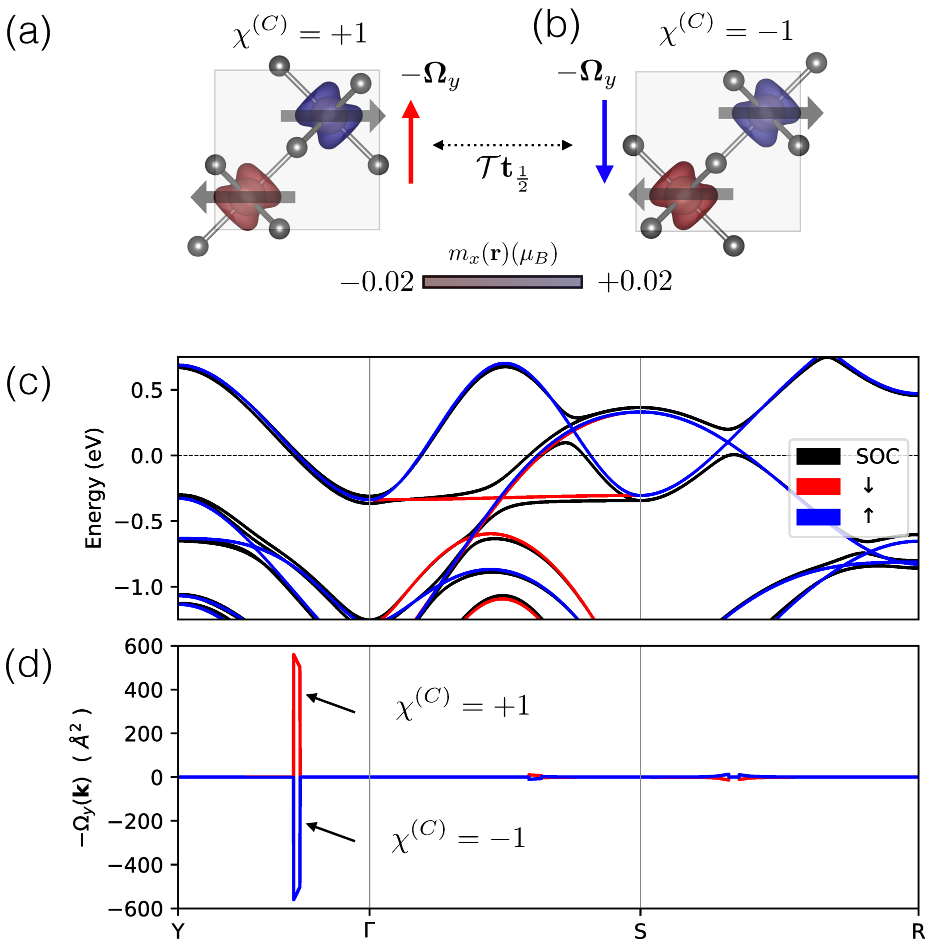

Figure 4.7: **Control of the Berry curvature in $\mathbf{RuO_2}$ by redistribution of nonmagnetic atoms.** (a) Positive and (b) negative crystal chirality (recall Fig. 1.11) depending on the distribution of the O atoms and the corresponding reorientation of magnetization density isosurfaces. The orientation of the Néel vector remains the same. (c) Detail of spin-polarized energy bands calculated without SOC (red and blue lines), and spin-orbit coupled energy bands (black line). (d) The crystal momentum resolved Berry curvature depending on the local crystal chirality in (a), and (b). First two panels were calculated in VASP, the other two panels by Wannier90.

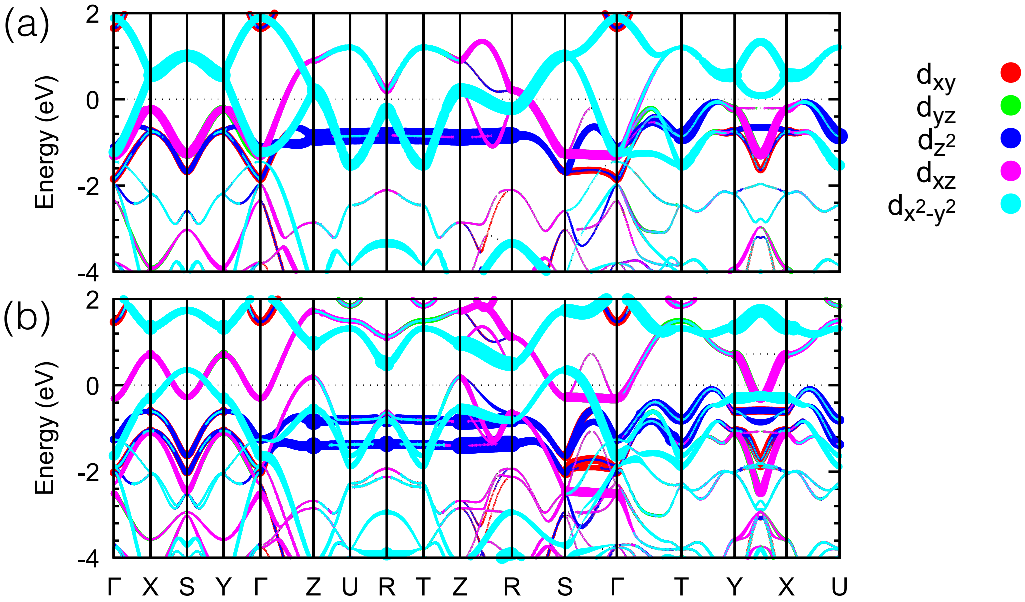

Figure 4.8: **Orbital composition and splitting of energy bands** in (a) nonmagnetic and (b) antiferromagnetic states of RuO_2.

rutile antiferromagnet, we observe strong asymmetry already in the calculation without SOC due to the asymmetric magnetization densities around Ru atoms. Furthermore, the antiferromagnetic splitting depends on the crystal momentum as we show in Fig. 4.8 where we compare the orbital composition of energy bands with and without antiferromagnetism. SOC is switched off in these calculations. We observe in the band structures also splitting of the Dirac nodal lines present in the nonmagnetic phase along $X-M-A$ symmetry line in the Brillouin zone [280].

Now we demonstrate that the Hall conductivity associated with this symmetry breaking mechanism can be very large. We calculate the Hall conductivity by the Bery curvature formula in Wannier90 code. For artificially constrained perfectly antiparallel spin moments along [100], the Hall vector $\boldsymbol{\sigma} \parallel [010]$ and we obtain $\sigma_{xz} = 36.4$ Scm^{-1}. For a canting angle $\approx 1°$ obtained from the DFT calculation, $\mathbf{M} \parallel [010]$ and $\sigma_{xz} = 35.7$ Scm^{-1}. In our paper [116] we present calculations of the full dependence of the CHE for $\mathbf{N} \parallel [100]$ on the canting angle between magnetizations of sublattices A and B. We can separate σ_{xz} into a contribution even in $\mathbf{M}$,

$$\sigma_{xz}^{\mathrm{CHE}} = \frac{\sigma_{xz}(\mathbf{N},\mathbf{M}) + \sigma_{xz}(\mathbf{N},-\mathbf{M})}{2}, \tag{4.21}$$

and odd in $\mathbf{M}$,

$$\sigma_{xz}^{\mathrm{AHE}} = \frac{\sigma_{xz}(\mathbf{N},\mathbf{M}) - \sigma_{xz}(\mathbf{N},-\mathbf{M})}{2}. \tag{4.22}$$

Here $\sigma_{xz}^{\mathrm{AHE}}$ is a contribution induced by the small net moment, analogous to the AHE in ferromagnets. Our calculations show [116] that this term is roughly linear in net magnetic moment $\mathbf{M}$ while $\sigma_{xz}^{\mathrm{AF}}$ is almost constant at small canting angles ϕ. This demonstrates that the small net magnetic moment has a negligible effect on σ_{xz}. This is in striking contrast to the recently studied antiferromagnets GdPtBi [236] and $EuTiO_3$ [281]. These antiferromagnets exhibit a $\mathcal{T}$-invariant

MPG in the ground state and the observed AHE can be attributed entirely to the canted moment induced by an applied external magnetic field.

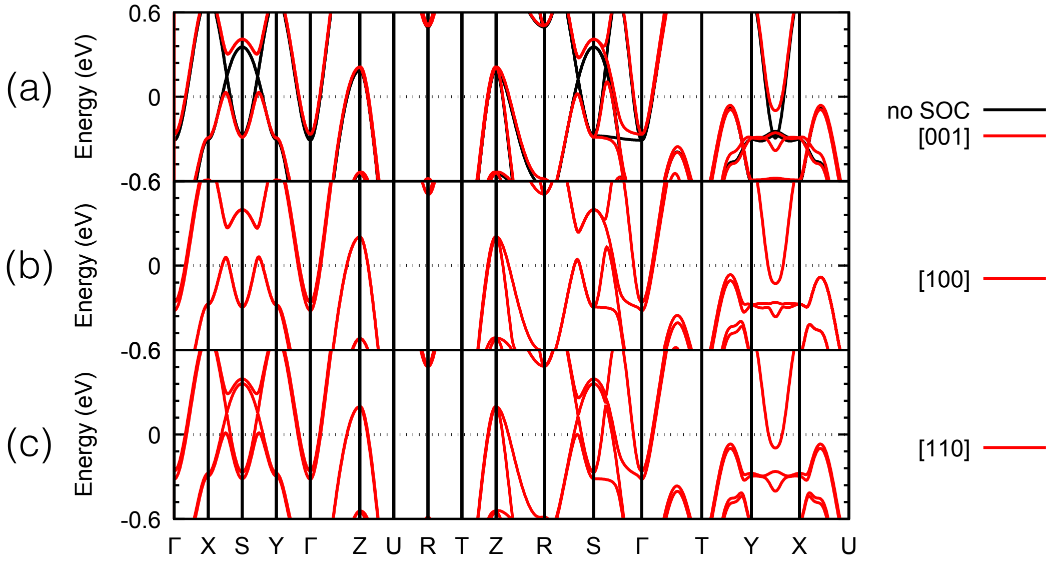

Figure 4.9: **Energy bands in dependence on Néel vector orientation** in antiferromagnetic RuO_2.

In analogy to the model results, the hybridization of linear band crossings and the gapping of nodal-line features [282] strongly depends on the Néel vector orientation [27] and reflects the change from the MSG $Pnn'm'$ for $\mathbf{N} \parallel [100]$ to the MSG $Cnn'm'$ for $\mathbf{N} \parallel [110]$ and we show in Fig. 4.9 the dependence of the Néel vector orientation. The changes in energy bands with the in-plane Néel vector rotation result in a highly anisotropic crystal Hal conductivity [249] as we present in our paper [116]. An extreme case is represented by the possibility to switch-off the Hall conductivity entirely when the Néel vector points along the [001] crystal axis. We have also calculated orbital magnetization in VASP and we conclude that for a generic orientation of the Néel vector, the Hall vector and orbital magnetization are not along the same direction since they correspond to microscopically different expressions [10].

Furthermore, we have studied [116] also the dependence of the Hall conductivity on the Hubbard U. Changes in Hubbard U are effectively tuning the size of the magnetic moments and we conclude that the Hall conductivity is not proportional to the sublattice magnetization [116].

4.5 Global crystal chirality in $CoNb_3S_6$

In this section we will present the electronic structure of the noncentrosymmetric quasi-two-dimensional $CoNb_3S_6$ collinear antiferromagnet. We will demonstrate the possibility to control the crystal Hall conductivity in this system by the global crystal chirality. Co is embedded here in the transition metal dichalcogenide and the resulting crystal structure of $CoNb_3S_6$ is noncentrosymmetric with SG P63mmn (number 182). The crystal structure lacks mirror symmetries and thus

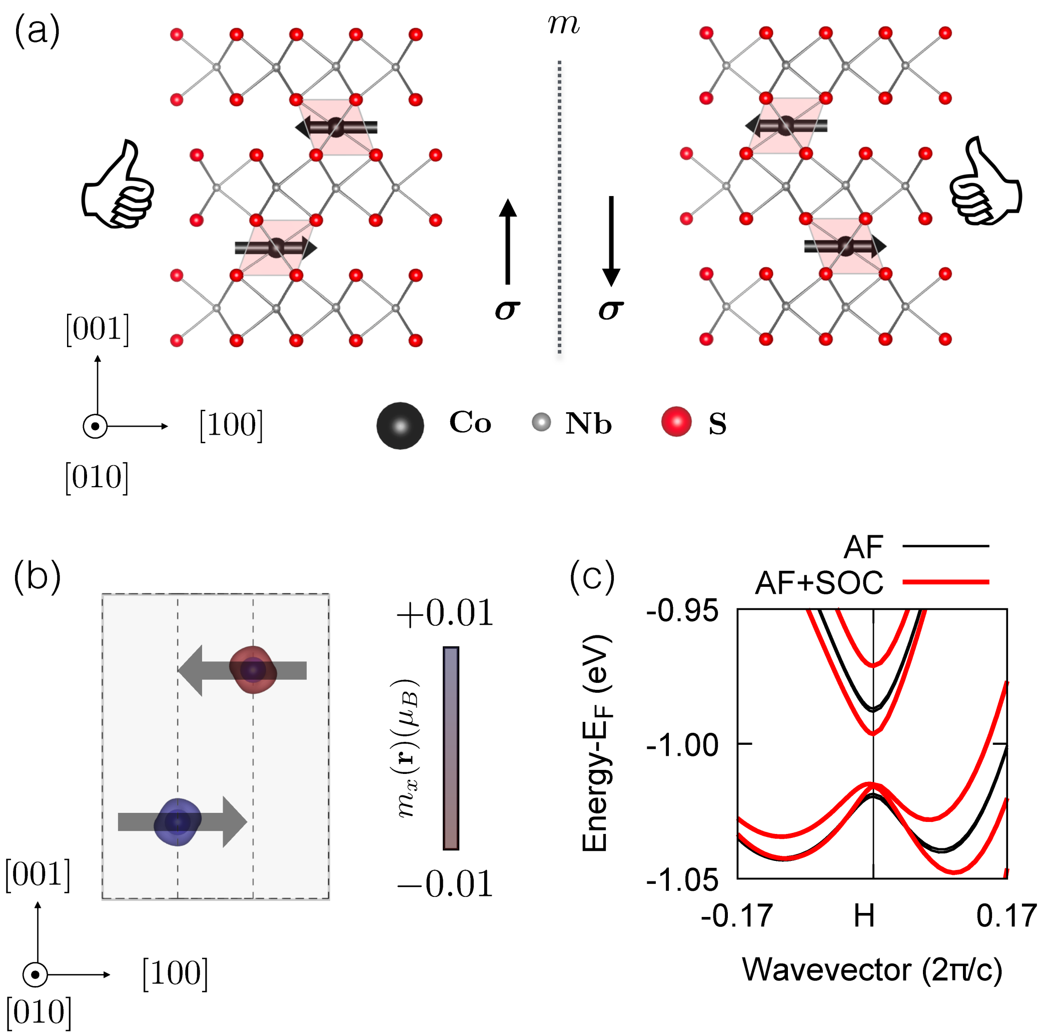

Figure 4.10: **Crystal Hall conductivity due to the global crystal chirality in $\mathbf{CoNb_3S_6}$ antiferromagnet.** (a) The crystal of $CoNb_3S_6$ antiferromagnet ("L", with a left-handed chirality) and its mirror m image ("R", with a right-handed chirality). Note that the mirror m maps the two chiralities onto each other by redistributing the nonmagnetic S atoms, while preserving the magnetic atoms positions and collinear antiferromagnetism orientation. (b) The calculated magnetization isosurfaces in the $CoNb_3S_6$ antiferromagnet exhibit low symmetry and illustrate the global chiral symmetry breaking. (c) Bandstructure detail of antiferromagnetic $CoNb_3S_6$ without (black line) and with (red line) SOC. We show a fraction of the $L - H - A$ path in the Brillouin zone.

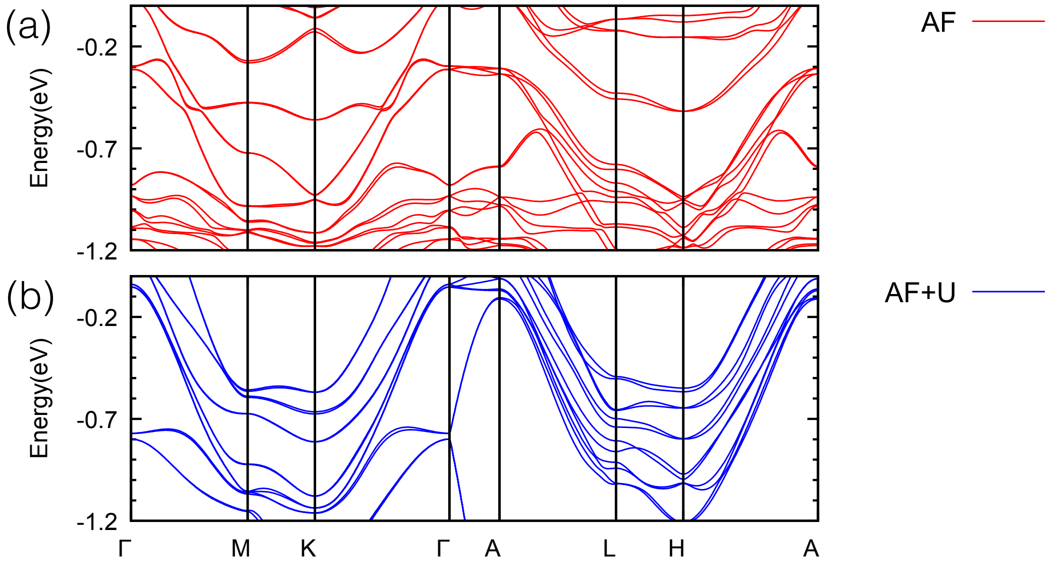

Figure 4.11: **Electronic structure of the $\mathbf{CoNb_3S_6}$ antiferromagnet.** (a) Energy bands of the antiferromagnetic $CoNb_3S_6$. (b) Energy bands of the antiferromagnetic $CoNb_3S_6$ with Hubbard U=4 eV. In both cases with SOC.

belongs to one of the 65 Shoncke SG; however, the SG is not chiral. We show the crystal of $CoNb_3S_6$ in Fig. 4.10(a).

The MSG of $CoNb_3S_6$ for the Néel vector along [100] is $C2'2'2_1$ and includes symmetry operations $\mathcal{TC}_{2x}, \mathcal{TS}_{2y}$, and $\mathcal{S}_{2z}$, and also symmetries coupled by $\mathbf{t} = (1/2, 1/2, 0)$, e.g., $\mathcal{TC}_{2x}\mathbf{t}$. The MLG is the same ($2'2'2$) for both RuO_2, and $CoNb_3S_6$, and thus also the structure of the conductivity tensor is identical in these crystals. The magnetic Co subsystem has a $\mathcal{PT}$ symmetry when the nonmagnetic atoms are ignored which would exclude the existence of a Hall vector. However, due to the symmetry breaking by the S atoms, analogically to O atoms in RuO_2, the structure gains a Hall vector and allows for the crystal Hall effect. If we take a collinear antiferromagnetic order with moments along the a-axis and the same size of the magnetic and crystallographic unit cells, our symmetry analysis shows that the Hall vector, i.e., the CHE, is allowed by symmetry. The MPG $2'2'2$ contains unprimed rotational axis $\mathcal{C}_2$ perpendicular to the hexagonal layers and $\mathbf{g} \parallel \mathbf{a}_{\mathcal{C}_2}$ according to our classification Tab. 4.1.

We can change the sign of the CHE by changing the spatial inversion symmetry breaking by the S atoms without manipulating the magnetic Co atoms. This corresponds to mirroring the crystal as we show in Fig. 4.10(a). In Fig. 4.10(b) we show also the magnetization density demonstrating the breaking of the both $\mathcal{T}$ and $\mathcal{P}$ symmetries.

The nonmagnetic and antiferromagnetic energy bands shown in Fig. 4.10(c) and 4.11(a-b) are compatible with topological quasiparticles. The nonmagnetic space group is compatible with an hourglass dispersion [187, 188] due to the presence of the nonsymmorphic rotational axis symmetry. Also, we note Kramers-Weyl dispersion around high symmetry points [89], with detailed examples shown in Fig. 4.10(c).

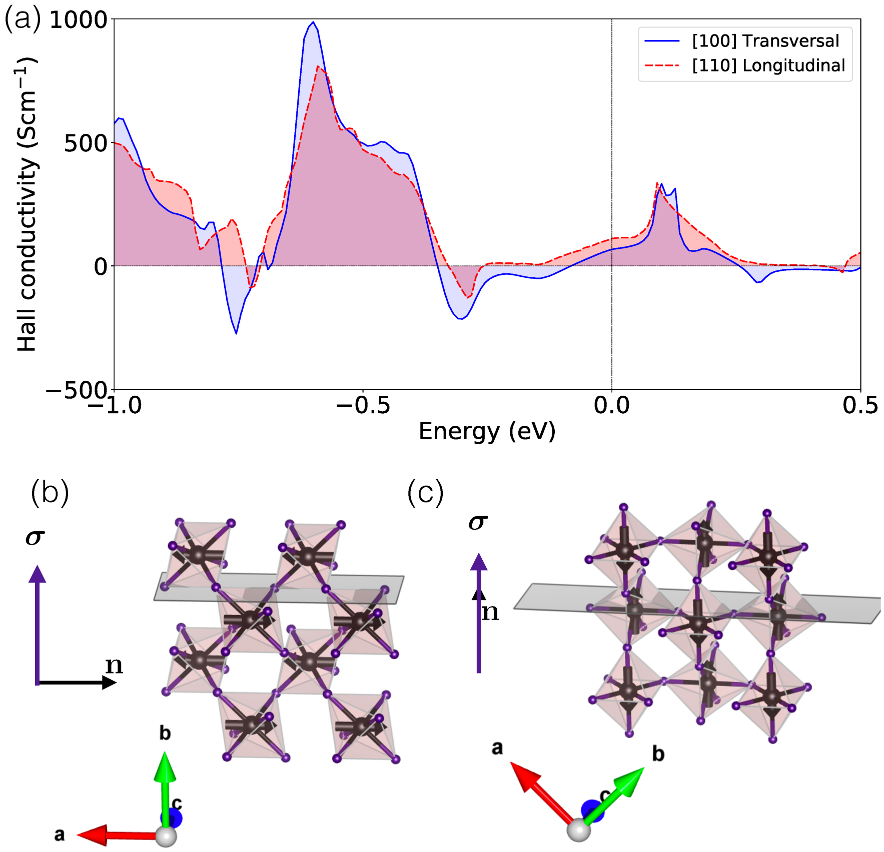

Figure 4.12: **Crystal Hall conductivity in RuO$_2$** (with crystal chirality +). (a) Total crystal Hall conductivity in dependence on Fermi level position for the two orientation of the Néel vector shown in (b) [100] and (c) [110].

4.6 Suggestion for an experimental detection

We discuss here the existing experimental Hall data on materials compatible with the CHE and we present the set-up for experimental observation of the CHE in RuO$_2$.

The spontaneous Hall effect has been recently measured in CoNb$_3$S$_6$ [235]. The authors attributed the Hall voltage to the presence of a small net moment combined with topological bands or non-collinear antiferromagnetism [235] while explicitly excluding any spontaneous Hall signal in the collinear antiferromagnetic phase. Interestingly, experimental neutron scattering data from the 1980s pointed towards an in-plane collinear antiferromagnetic order [283]. This study reported in the collinear antiferromagnetic states doubling of the magnetic unit cell with respect to the crystallographic unit cell. Such a structure explicitly prohibits the spontaneous Hall voltage. However, as we have shown in the previous paragraph, there exists a collinear antiferromagnetic state which does support the Hall signal. However, in our DFT calculations, the magnetic moments are underestimated. We thus use Hubbard $U \sim$4 eV which yields better agreement with experiment in terms of the sublattice magnetization magnitude 2.2 μ_B [235]. Remarkably, the experiment is performed on heavily hole-doped samples with a deficiency of S [235] corresponding roughly to $\sim$ 150 electronic states filled. This filling corresponds, according to our calculations, to the Fermi level shift of -0.6 eV. We calculate for the Fermi energy set to ∼-0.72 eV a spontaneous Hall conductivity ∼ 85 S/cm [116] and thus our first principle value is consistent with the measured Hall conductivity of 27 S/cm. The lower experimental value can be explained by the multi-domain state of the experimental sample.

Now we turn our attention to RuO_2. We start by discussing the possible growth directions for observing the crystal Hall effect in the RuO_2 antiferromagnet. RuO_2 can be grown in bulk and thin film. Both bulk crystals, as well as 25 nm thin films oriented in the (100) plane, were recently demonstrated to host the antiferromagnetic order [192, 242, 277]. We summarize the symmetry and parameters obtained from our first-principle calculations[116] in Tab. 4.4 for different Néel vector orientations.

N	MSG	MPG	lattice (Å)	**M** (μ_B)
[001]	$P4'_2/mnm'$	$4'/mm'm$	a=4.5331 c=3.1241	0
[100]	$Pnn'm'$	$m'm'm$	a=4.528 b=4.536 c=3.124	∥ [010] 0.05
[110]	$Cmm'm'$	$m'm'm$	a=4.5337 c=3.124	∥ $[\bar{1}\bar{1}0]$ 0.0075

Table 4.4: Magnetic space/point group (MSG/MPG) in RuO_2 antiferromagnet and calculated lattice constants, net magnetic moment **M** in RuO_2 for different orientations of the Néel vector **N**.

For instance, in a (010) thin film, it is important to ensure that the easy axis has a projection to the [100]-axis. Forcing the easy axis into the (001)-plane can be achieved, according to our magnetocrystalline anisotropy calculations, by a substitutional disorder (e.g. by Ir which has a similar atomic radius as Ru and IrO_2 exists) or by the application of an external magnetic spin-flop field. An indication of the crystal Hall effect was recently observed in thin films of RuO_2 in strong magnetic fields which were used to orient the magnetic domains. The extrapolated experimental Hall conductivity of ∼300 S/cm is consistent with our first principle calculations shown in Fig. 4.12(a) for orientations of the Néel vector along [100] and [110] crystalline axes illustrated in Fig. 4.12(b) and (c) respectively. The CHE conductivity exhibits peak values of ∼ 1000 S/cm. This corresponds to record magnitudes reported for the AHE in ferromagnets with Weyl points or nodal-lines or non-collinear Weyl antiferromagnets [65, 232, 284].

4.7 Summary: theory of spontaneous and crystal Hall effects

An antiferromagnetic system with ferromagnetic Laue group exhibits a Hall vector. The orientation of the Hall vector can be determined from

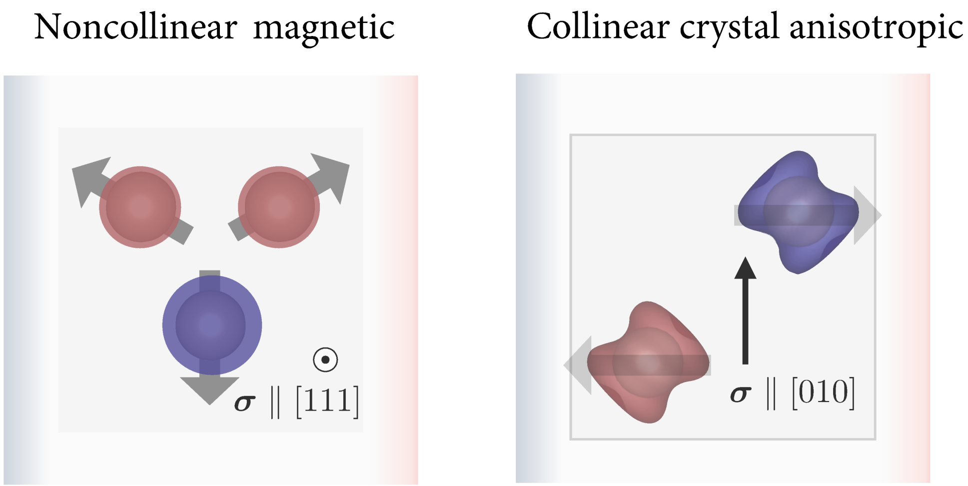

Figure 4.13: Spontaneous symmetry breaking due to the non-collinear antiferromagnetism (left) or from anisotropic local magnetisation isosurfaces of collinear antiferromagnetism (right).

the following criteria derived from Tab. 4.1 [116]:

1. In the low symmetric MLG, 1 the orientation of the Hall vector is set by the electronic structure.
2. In systems with $2'$ rotational axis, the Hall vector points perpendicular to the symmetry axis and the orientation within this plane is set by the electronic structure.
3. The n fold rotational axis determines the Hall vector orientation uniquely to be parallel to the rotational axis.

All the remaining MLGs can be derived from these symmetry rules. For instance, in $2'2'2$, the Hall vector is perpendicular to both $2'$ and parallel to 2.

Crystal Hall effect. We have identified a new spontaneous Hall effect mechanism arising from *anisotropic collinear antiferromagnetism*. In contrast to the spontaneous Hall effect in non-collinear antiferromagnets shown in Fig 4.13(left), the crystal Hall effect relies on the symmetry lowering due to the low symmetry magnetization density isosurfaces as illustrated in Fig. 4.13(right). The symmetry lowering can be remarkably strong in contrast to well-known effects in antiferromagnets with ferromagnetic symmetry groups, e.g., the tiny net moment arising from canting due to the relativistic DMI. In systems with this strong crystalline symmetry breaking, the magnetic order cannot be described only as magnetization arrows determined from the spin density projected on the atomic sites. The magnetic multipole theory of symmetry breaking in anomalous Hall effect in non-collinear antiferromagnets excludes time-reversal symmetry breaking quadrupole. In contrast, the symmetry breaking in crystal Hall effect in our collinear antiferromagnets can be seen as toroidal magnetic quadrupole order [98].

Anisotropic collinear antiferromagnetism. In the system with allowed but zero net moment, an additional order parameter allowing for the Hall conductivity $\sigma_{ij}(\mathbf{H}, \mathbf{S}, \boldsymbol{\chi})$ (e.g. crystal chirality or multipolar order capturing the complete magnetization density) is required to correctly describe the Onsager reciprocity on the phenomenological level. A consequence of this observation is that the crystal Hall conductivity can be controlled by swapping the local or global crystal chirality. Many antiferromagnetic systems exhibit magnetization density isosurfaces of high symmetry: e.g. Mn_2Au, $SrMn_2Bi_2$, or orthorhombic CuMnAs. We have found the asymmetric anisotropic magnetization density isosurfaces in RuO_2 antiferromagnet and $CoNb_3S_6$.

Topological quasiparticles compatible with Hall conductivity. The MLG determines the Hall vector orientation, MPG determines the crystal momentum Berry curvature, and finally the MSG constraints the energy dispersion and topological quasiparticles. Our symmetry analysis shows that the Hall vector symmetry groups are not compatible with 3D Dirac quasiparticles, however, other topological quasiparticles are possible: Weyl fermions [94], nodal lines [94] and chains, Kramers-Weyl fermions, or hourglass-like dispersions to name a few. The band degeneracies can be determined straightforwardly by analysing the symmetry tables for ferromagnetic Type-I and Type-III MSGs as explained for a general case in Chapter 1.

Anisotropy of Hall conductivity. In contrast to the spontaneous anomalous Hall effect in ferromagnets, in certain antiferromagnets, it is possible to switch on and off the crystal or anomalous Hall effect by rotating the antiferromagnetic order. This represents the ultimate limit of the spontaneous Hall anisotropy.

Magnitude and scaling of the Hall conductivity. Our studies show that the Hall conductivity is in general neither proportional to magnetization and sublattice magnetization, nor to SOC strength, as often anticipated [63, 152]. The reason is that in metals, many bands contribute to the Hall linear response. The main contribution to the Hall conductivity in RuO_2 is from the hot spots in the Berry curvature. The hot spots are generated by the SOC which splits the energy bands. The degeneracy of the energy bands in the calculations with the switch off SOC can be linked to additional crystalline symmetries in the spin space group. Our ab initio calculations in RuO_2 antiferromagnet show that the crystal Hall conductivity can be as large as in ferromagnets.

Crystal Hall symmetry breaking applications. The crystal Hall symmetry breaking can be found in an abundant class of collinear antiferromagnets. Also, analogical effects relying on this symmetry breaking can be identified: thermal [285] and optical [286] counterparts or spin-current variants of the Hall effect. An example is even-in time-reversal pure spin current (preserving spin quantum number). The crystal Hall effect requires SOC to generate transversal charge current. Its spin counterpart does not require the presence of SOC and the crystalline symmetry breaking generates spin current even when the SOC is neglected.

Shape of Hall hysteresis loop. Crystal Hall effect offers an alternative plausible explanation of the Hall conductivities conventionally taken as a signature of complex magnetic structure and topological Hall effect in noncentrosymmetric systems [241]. Topological Hall effect (spontaneous Hall effect due to the nontrivial non-coplanar magnetic textures) has a characteristic nonmonotonic hysteresis loop shape. Such a shape can be obtained alternatively as a convolution of two spontaneous Hall signals from material regions with the opposite Hall sign [287]. These two regions might correspond to the opposite sign of the crystal Hall effect. The hysteresis loop in the spontaneous Hall effect in combination with the multidomain nature of antiferromagnets can be potentially used in hardware neural networks as a tunable sigmoid element.

Conclusion

”There is no physical law precluding particles from being organised in ways that perform even more advanced computations than the arrangements of particles in human brains.”

Steven Hawking

We have explored in this thesis topological antiferromagnetic spintronics materials and effects by means of symmetry analysis and first principle electronic structure calculations. Understanding of topological magnetic phases of matter is more complicated than the one in nonmagnetic topological insulators. The study of topological magnetic metals requires nonabelian Berry curvature, understanding of the complex many-particle relativistic magnetic ordering, and the investigation of a larger number of symmetry groups - 1651 instead of the conventional 230 nonmagnetic groups. This also increases the computational cost of first-principle calculations.

Here we have summarized main results of the topological band theory and symmetry analysis of magnetic energy bands, followed by a description of our state-of-the-art relativistic first-principles calculations of the electronic structure in complex spin-orbit coupled magnets. Our identification of antiferromagnetic Kramers theorem led to the discovery of antiferromagnetic Dirac fermions, and the classification of band-degeneracies in antiferromagnets in terms of spatial inversion and time-reversal discrete space group symmetries. We have implemented our relativistic magnetic Hamiltonians in python language and with the help of PythTB package we have studied their topological properties. We have developed a computational framework employing existing VASP and TB-LMTO codes on supercomputers. Our parallelization of transport Green’s function TB-LMTO code allowed us to dramatically speed up calculations, and let us calculate complex topological antiferromagnetic materials. Our calculations and visualisations of Bloch spectral functions was used to understand charge transport from first principles and allows us to bridge the so far black box *ab initio* calculations with phenomenological models.

In Chapters 3 and 4 we have applied this theory on two examples of novel effects we predicted: the relativistic metal-insulator transition from antiferromagnetic Dirac fermions, and the crystal Hall effect from collinear antiferromagnetism. We have studied the symmetry dependence of Dirac fermions in antiferromagnetic CuMnAs. Our first principle calculations successfully explain AMR experimentally observed in NiMnSb: its negative sign, crystalline components, and magnitude. Our calculations also reveal a large AMR in Mn_2Au which can be linked to the disorder propagation of band touchings which is sensitive to the Néel vector orientation.

In the second part, we have studied the spontaneous Hall effect in antiferromagnets and we have revealed its generic properties: (i) nonscaling with (sublattice) magnetization, spin-orbit coupling, electronic correlation, (ii) strong anisotropy possible in antiferromagnets, (iii) symmetry classification of Hall vectors, (iv) sensitivity to the full magnetization density (not only magnetization vector projections), and (v) relation to spin space group splitting and compatibility with topological quasiparticles beyond standard Weyl fermions. We have identified a novel spontaneous symmetry breaking relying on low symmetry local magnetization isosurfaces aka *anisotropic collinear antiferromagnetism.* This guided us to prediction of the crystal Hall effect (CHE) in collinear antiferromagnets, systems in the past commonly believed to exclude spontaneous Hall signals. We have identified a strong crystal Hall conductivity in RuO_2 from our first principle calculations.

Besides the fundamental dimension of our research and the usage of AMR and CHE as sensing tools in antiferromagnetic spintronics, the effects can have other promising applications. The intrinsic anisotropic magnetoresistance from Dirac fermions can be controlled by the ultrafast Néel spin-orbit torques in the metallic phase and voltage gating in the semiconducting phase. The effect can be possibly used in future for improving magnetic storage scaling or as topological antiferromagnetic transistor function based on the topological metal-insulator transition. The CHE symmetry breaking mechanism can produce novel types of low dissipation (spin) currents. For instance, the existing realisation of the quantum anomalous Hall effect in magnetically *doped* topological insulators suffers from tiny band-gaps, fragile diluted magnetism, low critical temperatures, and less robust quantization of the Hall conductivity. Furthermore, finding *intrinsic* ferromagnetic or non-collinear and non-coplanar (possibly) antiferromagnetic topological insulator seems to be a formidable task since these orders seem to be rarely insulating. In contrast, collinear antiferromagnets commonly host robust magnetism, are compatible with semiconducting electronic structure and high critical temperatures. Our Hall signal in collinear antiferromagnets thus represents an important step in paradigm change from *nonrelativistic, diluted, interfacial, ferromagnetic, nonlinear antiferromagnetic heterostructures* to *relativistic, intrinsic collinear antiferromagnetic* quantum spontaneous states. These states hold great promise for low dissipation nanoelectronics.

Our relativistic magnetic first principle calculations of AMR in NiMnSb, Mn_2Au and spontaneous Hall conductivity in RuO_2, and density of states in tetragonal CuMnAs were confirmed in experiments. This solidifies our computational framework, reveals the potential of our effects in nanoelectronics and opens new directions in the research of topological antiferromagnetic spintronics. We find the antiferromagnetic systems particularly interesting as they can unify neighbouring, as well as, remote fields of topological quasiparticles, spintronics, physics of correlated systems, or axion dark matter.

Bibliography

[1] Nassim Nicholas Taleb. *The black swan : the impact of the highly improbable.* Random House Trade Paperbacks, 2010.

[2] Louis Néel. Magnetism and Local Molecular Field. *Science*, 174(4013):985–992, dec 1971.

[3] T. Jungwirth, Jairo Sinova, A. Manchon, X. Marti, J. Wunderlich, and C. Felser. The multiple directions of antiferromagnetic spintronics. *Nature Physics*, 14(3):200–203, may 2018.

[4] Naoki Kiyohara, Takahiro Tomita, and Satoru Nakatsuji. Giant Anomalous Hall Effect in the Chiral Antiferromagnet Mn3Ge. *Physical Review Applied*, 5(6):064009, may 2016.

[5] Zhiqi Liu. Private communication, 2019.

[6] P W Anderson. More is different. *Science (New York, N.Y.)*, 177(4047):393–6, aug 1972.

[7] Joel E. Moore. The birth of topological insulators. *Nature*, 464(7286):194–198, mar 2010.

[8] Klaus von Klitzing. Quantum Hall Effect: Discovery and Application. *Annual Review of Condensed Matter Physics*, 8(1):13–30, mar 2017.

[9] M Nakahara. *Geometry, Topology and Physics.* Graduate Student Series in Physics. CRC Press, 2 edition, feb 2003.

[10] David Vanderbilt. *Berry Phases in Electronic Structure Theory.* Cambridge University Press, oct 2018.

[11] Conyers Herring. Accidental degeneracy in the energy bands of crystals. *Physical Review*, 52(4):365–373, may 1937.

[12] A. A. Abrikosov and S. D. Beneslavskii. Possible existence of substances intermediate between metals and dielectrics. *Soviet Physics JETP*, 32(4):699, may 1971.

[13] Jairo Sinova, Dimitrie Culcer, Q. Niu, N. A. Sinitsyn, T. Jungwirth, and A. H. MacDonald. Universal intrinsic spin Hall effect. *Physical Review Letters*, 92(12):126603, may 2004.

[14] Shuichi Murakami, N. Nagaosa, and Shou-Cheng Zhang. Dissipationless Quantum Spin Current at Room Temperature. *Science (New York, N.Y.)*, 301:1348–1351, may 2003.

[15] A. H. Castro Neto, F. Guinea, N. M. R. Peres, K. S. Novoselov, and A. K. Geim. The electronic properties of graphene. *Reviews of Modern Physics*, 81(1):109–162, jan 2009.

[16] M. Z. Hasan and C. L. Kane. Colloquium: Topological insulators. *Reviews of Modern Physics*, 82(4):3045–3067, may 2010.

[17] Gordon W. Semenoff. Condensed-Matter Simulation of a Three-Dimensional Anomaly. *Physical Review Letters*, 53(26):2449–2452, dec 1984.

[18] D. P. DiVincenzo and E. J. Mele. Self-consistent effective-mass theory for intralayer screening in graphite intercalation compounds. *Physical Review B*, 29(4):1685–1694, feb 1984.

[19] Shuichi Shuichi Murakami. Phase transition between the quantum spin Hall and insulator phases in 3D: emergence of a topological gapless phase. *New Journal of Physics*, 9(9):356–356, sep 2007.

[20] N. P. Armitage, E. J. Mele, and Ashvin Vishwanath. Weyl and Dirac semimetals in three-dimensional solids. *Reviews of Modern Physics*, 90(1):015001, jan 2018.

[21] Barry Bradlyn, Jennifer Cano, Zhijun Wang, M. G. Vergniory, C. Felser, R. J. Cava, and B. Andrei Bernevig. Beyond Dirac and Weyl fermions: Unconventional quasiparticles in conventional crystals. *Science*, 353(6299):aaf5037–aaf5037, may 2016.

[22] Wladimir A Benalcazar, B Andrei Bernevig, and Taylor L Hughes. Quantized electric multipole insulators. *Science (New York, N.Y.)*, 357(6346):61–66, jul 2017.

[23] Libor Šmejkal and Tomáš Jungwirth. Symmetry and topology in antiferromagnetic spintronics. In Jiadong Zang, Vincent Cros, and Axel Hoffmann, editors, *Topology in magnetism*, pages 267–298. Springer International Publishing, 2018.

[24] Jennifer Cano, Barry Bradlyn, and M. G. Vergniory. Multifold nodal points in magnetic materials. *APL Materials*, 7(10):101125, oct 2019.

[25] C. Herring. Magnetism: Exchange interactions among itinerant electrons. *Magnetism*, page 407, may 1966.

[26] A. P. Cracknell and D. ter. Haar. *Magnetism in Crystalline Materials: Applications of the Theory of Groups of Cambiant Symmetry.* Oxford University Press, 2010.

[27] L. Šmejkal, J. Železný, Jairo Sinova, and T. Jungwirth. Electric Control of Dirac Quasiparticles by Spin-Orbit Torque in an Antiferromagnet. *Physical Review Letters*, 118(10):106402, mar 2017.

[28] Peizhe Tang, Quan Zhou, Gang Xu, and Shou Cheng Zhang. Dirac fermions in an antiferromagnetic semimetal. *Nature Physics*, 12(12):1100–1104, may 2016.

[29] M. V. Berry. Quantal Phase Factors Accompanying Adiabatic Changes. *Proceedings of the Royal Society A: Mathematical, Physical and Engineering Sciences*, 392(1802):45–57, mar 1984.

[30] J. J. Sakurai. *Advanced Quantum Mechanics.* Addison-Wesley, may 2018.

[31] J. Zak. Berry's phase for energy bands in solids. *Physical Review Letters*, 62(23):2747–2750, jun 1989.

[32] Taylor L. Hughes B. Andrei Bernevig. *Topological Insulators and Topological Superconductors.* Princeton University Press, 2013.

[33] D. J. Thouless, M. Kohmoto, M. P. Nightingale, and M. den Nijs. Quantized Hall Conductance in a Two-Dimensional Periodic Potential. *Physical Review Letters*, 49(6):405–408, aug 1982.

[34] Alexander Altland and Martin R. Zirnbauer. Nonstandard symmetry classes in mesoscopic normal-superconducting hybrid structures. *Physical Review B*, 55(2):1142–1161, jan 1997.

[35] Xiao Liang Qi, Taylor L. Hughes, and Shou Cheng Zhang. Topological field theory of time-reversal invariant insulators. *Physical Review B*, 78(19):195424, may 2008.

[36] Bohm Jung Yang and Naoto Nagaosa. Classification of stable three-dimensional Dirac semimetals with nontrivial topology. *Nature Communications*, 5:4898, may 2014.

[37] T. Jungwirth, X. Marti, P. Wadley, and J. Wunderlich. Antiferromagnetic spintronics. *Nature Nanotechnology*, 11(3):231–241, may 2016.

[38] Libor Šmejkal, Yuriy Mokrousov, Binghai Yan, and Allan H. MacDonald. Topological antiferromagnetic spintronics. *Nature Physics*, 14(3):242–251, mar 2018.

[39] Mark Staley. Understanding quaternions and the Dirac belt trick. *European Journal of Physics*, 31(3):467–478, may 2010.

[40] E. Wigner. Ueber die Operation der Zeitumkehr in der Quantenmechanik. *Nachrichten von der Gesellschaft der Wissenschaften zu Göttingen, Mathematisch-Physikalische Klasse*, 1932:546–559, 1932.

[41] H A Kramers. Théorie générale de la rotation paramagnétique dans les cristaux. *Proc. Amsterdam Acad.*, 33(959), 1930.

[42] Liang Fu and C. L. Kane. Topological insulators with inversion symmetry. *Physical Review B*, 76(4):045302, may 2007.

[43] David Vanderbilt. *Berry Phases in Electronic Structure Theory : Electric Polarization, Orbital Magnetization and Topological Insulators.*

[44] Stefan Blügel, Yuriy Mokrousov, Thomas Schäpers, Yoichi Ando, and Topological Insulators. *Lecture Notes of the 48 th IFF Spring School 2017 Topological Matter.* 2017.

[45] Patrick Bruno, Stefan Blügel, Thomas Brückel, and Claus M Schneider. E9 Berry phase effects in magnetism. In *Spring School Julich*, 2005.

[46] Michael. Spivak. *Calculus on manifolds : a modern approach to classical theorems of advanced calculus*. W. A. Benjamin, Inc. (reprinted by Addison-Wesley (Reading, Mass.) and Westview Press (Boulder, Colo.)), New York, 2018.

[47] Chao-Xing Liu, Shou-Cheng Zhang, and Xiao-Liang Qi. The Quantum Anomalous Hall Effect: Theory and Experiment. *Annual Review of Condensed Matter Physics*, 7(1):301–321, mar 2016.

[48] Dominik Gresch, Gabriel Autès, Oleg V. Yazyev, Matthias Troyer, David Vanderbilt, B. Andrei Bernevig, and Alexey A. Soluyanov. Z2Pack: Numerical implementation of hybrid Wannier centers for identifying topological materials. *Physical Review B*, 95(7):075146, may 2017.

[49] Bohm Jung Yang, Troels Arnfred Bojesen, Takahiro Morimoto, and Akira Furusaki. Topological semimetals protected by off-centered symmetries in nonsymmorphic crystals. *Physical Review B*, 95(7):075135, may 2017.

[50] Steve M. Young and Benjamin J. Wieder. Filling-Enforced Magnetic Dirac Semimetals in Two Dimensions. *Physical Review Letters*, 118(18):186401, may 2017.

[51] T. Jungwirth, Qian Niu, and A. H. MacDonald. Anomalous Hall Effect in Ferromagnetic Semiconductors. *Physical Review Letters*, 88(20):4, may 2002.

[52] F. D.M. Haldane. Berry curvature on the fermi surface: Anomalous hall effect as a topological fermi-liquid property. *Physical Review Letters*, 93(20):206602, may 2004.

[53] Xinjie Wang, Jonathan R. Yates, Ivo Souza, and David Vanderbilt. Ab initio calculation of the anomalous Hall conductivity by Wannier interpolation. *Physical Review B*, 74(19):1–15, may 2006.

[54] Daniel Gosálbez-Martínez, Ivo Souza, and David Vanderbilt. Chiral degeneracies and Fermi-surface Chern numbers in bcc Fe. *Physical Review B*, 92(8):085138, may 2015.

[55] M. Gradhand, V. Fedorov, F. Pientka, P. Zahn, I. Mertig, L. Györffy, M. Gradhand, D. V. Fedorov, F. Pientka, P. Zahn, I. Mertig, and B. L. Györffy. First-principle calculations of the Berry curvature of Bloch states for charge and spin transport of electrons. *Journal of Physics Condensed Matter*, 24(21):213202, may 2012.

[56] P Streda. Theory of quantised Hall conductivity in two dimensions. *Journal of Physics C: Solid State Physics*, 15(22):L717–L721, aug 1982.

[57] Andrew M Essin, Joel E Moore, and David Vanderbilt. Magnetoelectric Polarizability and Axion Electrodynamics in Crystalline Insulators. *Physical Review Letters*, 102(14):146805, apr 2009.

[58] Frank Wilczek. Two applications of axion electrodynamics. *Physical Review Letters*, 58(18):1799–1802, may 1987.

[59] Rundong Li, Jing Wang, Xiao-Liang Qi, and Shou-Cheng Zhang. Dynamical axion field in topological magnetic insulators. *Nature Physics*, 6(4):284–288, apr 2010.

[60] David J. E. Marsh, Kin Chung Fong, Erik W. Lentz, Libor Šmejkal, and Mazhar N. Ali. Proposal to Detect Dark Matter using Axionic Topological Antiferromagnets. *Physical Review Letters*, 123(12):121601, sep 2019.

[61] Nicodemos Varnava and David Vanderbilt. Surfaces of axion insulators. *Physical Review B*, 98(24):245117, dec 2018.

[62] F. D M Haldane. Model for a quantum hall effect without landau levels: Condensed-matter realization of the "parity anomaly". *Physical Review Letters*, 61(18):2015–2018, may 1988.

[63] M.-T. Suzuki, T. Koretsune, M. Ochi, and R. Arita. Cluster multipole theory for anomalous Hall effect in antiferromagnets. *Physical Review B*, 95(9):094406, mar 2017.

[64] Tahir Yusufaly. Tight-Binding Formalism in the Context of the PythTB Package Basic definitions. pages 1–9, 2012.

[65] Naoto Nagaosa, Jairo Sinova, Shigeki Onoda, A. H. MacDonald, and N. P. Ong. Anomalous Hall effect. *Reviews of Modern Physics*, 82(2):1539–1592, may 2010.

[66] Arthur Cracknell Christopher Bradley. The Mathematical Theory of Symmetry in Solids, 2010.

[67] Stanley C Miller; William F Love. *Tables of irreducible representations of space groups and co-representations of magnetic space groups*. Boulder, Colo., Pruett Press, 1967.

[68] C. J. Bradley and B. L. Davies. Magnetic groups and their corepresentations. *Reviews of Modern Physics*, 40(2):359–379, may 1968.

[69] Andreas P Schnyder. Lecture notes on: Accidental and symmetry-enforced band crossings in topological semimetals. Technical report, 2018.

[70] Guiyuan Hua, Simin Nie, Zhida Song, Rui Yu, Gang Xu, and Kailun Yao. Dirac semimetal in type-IV magnetic space groups. *Physical Review B*, 98(20):201116, nov 2018.

[71] Oskar Vafek and Ashvin Vishwanath. Dirac Fermions in Solids: From High-Tc Cuprates and Graphene to Topological Insulators and Weyl Semimetals. *Annual Review of Condensed Matter Physics*, 5(1):83–112, mar 2014.

[72] Y. X. Zhao and Andreas P. Schnyder. Nonsymmorphic symmetry-required band crossings in topological semimetals. *Physical Review B*, 94(19):195109, may 2016.

[73] Chen Fang and Liang Fu. New classes of three-dimensional topological crystalline insulators: Nonsymmorphic and magnetic. *Physical Review B*, 91(16):161105, apr 2015.

[74] Roger S.K. Mong, Andrew M. Essin, and Joel E. Moore. Antiferromagnetic topological insulators. *Physical Review B*, 81(24):245209, may 2010.

[75] Chen Fang, Matthew J. Gilbert, and B. Andrei Bernevig. Topological insulators with commensurate antiferromagnetism. *Physical Review B*, 88(8):085406, may 2013.

[76] Steve M. Young and Charles L. Kane. Dirac Semimetals in Two Dimensions. *Physical Review Letters*, 115(12):126803, sep 2015.

[77] S. M. Young, S. Zaheer, J. C Y Teo, C. L. Kane, E. J. Mele, and A. M. Rappe. Dirac semimetal in three dimensions. *Physical Review Letters*, 108(14):140405, may 2012.

[78] Zhijun Wang, Yan Sun, Xing Qiu Chen, Cesare Franchini, Gang Xu, Hongming Weng, Xi Dai, and Zhong Fang. Dirac semimetal and topological phase transitions in A 3Bi (A=Na, K, Rb). *Physical Review B*, 85(19):195320, may 2012.

[79] Zhijun Wang, Hongming Weng, Quansheng Wu, Xi Dai, and Zhong Fang. Three-dimensional Dirac semimetal and quantum transport in Cd3As2. *Physical Review B*, 88(12):125427, sep 2013.

[80] Jing Wang. Antiferromagnetic Dirac semimetals in two dimensions. *Physical Review B*, 95(11):115138, mar 2017.

[81] A. Burkov. Topological semimetals. *Nature Materials*, 15(11):1145–1148, may 2016.

[82] Libor Šmejkal, Tomáš Jungwirth, and Jairo Sinova. Route towards Dirac and Weyl antiferromagnetic spintronics. *Physica Status Solidi - Rapid Research Letters*, 11(4), may 2017.

[83] H. B. Nielsen and M. Ninomiya. A no-go theorem for regularizing chiral fermions. *Physics Letters B*, 105(2-3):219–223, may 1981.

[84] Alexey A. Soluyanov, Dominik Gresch, Zhijun Wang, Quansheng Wu, Matthias Troyer, Xi Dai, and B. Andrei Bernevig. Type-II Weyl semimetals. *Nature*, 527(7579):495–498, nov 2015.

[85] Su Yang Xu, Ilya Belopolski, Nasser Alidoust, Madhab Neupane, Guang Bian, Chenglong Zhang, Raman Sankar, Guoqing Chang, Zhujun Yuan, Chi Cheng Lee, Shin Ming Huang, Hao Zheng, Jie Ma, Daniel S. Sanchez, Bao Kai Wang, Arun Bansil, Fangcheng Chou, Pavel P. Shibayev, Hsin Lin, Shuang Jia, and M. Zahid Hasan. Discovery of a Weyl fermion semimetal and topological Fermi arcs. *Science*, 349(6248):613–617, may 2015.

[86] B. Q. Lv, H. M. Weng, B. B. Fu, X. P. Wang, H. Miao, J. Ma, P. Richard, X. C. Huang, L. X. Zhao, G. F. Chen, Z. Fang, X. Dai, T. Qian, and H. Ding. Experimental discovery of Weyl semimetal TaAs. *Physical Review X*, 5(3):031013, may 2015.

[87] L. X. Yang, Z. K. Liu, Y. Sun, H. Peng, H. F. Yang, T. Zhang, B. Zhou, Y. Zhang, Y. F. Guo, M. Rahn, D. Prabhakaran, Z. Hussain, S. K. Mo, C. Felser, B. Yan, and Y. L. Chen. Weyl semimetal phase in the noncentrosymmetric compound TaAs. *Nature Physics*, 11(9):728–732, may 2015.

[88] Guoqing Chang, Bahadur Singh, Su-Yang Xu, Guang Bian, Shin-Ming Huang, Chuang-Han Hsu, Ilya Belopolski, Nasser Alidoust, Daniel S. Sanchez, Hao Zheng, Hong Lu, Xiao Zhang, Yi Bian, Tay-Rong Chang, Horng-Tay Jeng, Arun Bansil, Han Hsu, Shuang Jia, Titus Neupert, Hsin Lin, and M. Zahid Hasan. Magnetic and noncentrosymmetric Weyl fermion semimetals in the R AlGe family of compounds (R = rare earth). *Physical Review B*, 97(4):041104, jan 2018.

[89] Guoqing Chang, Benjamin J Wieder, Frank Schindler, Daniel S. Sanchez, Ilya Belopolski, Shin-Ming Huang, Bahadur Singh, Di Wu, Tay-Rong Chang, Titus Neupert, Su-Yang Xu, Hsin Lin, and M. Zahid Hasan. Topological quantum properties of chiral crystals. *Nature Materials*, 17(11):978–985, nov 2018.

[90] Bo Wan, Frank Schindler, Ke Wang, Kai Wu, Xiangang Wan, Titus Neupert, and Hai-Zhou Lu. Theory for the negative longitudinal magnetoresistance in the quantum limit of Kramers Weyl semimetals. *Journal of Physics: Condensed Matter*, 30(50):505501, dec 2018.

[91] Inti Sodemann and Liang Fu. Quantum Nonlinear Hall Effect Induced by Berry Curvature Dipole in Time-Reversal Invariant Materials. *Physical Review Letters*, 115(21), nov 2015.

[92] Qiong Ma, Su-Yang Xu, Huitao Shen, David MacNeill, Valla Fatemi, Tay-Rong Chang, Andrés M. Mier Valdivia, Sanfeng Wu, Zongzheng Du, Chuang-Han Hsu, Shiang Fang, Quinn D. Gibson, Kenji Watanabe, Takashi Taniguchi, Robert J. Cava, Efthimios Kaxiras, Hai-Zhou Lu, Hsin Lin, Liang Fu, Nuh Gedik, and Pablo Jarillo-Herrero. Observation of the nonlinear Hall effect under time-reversal-symmetric conditions. *Nature*, 565(7739):337–342, jan 2019.

[93] Jinyu Zou, Zhuoran He, and Gang Xu. The study of magnetic topological semimetals by first principles calculations. *npj Computational Materials*, 5(1):96, dec 2019.

[94] K. Kuroda, T. Tomita, M.-T. Suzuki, C. Bareille, A. A. Nugroho, P. Goswami, M. Ochi, M. Ikhlas, M. Nakayama, S. Akebi, R. Noguchi, R. Ishii, N. Inami, K. Ono, H. Kumigashira, A. Varykhalov, T. Muro, T. Koretsune, R. Arita, S. Shin, Takeshi Kondo, and S. Nakatsuji. Evidence for magnetic Weyl fermions in a correlated metal. *Nature Materials*, 16(11):1090–1095, sep 2017.

[95] J. Godinho, H. Reichlova, D. Kriegner, V. Novak, K. Olejnik, Z. Kaspar, Z. Soban, P Wadley, Richard P. Campion, R. M. Otxoa, P. E. Roy, J. Zelezny, T. Jungwirth, and J. Wunderlich. Electrically induced and detected Néel vector reversal in a collinear antiferromagnet. *Nature Communications*, 9:4686, 2018.

[96] Gerald D. Mahan. *Many-particle physics*. Kluwer Academic/Plenum Publishers, 2000.

[97] W. H. Kleiner. Space-time symmetry of transport coefficients. *Physical Review*, 142(2):318–326, may 1966.

[98] Satoru Hayami, Megumi Yatsushiro, Yuki Yanagi, and Hiroaki Kusunose. Classification of atomic-scale multipoles under crystallographic point groups and application to linear response tensors. *Physical Review B*, 98(16):165110, oct 2018.

[99] A. Crépieux and P. Bruno. Relativistic corrections in magnetic systems. *Physical Review B*, 64(9):094434, may 2001.

[100] Frank Freimuth, Stefan Blügel, and Yuriy Mokrousov. Spin-orbit torques in Co/Pt(111) and Mn/W(001) magnetic bilayers from first principles. *Physical Review B*, 90(17):174423, nov 2014.

[101] Jakub Železný, Yang Zhang, Claudia Felser, and Binghai Yan. Spin-Polarized Current in Noncollinear Antiferromagnets. *Physical Review Letters*, 119(18):187204, nov 2017.

[102] J. Železný, H. Gao, K. Výborný, J. Zemen, J. Mašek, Aurélien Manchon, J. Wunderlich, Jairo Sinova, and T. Jungwirth. Relativistic Néel-order fields induced by electrical current in antiferromagnets. *Physical Review Letters*, 113(15):157201, may 2014.

[103] P. Wadley, B. Howells, J. Železný, C. Andrews, V. Hills, Richard P. Campion, V. Novák, K. Olejník, F. Maccherozzi, S. S. Dhesi, S. Y. Martin, T. Wagner, J. Wunderlich, F. Freimuth, Y. Mokrousov, J. Kuneš, J. S. Chauhan, M. J. Grzybowski, A. W. Rushforth, Kw Edmond, B. L. Gallagher, and T. Jungwirth. Electrical switching of an antiferromagnet. *Science*, 351(6273):587–590, may 2016.

[104] S. Yu Bodnar, L. Šmejkal, I. Turek, T. Jungwirth, O. Gomonay, Jairo Sinova, A. A. Sapozhnik, H.-J. Elmers, M. Kläui, and M. Jourdan. Writing and reading antiferromagnetic Mn2Au by Néel spin-orbit torques and large anisotropic magnetoresistance. *Nature Communications*, 9(1):348, dec 2018.

[105] Hua Chen, Qian Niu, and A. H. Macdonald. Anomalous hall effect arising from noncollinear antiferromagnetism. *Physical Review Letters*, 112(1):017205, may 2014.

[106] J. Železný, H. Gao, Aurélien Manchon, Frank Freimuth, Yuriy Mokrousov, J. Zemen, J. Mašek, Jairo Sinova, and T. Jungwirth. Spin-orbit torques

in locally and globally noncentrosymmetric crystals: Antiferromagnets and ferromagnets. *Physical Review B*, 95(1):014403, may 2017.

[107] C L Kane and E J Mele. Quantum Spin Hall Effect in Graphene. *Physical Review Letters*, 95(22):226801, nov 2005.

[108] Akihiko Sekine and Kentaro Nomura. Axionic Antiferromagnetic Insulator Phase in a Correlated and Spin–Orbit Coupled System. *Journal of the Physical Society of Japan*, 83(10):104709, oct 2014.

[109] C. Ciccarelli, L. Anderson, V. Tshitoyan, A. J. Ferguson, F. Gerhard, C. Gould, L. W. Molenkamp, J. Gayles, J. Železný, L. Šmejkal, Z. Yuan, Jairo Sinova, F. Freimuth, and T. Jungwirth. Room-temperature spin-orbit torque in NiMnSb. *Nature Physics*, 12(9):855–860, may 2016.

[110] Haijun Zhang, Chao-Xing Liu, Xiao-Liang Qi, Xi Dai, Zhong Fang, and Shou-Cheng Zhang. Topological insulators in Bi2Se3, Bi2Te3 and Sb2Te3 with a single Dirac cone on the surface. *Nature Physics*, 5(6):438–442, may 2009.

[111] Xiuwen Zhang, Qihang Liu, Jun Wei Luo, Arthur J. Freeman, and Alex Zunger. Hidden spin polarization in inversion-symmetric bulk crystals. *Nature Physics*, 10(5):387–393, may 2014.

[112] Youichi Yanase. Magneto-electric effect in three-dimensional coupled zigzag chains. *Journal of the Physical Society of Japan*, 83(1):014703, 2014.

[113] Bohm-Jung Yang, Troels Arnfred Bojesen, Takahiro Morimoto, and Akira Furusaki. Topological semimetals protected by off-centered symmetries in nonsymmorphic crystals. *PHYSICAL REVIEW B*, 95:75135, 2017.

[114] X. Marti, I. Fina, C. Frontera, Jian Liu, P. Wadley, Q. He, R. J. Paull, J. D. Clarkson, J. Kudrnovský, I. Turek, J. Kuneš, D. Yi, Jiun-Haw Chu, C. T. Nelson, L. You, E. Arenholz, S. Salahuddin, J. Fontcuberta, T. Jungwirth, and R. Ramesh. Room-temperature antiferromagnetic memory resistor. *Nature Materials*, 13(4):367–374, apr 2014.

[115] Tomáš Bzdušek, Quansheng Wu, Andreas Rüegg, Manfred Sigrist, and Alexey A Soluyanov. Nodal-chain metals. *Nature Publishing Group*, 538, 2016.

[116] Libor Šmejkal, Rafael González-Hernández, Tomáš Jungwirth, and Jairo Sinova. Crystal Hall effect in Collinear Antiferromagnets. *arXiv:1901.00445*, 2019.

[117] Jiaheng Li, Yang Li, Shiqiao Du, Zun Wang, Bing-Lin Gu, Shou-Cheng Zhang, Ke He, Wenhui Duan, and Yong Xu. Intrinsic magnetic topological insulators in van der Waals layered MnBi2Te4-family materials. *Science Advances*, 5(6):eaaw5685, aug 2018.

[118] Paul Strange. *Relativistic Quantum Mechanics*. Cambridge University Press, Cambridge, 1998.

[119] Roger. Penrose. *The road to reality : a complete guide to the laws of the universe.* Vintage Books, 2007.

[120] Jülich Summer School. *Schlüsseltechnologien / Key Technologies Band / Volume 74 Computing Solids Models, ab-initio methods and supercomputing Lecture Notes Computing Solids Models, ab-initio methods and supercomputing Lecture Notes.* 2014.

[121] J Kübler. *Theory of Itinerant Electron Magnetism.* International Series of Monographs on Physics. OUP Oxford, 2000.

[122] H. J. F. Jansen, G. S. Schneider, and H. Y. Wang. Calculation of Magnetocrystalline Anisotropy in Transition Metals. pages 57–100. 2003.

[123] E. M. (Evgenii Mikhailovich) Lifshits and L. P. (Lev Petrovich) Pitaevskii. *Relativistic quantum theory.* Pergamon Press, 1974.

[124] W. Hohenberg, P.; Kohn. Hohenberg, P.; Kohn, W. *Phys. Rev.*, 136(3B):B864–B871, may 1964.

[125] W. Kohn and L. J. Sham. Self-consistent equations including exchange and correlation effects. *Physical Review*, 140(4A):A1133–A1138, may 1965.

[126] Ph Kurz, F. Förster, L. Nordström, G. Bihlmayer, and Stefan Blügel. Ab initio treatment of noncollinear magnets with the full-potential linearized augmented plane wave method. *Physical Review B*, 69(2):24415, may 2004.

[127] H. Eschrig, G. Seifert, and P. Ziesche. Current density functional theory of quantum electrodynamics. *Solid State Communications*, 56(9):777–780, dec 1985.

[128] Zhiyong Zhu, Yingchun Cheng, and Udo Schwingenschlögl. Band inversion mechanism in topological insulators: A guideline for materials design. *Physical Review B*, 85(23):235401, jun 2012.

[129] L. D. (Lev Davidovich) Landau and E. M. (Evgenii Mikhailovich) Lifshits. *Quantum mechanics : non-relativistic theory.* Butterworth-Heinemann, 1991.

[130] D D Koelling and B N Harmon. A technique for relativistic spin-polarised calculations. *Journal of Physics C: Solid State Physics*, 10(16):3107–3114, aug 1977.

[131] A H MacDonald, W E Picket, and D D Koelling. A linearised relativistic augmented-plane-wave method utilising approximate pure spin basis functions. *Journal of Physics C: Solid State Physics*, 13(14):2675–2683, may 1980.

[132] Soner Steiner, Sergii Khmelevskyi, Martijn Marsmann, and Georg Kresse. Calculation of the magnetic anisotropy with projected-augmented-wave methodology and the case study of disordered fe 1 x co x alloys. *Physical Review B*, 93(22):224425, jun 2016.

[133] O. Krogh Andersen. Linear methods in band theory. *Physical Review B*, 12(8):3060–3083, oct 1975.

[134] S. H. Vosko, L. Wilk, and M. Nusair. Accurate spin-dependent electron liquid correlation energies for local spin density calculations: a critical analysis. *Canadian Journal of Physics*, 58(8):1200–1211, may 1980.

[135] John P. Perdew, Adrienn Ruzsinszky, Jianmin Tao, Viktor N. Staroverov, Gustavo E. Scuseria, and Gábor I. Csonka. Prescription for the design and selection of density functional approximations: More constraint satisfaction with fewer fits. *The Journal of Chemical Physics*, 123(6):062201, aug 2005.

[136] *Computing Solids Models, ab-initio methods and supercomputing Lecture Notes Computing Solids Models, ab-initio methods and supercomputing Lecture Notes.* 2014.

[137] John P. Perdew, Kieron Burke, and Matthias Ernzerhof. Generalized gradient approximation made simple. *Physical Review Letters*, 77(18):3865–3868, may 1996.

[138] John P. Perdew, Kieron Burke, and Matthias Ernzerhof. Generalized Gradient Approximation Made Simple [Phys. Rev. Lett. 77, 3865 (1996)]. *Physical Review Letters*, 78(7):1396–1396, feb 1997.

[139] Yingkai Zhang and Weitao Yang. Comment on “Generalized Gradient Approximation Made Simple”. *Physical Review Letters*, 80(4):890–890, jan 1998.

[140] Vladimir I. Anisimov, Jan Zaanen, and Ole K. Andersen. Band theory and Mott insulators: Hubbard U instead of Stoner I. *Physical Review B*, 44(3):943–954, jul 1991.

[141] S. L. Dudarev, G. A. Botton, S. Y. Savrasov, C. J. Humphreys, and A. P. Sutton. Electron-energy-loss spectra and the structural stability of nickel oxide: An LSDA+U study. *Physical Review B*, 57(3):1505–1509, jan 1998.

[142] Eva Pavarini, Erik Koch, and Shiwei Zhang. *Modeling and Simulation Many-Body Methods for Real Materials Many-Body Methods for Real Materials.*

[143] Stefan Blügel. A 7 Density Functional Theory in Practice. Technical report.

[144] A. K. Rajagopal and J. Callaway. Inhomogeneous Electron Gas. *Physical Review B*, 7(5):1912–1919, mar 1973.

[145] H. Ebert. Two ways to perform spin-polarized relativistic linear muffin-tin-orbital calculations. *Physical Review B*, 38(14):9390–9397, nov 1988.

[146] VP Antropov IV Solov'ev, AB Shik. New method for calculating the electronic structure of magnetic crystals containing heavy d and f elements. *Sov. Phys. Solid State*, 1989.

[147] I. V. Solovyev, A. I. Liechtenstein, V. A. Gubanov, V. P. Antropov, and O. K. Andersen. Spin-polarized relativistic linear-muffin-tin-orbital method: Volume-dependent electronic structure and magnetic moment of plutonium. *Physical Review B*, 43(18):14414–14422, jun 1991.

[148] Alexander B Shick, A B Shick, V Drchal, J Kudrnovsky, and P Weinberger. Relativistic first-principles electronic structure theory of random magnetic alloys. History of Science View project Forbidden Music View project Electronic structure and magnetic properties of random alloys: Fully relativistic spin-polarized linear muffi. Technical report, 1996.

[149] Hans L. Skriver. *The LMTO Method*, volume 41 of *Springer Series in Solid-State Sciences*. Springer Berlin Heidelberg, Berlin, Heidelberg, 1984.

[150] Peter Weinberger Ilja Turek, Václav Drchal, Josef Kudrnovsky, Mojmír Sob. *Electronic Structure of Disordered Alloys, Surfaces and Interfaces.* Springer, 1997.

[151] Rajendra Prasad. *Electronic Structure of Materials.* Taylor & Francis, 2014.

[152] I. Turek, J. Kudrnovsky, and V. Drchal. Ab initio theory of galvanomagnetic phenomena in ferromagnetic metals and disordered alloys. *Physical Review B*, 86(1):014405, jul 2012.

[153] Antonios Gonis. *Green functions for ordered and disordered systems.* 1992.

[154] Paul Soven. Coherent-Potential Model of Substitutional Disordered Alloys. *Physical Review*, 156(3):809–813, apr 1967.

[155] D. W. Taylor. Vibrational Properties of Imperfect Crystals with Large Defect Concentrations. *Physical Review*, 156(3):1017–1029, apr 1967.

[156] B. Velický, S. Kirkpatrick, and H. Ehrenreich. Single-Site Approximations in the Electronic Theory of Simple Binary Alloys. *Physical Review*, 175(3):747–766, nov 1968.

[157] Eleftherios N. Economou. *Green's Functions in Quantum Physics*, volume 7 of *Springer Series in Solid-State Sciences.* Springer Berlin Heidelberg, Berlin, Heidelberg, 2006.

[158] David Wagenknecht, Libor Šmejkal, Zdeněk Kašpar, Jairo Sinova, Tomáš Jungwirth, Josef Kudrnovsky, Karel Carva, and Ilja Turek. Temperature-dependent resistivity and anomalous Hall effect in NiMnSb from first principles. *Physical Review B*, 99(17):174433, may 2019.

[159] Ilja Turek. Bodove poruchy a neusporadane slitiny, 2007.

[160] A. Bastin, C. Lewiner, O. Betbeder-matibet, and P. Nozieres. Quantum oscillations of the hall effect of a fermion gas with random impurity scattering. *Journal of Physics and Chemistry of Solids*, 32(8):1811–1824, jan 1971.

[161] A. Crépieux and P. Bruno. Theory of the anomalous Hall effect from the Kubo formula and the Dirac equation. *Physical Review B*, 64(1):014416, may 2001.

[162] I. Turek, J. Kudrnovsky, and V. Drchal. Fermi sea term in the relativistic linear muffin-tin-orbital transport theory for random alloys. *Physical Review B*, 89(6):064405, feb 2014.

[163] K Carva, I Turek, J Kudrnovsky, and O Bengone. Disordered magnetic multilayers: Electron transport within the coherent potential approximation. *Physical Review B*, 73(14):144421, apr 2006.

[164] I. Turek, J. Kudrnovsky, V. Drchal, L. Szunyogh, and P. Weinberger. Interatomic electron transport by semiempirical and ab initio tight-binding approaches. *Physical Review B*, 65(12):125101, feb 2002.

[165] Tomas Zalezak. *Relativisticka teorie transportnich vlastnosti magnetickych slitin*. PhD thesis, 2008.

[166] D. R. Hamann. Semiconductor charge densities with hard-core and soft-core pseudopotentials. *Physical Review Letters*, 42(10):662–665, may 1979.

[167] P. E. Blöchl. Projector augmented-wave method. *Physical Review B*, 50(24):17953–17979, dec 1994.

[168] G. Kresse and D. Joubert. From ultrasoft pseudopotentials to the projector augmented-wave method. *Phys. Rev. B*, 59:1758–1775, Jan 1999.

[169] Ivo Souza, Nicola Marzari, and David Vanderbilt. Maximally localized Wannier functions for entangled energy bands. *Physical Review B*, 65(3):1–13, may 2002.

[170] Nicola Marzari and David Vanderbilt. Maximally localized generalized Wannier functions for composite energy bands. *Physical Review B*, 56(20):12847–12865, may 1997.

[171] Nicola Marzari, Arash A. Mostofi, Jonathan R. Yates, Ivo Souza, and David Vanderbilt. Maximally localized Wannier functions: Theory and applications. *Reviews of Modern Physics*, 84(4):1419–1475, oct 2012.

[172] David Wagenknecht, Josef Kudrnovský, Libor Šmejkal, Karel Carva, and Ilja Turek. Electrical transport with temperature-induced spin disorder in NiMnSb. *Journal of Magnetism and Magnetic Materials*, 474:517–521, mar 2019.

[173] F. MácA, J. Mašek, O. Stelmakhovych, X. Martí, H. Reichlová, K. Uhlířová, P. Beran, P. Wadley, V. Novák, and T. Jungwirth. Room-temperature antiferromagnetism in CuMnAs. *Journal of Magnetism and Magnetic Materials*, 324(8):1606–1612, may 2012.

[174] I A Campbell, A Fert, and O Jaoul. The spontaneous resistivity anisotropy in Ni-based alloys. *Journal of Physics C: Solid State Physics*, 3(1S):S95–S101, may 1970.

[175] Satoshi Kokado, Masakiyo Tsunoda, Kikuo Harigaya, and Akimasa Sakuma. Anisotropic Magnetoresistance Effects in Fe, Co, Ni, Fe 4 N, and Half-Metallic Ferromagnet: A Systematic Analysis. *Journal of the Physical Society of Japan*, 81(2):024705, feb 2012.

[176] Alexis P. Malozemoff. Anisotropic magnetoresistance with cubic anisotropy and weak ferromagnetism: A new paradigm. *Physical Review B*, 34(3):1853–1863, aug 1986.

[177] Karel Výborný, Jan Kučera, Jairo Sinova, A. W. Rushforth, B. L. Gallagher, and T. Jungwirth. Microscopic mechanism of the noncrystalline anisotropic magnetoresistance in (Ga,Mn)As. *Physical Review B*, 80(16):165204, may 2009.

[178] A. W. Rushforth, K. Výborný, C. S. King, K. W. Edmonds, Richard P. Campion, C. T. Foxon, J. Wunderlich, A. C. Irvine, V. Novák, K. Olejník, A. A. Kovalev, Jairo Sinova, T. Jungwirth, and B. L. Gallagher. The origin and control of the sources of AMR in (Ga,Mn)As devices. *Journal of Magnetism and Magnetic Materials*, 321(8):1001–1008, may 2009.

[179] P. Wadley, V. Novák, Richard P. Campion, C. Rinaldi, X. Martí, H. Reichlová, J. Železný, J. Gazquez, M. A. Roldan, M. Varela, D. Khalyavin, S. Langridge, D. Kriegner, F. MácA, J. Mašek, R. Bertacco, V. Holý, A. W. Rushforth, K. W. Edmonds, B. L. Gallagher, C. T. Foxon, J. Wunderlich, and T. Jungwirth. Tetragonal phase of epitaxial room-temperature antiferromagnet CuMnAs. *Nature Communications*, 4:2322, may 2013.

[180] P. Wadley, V. Hills, M. R. Shahedkhah, K. W. Edmonds, Richard P. Campion, V. Novák, B. Ouladdiaf, D. Khalyavin, S. Langridge, V. Saidl, P. Nemec, A. W. Rushforth, B. L. Gallagher, S. S. Dhesi, F. MacCherozzi, J. Železný, and T. Jungwirth. Antiferromagnetic structure in tetragonal CuMnAs thin films. *Scientific Reports*, 5:17079, may 2015.

[181] Leslie M. Schoop, Mazhar N. Ali, Carola Straßer, Andreas Topp, Andrei Varykhalov, Dmitry Marchenko, Viola Duppel, Stuart S.P. Parkin, Bettina V. Lotsch, and Christian R. Ast. Dirac cone protected by nonsymmorphic symmetry and three-dimensional Dirac line node in ZrSiS. *Nature Communications*, 7(May):11696, may 2016.

[182] Joachim Mündelein and Hans-Uwe Schuster. Darstellung und Kristallstruktur der Verbindungen MnCuX (X = P, As, PxAs1-x) Preparation and Crystal Structure of Compounds MnCuX (X = P, As, PxAs1-x). Technical report, 1992.

[183] Chen Fang, Yige Chen, Hae Young Kee, and Liang Fu. Topological nodal line semimetals with and without spin-orbital coupling. *Physical Review B*, 92(8):081201, may 2015.

[184] W. F. Brinkman and R. J. Elliott. Theory of Spin-Space Groups. *Proceedings of the Royal Society A: Mathematical, Physical and Engineering Sciences*, 294(1438):343–358, may 1966.

[185] FLEUR code.

[186] K. Dewhurst. Elk code.

[187] Zhijun Wang, A Alexandradinata, R J Cava, and & B Andrei Bernevig. Hourglass fermions. *Nature*, 532, 2016.

[188] J Zhang, Y.-H Chan, C.-K Chiu, M G Vergniory, L M Schoop, and A P Schnyder. Topological band crossings in hexagonal materials. *Physical Review Materials*, 2:74201, 2018.

[189] Klára Uhlířová, Elen Duverger-Nédellec, Ross H. Colman, Jiří Volný, Barbora Vondráčková, and Karel Carva. The stability and physical properties of the tetragonal phase of bulk CuMnAs antiferromagnet. *Journal of Alloys and Compounds*, 771:680–685, jan 2019.

[190] Youngseok Kim, Kisung Kang, André Schleife, and Matthew J. Gilbert. Voltage-induced switching of an antiferromagnetically ordered topological Dirac semimetal. *Physical Review B*, 97(13):134415, apr 2018.

[191] Kevin Garello, Ioan Mihai Miron, Can Onur Avci, Frank Freimuth, Yuriy Mokrousov, Stefan Blügel, Stéphane Auffret, Olivier Boulle, Gilles Gaudin, and Pietro Gambardella. Symmetry and magnitude of spin-orbit torques in ferromagnetic heterostructures. *Nature Nanotechnology*, 8(8):587–593, may 2013.

[192] Condensed Matter Field Theory - Alexander Altland, Ben D. Simons - Google Books.

[193] T. R. Mcguire and R. I. Potter. Anisotropic Magnetoresistance in Ferromagnetic 3D Alloys. *IEEE Transactions on Magnetics*, 11(4):1018–1038, may 1975.

[194] H. Ebert, A. Vernes, and J. Banhart. Magnetoresistance, Anisotropic. *Encyclopedia of Materials: Science and Technology*, pages 5079–5083, jan 2001.

[195] W. Thomson. On the Electro-Dynamic Qualities of Metals:–Effects of Magnetization on the Electric Conductivity of Nickel and of Iron. *Proceedings of the Royal Society of London*, 8(0):546–550, may 1856.

[196] J. M. Daughton. Magnetoresistive memory technology. *Thin Solid Films*, 216(1):162–168, may 1992.

[197] B. G. Park, J. Wunderlich, X. Martí, V. Holý, Y. Kurosaki, M. Yamada, H. Yamamoto, A. Nishide, J. Hayakawa, H. Takahashi, A. B. Shick, and T. Jungwirth. A spin-valve-like magnetoresistance of an antiferromagnet-based tunnel junction. *Nature Materials*, 10(5):347–351, may 2011.

[198] D. Kriegner, K. Výborný, K. Olejník, H. Reichlová, V. Novák, X. Marti, J. Gazquez, V. Saidl, P. Němec, V. V. Volobuev, G. Springholz, V. Holý, and T. Jungwirth. Multiple-stable anisotropic magnetoresistance memory in antiferromagnetic MnTe. *Nature Communications*, 7:11623, may 2016.

[199] K. Olejník, V. Schuler, X. Marti, V. Novák, Z. Kašpar, P. Wadley, Richard P. Campion, K. W. Edmonds, B. L. Gallagher, J. Garces, M. Baumgartner, P. Gambardella, and T. Jungwirth. Antiferromagnetic CuMnAs multi-level memory cell with microelectronic compatibility. *Nature Communications*, 8:15434, may 2017.

[200] J Banhart and H. Ebert. First-Principles Theory of Spontaneous-Resistance Anisotropy and Spontaneous Hall Effect in Disordered Ferromagnetic Alloys. *Europhysics Letters (EPL)*, 32(November):517–522, nov 2018.

[201] H. Ebert, A. Vernes, and J. Banhart. The influence of spin–orbit coupling and a current dependent potential on the residual resistivity of disordered magnetic alloys. *Solid State Communications*, 113(2):103–107, nov 1999.

[202] J Smit. Magnetoresistance of ferromagnetic metals and alloys at low temperatures. *Physica*, 17(6):612–627, jun 1951.

[203] E. De Ranieri, A. W. Rushforth, K. Výborný, U. Rana, E. Ahmad, Richard P. Campion, C. T. Foxon, B. L. Gallagher, A. C. Irvine, J. Wunderlich, and T. Jungwirth. Lithographically and electrically controlled strain effects on anisotropic magnetoresistance in (Ga,Mn)As. *New Journal of Physics*, 10(6):065003, jun 2008.

[204] Nguyen Anh Tuan and Nguyen Phuc Duong. Structural, magnetic, and magnetotransport properties of NiMnSb thin films deposited by flash evaporation. *Applied Physics Letters*, 99(16):162507, oct 2011.

[205] B. Howells, M. Wang, K. W. Edmonds, P. Wadley, R. P. Campion, A. W. Rushforth, C. T. Foxon, and B. L. Gallagher. Crystalline anisotropic magnetoresistance in quaternary ferromagnetic semiconductor (Ga,Mn)(As,Sb). *Applied Physics Letters*, 102(5):052407, feb 2013.

[206] A. Yamasaki, L. Chioncel, A. I. Lichtenstein, and O. K. Andersen. Model Hamiltonian parameters for half-metallic ferromagnets NiMnSb and Cr O 2. *Physical Review B*, 74(2):024419, jul 2006.

[207] F. Gerhard, C. Schumacher, C. Gould, and L. W. Molenkamp. Control of the magnetic in-plane anisotropy in off-stoichiometric NiMnSb. *Journal of Applied Physics*, 115(9):094505, mar 2014.

[208] I Galanakis and Ph Mavropoulos. Spin-polarization and electronic properties of half-metallic Heusler alloys calculated from first principles. *Journal of Physics: Condensed Matter*, 19(31):315213, aug 2007.

[209] J Rusz, L Bergqvist, J Kudrnovsky, and I Turek. Exchange interactions and Curie temperatures in Ni 2 x MnSb alloys: First-principles study.

[210] C. Hordequin, J. Pierre, and R. Currat. Magnetic excitations in the half-metallic NiMnSb ferromagnet: From Heisenberg-type to itinerant behaviour. *Journal of Magnetism and Magnetic Materials*, 162(1):75–84, sep 1996.

[211] Fangfang Wang, Tadashi Fukuhara, Kunihiko Maezawa, Katsuhiko Nishimura, Fumihiko Shimizu, and Shinichi Masubuchi. Synthesis and Characterization of Single Crystal NiMnSb. *Japanese Journal of Applied Physics*, 49(2):025502, feb 2010.

[212] M J Otto, R A M van Woerden, P J van der Valk, J Wijngaard, C F van Bruggen, and C Haas. Half-metallic ferromagnets. II. Transport properties of NiMnSb and related inter-metallic compounds. *Journal of Physics: Condensed Matter*, 1(13):2351–2360, apr 1989.

[213] J. Kudrnovsky, V. Drchal, and I. Turek. Physical properties of FeRh alloys: The antiferromagnetic to ferromagnetic transition. *Physical Review B*, 91(1):014435, may 2015.

[214] Markus Meinert, Dominik Graulich, and Tristan Matalla-Wagner. Electrical Switching of Antiferromagnetic Mn2Au and the Role of Thermal Activation. *Physical Review Applied*, 9(6):064040, jun 2018.

[215] Vitoria M.T.S. Barthem, C. V. Colin, H. Mayaffre, M. H. Julien, and D. Givord. Revealing the properties of Mn 2 Au for antiferromagnetic spintronics. *Nature Communications*, 4:2892, may 2013.

[216] A. B. Shick, S. Khmelevskyi, O. N. Mryasov, J. Wunderlich, and T. Jungwirth. Spin-orbit coupling induced anisotropy effects in bimetallic antiferromagnets: A route towards antiferromagnetic spintronics. *Physical Review B*, 81(21):212409, may 2010.

[217] M. Jourdan, H. Bräuning, A. Sapozhnik, H. J. Elmers, H. Zabel, and M. Kläui. Epitaxial Mn2Au thin films for antiferromagnetic spintronics. *Journal of Physics D: Applied Physics*, 48(38):385001, may 2015.

[218] Hongbin Zhang, Kristjan Haule, and David Vanderbilt. Metal-Insulator Transition and Topological Properties of Pyrochlore Iridates. *Physical Review Letters*, 118(2):026404, may 2017.

[219] Eve Emmanouilidou, Huibo Cao, Peizhe Tang, Xin Gui, Chaowei Hu, Bing Shen, Junyi Wu, Shou Cheng Zhang, Weiwei Xie, and Ni Ni. Magnetic order induces symmetry breaking in the single-crystalline orthorhombic CuMnAs semimetal. *Physical Review B*, 96(22):1–5, may 2017.

[220] M. C. Rahn, J.-R. Soh, S. Francoual, L. S. I. Veiga, J. Strempfer, J. Mardegan, D. Y. Yan, Y. F. Guo, Y. G. Shi, and A. T. Boothroyd. Coupling of magnetic order and charge transport in the candidate dirac semimetal eucd$_2$as$_2$. *Phys. Rev. B*, 97:214422, Jun 2018.

[221] Zhiyong Lin, Chongze Wang, Pengdong Wang, Seho Yi, Lin Li, Qiang Zhang, Yifan Wang, Zhongyi Wang, Yan Sun, Zhe Sun, Jun-Hyung Cho, Changgan Zeng, and Zhenyu Zhang. Dirac Fermions in Antiferromagnetic FeSn Kagome Lattices with Combined Space Inversion and Time Reversal Symmetry. jun 2019.

[222] Zhi-Guo Chen, Luyang Wang, Yu Song, Xingye Lu, Huiqian Luo, Chenglin Zhang, Pengcheng Dai, Zhiping Yin, Kristjan Haule, and Gabriel Kotliar. Two-Dimensional Massless Dirac Fermions in Antiferromagnetic AFe2As2. *Physical Review Letters*, 119(9):096401, aug 2017.

[223] Yuya Ominato, Koji Kobayashi, and Kentaro Nomura. Anisotropic magnetotransport in Dirac-Weyl magnetic junctions. *PHYSICAL REVIEW B*, 95:85308, 2017.

[224] E. H. Hall. On a New Action of the Magnet on Electric Currents. *American Journal of Mathematics*, 2(3):287, sep 1879.

[225] E.H. Hall. On the “Rotational Coefficient” in nickel and cobalt. *The London, Edinburgh, and Dublin Philosophical Magazine and Journal of Science*, 12(74):157–172, sep 1881.

[226] J. Smit. The spontaneous hall effect in ferromagnetics I. *Physica*, 21(6-10):877–887, jan 1955.

[227] J. Smit. The spontaneous hall effect in ferromagnetics II. *Physica*, 24(1-5):39–51, may 1958.

[228] Robert Karplus and J. M. Luttinger. Hall effect in ferromagnetics. *Physical Review*, 95(5):1154–1160, may 1954.

[229] Yo MacHida, Satoru Nakatsuji, Shigeki Onoda, Takashi Tayama, and Toshiro Sakakibara. Time-reversal symmetry breaking and spontaneous Hall effect without magnetic dipole order. *Nature*, 463(7278):210–213, may 2010.

[230] A. Neubauer, C. Pfleiderer, B. Binz, A. Rosch, R. Ritz, P. G. Niklowitz, and P. Böni. Topological Hall Effect in the A Phase of MnSi. *Physical Review Letters*, 102(18):186602, may 2009.

[231] Satoru Nakatsuji, Naoki Kiyohara, and Tomoya Higo. Large anomalous Hall effect in a non-collinear antiferromagnet at room temperature. *Nature*, 527(7577):212–215, may 2015.

[232] Ajaya K. Nayak, Julia Erika Fischer, Yan Sun, Binghai Yan, Julie Karel, Alexander C. Komarek, Chandra Shekhar, Nitesh Kumar, Walter Schnelle, Jürgen Kübler, Claudia Felser, and Stuart S.P. Parkin. Large anomalous Hall effect driven by a nonvanishing Berry curvature in the noncolinear antiferromagnet Mn3Ge. *Science Advances*, 2(4):e1501870–e1501870, may 2016.

[233] J Wu, A T Bollinger, X He, and I Božović. Spontaneous breaking of rotational symmetry in copper oxide superconductors. *Nature*, 547(7664):432–435, jul 2017.

[234] Christoph Sürgers, Gerda Fischer, Patrick Winkel, and Hilbert V. Löhneysen. Large topological Hall effect in the non-collinear phase of an antiferromagnet. *Nature Communications*, 5:3400, may 2014.

[235] Nirmal J. Ghimire, A. S. Botana, J. S. Jiang, Junjie Zhang, Y.-S. Chen, and J. F. Mitchell. Large anomalous Hall effect in the chiral-lattice antiferromagnet CoNb3S6. *Nature Communications*, 9(1):3280, dec 2018.

[236] T. Suzuki, R. Chisnell, A. Devarakonda, Y. T. Liu, W. Feng, D. Xiao, J. W. Lynn, and J. G. Checkelsky. Large anomalous Hall effect in a half-Heusler antiferromagnet. *Nature Physics*, 12(12):1119–1123, may 2016.

[237] LD Landau and EM Lifshitz. Electrodynamics of Continuous Media Course of Theoretical Physics. may 1965.

[238] F. E. Neumann. Vorlesungen über die Theorie der Elastizität der festen Körper und des Lichtäthers. In *Leipzig, B. G. Teubner-Verlag, edited by O. E. Meyer*. 1885.

[239] Robert E. (Robert Everest) Newnham. *Properties of materials : anisotropy, symmetry, structure*. Oxford University Press, 2005.

[240] M. Seemann, D. Ködderitzsch, S. Wimmer, and H. Ebert. Symmetry-imposed shape of linear response tensors. *Physical Review B*, 92(15):155138, oct 2015.

[241] Lorenzo Vistoli, Wenbo Wang, Anke Sander, Qiuxiang Zhu, Blai Casals, Rafael Cichelero, Agnès Barthélémy, Stéphane Fusil, Gervasi Herranz, Sergio Valencia, Radu Abrudan, Eugen Weschke, Kazuki Nakazawa, Hiroshi Kohno, Jacobo Santamaria, Weida Wu, Vincent Garcia, and Manuel Bibes. Giant topological Hall effect in correlated oxide thin films. *Nature Physics*, pages 67–72, oct 2018.

[242] Z. H. Zhu, J. Strempfer, R. R. Rao, J. Pelliciari, Y. Choi, T. Kawaguchi, H. You, Y. Shao-Horn, and R. Comin. Anomalous Antiferromagnetism in Metallic RuO2 Determined by Resonant X-ray Scattering. *ArXiv e-prints*, (1806.02036), jun 2018.

[243] Michael. Tinkham. *Group theory and quantum mechanics*. Dover Publications, 2003.

[244] Samuel V Gallego, J Manuel Perez-Mato, Luis Elcoro, Emre S Tasci, Robert M Hanson, Mois I Aroyo, and Gotzon Madariaga. MAGNDATA: towards a database of magnetic structures. II. The incommensurate case. *J. Appl. Cryst*, 49:1941–1956, 2016.

[245] Samuel V Gallego, J Manuel Perez-Mato, Luis Elcoro, Emre S Tasci, Robert M Hanson, Koichi Momma, Mois I Aroyo, and Gotzon Madariaga. MAGNDATA: towards a database of magnetic structures. I. The commensurate case. *J. Appl. Cryst*, 49:1750–1776, 2016.

[246] A. S. Borovik-Romanov, H. Grimmer, and M. Kenzelmann. Magnetic properties. pages 106–152. dec 2013.

[247] E.A. Turov. *Physical properties of magnetically ordered crystals*. Academic Press, New York, 1965.

[248] R. C. Fivaz. Transport Theory for Ferromagnets. *Physical Review*, 183(2):586–594, jul 1969.

[249] Eric Roman, Yuriy Mokrousov, and Ivo Souza. Orientation Dependence of the Intrinsic Anomalous Hall Effect in hcp Cobalt. *Physical Review Letters*, 103(9):097203, aug 2009.

[250] S. Shtrikman and H. Thomas. Remarks on linear magneto-resistance and magneto-heat-conductivity. *Solid State Communications*, 3(7):147–150, jul 1965.

[251] H. Grimmer. General relations for transport properties in magnetically ordered crystals. *Acta Crystallographica Section A*, 49(5):763–771, may 1993.

[252] Hans Grimmer. Thermoelectric transport properties in magnetically ordered crystals. *Acta Crystallographica Section A Foundations and Advances*, 73(4):333–345, jul 2017.

[253] I E Dzialoshinskii. Thermodynamic Theory of Weak Ferromagnetism In Antiferromagnetic Substances. *J. Exptl. Theoret. Phys. (U.S.S.R.)*, 5(6):1547–1562, 1957.

[254] Tôru Moriya. Anisotropic superexchange interaction and weak ferromagnetism. *Physical Review*, 120(1):91–98, may 1960.

[255] D.A. Smith. New mechanisms for magnetic anisotropy in localised S-state moment materials. *Journal of Magnetism and Magnetic Materials*, 1(3):214–225, jan 1976.

[256] A. Fert and Peter M. Levy. Role of Anisotropic Exchange Interactions in Determining the Properties of Spin-Glasses. *Physical Review Letters*, 44(23):1538–1541, jun 1980.

[257] I. Dzyaloshinsky. A thermodynamic theory of “weak” ferromagnetism of antiferromagnetics. *Journal of Physics and Chemistry of Solids*, 4(4):241–255, jan 1958.

[258] L. Szunyogh, B. Lazarovits, L. Udvardi, J. Jackson, and U. Nowak. Giant magnetic anisotropy of the bulk antiferromagnets IrMn and IrMn3from first principles. *Physical Review B*, 79(2):020403, may 2009.

[259] M. Elhajal, B. Canals, and C. Lacroix. Symmetry breaking due to Dzyaloshinsky-Moriya interactions in the kagomé lattice. *Physical Review B*, 66(1):014422, jul 2002.

[260] E. V. Gomonaj and V. A. L’vov. Phenomenologic study of phase transitions in noncollinear antiferromagnets of metallic perovskite type. *Phase Transitions*, 38(1):15–31, may 1992.

[261] Olena Gomonay. Berry-phase effects and electronic dynamics in a noncollinear antiferromagnetic texture. *Physical Review B*, 91(14):144421, may 2015.

[262] Weifeng Zhang, Wei Han, See Hun Yang, Yan Sun, Yang Zhang, Binghai Yan, and Stuart S.P. Parkin. Giant facet-dependent spin-orbit torque and spin Hall conductivity in the triangular antiferromagnet IrMn3. *Science Advances*, 2(9):e1600759, may 2016.

[263] Z. Q. Liu, H. Chen, J. M. Wang, J. H. Liu, K. Wang, Z. X. Feng, H. Yan, X. R. Wang, C. B. Jiang, J. M. D. Coey, and A. H. MacDonald. Electrical switching of the topological anomalous Hall effect in a non-collinear antiferromagnet above room temperature. *Nature Electronics*, 1(3):172–177, may 2018.

[264] I E Dzialoshinskii. The mangetic structure of fluorides of the transition metals. *JETP*, 33:1454–1456, 1957.

[265] A S Borovik-Romanov, A N Bazhan, and N M Kreines. The weak ferromagnetism of NiF2. *JETP*, 1974.

[266] Shigeki Onoda, Naoyuki Sugimoto, and Naoto Nagaosa. Intrinsic versus extrinsic anomalous hall effect in ferromagnets. *Physical Review Letters*, 97(12):126602, may 2006.

[267] L. Berger. Side-Jump Mechanism for the Hall Effect of Ferromagnets. *Physical Review B*, 2(11):4559–4566, dec 1970.

[268] Masaru Onoda and Naoto Nagaosa. Topological Nature of Anomalous Hall Effect in Ferromagnets. *Journal of the Physical Society of Japan*, 71(1):19–22, may 2002.

[269] Ganesh Sundaram and Qian Niu. Wave-packet dynamics in slowly perturbed crystals: gradient corrections and berry-phase effects. *Physical Review B*, 59(23):14915–14925, may 1999.

[270] K. V. Klitzing, G. Dorda, and M. Pepper. New Method for High-Accuracy Determination of the Fine-Structure Constant Based on Quantized Hall Resistance. *Physical Review Letters*, 45(6):494–497, aug 1980.

[271] P. Matl, N. P. Ong, Y. F. Yan, Y. Q. Li, D. Studebaker, T. Baum, and G. Doubinina. Hall effect of the colossal magnetoresistance manganite LaCaMnO3. *Physical Review B*, 57(17):10248–10251, may 1998.

[272] Y. Taguchi, Y. Oohara, H. Yoshizawa, N. Nagaosa, and Y. Tokura. Spin chirality, berry phase, and anomalous hall effect in a frustrated ferromagnet. *Science*, 291(5513):2573–2576, may 2001.

[273] C.-Z. Chang, J. Zhang, X. Feng, Jie Shen, Z. Zhang, Minghua Guo, Kang Li, Yunbo Ou, Pang Wei, L.-L. Wang, Z.-Q. Ji, Yang Feng, Shuaihua Ji, Xi Chen, Jinfeng Jia, Xi Dai, Zhong Fang, S.-C. Zhang, Ke He, Yayu Wang, Li Lu, X.-C. Ma, and Q.-K. Xue. Experimental Observation of the Quantum Anomalous Hall Effect in a Magnetic Topological Insulator. *Science*, 340(6129):167–170, apr 2013.

[274] Tian Liang, Jingjing Lin, Quinn Gibson, Satya Kushwaha, Minhao Liu, Wudi Wang, Hongyu Xiong, Jonathan A. Sobota, Makoto Hashimoto, Patrick S. Kirchmann, Zhi-Xun Shen, R. J. Cava, and N. P. Ong. Anomalous Hall effect in ZrTe5. *Nature Physics*, 14(5):451–455, may 2018.

[275] J. Kübler and C. Felser. Non-collinear antiferromagnets and the anomalous Hall effect. *Epl*, 108(6):67001, may 2014.

[276] E. Krén, G. Kádár, L. Pál, J. Sólyom, and P. Szabó. Magnetic structures and magnetic transformations in ordered Mn3(Rh, Pt) alloys. *Physics Letters*, 20(4):331–332, mar 1966.

[277] T. Berlijn, P. C. Snijders, O. Delaire, H. D. Zhou, T. A. Maier, H. B. Cao, S. X. Chi, M. Matsuda, Y. Wang, M. R. Koehler, P. R.C. Kent, and H. H. Weitering. Itinerant Antiferromagnetism in RuO2. *Physical Review Letters*, 118(7):2–7, may 2017.

[278] IE Dzyaloshinskii. The Magnetic Structure of Fluorides of the Transition Metals. *Sov. Phys. JETP*, 6(6):1120–1122, may 1958.

[279] Yugui Yao, Leonard Kleinman, A. H. MacDonald, Jairo Sinova, T. Jungwirth, Ding sheng Wang, Enge Wang, and Qian Niu. First Principles Calculation of Anomalous Hall Conductivity in Ferromagnetic bcc Fe. *Physical Review Letters*, 92(3):4, may 2004.

[280] Yan Sun, Yang Zhang, Chao-Xing Liu, Claudia Felser, and Binghai Yan. Dirac nodal lines and induced spin Hall effect in metallic rutile oxides. *Physical Review B*, 95(23):235104, jun 2017.

[281] Kei S. Takahashi, Hiroaki Ishizuka, Tomoki Murata, Qing Y. Wang, Yoshinori Tokura, Naoto Nagaosa, and Masashi Kawasaki. Anomalous Hall effect derived from multiple Weyl nodes in high-mobility EuTiO 3 films. *Science Advances*, 4(7):eaar7880, 2018.

[282] Kyoo Kim, Junho Seo, Eunwoo Lee, K. T. Ko, B. S. Kim, Bo Gyu Jang, Jong Mok Ok, Jinwon Lee, Youn Jung Jo, Woun Kang, Ji Hoon Shim, C. Kim, Han Woong Yeom, Byung Il Min, Bohm Jung Yang, and Jun Sung Kim. Large anomalous Hall current induced by topological nodal lines in a ferromagnetic van der Waals semimetal. *Nature Materials*, 17(September):1–6, 2018.

[283] S S P Parkin, E A Marseglia, and P J Brown. Magnetic structure of Co 1/3 NbS 2 and Co 1/3 TaS 2. *Journal of Physics C: Solid State Physics*, 16(14):2765–2778, may 1983.

[284] Enke Liu, Yan Sun, Nitesh Kumar, Lukas Muechler, Aili Sun, Lin Jiao, Shuo Ying Yang, Defa Liu, Aiji Liang, Qiunan Xu, Johannes Kroder, Vicky Süß, Horst Borrmann, Chandra Shekhar, Zhaosheng Wang, Chuanying Xi, Wenhong Wang, Walter Schnelle, Steffen Wirth, Yulin Chen, Sebastian T.B. Goennenwein, and Claudia Felser. Giant anomalous Hall effect in a ferromagnetic kagome-lattice semimetal. *Nature Physics*, 14(November):1125–1132, 2018.

[285] Muhammad Ikhlas, Takahiro Tomita, Takashi Koretsune, Michi-To Suzuki, Daisuke Nishio-Hamane, Ryotaro Arita, Yoshichika Otani, and Satoru Nakatsuji. Large anomalous Nernst effect at room temperature in a chiral antiferromagnet. *Nature Physics*, 13(11):1085–1090, jul 2017.

[286] Tomoya Higo, Huiyuan Man, Daniel B. Gopman, Liang Wu, Takashi Koretsune, Olaf M.J. Van 'T Erve, Yury P. Kabanov, Dylan Rees, Yufan Li, Michi To Suzuki, Shreyas Patankar, Muhammad Ikhlas, C. L. Chien, Ryotaro Arita, Robert D. Shull, Joseph Orenstein, and Satoru Nakatsuji. Large magneto-optical Kerr effect and imaging of magnetic octupole domains in an antiferromagnetic metal. *Nature Photonics*, 12(2):73–78, may 2018.

[287] A. Gerber. Interpretation of experimental evidence of the topological Hall effect. *Physical Review B*, 98(21):214440, dec 2018.